Hybrid INDI with enhanced FEP for the Flying-V

T.J.J. Traas 4653823

Delft University of Technology

TU Delft

Hybrid INDI with enhanced FEP for the Flying-V

by

T.J.J. Traas 4653823

in partial fulfillment of the requirements for the degree of
Master of Science
in Aerospace Engineering at the Delft University of Technology,
to be defended publicly on 9 October 2024 at 10 AM.

Thesis committee:	Chair:	ir. O. Stroosma
	Supervisor:	Dr. ir. E. van Kampen
	Additional Member	ir. D. Atmaca
	External examiner:	Dr.ir. E. Mooij
Project Duration:	3 January 2024 - 9 October 2024	

Cover image Flying-V from: `https://www.tudelft.nl/en/ae/flying-v/` visited at 10-09-2024.
Cover image background from:
`https://4kwallpapers.com/nature/sunrise-blue-sky-panorama-early-morning-dawn-5k-3644.html`
visited at 10-09-2024.

Preface

With this report, my time as a student comes to an end. During my bachelor's in Mechanical Engineering at the University of Twente, I learned about Control System Theory, which got me enthusiastic about a sector I didn't know existed but is all around us. As an Aerodynamics Engineer at Solar Team Twente, I wanted to combine my knowledge of aerodynamics and control systems, leading me to follow my master's in Control & Simulation at the Aerospace Faculty at the Delft Unversity of Technology.

The Flying-V project has intrigued me for as long as I can remember, and I am happy I got in touch with Dr. Ir. Erik-Jan van Kampen, who wanted to be my supervisor in a Flying-V-related Flight Control System project. I would especially like to thank him, as he helped me through some challenging aspects of this project. Furthermore, I would like to thank my colleagues Direnc, Ali, Bea, and Ramzi for working on the flight control system of the Flying-V, with whom I have had nice discussions and gave me a common feeling of working on a project. Project-based work and pioneering are two main aspects I enjoyed most while working on this project, which involves designing the aircraft of the future.

In addition to the academic guidance, I would like to thank my parents and girlfriend, who helped me see things in perspective and gave me the correct impulse whenever I needed it.

Tim Traas
Rotterdam, 23rd September, 2024

Summary

As air travel becomes increasingly more accessible than ever, driven by leaps in efficiency and safety, the aviation industry faces a pressing dilemma: reducing pollution and resource depletion, aspects that are fundamentally embedded in its operations. The Flying-V aircraft shows potential to become one of the most remarkable technological advancements in commercial aviation since the introduction of jet propulsion, increasing aerodynamic efficiency by an estimated 25%. However, before such an innovative design can become mainstream in the sector, research has to be done.

This research contributes to a collaborative effort of Delft University of Technology to develop the Flight Control System (FCS) of the Flying-V, capable of achieving Level 1 Handling Qualities (HQ) in normal law when the FCS is operational. These HQ requirements are evaluated by looking in at commonly used requirements from MIL-STD-1797A and EASA CS-25.

Van Overeem et al. and Stougie et al. have focused on implementing an Incremental Nonlinear Dynamic Inversion (INDI) control law but faced stability margin issues due to sensor delays and a deficient Flight Envelope Protection (FEP) structure. This research identified errors in the original simulation model that led to incorrect conclusions. The corrected model failed to meet pitch attitude bandwidth and equivalent time delay requirements, and the existing FEP structure proved inadequate to more excessive control inputs, causing instability for longitudinal, lateral, and direction control inputs.

A new type of controller, called a Hybrid INDI controller, has been suggested to enhance stability margins. This controller combines sensor-based and model-based information using a Complementary Filter (CF). While the stability margins have been improved to meet the phase margin requirements, not all gain margin requirements have been met due to limited control authority. The Low Order Equivalent System (LOES) approximation poses a problem with validating the different HQ, and there is inconclusive data about which HQ shall be used in succeeding research.

To improve the safety of the FCS, a different FEP structure has been implemented. Specifically, it is based on an exponential potential function Command Limiting structure. This structure stabilizes the FCS and provides adequate protection when the aircraft is on cruise. However, in the approach condition, the control inputs saturate the control surfaces, thus degrade the protection and safety of the FEP.

Contents

Acronyms

AM	Augmentation Matrix
AoA	Angle of Attack
BWB	Blended Wing Body
CA	Control Allocation
CAP	Control Anticipation Parameter
CF	Complementary Filter
CFD	Computational Fluid Dynamics
CoG	Center of Gravity
CoP	Center of Pressure
CS$_{activity}$	Control Surface Activity
CS$_{max}$	Maximum Control Surface Deflection
CTW	Conventional Tube-and-Wing
EASA	European Union Aviation Safety Agency
EoM	Equations of Motion
ESO	Extended-State-Observer
FAA	Federal Aviation Administration
FCS	Flight Control System
FEP	Flight Envelope Protection
FTD	Flight Test Data
HOS	High Order Equivalent System
HQ	Handling Qualities
IMU	Inertial Measurement Unit
INDI	Incremental Nonlinear Dynamic Inversion
LDCP	Lateral Control Departure Parameter
LOES	Low Order Equivalent System
LQR	Linear Quadratic Regulator
MAC	Mean Aerodynamic Chord
MIMO	Multiple Input-Multiple Output
MPC	Model Predictive Control
MTOM	Maximum Take-off Mass
MUAD	Maximum Unnoticeable Added Dynamics
NDI	Nonlinear Dynamic Inversion
OBM	On-Board-Model
OEI	One Engine Inoperative
OS	Overshoot
PCH	Pseudo Control Hedging
RL	Reinforcement Learning
RRMSE	Relative Root Mean Squared Error
SAC	Soft Actor-Critic
ST	Settling Time
TD3	Twin-Delayed Deep Deterministic Policy Gradient
VLM	Vortex Lattice Method
WTE	Wind Tunnel Experiment
ZoH	Zero-Order-Hold

Nomenclature

Symbols

$\bar{q}$	Dynamic pressure
$\boldsymbol{I_C}$	Moment of inertia matrix around Center of Gravity
$\mathbb{R}$	Rotational Matrix
I	Identity matrix
$I_{xx,yy,zz}$	Moment of inertia matrix around Center of Gravity, about the X, Y and Z-axis respectively
I_{xz}	Product of inertia matrix around Center of Gravity, rotating around the X-axis, measured around the Y-axis
l	Roll moment in body-fixed reference frame
M	Mach number
m	Pitch moment in body-fixed reference frame
n	Yaw moment in body-fixed reference frame
$p_{CoP,c.g.}$	Coordinate of Center of Pressure or Center of Gravity respectively
t	Time
T_{θ_2}	Incidence lag
V_∞	Free stream velocity
V_{FTO}	Final take-off speed
V_{REF}	Landing reference speed
V_{TAS}	True Air Speed

Greek Symbols

$\boldsymbol{\omega}$	Body rate vector
$\delta_{CS1_{L/R}}$	Control surface deflection of inboard elevon, left or right respectively
$\delta_{CS2_{L/R}}$	Control surface deflection of outboard elevon, left or right respectively
$\delta_{CS3_{L/R}}$	Control surface deflection of rudder, left or right respectively
c..	Abbreviation of cos ..
s..	Abbreviation of sin ..
ν	Virtual control command
ω_n	Undamped natural frequency
ϕ	Euler roll angle
ψ	Euler yaw angle
ρ_{air}	Air density
τ	Time delay
θ	Euler pitch angle
ζ	Damping of an oscillation

Subscripts

$\mathcal{A}$	State given in Aerodynamic Reference Frame
$\mathcal{B}$	State given in Body-Fixed Reference Frame
$\mathcal{E}$	State given in Vehicle-Carried Normal Earth Reference Frame

List of Figures

List of Tables

1 Introduction

The development of aviation represents a significant milestone in human history. This journey began with the Wright brothers' inaugural flight at Kitty Hawk in 1903 and has since evolved into today's extensive global air transport networks. A pivotal moment in this evolution was the introduction of jet propulsion in the mid-20th century, enhancing the speed and range of air travel and effectively making the world smaller. Flying, once an exclusive privilege for the elite, has become a regular mode of transport, with the aviation sector persistently broadening its scope. The remarkable growth in air travel in recent decades can be attributed to several factors: the progress of economic globalization, technological breakthroughs, and the rise of a travel-enthusiastic middle class. The accessibility of air travel has significantly increased, paralleled by advancements in efficiency and safety. These improvements are largely due to ongoing innovations in aircraft design, propulsion systems, and avionics.

However, this growth has not been without challenges. With the increasing demand for air travel, there has been increasing criticism regarding environmental impact, noise pollution, and resource depletion. The aviation industry is therefore looking for different methods to solve these issues, however, since the introduction of commercial aircraft, the concept of fuselage, wing and tail also known as Conventional Tube-and-Wing (CTW) has never changed. One of the most promising innovations is the flying wing aircraft concept, which combines all components of a CTW into one functional design. This concept has been used multiple times, for example, in the iconic B-2 Spirit from Northrop Grumman, but was solely used for military applications. Liebeck first applied this concept, named the Blended Wing Body (BWB), for commercial aviation [1]. He posed a 15% decrease in take-off weight and a 27% reduction in fuel burn per aircraft seat. Although these advantages are significant, challenges still have to be overcome before such an aircraft can replace the CTW. There are problems with the static and dynamic stability, structural shaping of the cabin, lift characteristics that make a normal approach impossible, aircraft scaling, and passenger comfort uncertainties. Therefore, research is needed to revolutionize the aviation industry, just as was done with the introduction of jet propulsion.

Delft University of Technology has since started research, with a change in concept, first introduced by Benad [2]. The Flying-V, as this aircraft is called, is a V-shaped aircraft, contrary to a BWB, which is more shaped like a triangle. There has since been a big contribution to the research, with many engineers contributing to different aspects of the plane. An advantage of the Flying-V concept is the flexible scalability of the aircraft, with the most prominent concept being compared to an Airbus A350-900 due to similar range and passenger capacity [3]. This research will focus on developing a more advanced Flight Control System (FCS) for the Flying-V. Previously, there has been research to assessing the handling qualities of the Flying-V [4], using wind tunnel test data [5], Computational Fluid Dynamics (CFD) simulation results [6], [7], data from a 4.6% scale model test flight [8], [9]. These models were also used to assess pilot-in-the-loop handling qualities in the SIMONA Full-Flight-Simulator of the Delft University of Technology [10]–[12]. It was concluded that the aircraft experiences pitch break-up above Angle of Attack (AoA) of 20 ° [8], the Dutch Roll eigenmode is unstable [4] and there is low lateral control authority [4]. Furthermore, without a FCS the pilot-in-the-loop handling qualities were not satisfactory [10], [11].

From these conclusions, Van Overeem [13] researched the implementation of an Incremental Nonlinear Dynamic Inversion (INDI) control system, which makes use of sensor data to linearize the nonlinear dynamic behavior of the aircraft, from which the system can be controlled. This implementation showed proper results; however only evaluated the flight envelope on two conditions: approach and cruise. Furthermore, unrealistic assumptions were made with ideal actuators and sensors. Stougie [14] continued with this research, maturing the FCS by also implementing a Flight Envelope Protection (FEP) system to account for the pitch break-up, which he found only occurred at an AoA of $\alpha \geq 30°$. With his implementation, the checked handling qualities were all satisfied for the highest level of qualification; however, he still found limitations to the current system. Especially, the effect of time delay on the sensors degrades the system's

performance quickly, making the system unstable with a time delay of $\tau =\geq 0.04$s. The reference sensors, as proposed by Stougie, have a time delay of $\tau = 0.1$s. This means the current sensors need to be replaced, or the system should be robust enough to handle time delays. Furthermore, the current FEP performs satisfactorily but shows an overshoot, which is not desirable for a protection system, together with limited validation points across the flight envelope.

For the time delay, an addition to INDI, named Hybrid INDI, was proposed by Stougie [14]. This method has been researched previously, but mostly for fighter aircraft [15]–[17]. Hybrid INDI makes use of the robustness against uncertainties from sensor-based INDI, while also taking into account the predicted model output, from the model-based Nonlinear Dynamic Inversion (NDI). This hybridization can be done using different methods and significantly improves robustness against time delay [18]. Therefore, this thesis will focus partly on implementing Hybrid INDI in the current FCS for the Flying-V.

To further improve the safety of the FCS, the FEP system will be improved. The current system does not stick within the set boundaries and does not include protections according to industry standards. This can be solved by applying more advanced techniques and extending the protected states of the FEP structure.

1.1. Research Definitions and Questions

With the current problems of the FCS, it is important to define specific definitions properly and clearly state this research's goal and research questions.

Definition 1: Sensor-Based INDI

Incremental Nonlinear Dynamic Inversion, commonly called incremental, uses sensor measurements instead of model information. This is the state-of-the-art controller structure implemented in the Flying-V, most recently by Stougie.

Definition 2: Model-Based INDI

Conventionally named Nonlinear Dynamic Inversion uses model information to control a system. The author deems it better to name it Model-Based INDI, as the combination of Sensor-Based INDI and Model-Based INDI makes Hybrid INDI.

Definition 3: Hybrid INDI

Hybrid INDI combines model-based predictions and sensor-based measurements with the dynamic inversion principle.

Definition 4: INDI/Hybrid INDI controller system

This name will be used throughout this research to refer to the controller structures combined with the respective dynamic models (actuator, aircraft, and sensors).

Definition 5: Controller structure

This naming will be used throughout this research to refer solely to the controllers in each controller system. The dynamic models are excluded.

Definition 6: Original controller system

Controller system made by Overeem et al. [13] and Stougie et al. [14], which has been the baseline model from which this research was started.

Definition 7: Updated controller system

According to the author, a controller system with adaptations to the original model to make the Flying-V controller structure more realistic and correct. The changes made to the original controller system have been documented in Chapter 5.

By incorporating these definitions into the research, the scope can be set, and it is essential to consider these definitions when reading this thesis. The goal of this thesis can be defined as follows:

"The goal of this research is to improve performance, mature the simulation model, and enhance safety focussing on envelope protection, within the context of the Flight Control System (FCS) of the Flying-V aircraft."

Specific questions are stated below to help reach this goal.

1. What are the current limitations of the Flight Control System of the Flying-V?
   - What requirements can be used to verify the FCS?
2. What is the state of the art in Hybrid INDI control and FEP?
3. How are performance and fault-tolerance affected by the implementation of Hybrid INDI as the Flight Control System of the Flying-V?
   (a) How does the Hybrid INDI controller handle model uncertainties in the mass, inertia, control surface characteristics, and aerodynamic uncertainties?
   (b) How does the Hybrid INDI controller handle sensor uncertainties looking at time delay and air density uncertainty?
4. How can FEP be improved to enhance the overall safety of the Flying-V aircraft?
5. How will the FCS perform with a Hybrid INDI including an enhanced FEP compared to the current FCS?

1.2. Research Plan

To address the research question provided above, the following research plan will be utilized to achieve the established goal. First, the research will start with a literature review, through which research questions 1 and 2 will be investigated to provide an answer to research questions 1 and 2. After this review, the original simulation model will be evaluated to conclude the research question 1.

Next, the updated controller structures for Hybrid INDI and FEP are implemented in separate models. For the Hybrid INDI implementation, the outer-loop controllers will be tuned to partly answer research question 3, comparing Hybrid INDI and sensor-based INDI. Following, uncertain parameters are introduced in the simulation model to answer the subquestions 3a and 3b from which the remainder of research question 3 can be answered.

Research question 4 will be answered by time-domain tests comparing the original and updated FEP structure. These tests will consist of longitudinal, lateral, and combined pilot command inputs, testing the limits of each respective protected state. Following from research questions 3 and 4, the performance of the Hybrid INDI control law combined with the updated FEP is compared with the original INDI control law with FEP and answered in research question 5.

Figure 1.1 shows an overview of the research plan and planning of this research, indicating at which step and in which corresponding chapter the given research questions are answered. Figure 1.1 also shows a planning of the different stages of this research, following by corresponding weeks in which these stages have been performed, with a total of 39 weeks in this research.

1.3. Report Outline

The outline of this report is as follows: there are three parts, starting with the scientific paper in Part I. Next, the literature study is presented in Part II, with information about different methods used in this research, summarized in the scientific paper. To go into more detail, the literature study has three main chapters within Part II. Firstly, in chapter 2, a background of the Flying-V concept is given, in which the research is highlighted that has been done. Furthermore, the necessary characteristics of the aircraft that are needed to model it are provided, and assumptions about these characteristics are concluded. Chapter 3 highlights the different methodologies for implementing a FCS highlights the Hybrid INDI and Flight Envelope Protection (FEP) methods, together with highlighting the limitations of the original controller system. Chapter 4 will review the different techniques to evaluate the FCS, eventually concluding with the methods that will be used in this research to assess the FCS. Part III will continue with additional results, contributing to the results shown in the scientific paper. Chapters 5 and 6 explain the changes made to the original simulation model, focusing on model modifications and the trim routine. Next, Chapter 8 presents additional, supporting results for the analysis of the Hybrid INDI control structure, and Chapter 10

shows additional results for the FEP in approach. Part IV concludes this research by answering the research questions and providing recommendations for future research. Appendix A presents supporting Figures for HQ assessment.

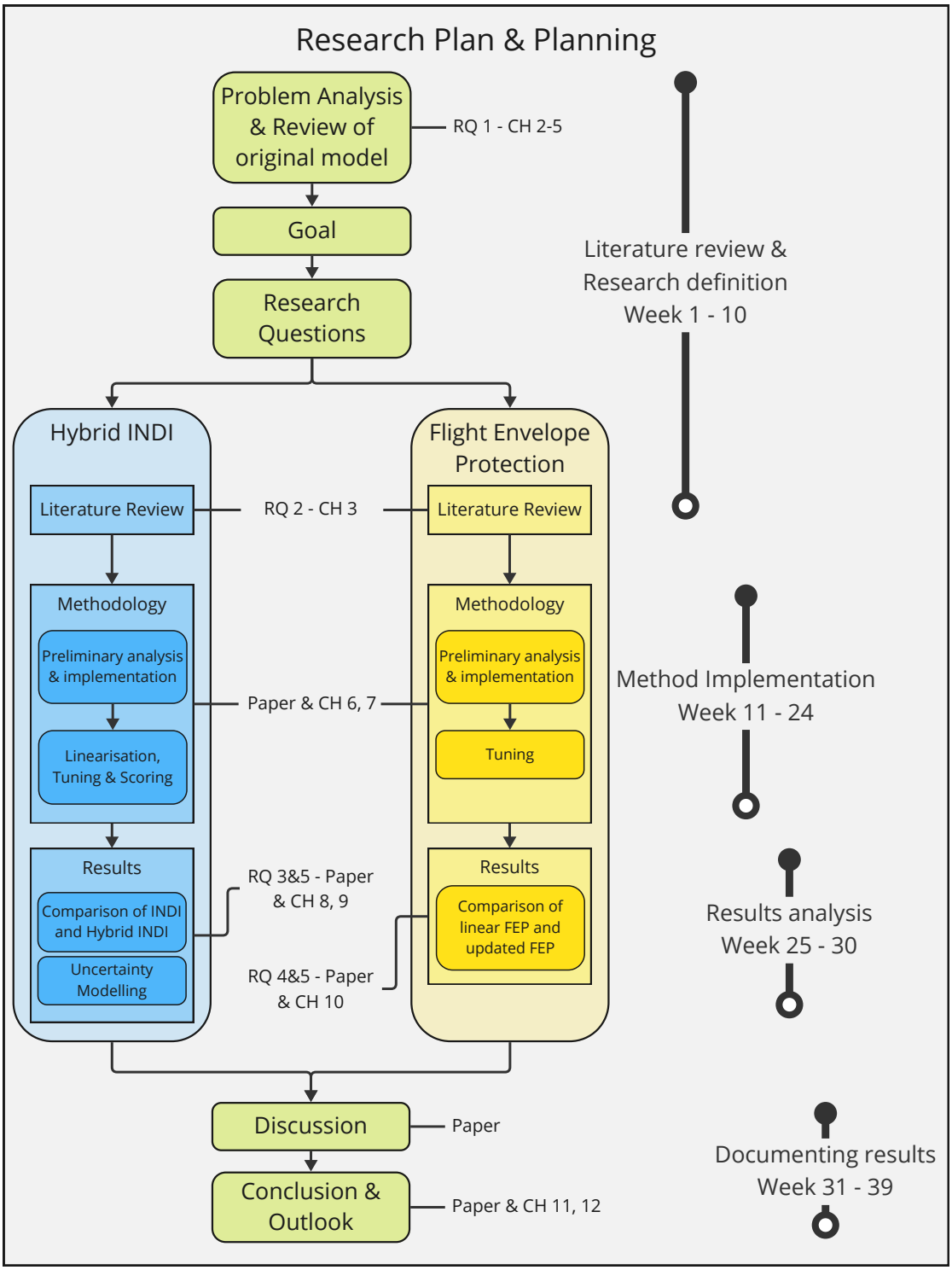

Figure 1.1: Research plan & planning

I

Scientific Paper

Hybrid INDI flight control with Flight Envelope Protection for the Flying-V

T.J.J. Traas ∗
Delft University of Technology, Delft, 2629HS, The Netherlands

The Flying-V aircraft could revolutionize commercial aviation, boasting a potential 25% increase in aerodynamic efficiency. Due to inherent design limitations regarding static stability, the need for a proper Flight Control System (FCS) is essential for the development of the aircraft. The concept of Hybrid Incremental Nonlinear Dynamic Inversion (INDI) was introduced to mitigate the insufficient stability margin encountered in existing sensor-based INDI systems due to sensor time delays to achieve Level 1 Handling Qualities (HQ). Furthermore, the research introduces an exponential potential function-based command limiting Flight Envelope Protection (FEP) to enhance safety compared to the currently implemented linear-based FEP. The study compares and evaluates the effectiveness of the updated system under various flight conditions and parametric uncertainties. Results show improved stability margins and a safer FEP. However, additional research is required into actuator saturation and control allocation issues during the approach condition and to enhance fault tolerance.

I. Introduction

DESPITE the aviation industry's accomplishment in connecting the world, the increasing demand for air travel has its downsides, increasing awareness of environmental impacts, noise pollution, and resource depletion. The range of conventional commercial aircraft has increased by 100% in the last 50 years, but one aspect has remained the same: the aircraft layout [1]. Conventional Tube-and-Wing (CTW), as this layout is called, has the drawback that its major component, the fuselage, contributes minimally to the lift generated and significantly adds to the drag, reducing the efficiency. One promising innovation is the flying wing aircraft concept, which merges all components of a CTW into a single design. While this concept, exemplified by the B-2 Spirit, has been primarily used for military applications, its potential for commercial aviation was first proposed by Liebeck with the Blended Wing Body (BWB), promising significant reductions in take-off weight and fuel consumption [2].

Delft University of Technology has further advanced this concept with the Flying-V. This V-shaped aircraft offers flexible scalability and is comparable to an Airbus A350-900 in range and passenger capacity [3], with an expected efficiency increase of 25%, compared to an Airbus A350-900 [4]. As this type of layout has not been used previously within commercial aviation, there are still deficiencies before the Flying-V can replace its predecessor CTW aircraft.

From a flight control standpoint, the objective of the Flying-V project is to achieve Level 1 Handling Qualities (HQ), with the incorporation of a Flight Control System (FCS) based on MIL-STD-1797A [5], a conventional aircraft design standard. From the most recent aerodynamic analyses of the bare airframe, it was concluded that the aircraft experiences pitch break-up above Angle of Attack (AoA) of 30° [6], the Dutch Roll eigenmode is unstable [7] and there is low lateral control authority [7]. Van Overeem et al. [8] implemented an Incremental Nonlinear Dynamic Inversion (INDI), after which Stougie et al. [6] matured the FCS by looking at time delay, implementing a Flight Envelope Protection (FEP) and evaluating HQ for cruise and approach. Stougie et al. concluded that the sensor-based INDI controller system did not meet the level 1 HQ requirement as time delay affected the stability margins [6]. The incorporated FEP showed an overshoot for the AoA for low magnitude inputs, suggesting the FEP structure should be improved.

The contributions of this paper are to improve the performance of the current FCS, mature the simulation model, and increase safety by enhancing the FEP of the FCS for the Flying-V aircraft. This will involve implementing a Hybrid INDI control law with an exponential potential function Command Limiting FEP structure and comparing it to the controller system, which is based on a sensor-based INDI controller with a linear-based FEP [6]. Hybrid INDI is widely recognized for its capacity to address the time delay drawback associated with sensor-based INDI FCS [9, 10], improving the stability margins. Furthermore, an exponential potential function Command Limiting FEP structure is a versatile method of applying state protection [11].

The structure of this paper is as follows: section II will explain the Flying-V characteristics and define model

∗MSc Student, Control and Simulation Division, Faculty of Aerospace Engineering, Kluyverweg 1

properties used throughout this research. Next, section III defines the original controller structure implemented by Stougie et al. [6] and updated controller system, highlighting the implementation of Hybrid INDI and all subsystems in the simulation model, including the updated FEP. Section IV will highlight the requirements for which the controller system will be tested and how these requirements are used to tune the controller structure. Furthermore, section V will show and elaborate on the results of this research, also highlighting the fault tolerance capabilities of the updated Hybrid INDI controller system and comparing to the linear FEP from Stougie et al. [6], with the updated FEP. Lastly, section VI will summarize the findings of this research and advise the direction of further research regarding the challenges FCS of the Flying-V, aiming to achieve the goal of level 1 HQ.

II. Flying-V Aircraft Characteristics

This section describes the characteristics of the Flying-V aircraft, which are fundamental for the controller structure implementation of this research. Firstly, the dimensions and control surface layout are defined. Next, the aerodynamic model is determined, and the flight conditions and their respective trim conditions are given. Next, conclusions about handling the bare airframe are described as limiting for the FCS design. Lastly, the characteristics of sensors and actuators used in this research are accompanied by the discretization method used to acquire linear models.

A. Dimensions & Control Surface Layout

The Flying-V V1000, researched by Cappuyns [7], is used as a base model for this research. The dimensions of that aircraft, with its respective control surface layout, are shown in Table 1 and Figure 1. The most important characteristics are the $p_{c.g.}$ and x_{pilot} as these determine how far the pilot is located from the Center of Gravity (CoG). In the research of van Overeem et al. [8] and Stougie et al. [6], this point was miscalculated, causing the load factor at the pilot station to be underestimated, which will later be shown as a crucial validation parameter. Vugts et al. [12] and Torelli et al. [13] performed flight simulator tests for the Flying-V aircraft, for which the distance was set to be 26.3m from $p_{c.g.}$ and x_{pilot}, with a $p_{c.g.}$ = 31.3m at 55% MAC. This gives x_{pilot} = 5.00 m.

B. Aerodynamic Model Definition

This section will briefly describe the aerodynamic model used in this research. The aerodynamic model has been directly taken from van Overeem et al. [8]. Firstly, the aerodynamic model limitations are highlighted after which the trimmed condition is shown.

1. Model Limitations

The model limitations present in the current research mostly depend on a lack of information about the bare airframe. Firstly, the aerodynamic model derived from van Cappuyns [7] and Overeem et al. [8] uses linear aerodynamic relations and lacks data for the control surface effectiveness. It is therefore assumed that the inboard elevon, $CS1$, does not influence roll or yaw axes, and $CS2$ and $CS3$ do not affect the pitch axis. Next, the used engine model assumes a maximum constant thrust across the flight envelope. In contrast, the maximum thrust provided in Table 3 is not specified for the flight condition since the maximum available thrust changes through the flight regime [14]. Lastly, there is a lack of understanding regarding the inertia differences between maximum and minimum mass at different CoG positions.

2. Trim condition

For linear analysis, used in tuning and validating the HQ, the trim condition must have zero residual state derivative to avoid changes in any state. It was found that the trim routine, implemented by van Overeem et al. [8] would not bring the aircraft in a trim condition for the prescribed flight condition, so it is uncertain if the results achieved from the linear analysis are accurate. The trim conditions for the two flight conditions considered in this research are shown in Table 2.

Table 2 Trimmed aircraft states at Approach and Cruise

	m $[kg]$	h $[m]$	M [-]	V_∞ $[m/s]$	α [°]	$CS1_{L/R}$ [°]	$CS2_{L/R}$ [°]	$CS3_{L/R}$ [°]	$T_{1/2}$ $[kN]$
Approach	2.10×10^5	1000	0.200	67.3	23.3	20.1	21.4	0	268
Cruise	2.40×10^5	13000	0.850	250.8	7.01	6.41	9.40	0	124

Table 1 Flying-V Properties [7, 12]

Parameter	Value	Unit
T_{dy}	±5.60	m
T_{dz}	0.800	m
S	883	m^2
c_{MAC}	18.7	m
$p_{c.g.}$	29.4	m
x_{pilot}	5.00	m
b	65.0	m
L	55.0	m
Height	17.0	[m]
Pax	314	[-]
Fuel Capacity	140.000	[l]
Cargo Capacity	160	[m^3]

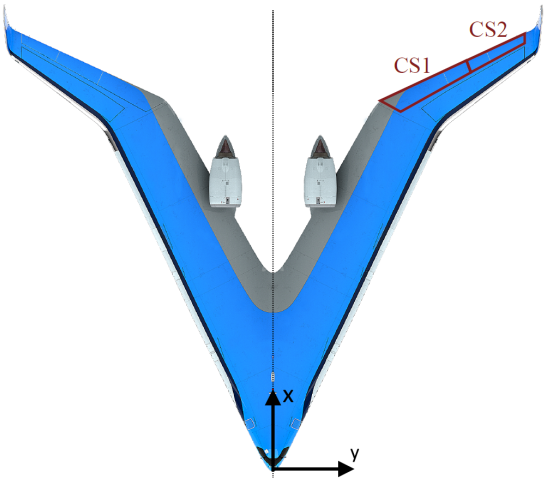

(a) Top view Flying-V

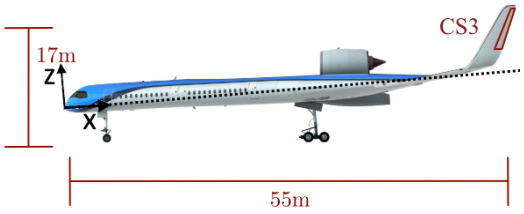

(b) Side view Flying-V

(c) Front view Flying-V

Fig. 1 Flying-V: 2 elevon control surface layout [7]

C. Actuators & Sensors

The actuator and sensor characteristics are crucial parameters for the performance of the control system. Equation 1 illustrates the transfer functions utilized in this study to characterize the dynamics of the control surface, engine, and sensor. These dynamics have been derived from Matamoros & de Visser [15]. It should be noted that the actuator dynamics from Matamoros & de Visser were derived for fighter aircraft. In contrast, conventional large passenger aircraft are typically in the order of $\zeta_{act} = 1$ and $\omega_{act} = 20$ rad/s [16]. In this research, the dynamics derived from Matamoros & de Visser are used with $\zeta_{act} = 1.11$ and $\omega_{act} = 63.2$ rad/s, as used by Stougie et al. [6].

$$H_{act} = \frac{\omega_{act}^2}{s^2 + 2\zeta_{act}\omega_{act}s + \omega_{act}^2} = \frac{4000}{s^2 + 140s + 4000}, \quad H_{eng} = \frac{1}{0.2s + 1}, \quad H_{sens} = \frac{1}{\tau_{filt}s + 1}e^{-\tau_d s} \tag{1}$$

Table 3 displays the actuator position and rate limits, as well as the utilized dynamics for each actuator. Next, Table 4 shows the characteristics used in this research. Stougie et al. changed the characteristics of several sensors, indicated by a right arrow, to achieve consistent Level 1 HQs, for the tested requirements [6].

Table 3 Control Effector Parameters [8, 17]

Control effector	Notation	Actuator limits	Rate limit [°/s]	Dynamics
Outboard Elevon	$CS1_L, CS1_R$	[-25, 25] [°]	80	$H_{act}(s)$
Inboard Elevon	$CS2_L, CS2_R$	[-25, 25] [°]	80	$H_{act}(s)$
Rudder	$CS3_L, CS3_R$	[-30, 30] [°]	120	$H_{act}(s)$
Engine thrust	δ_{T1}, δ_{T2}	$[0, 3.176 \cdot 10^5]$ [N]	-	$H_{eng}(s)$

Table 4 Baseline Sensor Characteristics [6]

Sensor	Sampling rate [Hz]	Time delay [s], τ_d	Noise $[\sigma^2]$	Bias	Filter time constant [s], τ_{filt}
p, q, r [rad/s]	50	$0.1 \rightarrow 0.04$	$1 \cdot 10^{-9}$	$3 \cdot 10^{-5}$	$0.05 \rightarrow 0.03$
ϕ, θ [rad]	50	0.1	$1 \cdot 10^{-9}$	$4 \cdot 10^{-3}$	0.05
V [m/s]	$\frac{1}{0.065}$	0.325	$1 \cdot 10^{-4}$	2.5	0.05
α [rad]	50	0.1	$7.5 \cdot 10^{-8}$	$3 \cdot 10^{-5}$	0.05
β [rad]	50	0.1	$7.5 \cdot 10^{-8}$	$3 \cdot 10^{-5}$	$0.05 \rightarrow 0.1$
A_x, A_y, A_z [g]	50	0.1	$1 \cdot 10^{-5}$	$2.5 \cdot 10^{-3}$	0.05

III. Controller Structure

As shown by Van Overeem et al. [8], the lateral eigenmodes are unstable, yielding the need for a FCS. To maintain performance and safety, gain scheduling techniques were used to extend the flight envelope [18]. In between these gain scheduling parameters, performance can still not be guaranteed due to non-linearities and uncertainties [19]. Therefore, Slotine & Li [19] proposed nonlinear control techniques, which have served as the foundation for numerous modern control techniques. The current implemented FCS of the Flying-V is based on INDI, a feedback linearization technique [6, 8]. This section will give the reader a basic understanding of the control law that has to do with INDI, leading to the implementation of Hybrid INDI.

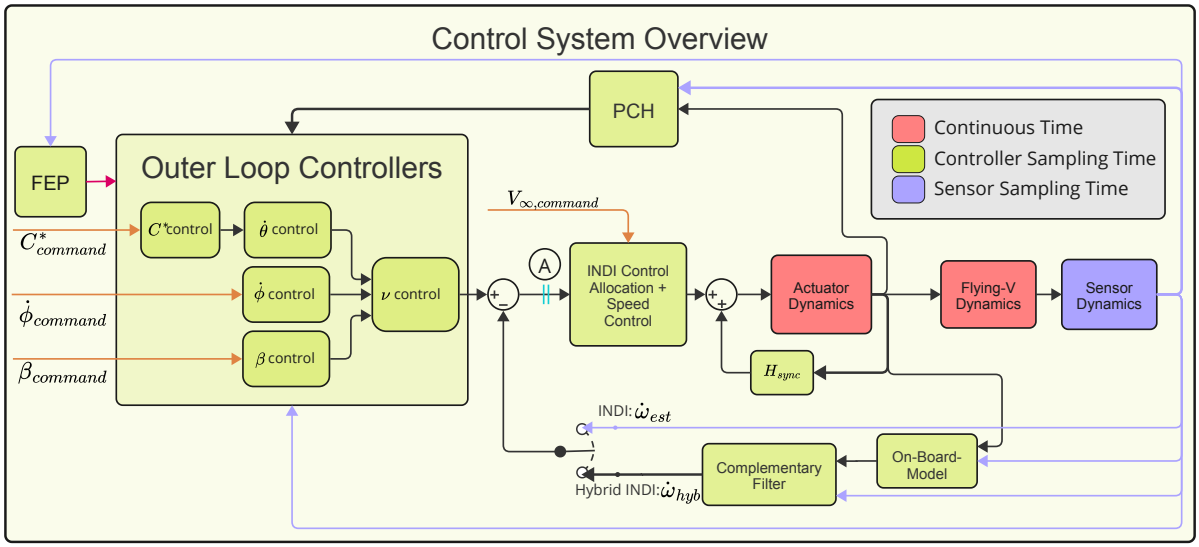

Fig. 2 INDI/Hybrid INDI Controller System Overview

A. Incremental Nonlinear Dynamic Inversion

The basic principle of INDI is strongly related to its model-based counterpart, Nonlinear Dynamic Inversion (NDI). The interested reader is referred to Pollack [16] for an elaborated background and derivation of the NDI control law. While a NDI offers an advantage over conventional linear control laws by simplifying gain scheduling, it is less effective in addressing model mismatch [20]. INDI addresses some of these limitations by reducing the need for a detailed On-Board-Model (OBM). It only requires the control effectiveness terms, which in itself can lead to a complex model [15]. The basic principle of INDI is derived below in Equations 2, 3, 4 and 5 but has been documented numerous times

[21, 22]. Consider a general control affine Multiple Input-Multiple Output (MIMO) system, shown in Equation 2.

$$\begin{aligned} \dot{\boldsymbol{x}} &= \boldsymbol{f}(\boldsymbol{x}) + \boldsymbol{G}(\boldsymbol{x})\boldsymbol{u} \\ \boldsymbol{y} &= \boldsymbol{h}(\boldsymbol{x}) \end{aligned} \tag{2}$$

Here, the state vector $\boldsymbol{x} \in \mathbb{R}^n$, input vector $\boldsymbol{u} \in \mathbb{R}^m$ and output vector $\boldsymbol{y} \in \mathbb{R}^m$ are described by the smooth mapping functions, $\boldsymbol{f}, \boldsymbol{G}$, and $\boldsymbol{h}$. A first-order Taylor expansion is taken around the point $\boldsymbol{x}_0, \boldsymbol{u}_0$.

$$\dot{\boldsymbol{x}} = \dot{\boldsymbol{x}}_0 + \frac{\partial}{\partial \boldsymbol{x}} \left[\boldsymbol{f}(\boldsymbol{x}) + \boldsymbol{G}(\boldsymbol{x})\boldsymbol{u}\right]_{\boldsymbol{x}_0, \boldsymbol{u}_0} (\boldsymbol{x} - \boldsymbol{x}_0) + \frac{\partial}{\partial \boldsymbol{u}} \left[\boldsymbol{f}(\boldsymbol{x}) + \boldsymbol{G}(\boldsymbol{x})\boldsymbol{u}\right]_{\boldsymbol{x}_0, \boldsymbol{u}_0} (\boldsymbol{u} - \boldsymbol{u}_0) \tag{3}$$

With INDI it is assumed that the sampling time of the controller system is sufficiently high to make the Time-Scale-Seperation assumption hold, which yields that the state-dependent increments $\partial \boldsymbol{f}(\boldsymbol{x})/\partial \boldsymbol{x}$ change an order of magnitude slower compared to the input-dependent increments, $\boldsymbol{G}(\boldsymbol{x})$, thus neglecting the state-dependent terms, further elaborated upon by Falkena [23]. Stougie et al. studied the effect of the sampling time and concluded that with the set sampling frequency of f_s=100 Hz, the tracking error does not impose problems concerning this assumption [6]. This gives that $\boldsymbol{x} \approx \boldsymbol{x}_0$ [22]. Furthermore, based on the control affine assumption, the mapping function $\boldsymbol{f}$ representing the system's dynamics is assumed to be independent of the input vector, $\boldsymbol{u}$. The resulting simplified MIMO system from Equation 2 is given in Equation 4, together with the definition of $\boldsymbol{G}(\boldsymbol{x})$ within this research.

$$\begin{aligned} \dot{\boldsymbol{x}} &\approx \dot{\boldsymbol{x}}_0 + \boldsymbol{G}(\boldsymbol{x})(\boldsymbol{u} - \boldsymbol{u}_0) \\ \text{where } \boldsymbol{G}(\boldsymbol{x}) &= \frac{\rho V_\infty^2 Sc}{2} {\boldsymbol{I_C}}^{-1} \begin{bmatrix} C_{l_{CS1_L}} & C_{l_{CS1_R}} & C_{l_{CS2_R}} & C_{l_{CS2_R}} & C_{l_{CS3}} \\ C_{m_{CS1_L}} & C_{m_{CS1_R}} & C_{m_{CS2_R}} & C_{m_{CS1_R}} & C_{m_{CS3}} \\ C_{n_{CS1_L}} & C_{n_{CS1_R}} & C_{n_{CS2_R}} & C_{n_{CS2_R}} & C_{n_{CS3}} \end{bmatrix} \\ \boldsymbol{y} &= \boldsymbol{h}(\boldsymbol{x}) \end{aligned} \tag{4}$$

By assuming $\dot{\boldsymbol{y}} = \dot{\boldsymbol{x}}$, even though there are sensor dynamics, the virtual control law for the INDI loop can be made. The control surfaces can be controlled by manipulating Equation 4 into Equation 5. The virtual command signal is defined as the desired $\dot{\boldsymbol{x}}$ and was chosen by Stougie et al. to be the rotational body accelerations, $\boldsymbol{\nu} = \dot{\boldsymbol{\omega}}$ [6]. Since $\boldsymbol{G}(\boldsymbol{x})$ is a non-square matrix, it will be replaced by $\mathcal{B}^{-1}(\boldsymbol{x})$, which is the Moore-Penrose inversion of $\boldsymbol{G}(\boldsymbol{x})$ [15].

$$\boldsymbol{u} = \boldsymbol{u}_0 + \mathcal{B}^{-1}(\boldsymbol{x})(\boldsymbol{\nu} - \dot{\boldsymbol{x}}_0) \tag{5}$$

Due to the absence of an angular acceleration sensor in the current controller system, the rotational body accelerations have to be approximated, which is currently done by a second-order filter [6]. As stated above, the sensor dynamics are neglected in the derivation above, but cannot be neglected and decrease performance and robustness of the current INDI controller structure [6], which is where Hybrid INDI comes in.

B. Hybrid INDI

Stougie et al. concluded that the desired level 1 HQ cannot be met with the base sensor implementation, shown in Table 4 [6]. The sensor characteristics were changed to achieve the set HQ. The biggest problem was the lack of gain and phase margin when breaking the loop at location A in Figure 2. Hybrid INDI was proposed as a suitable solution to make the system less reliant on the sensor characteristics and achieve a trade-off between fault-tolerance characteristics from Sensor-Based INDI and the performance of Model-Based INDI, which has already been highlighted in previous research [9, 10, 24, 25]. The addition and changes to the conventional, existing Sensor-Based INDI controller system for the Flying-V are shown in Figure 2. Instead of using a second order filter to approximate $\dot{\omega}_{est}$, the knowledge of the aerodynamic model and Equations of Motion (EoM) of the system, the OBM, can be used to estimate a state derivative of the virtual control inputs. Together with the measured body rates, using a Complementary Filter (CF), the estimated $\dot{\omega}_{hyb}$ can be used as a feedback signal for the inner loop.

1. Complementary Filter

The chosen method for this research to combine the predicted body accelerations by the OBM and the measured body rates by the Inertial Measurement Unit (IMU) is the CF. As the name suggests, the CF uses information that complements

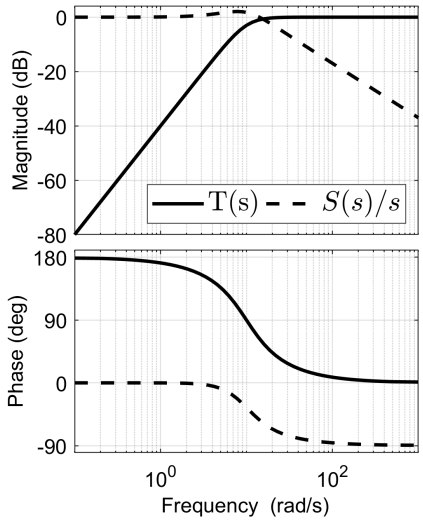

Fig. 3 Frequency response of CF

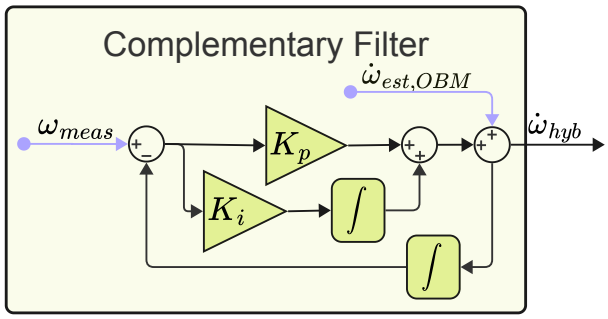

Fig. 4 Complementary Filter Overview

the advantages and weaknesses of the incoming signals. High-frequency noise from the IMU is attenuated by a low-pass filter, and low-frequency model inaccuracies from the OBM are filtered by a high-pass filter. The schematic overview of the CF used in the Hybrid INDI controller system is shown in Figure 4, with the transfer function shown in Equation 6. This structure has been used by Kim et al. [10] and poses an efficient method to attenuate sensor delay and noise, compared to conventional INDI.

$$\hat{\boldsymbol{x}} = \boldsymbol{T}(s)\dot{\boldsymbol{x}}_{obm}(s) + \boldsymbol{S}(s)\boldsymbol{x}_{meas}(s) = \frac{s^2}{s^2 + \boldsymbol{K}_p s + \boldsymbol{K}_i}\dot{\boldsymbol{x}}_{obm}(s) + \frac{(\boldsymbol{K}_p s + \boldsymbol{K}_i)s}{s^2 + \boldsymbol{K}_p s + \boldsymbol{K}_i}\boldsymbol{x}_{meas}(s) \tag{6}$$

The measured body rates, ω_{meas}, coming from the IMU are essentially filtered using a linear PI controller, with controller gains, K_p=$2\zeta_{CF}\omega_{n,CF}$ and K_i=$\omega_{n,CF}$. The frequency response of a given CF, with $\zeta_{CF} = \sqrt{2}/2$ and $\omega_{n,CF} = 10$ rad/s is shown in Figure 3. The selection of these parameters determines the dependency on either model-based or sensor-based INDI. A higher $\omega_{n,CF}$ will generally give a better response to uncertainties and external disturbances, while decreasing $\omega_{n,CF}$ will counteract the sensor characteristics and will increase phase margins [10, 26]. Within this research, the damping will be set to $\zeta_{CF} = \sqrt{2}/2$, generally considered as a satisfactory damping coefficient. The variable, ζ_{CF}, is fixed to reduce the number of free variables when tuning.

2. Control Allocation

From Equation 4, the smooth mapping function $\boldsymbol{G}(\boldsymbol{x})$, representing the control surface effectiveness matrix, is inverted to achieve the inner loop control law. However, as three axes are being controlled for the angular accelerations by five control surfaces, where the rudder movement is synchronized, the control problem is over-defined, and Control Allocation (CA) is implemented. The CA scheme of this research was fully based on the implementation of Stougie et al. [6], based on Li et al. [27].

The maximum requested incremental control deflections are calculated using Equation 7. Stougie et al. set up different scenarios to take into account control surface saturation. In case of saturation, the respective control surface would be removed from the matrix $\boldsymbol{G}(\boldsymbol{x})$. For a more elaborated description of this algorithm, the author refers to Stougie et al. [6].

$$\Delta\boldsymbol{u}_{max} = \min\left(\dot{\boldsymbol{u}}_{max}\frac{\omega_{act}}{2\zeta_{act}}, \boldsymbol{u}_{max} - \boldsymbol{u}\right) \text{ and } \Delta\boldsymbol{u}_{min} = \max\left(\dot{\boldsymbol{u}}_{min}\frac{\omega_{act}}{2\zeta_{act}}, \boldsymbol{u}_{min} - \boldsymbol{u}\right) \tag{7}$$

After running the algorithm, the matrix $\boldsymbol{G}(\boldsymbol{x})$ is inverted based on the remaining control surfaces. Nominally, the matrix would be inverted using a Moore-Penrose inversion, providing the inverted matrix, $\mathcal{B}^{-1}(\boldsymbol{x})$. If there are saturated control surfaces, this method is adjusted, as the size of $\boldsymbol{G}(\boldsymbol{x})$ would change [6].

C. Synchronisation Filter

This section describes the implementation of the synchronization filter for the Hybrid INDI controller system. Synchronization is necessary to implement INDI, as shown in previous research [28, 29]. Synchronization is needed between the input and virtual command signals as the measured state derivatives provide the controller with a command signal, which is affected by the feedback loop characteristics.

In the controller system implemented by Stougie et al. [6], the control surface command signal is synchronized using the filter dynamics to acquire the body acceleration signal. The commanded control surface signal is multiplied by the filter dynamics for the virtual command signal, taking into account an additional 2ms, on top of the known body rate sensor time delay, to compensate for the lag due to the filter dynamics and unaccounted delays [6, 21].

The synchronization filter becomes more complex for systems that use Hybrid INDI. As the filtering and hybridization have to be fed back, this has to be compensated. Therefore, the synchronization filter is chosen depending on the method selected for hybridization. As a CF is used in this research and it is assumed that the input signal is the measured control surface deflection, the used CF is shown in Equation 8 [25, 26].

$$\boldsymbol{H_{sync}} = \left[T(s) + \frac{S(s)}{s} L(s) \right] e^{-\tau_{sync} s} \tag{8}$$

Here the $T(s)$ and $S(s)$ functions are the same as for the CF, shown in section III.B.1. The function $L(s)$ represents the assumed sensor dynamics $\hat{H}_{sens}$, shown in Equation 1. The tuneable synchronization delay is set to $\tau_{sync} = 0.11s$, considering a unit delay on top of the assumed sensor delay [30].

D. Pseudo Control Hedging

A limitation of INDI based control methods is the saturation of control surfaces, which is not fed back to the inner-loop structure. Therefore, Pseudo Control Hedging (PCH) decreases the virtual command input, reducing performance degradation [21, 22]. PCH can be used successfully for certification, as the adaptation is made in the command signal [28]. The hedged virtual command signal is computed by subtracting the virtual command hedge, $\boldsymbol{\nu}_h$, from the desired command signal, $\boldsymbol{\nu}_{cmd}$. The virtual command hedge is computed using Equation 9, obtained from Grondmann [28].

$$\boldsymbol{\nu}_h = \boldsymbol{G(x)}(\boldsymbol{u}_{cmd} - \boldsymbol{u}_{actual}) \tag{9}$$

E. Outerloop Controllers

Figure 2 shows that the inner loop is controlled using different linear outer loop controllers. This section will elaborate on the different controllers. Since most controllers have remained unchanged, compared to the implementation by Stougie et al. [6], those will only be highlighted briefly.

1. C^* controller

The control system that has been changed compared to Stougie et al. [6] is the C^* implementation. The C^* control law has been implemented, as pilots cannot control pitch rate and load factor independently [31]. Furthermore, this control law is used in Airbus aircraft, enhancing pilots' familiarity when flying with the Flying-V [6, 32]. The C^* controller combines pitch rate and load factor feedback, defined by Equation 10:

$$C^* = \frac{V_{CO}}{g} q + n_{z,pilot} \tag{10}$$

where V_{CO} is the cross-over speed at which pitch rate and load factor are balanced in control input, set to 130 m/s [31]. A compensation term, $\frac{\cos(\theta)}{\cos(\phi)}$, is added as this limits the C^*_{cmd} from the pilot in turns and high pitch attitude [6, 33]. The C^* command is translated into a load factor command at the pilot station, limited by the FEP, after which $\dot{\theta}_{cmd}$ is calculated. There have been some modifications to the updated controller structure compared to the structure from Stougie et al. [6]. Firstly, the K_{nzs} gain is removed, which operates as an integrator for the C^* controller. However, it was found that this integrator would overflow, as the load factor does not need a C^*_{cmd} to be non-negative. Secondly, the load factor feedback to the controller has to be for the pilot station, which was previously done with the $n_{z,c.g.}$. Next, the feedback before gain K_d must be a gravity component compensation. In the implementation from Stougie et al. [6], 1 g was subtracted from the load factor to calculate the $\Delta n_{z,pilot}$, which gave trimming issues. Lastly, V_{CO} has been implemented, compared to a feedback of the airspeed, as this coincides better with the literature and general purpose of the C^* controller [31].

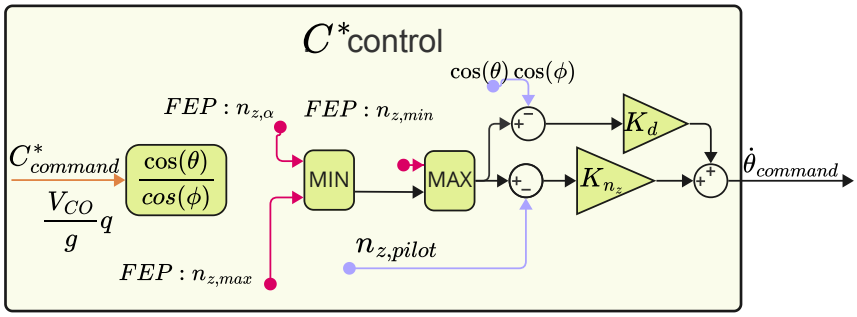

Fig. 5 INDI/Hybrid INDI Controller System Overview

2. Euler rate & Sideslip controller

The layout for the Euler rate and side slip controller per Stougie et al. [6] has remained the same. The Euler rate controllers are second-order filters with a feedforward term to increase tracking performance [27]. Furthermore, the PCH signal is subtracted from the desired command signal as described in section III.D.

The sideslip controller uses a pilot β_{cmd} and uses the representation of Equation 11, based on Lombaerts & Looye [34].

$$r_{ref} = \frac{1}{V_\infty}\left(wp - A_y\right) - \left[\frac{1}{s}K_{\beta_i}\left(\beta_{cmd} - \beta\right) - K_\beta \beta\right] - r_{meas} \tag{11}$$

3. Linear Virtual Command Controller

The last outer-loop controller converts the inputs to each virtual command input, $\boldsymbol{\nu}$. This linear controller structure has been based on research from Lombaerts et al. [33] and Grondman et al. [28] and implemented by Stougie et al. [6]. Each virtual command input is shown in Equation 12.

$$\begin{aligned} \nu_p &= \left(K_\phi + \frac{K_{\phi I}}{s}\right) \cdot \phi_{ref} + K_{\dot{\phi}} \cdot \dot{\phi}_{ref} + K_{\ddot{\phi}} \cdot \ddot{\phi}_{ref} \\ \nu_q &= K_\theta \cdot \theta_{ref} + K_{\dot{\theta}} \cdot \dot{\theta}_{ref} + K_{\ddot{\theta}} \cdot \ddot{\theta}_{ref} \\ \nu_r &= K_r \cdot r_{ref} \end{aligned} \tag{12}$$

4. Speed Controller

Next to the outer-loop controllers for the virtual command signal, a proportional controller for the thrust control is implemented, using the representation shown in Equation 13.

$$T_{cmd} = K_T\left(V_{\infty,cmd} - V_{\infty,meas}\right) + T_{trim} \tag{13}$$

F. Flight Envelope Protection

Stougie et al. concluded that their implementation for the FEP is not satisfactory, giving overshoot on the α protection [6]. The implementation of Stougie et al. [6] consisted of a linear controller activated when the protected state surpasses a threshold value. In the linear FEP, the protected states are; $n_{z,pilot}$, α and ϕ. The general representation was derived from Lombaerts et al. [33].

This research employs an exponential potential function to implement a command limitation for FEP, as per the methodology outlined by Sun et al. [35]. Consider a state, x_1, which will be protected, where its state derivative, x_2, is known, together with the reference signal of $x_{2,ref}$, assuming a rate controller, the implemented FEP is shown in

Equation 14. It should be noted that for minimum protection, the minimum value should be smaller or equal to zero.

$$
\begin{aligned}
x_{2,FEP,max} &= x_{2,ref}\left(1-u_p^+\right), \quad \text{where } u_p^+ = \begin{cases} e^{\eta\left(x_1(t)-x_{1,max}+\zeta x_2(t)\right)}, \text{ if } e^{\eta\left(x_1(t)-x_{1,max}+\zeta x_2(t)\right)} \leq 1 \\ r_p^+, \text{ if } e^{\eta\left(x_1(t)-x_{1,max}+\zeta x_2(t)\right)} > 1 \end{cases} \\
x_{2,FEP,min} &= x_{2,ref}\left(1-u_p^-\right), \quad \text{where } u_p^- = \begin{cases} e^{-\eta\left(x_1(t)-x_{1,min}+\zeta x_2(t)\right)}, \text{ if } e^{-\eta\left(x_1(t)-x_{1,min}+\zeta x_2(t)\right)} \leq 1 \\ r_p^-, \text{ if } e^{-\eta\left(x_1(t)-x_{1,min}+\zeta x_2(t)\right)} > 1 \end{cases}
\end{aligned} \tag{14}
$$

For this representation, two tuning parameters per protected state, namely η and ζ, are similar to a proportional and derivative gain, respectively. Increasing η will increase the margin before the FEP will become active, where the damping coefficient, ζ, will set how strict the FEP will dampen the rate at which the state derivative x_2 is approaching the protected state. Furthermore, there is a design term, $r_p^{+/-}$, which was found to be dependent on which state is protected.

The protected states in this research are load factor, AoA, pitch attitude, and roll attitude. From industry standards, it is clear there is also an overspeed protection, but this is only audible, so it does not have to be implemented in the control law [36]. The limits for each state are given in Table 5, derived from commonly used state protection limits by Airbus [36]. Some state limits depend on the flight condition or coupled states. Starting with the AoA protection,

Table 5 Protect states and limits for FEP

State	$n_{z,max}$ $[g]$	$n_{z,min}$ $[g]$	α_{max} $[^\circ]$	$\theta_{max}[^\circ]$	$\theta_{min}[^\circ]$	$\phi_{max}[^\circ]$	$\phi_{min}[^\circ]$
Limit	2.5	-1	22-24	30	-15	66/33	-66/-33

as was stated by Stougie et al. [6], the limits are dependent on the air density, varying from 22° at approach to 24° at cruise. Furthermore, the roll protection is dependent on the load factor command. For a pure roll input, the limits are set to be ±66°, whereas with a C^*_{cmd}, the limits are set to be ±33°. Therefore, the constant $r_p^{+/-}$ is especially of use for bank protection, as it is chosen to set $r_p^{+/-} = 1 + \frac{5\pi}{180}$, which will bring the limit back from 66° to 33°, with a protection rate of $5^\circ/s$.

IV. Handling Qualities & Tuning

This section will cover the methods of acquiring the results and validating the performance and fault tolerance of the Hybrid INDI control system with enhanced FEP for Flying-V. Firstly, the HQ requirements are explained, together with the method of tuning the outer-loop controllers, for which most of the methods are used and derived from Stougie et al. [6]. As this research aims to compare the nominal performance of the Flying-V, comparing INDI and Hybrid INDI, this is done for both controller structures. Next, the Hybrid INDI Controller is evaluated based on different parametric uncertainties and tested on how the set requirement, on which the nominal system was assessed, changes. Lastly, the test cases on which the Command Limited FEP are tested are described and compared with the linear-based FEP.

A. Tuning Routine

Similar to the tuning routine of Stougie et al., the input-output response from pilot command to measured state would be linearized, using the Control System Toolbox from MATLAB ®∗. The relevant states are $n_{z,c.g.}$, q, θ, ϕ, and β, all evaluated in a closed-loop response. Furthermore, the virtual command error, point A in Figure 2, is assessed in a broken loop, breaking each loop one by one, providing information about the margins of the inner loop [16]. The set requirements for the HQ are derived from MIL-STD-1797A [5] and shown in Table 6. Most of the HQ are determined using a Low Order Equivalent System (LOES) approximation, matching the High Order Equivalent System (HOS) frequency response within a set region of 0.1 - 10 rad/s. For a more elaborate definition of each defined HQ requirement, the reader is advised to read Stougie et al. [6]. A difference from the criterion set by Stougie et al. is the bandwidth criterion, given in Figure 6 as it is coupled. Furthermore, Stougie et al. presented the incorrect HQ minima and maxima for several HQs, regarding approach and cruise. Table 6 presents the correct HQ requirements for the selected parameters, indicated in columns B, for cruise and C, for approach [5].

Together with the linear analysis and scoring of the HQ requirements, three different step response tests are done to test the Maximum Control Surface Deflection (CS_{max}), Control Surface Activity ($CS_{activity}$), Settling Time (ST),

∗https://nl.mathworks.com/help/control/index.html

Overshoot (OS). The test cases have remained the same with respect to Stougie et al. [6] to make a direct comparison. The difference is, however, the sideslip tracking of the controller as from tests of the sensor-based INDI controller system; it was shown that the controller system could not track any reference sideslip angle larger than $|\beta| \approx 3°$. EASA states the need for a steady-heading sideslip of $\beta = 15°$, and thus, this is chosen as the desired step response test [5, CS25.177(c)]. From the trim routine, the lowest-scored systems are combined, and the nominal system is found, for which the results are shown in Table 8.

Table 6 INDI and Hybrid INDI comparison with Base Sensors [5]
Category B: Cruise Category C: Approach

Longitudinal tuning objectives			
Description	**Type**	**Min**	**Max**
		B C	B C
Response to C^* step command of 1.8 (ΔC^*= 0.8) at t = 1 s, T_{sim} = 60 s			
CS_{max} [°]	Min	-	-
$CS_{activity}$ [°/s]	Min	-	-
ST [s]	Min	-	-
OS [%]	Min	-	-
Linear Analysis			
GM ν_q $[dB]$	Constr.	6	-
PM ν_q [°]	Constr.	45	-
ω_{sp} $[rad/s]$	Constr.	- 0.87	-
ζ_{sp} $[-]$	Constr.	0.30 / 0.50	2.0 / 1.3
CAP $[g^{-1}s^{-2}]$	Constr.	0.085 / 0.16	3.6
$score_{LOES}$ $[-]$	Constr.	-	15

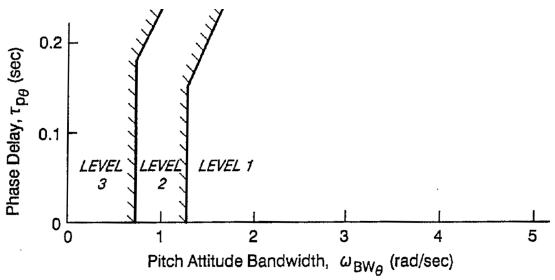

Fig. 6 Bandwidth Criteria [37]

Longitudinal tuning objectives			
Description	**Type**	**Min**	**Max**
		B C	B C
Response to $\dot{\phi}$ block command of ±3° at t = 1 - 7s, T_{sim} = 18 s			
CS_{max} [°]	Min	-	-
$CS_{activity}$ [°/s]	Min	-	-
ST [s]	Min	-	-
OS [%]	Min	-	-
Response to β step command of $-15°$ at t = 1 s, T_{sim} = 120 s			
CS_{max} [°]	Min	-	-
$CS_{activity}$ [°/s]	Min	-	-
ST [s]	Min	-	-
OS [%]	Min	-	-
Linear Analysis			
GM ν_p $[dB]$	Constr.	6	-
PM ν_p [°]	Constr.	45	-
GM ν_r $[dB]$	Constr.	6	-
PM ν_r [°]	Constr.	45	-
$1/T_s$ $[s^{-1}]$	Constr.	-0.035 / -0.058	-
T_r $[s]$	Constr.	-	1.4 / 1.0
ω_{dr} $[rad/s]$	Constr.	0.5	-
ζ_{dr} $[-]$	Constr.	0.08	-
$\omega_{dr}\zeta_{dr}$ $[rad/s]$	Constr.	0.15 / 0.10	-
$score_{LOES}$ $[-]$	Constr.	-	15

B. Uncertainty modeling

Using the nominal tuned system, the Hybrid INDI system is further researched regarding its capability of uncertainty rejection of different parametric values used in the controller system. These parametric uncertainties are shown in Table 7. The Robust Control Toolbox from MATLAB® † is used to assess the influence of the set parameters on the set requirements shown in Table 6, with the possibility to look at time and frequency domain. The controller system will be linearized using the uncertain parameters from which samples can be generated, and each set of parameters will be addressed by a randomly assigned value within the set range. The evaluations are done for 750 samples.

†https://www.mathworks.com/products/robust.html

Table 7 Uncertain parameters

Parameter	Definition	Uncertainty
I_{xx}, I_{yy}, I_{zz}	Principal inertial parameters	±30 [%]
I_{xz}	Off-diagonal inertial parameter	$\pm 1 \times 10^4 \ \ [kg \cdot m^2]$
m	Mass	$[2.1 - 2.4] \times 10^5 \ \ [kg]$
$\omega_{CS1_L}, \omega_{CS1_R}, \omega_{CS2_L}, \omega_{CS2_R}, \omega_{CS3}$	Actuator eigenfrequency	±30 [%]
$C_{(X,Z,M),CS1}, C_{(Y,L,N),CS2}, C_{(Y,L,N),CS3}$	Aerodynamic control surface effectiveness	±30 [%]
ρ	Air density measurement	±30 [%]
τ_{del}	Body rate sensor delay	[0, 0.080, 0.10, 0.12]

V. Results & Analysis

This section will discuss the results of the Hybrid INDI implementation and performance validation compared to the sensor-based INDI model. Firstly, the sensor-based INDI and Hybrid INDI models are compared for the base sensor configuration shown in Table 4. Next, the fault tolerance of the Hybrid INDI controller structure is tested by implementing uncertainties, shown in Table 7 and looking at the influence on time domain step response and frequency domain HQ scores. Lastly, the new FEP implementation is tested using different test cases, comparing it to the linear FEP system.

A. Nominal system analysis

For the nominal system response of both the sensor-based INDI controller and Hybrid INDI, the test cases shown in Table 6 are tested. The results for the different requirements are shown in Table 8. It should be noted that the comparison for INDI is done with an updated controller system, compared to what Stougie et al. [6] acquired their results from. The results presented by Stougie et al. [6] were obtained using modified sensor characteristics, but errors in the simulation model affected the assessed performance. Therefore, the results shown in Table 8 for the INDI results are not the same model as per Stougie et al. [6]. The INDI and Hybrid INDI models were both tuned to make a satisfactory compromise to HQ scores and time-domain response. Looking at the results from Table 8, there are certain aspects that are evidently different between the INDI and Hybrid INDI control laws.

Firstly, the most significant impact of Hybrid INDI is the increase in phase margin, which is satisfactory for all control axes in both approach and cruise. However, the gain margin for the yaw axis turned out to be low, which is to be expected as, from previous research, low control authority was found for the yaw axis [38]. For the approach condition, the gain margin for the roll axis was found to be low as well, which can be explained by the low control surface effectiveness at low speed and high AoA, which is needed for the trim condition at approach, shown in Table 2.

Next, the LOES fit algorithm had difficulty fitting the response of both longitudinal and lateral closed-loop transfer functions, shown in Table 8, to the acquired eigenmode frequency and damping characteristics. This means that the linearisations of the input-output relations cannot fit the same eigenmode characteristics. This is problematic as it can give incorrect HQ results. Since the problem arises especially in approach condition, dynamic characteristics for the Flying-V could make the frequency response behave differently to the conventional LOES approximation, which was set up decades ago [5]. The unsatisfactory Control Anticipation Parameter (CAP) and aperiodic roll mode are determined by the LOES approximation and could therefore be computed incorrectly.

For the bandwidth, using the requirement boundaries from Stougie et al., the requirement would not have been met for any flight condition and control law [6]. However, using the revision from Mitchell et al. [37], the requirements are met, albeit barely for approach condition. It should be noted that the results from Stougie et al. could not be recreated for adjusted sensors and base sensors, and the bandwidth was further decreased with the updated model structure. Due to the inconclusiveness of the validity of this requirement, proper research to valid HQ assessment shall be done to evaluate which HQ shall be used to assess controller systems [5, 37, 39, 40].

Looking at the time response characteristics, the implementations of the INDI and Hybrid INDI differ slightly but generally behave similarly. In the approach condition, the response settling time tends to be longer due to control surface saturation, resulting in a lack of control authority. Furthermore, as the integrator term has been removed in the C^*-controller, as shown in section III.E.1, the settling time takes longer than the sensor-based implementation. The most significant difference is the settling time of the sideslip response, where the sensor-based INDI takes 6.5 times longer to settle compared to the Hybrid INDI structure.

Table 8 INDI and Hybrid INDI comparison with Base Sensors
Level 1 HQ: **Level 2 HQ:**

(a) Longitudinal handling quality requirements

Description	Approach		Cruise	
	INDI	**Hybrid**	**INDI**	**Hybrid**
Response to C^* step command of 1.8 (ΔC^*= 0.8) at t = 1 s, T_{sim} = 60 s				
OS [%]	48.9	-18.3	25.4	26.8
ST [s]	41.8	56.2	11.9	4.73
$CS_{activity}$ [°/s]	2.82	1.79	5.40	4.45
CS_{max} [°]	23.8	23.8	9.44	9.52
Linear Analysis				
GM q [dB]	4.80	6.00	5.58	6.78
PM q [°]	32.80	46.3	36.9	49.8
ω_{sp} [rad/s]	2.02	1.89	1.10	1.81
ζ_{sp} [-]	0.673	0.724	0.579	0.870
CAP [$g^{-1}s^{-2}$]	0.111	0.615	0.132	0.345
ω_{BW} [rad/s]	1.65	1.67	1.36	1.84
τ_p [s]	0.184	0.214	0.175	0.197
$score_{LOES}$ [-]	44.5	28.1	26.2	7.78

(b) Lateral handling quality requirements

Description	Approach		Cruise	
	INDI	**Hybrid**	**INDI**	**Hybrid**
Response to $\dot{\phi}$ block command of ±3° at t = 1 - 7s, T_{sim} = 18 s				
OS [%]	18.2	24.8	28.5	42.2
ST [s]	5.72	5.40	5.11	5.24
$CS_{activity}$	32.2	37.8	10.6	10.3
CS_{max} [°]	30	30	11.9	11.1
Response to β step command of −15° at t = 1 s, T_{sim} = 120 s				
OS [%]	13.3	17.1	0.749	1.49
ST [s]	64.3	62.1	90.2	13.8
$CS_{activity}$	3.6	5.8	4.77	3.50
CS_{max} [°]	48.7	30	20.7	21.7
Linear Analysis				
GM p [dB]	4.22	4.39	6.20	6.40
PM p [°]	26.1	48.5	35.8	48.8
GM r [dB]	5.25	4.39	5.56	5.33
PM r [°]	35.0	51.3	35.7	46.7
$\frac{1}{T_s}$ [s^{-1}]	0.1088	0.086	0.0425	0.236
T_r [s]	6.549	0.561	0.865	0.801
ω_{dr} [rad/s]	3.702	1.76	1.53	1.83
ζ_{dr} [-]	1.66	0.238	0.387	0.741
$\omega_{dr}\zeta_{dr}$ [rad/s]	0.420	0.492	0.593	1.36
$LOES_{lat}$ [-]	34.3	1.85	11.3	8.74

B. Fault Tolerance of Hybrid INDI

This section will highlight the influence of uncertainties on the time and frequency domain response for the Hybrid INDI controller. As was highlighted in section IV.B, the tuned nominal Hybrid INDI controller system is linearized, with parametric uncertainties embedded within the model. These uncertainties are shown in Table 7. Firstly, the influence of the cross-over frequency of the complementary filter, $\omega_{n,comp.filt.}$, is tested on the margins taken at point A in Figure 2, for both model and sensor uncertainties. This will properly indicate the optimal cross-over frequency, considering the parametric uncertainties. Next, the influence of each uncertainty is given in the frequency domain, indicating which uncertainty has the most influence near cross-over, which impacts stability margins. To demonstrate the fault tolerance in the time and frequency domain, the performance metrics from Table 6 are tested with uncertainties, looking at the boundaries and distribution of the set requirements.

1. Complementary Filter influence on stability margins

With the implementation of Hybrid INDI, the trade-off between sensor-based and model-based INDI is set with the cross-over frequency of the complementary filter. This is a design variable to achieve satisfactory stability margins. With low $\omega_{n,comp.filt.}$, the CF gives priority to model-based INDI and with high $\omega_{n,comp.filt.}$ there is more priority to sensor-based INDI. As a rule of thumb, the nominal CF cross-over is at the cross-over for the sensor dynamics. For the current inner-loop structure, this gives the dynamics of the body rate sensors, which has its cross-over at ω_{filt} =20 rad/s.

With model uncertainties, it is expected that the stability margins will be lower at low frequencies, whereas with

sensor uncertainties, the margins will be lower at high frequencies.

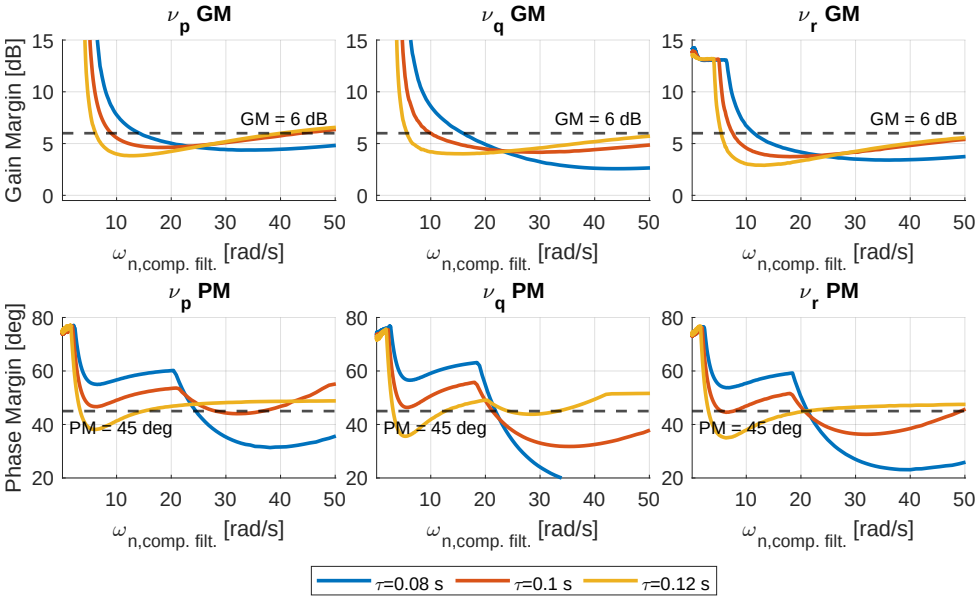

Fig. 7 Sensor Uncertainty Margins as a function of Complementary Filter cross-over

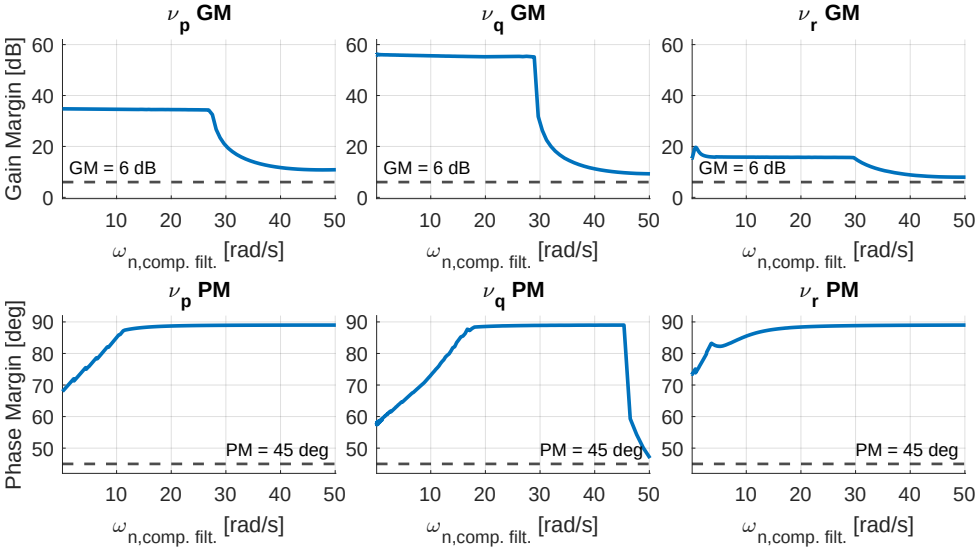

Fig. 8 Model Uncertainty Margins as a function of Complementary Filter cross-over

Figure 7 shows the impact of the CF for sensor uncertainties, where the time delay and air density measurements are varied. The increments of the time delay uncertainty are given in steps of 2ms, as this is the sampling time of the body rate sensor. If the time delay fits within an integer multiple of the sampling time of the sensor, the margins will be the same. The trend seen in Figure 7 is as expected, where both the gain and phase margins of the different axes are high when the signal relies on the model information. Around the cross-over frequency of the sensor dynamics of 20 rad/s, there is a significant decrease in phase margin, yielding below the level 1 HQ requirements. This drop-off is most noticeable for an underestimation of time delay but remains mostly flat for an overestimation. This can be

explained by the compensatory time delay in the synchronization filter, synchronizing the signal more accurately at an over-estimated time delay, as was shown by Lyu et al. [26]. Interesting to note is the local minima for the gain margins, at low $\omega_{n,comp.filt.}$, indicating that the gain margins depend more on sensor-based INDI.

Looking at Figure 8, all the model uncertainties have been sampled, for which it is expected that the controller system will become more dependent on sensor-based INDI i.e. a high $\omega_{n,comp.filt.}$. It should be noted that the ideal scenario is tested, where the sensor delay of the body rate sensors is set to τ=0s. From Figure 8, it is clear that the preference goes to a high $\omega_{n,comp.filt.}$ when looking at the phase margins. However, this trend is not shown for the gain margins. Especially, the pitch axis seems to perform better when it is dependent on the model-based INDI. Furthermore, the gain margins for roll and yaw both show an anomaly at low $\omega_{n,comp.filt.}$, where there is a sudden increase in the gain margin but a decrease in phase margin, indicating some resonance behavior, which makes the frequency drop-off faster. After this, the margins remain flat, with maximum phase margin, but the gain margins seem to be at a maximum around 7 dB. From these results, to make a proper trade-off, the preference for a low $\omega_{n,comp.filt.}$=8 rad/s is taken to guarantee satisfactory gain and phase margins for both model and sensor uncertainties. The following results are formed using this $\omega_{n,comp.filt.}$.

2. Uncertain Step result

Using 750 samples, the step response for longitudinal, lateral, and directional inputs under uncertain sensor and model uncertainty combinations are tested. The results are displayed in Figure 9 for the provided test cases. The blue line indicates the nominal response of the system to the indicated pilot command input. The shaded grey shows the boundaries of the different response parameters. These results are made for cruise conditions and exhibit similar behavior for the approach. It is evident that the system lacks robustness, as certain combinations of uncertainties can lead to system instability.

Table 9 Percentage of samples within threshold

	C^*_{cmd}	$\dot{\phi}_{cmd}$	β_{cmd}
Approach	90.3 %	82.8 %	87.7 %
Cruise	94.1 %	84.1 %	87.9 %

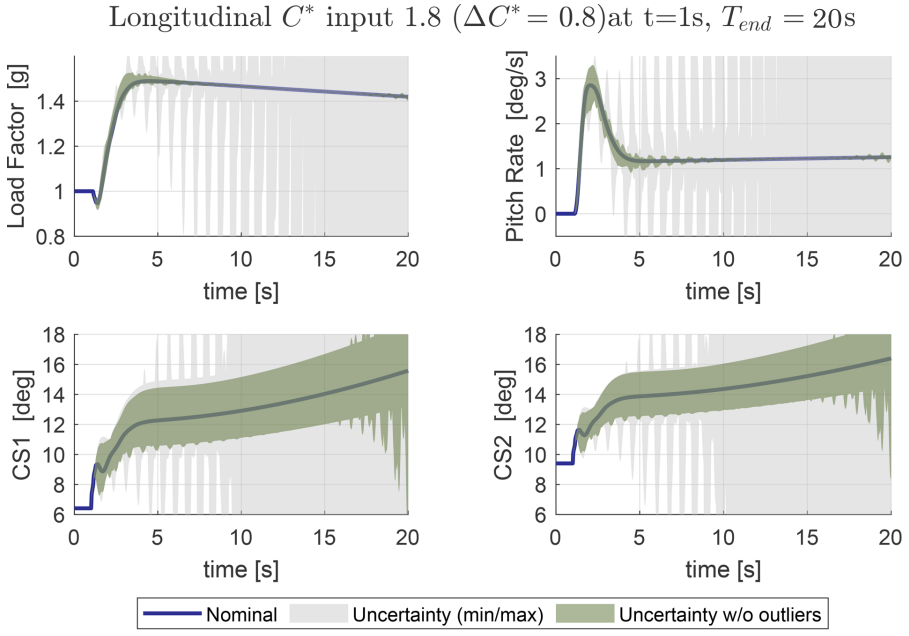

(a) Step response C^*_{cmd}

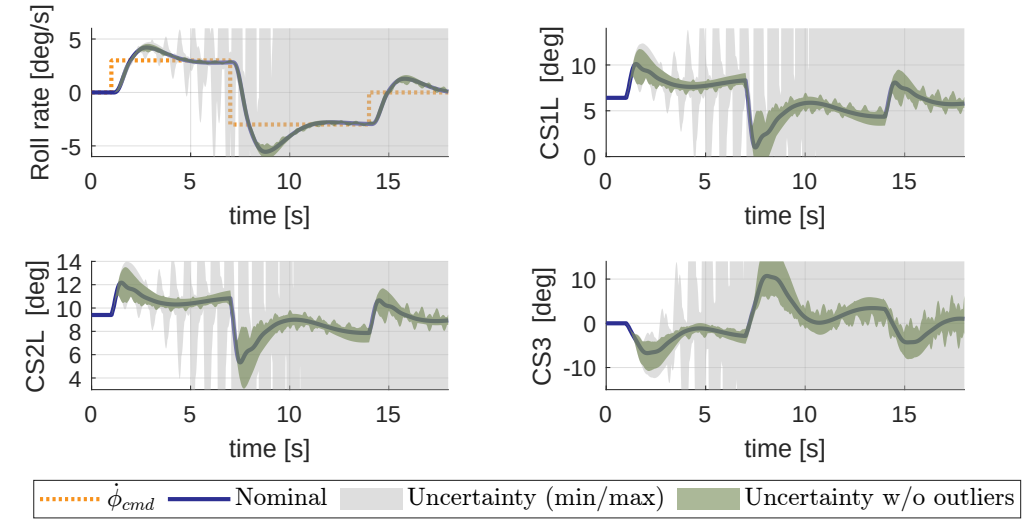

(b) Step response $\dot{\phi}_{cmd}$

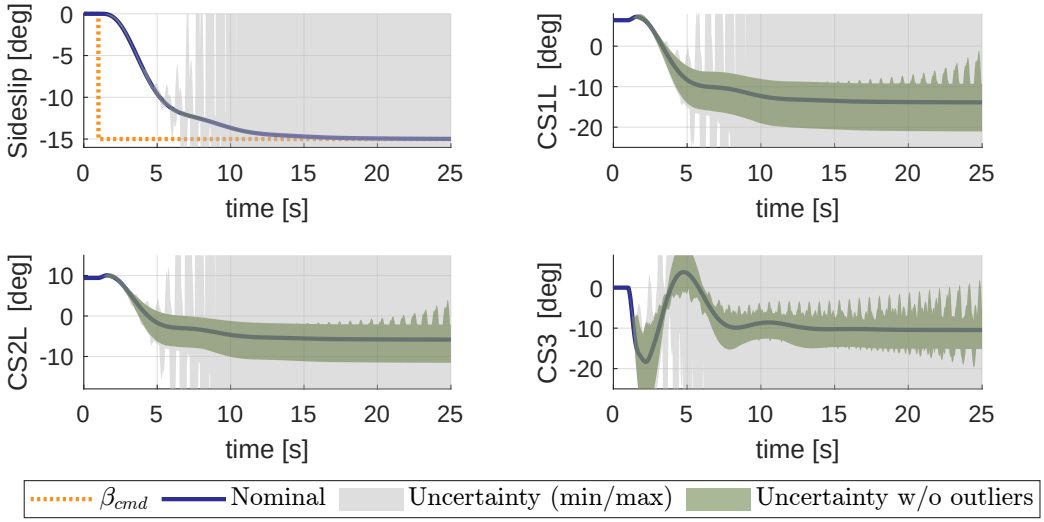

(c) Step response β_{cmd}

Fig. 9 Step response at Cruise condition, 750 Samples of uncertainty parameters

To quantify the stability of the control system with the given uncertainty samples, a metric is given for how many samples the uncertainty bounds stay within a certain threshold. The Root Mean Squared Error (RMSE) is calculated for the nominal system. Using the RMSE parameter, the threshold is calculated using the function isoutlier()‡ in MATLAB ®, which filters outliers based on values that are outside 3 Median Absolute Deviation. For each respective variable in Figures 9, the outliers are selected and removed, from which N samples remain, from which the shaded green area is generated, which represents the minimum and maximum values per datapoint, for sampled uncertainty within the threshold. The percentage of samples that fall within the set threshold per input channel and flight condition are given in Table 9, and indicate that for more than 80% of the uncertainty combinations, all input channels fall within the set threshold, where the roll rate command shows the least fault tolerance concerning the set parametric uncertainties.

To elaborate upon these results, Figure 10 shows the influence of the different uncertainty parameters at various frequencies. The most critical cross-over region will determine the system's stability. The individual contributions of the different parameters are taken, so no coupling effects are shown. It will, therefore, be assumed that only two parameters will enhance the uncertainty region where they were already contributing. Near the cross-over region, it is interesting

‡https://nl.mathworks.com/help/matlab/ref/isoutlier.html

that the aerodynamic and inertia uncertainty are the main contributors near the cross-over frequency around ω_{c,ν_p} ≈5 rad/s. However, when looking at the phase plot, the aerodynamic uncertainty hardly contributes to this frequency. The phase cross-over might be a more concerning frequency region, around ω_{c,ν_p} ≈8.5 rad/s. Here, sensor delay, inertia, and aerodynamic uncertainties contribute to the phase response, whereas time delay dominates the gain. However, as the gain response remains close to 0 dB, this likely contributes to the instability. It should be noted that the uncertainty in air density and mass are negligible, looking at the frequency response, which shows that the controller system behaves correctly to these uncertainties.

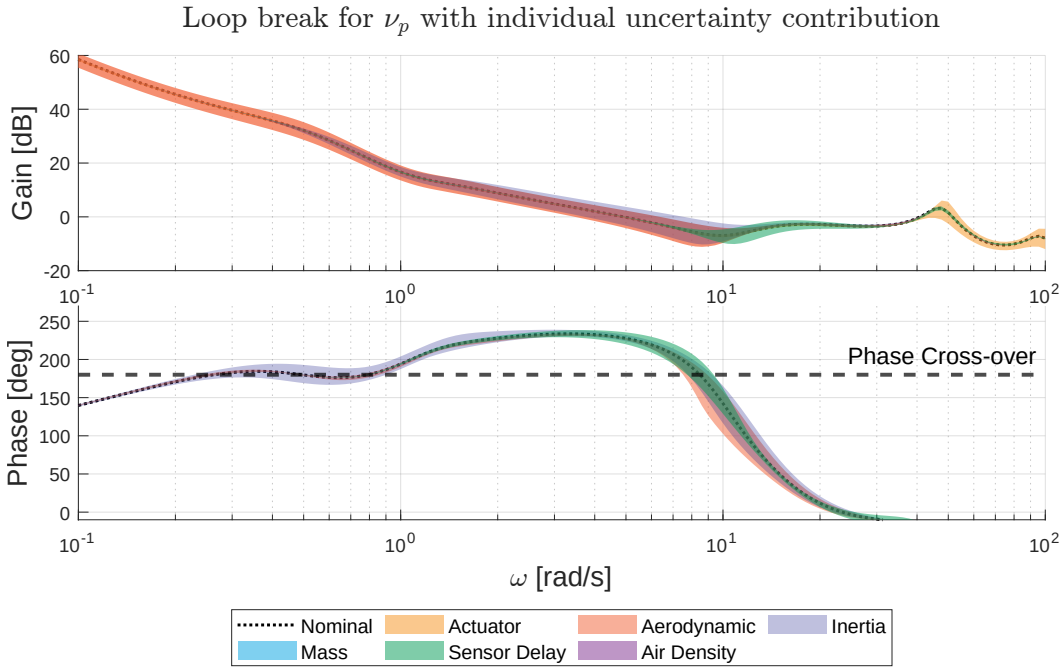

Fig. 10 Broken loop uncertainty at point A for ν_p, with individual uncertainty contribution

3. Handling Quality Uncertainty

To evaluate the fault tolerance of the implemented Hybrid INDI, the HQ requirements set from Table 6 are tested using the different uncertain parameter contributions and scored accordingly, shown in Figure 11. Each boxplot's lower and upper edges represent the 25th and 75th percentiles, and the blue line indicates the median. The results of the Figure 11 should be interpreted as follows: all HQ are normalized according to their respective score for the nominal system. For each requirement, the minimum and maximum requirements are shown and normalized for each respective requirement. For example, for the phase margin requirement of the yaw channel, $PM\nu_r$, which is not met, the normalized minima are larger than 1, which means the nominal value also does not meet the set requirements. Figure 11 indicates which requirements will likely be met with the set uncertainty parameters. For this simulation, 750 uncertain parameter combinations have been simulated for the cruise condition. From Figure 11, it can be seen that the stability margins, apart from the gain margin for yaw, have the majority of samples meeting the set requirements, as the median is larger than the minimum value. However, there is a large spread with outliers for the phase margins of the system. The same is seen for the approach condition; however, since the nominal values for roll and yaw gain margin did not meet the requirements initially, the result is similar to that of the gain margin of ν_r from Figure 11.

Looking at the longitudinal HQ, there are several interesting things to note. Firstly, the LOES approximation of the longitudinal system is widespread, which influences the approximation of the short-period eigenmode. The median is larger than the maximum value, indicating that most of the LOES approximations are unsatisfactory, which should be kept in mind for the following point. Secondly, the eigenmode frequency for a short period is met for most cases. However, the damping is likely to become too large, where the CAP is likely to become too small, indicating a large

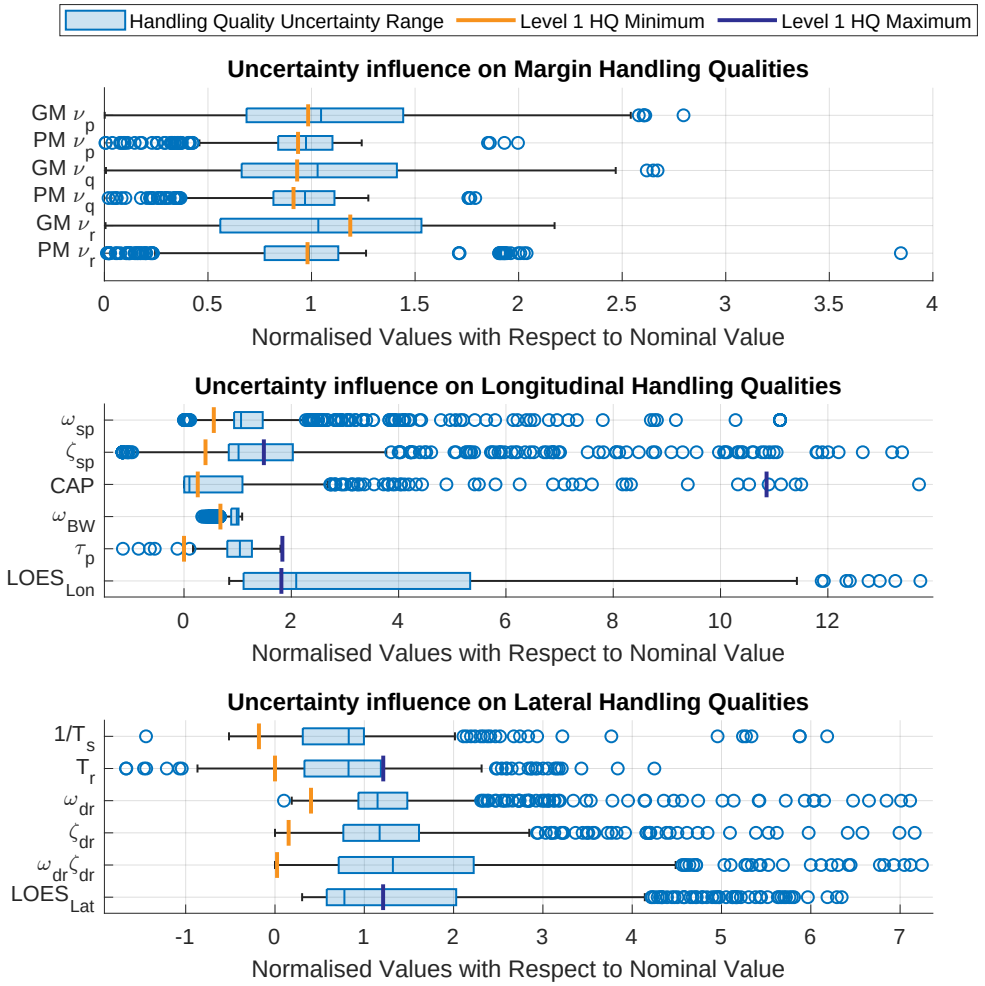

Fig. 11 Boxplots with uncertainties for set HQ requirements in cruise, 750 samples

T_{θ_2}. Lastly, the uncertainties hardly influence the pitch response's bandwidth and time delay parameters. Since these parameters do not depend on the LOES approximation, they are fault tolerant to the set uncertainties. For the approach condition, the short period characteristics and CAP do stay within the set requirements for the interquartile range. However, since the LOES approximation for the approach condition was already unsatisfactory for the longitudinal response, this should be kept in mind.

Lastly, for the lateral HQ analysis, it can be said with more certainty that the set requirements are met as the lateral LOES approximation stays within requirements for most samples, and all mode response requirements are satisfactory for the interquartile range, also concluded for the approach condition.

C. Flight Envelope Protection

The second part of this research is focussed on improving the FEP to enhance safety by keeping the protected states within the set limits and remove the overshoot for the AoA as was found by Stougie et al. [6]. When further evaluating the linear FEP, it was concluded that the test cases for the FEP were not severe enough to properly test the safety of the FEP. The test cases from Stougie et al. [6] were:

- Longitudinal command: C^*_{cmd} = 2, at t=5s until t=250s
- Combined command: C^*_{cmd} = 2, at t=5s until t=250s, $\dot{\phi}_{cmd}$ = 5°/s, at t=5s until t=15s

However, a pure roll command was not shown, which becomes unstable for $\dot{\phi}_{cmd}$ = 5°/s, at t=5s until t=15s. Also, since the limits of the FEP for $n_{z,pilot}$ are set to 2.5g, the author believes a test case should at least consist of a C^* command larger than 2.5. Furthermore, as is given by EASA [41, CS25.147(f)], the aircraft should be able to do a bank-to-bank

from 30° until -30° under 7 seconds, giving an average roll rate of 8.57°/s. As the aircraft starts trim condition, the lateral command will be set to $\dot{\phi}_{cmd}$ = 20°/s. Therefore, in this research, the following test cases for the FEP are given:

- Longitudinal command: C^*_{cmd} = +3 at t=1s until t=130s, C^*_{cmd} = -3 at t=130s until t=150s, T_{sim}=200s
- Lateral command: $\dot{\phi}_{cmd}$ +-20°/s using 321 step command at t =1s until t = 181s, T_{sim}=200s
- Combined command: C^*_{cmd} = +3 at t=20s until t=130s, C^*_{cmd} = -3 at t=130s until t=180s and $\dot{\phi}_{cmd}$ = ± 20°/s, at t=3s until t=153s, T_{sim}=200s

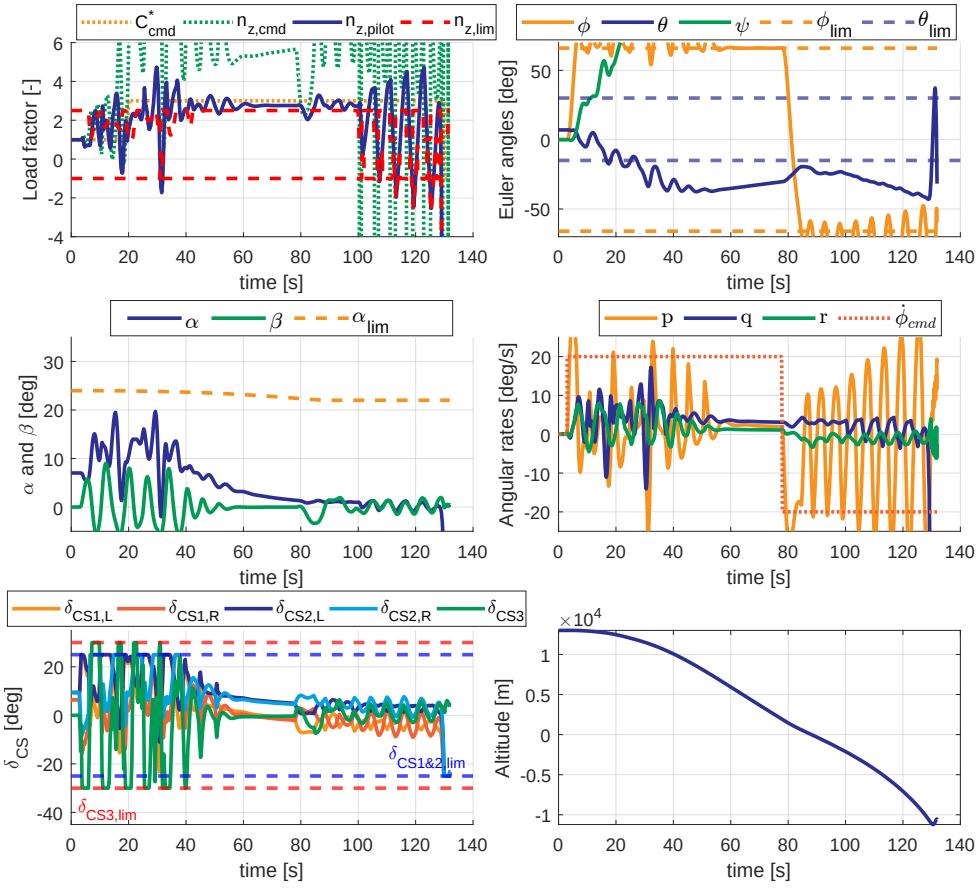

Fig. 12 Linear FEP Cruise: Combined command

All test cases have been conducted using the Hybrid INDI model, as the revised FEP structure incorporates a model prediction for $\dot{\alpha}$. With the given test cases, none of the Linear FEP responses remained stable for both cruise and approach. It proves the linear FEP implementation is not satisfactory. Figure 12 shows an example of such instability, where the linear FEP structure is tested using the combined command input.

Multiple gains could be tuned for the updated FEP, but it was shown that these do not need to be gain scheduled, significantly reducing complexity for multiple operating points. The results for the combined input are shown in Figures 13 and 14 for both cruise and approach, respectively. These results show the improved aspects, limitations, and problems with the newly implemented FEP.

Looking at Figure 13, it is clear that all FEP systems are activated when their respective protected state comes close to the set limit. Starting with α and n_z, since these limits are restricting the $n_{z,cmd}$ which is converted to the $\dot{\theta}_{cmd}$, as shown in Figure 5. When the C^*_{cmd} is given, the initial load factor is increased, for which the load factor limit, $n_{z,lim}$, is decreased to have the load factor stay within boundaries. For the α protection, it can be seen that after a more extended period, at which the θ protection has been active, α reaches its limit, defined as 24° at cruise by Stougie et al. [6]. When the α_{lim} is reached, the $\dot{\theta}_{cmd}$ is adjusted, which can be seen by a decrease in θ.

For the θ protection, the system behaves as expected but has a brief overshoot at $t \approx 85$s, where the pitch attitude

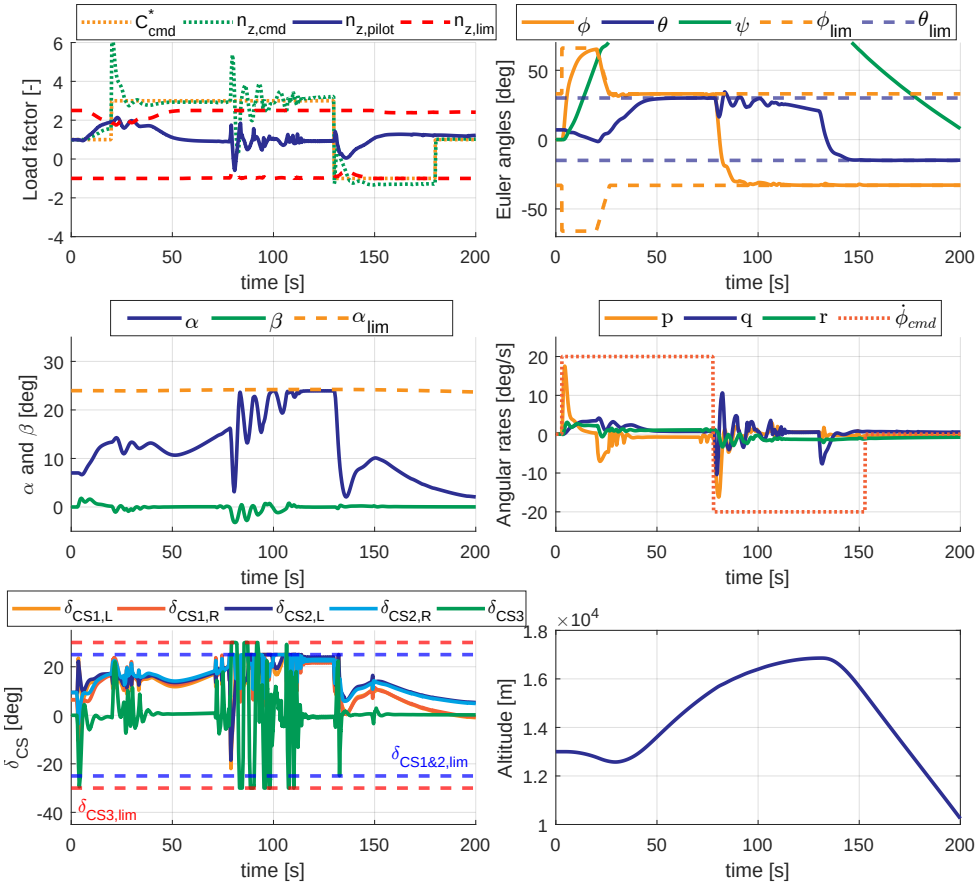

Fig. 13 Updated FEP Cruise: Combined command

increases to $\theta \approx 34°$. A coupling between the $\dot{\phi}_{cmd}$ and pitch rate introduces a pitch response when a roll input is given. The coupling is due to the load factor control in the C^* controller as the turn will introduce a load factor at the pilot, which is not introduced by a C^*_{cmd}. Therefore, the error will be negative, pushing the aircraft down in a turn. In the combined input, when the $\dot{\phi}_{cmd}$ is reversed, this gives a sudden decrease in load factor, from which the controller responds by pushing the nose up. This is to be expected with the current controller structure, but a different controller structure can be implemented to mitigate this problem.

Looking at the ϕ protection, the aircraft steadily approaches the set limit of $\phi_{lim} = 66°$. When the C^* command is given, this limit is decreased to $\phi_{lim} = 33°$, decreasing with 5°/s until reaching 33°. It should be noted that the bank-to-bank time satisfies the requirement, reaching $\phi = -30°$ within t = 4.42s in cruise and t = 4.465s for approach. Next, the approach condition is shown in Figure 14, which does not satisfy the protection boundaries. This Figure represents the current limitation of the updated controller system. At approach, the test cases for a pure longitudinal response stay within boundaries, but do not respond to a positive C^* input as the α_{lim} is reached in trim condition. For the lateral and combined inputs, the FEP does not keep the protected states within their boundaries as there is saturation of the control surfaces. When the lateral input command is given, the roll protection keeps ϕ within boundaries. Still, the control surfaces are saturated and cannot protect the other states. However, since there is no longitudinal input, the AoA remains within limits. Due to the coupling of the roll and pitch channels, the pitch protection is therefore exceeded. As for the combined input, as shown in Figure 14, the control surfaces are saturated, with a positive C^*_{cmd}. At $t \approx 100s$, there is an increase in AoA due to a $n_{z,cmd}$, as the ϕ angle is approaching its protection limit. Due to the coupling of channels, this gives a sudden rise in AoA, which cannot be compensated as there is actuator saturation. When the roll maneuver is approaching has settled on its limit, the actuators can push the nose of the aircraft down, reducing the AoA and bringing it back to its limit.

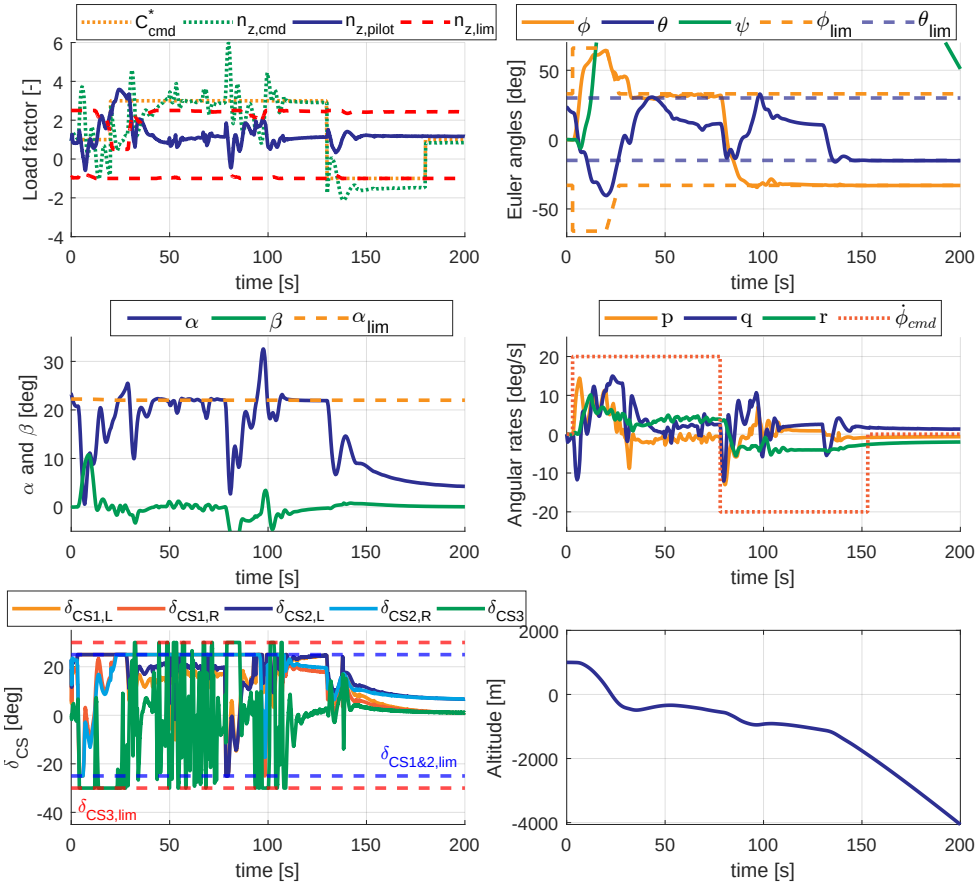

Fig. 14 Updated FEP Approach: Combined command

VI. Conclusion

This research describes implementing an updated controller system for the Flying-V to enhance the current Flight Control System (FCS), aiming to achieve level 1 Handling Qualities (HQ) as per MIL-STD-1797A [5]. A Hybrid Incremental Nonlinear Dynamic Inversion (INDI) control law using a Complementary Filter (CF) is supported by an exponential potential function Command Limiting Flight Envelope Protection (FEP). The Hybrid INDI control structure aims to address stability margin issues caused by time delay, showcasing superior performance compared to the sensor-based INDI control structure. However, due to insufficient gain margin in roll and yaw channels and exceeding Low Order Equivalent System (LOES) approximation boundaries, further investigation is needed to meet the level 1 HQ criteria. The method used to assess which HQs are used, and their validity for the Flying-V use case should be researched further.

Moreover, the study assesses the fault tolerance of the controller structure under parametric uncertainties, highlighting its limitations in addressing coupled uncertainties such as aerodynamics, inertia, and time delay. While lateral HQ fault tolerance meets satisfactory standards, longitudinal HQ shows less fault tolerance. Remember that the fit of the LOES often falls short and dominant for most HQ metrics.

Additionally, the updated FEP introduces an exponential Command Limiting structure to protect load factor, Angle of Attack (AoA), pitch attitude, and roll attitude. Testing reveals the linear FEP's unsatisfactory performance when subjected to newly generated, more challenging test cases. The updated FEP indicates reliability under cruise conditions but unsatisfactory performance during approach due to actuator saturation.

Additional research is needed to address the validity of the HQ assessment. Next, the Control Allocation (CA) scheme, particularly its interaction with the FEP and Pseudo Control Hedging (PCH) structure under actuator saturation, should be researched further, as this is a current limitation.

References

[1] Martinez-Val, R., Palacin, J. F., and Perez, E., "The evolution of jet airliners explained through the range equation," *Proceedings of the Institution of Mechanical Engineers, Part G: Journal of Aerospace Engineering*, Vol. 222, No. 6, 2008, pp. 915–919. https://doi.org/10.1243/09544100JAERO338.

[2] Liebeck, R., "Design of the Blended Wing Body Subsonic Transport," *Journal of Aircraft*, Vol. 41, No. 1, 2004, pp. 10–25. https://doi.org/10.2514/1.9084.

[3] Oosterom, W., and Vos, R., "Conceptual Design of a Flying-V Aircraft Family," *AIAA AVIATION 2022 Forum*, American Institute of Aeronautics and Astronautics, Reston, Virginia, 2022. https://doi.org/10.2514/6.2022-3200.

[4] Benad, J., "The Flying V - A new Aircraft Configuration for Commercial Passenger Transport," *Deutscher Luft- und Raumfahrtkongress 2015, Rostock*, Deutsche Gesellschaft für Luft- und Raumfahrt, 2015. https://doi.org/10.25967/370094.

[5] Anonymous, "Flying Qualities of Piloted Aircraft," Tech. Rep. MIL-STD-1797A Notice 3, Department of Defense, 8 2004.

[6] Stougie, J., Pollack, T. S., and Van Kampen, E., "Incremental Nonlinear Dynamic Inversion control with Flight Envelope Protection for the Flying-V," *AIAA SCITECH 2024 Forum*, American Institute of Aeronautics and Astronautics, Orlando, Florida, 2024. https://doi.org/10.2514/6.2024-2565.

[7] Cappuyns, T., "Handling Qualities of a Flying V Configuration," Ph.D. thesis, TU Delft, 2019. URL http://resolver.tudelft.nl/uuid:69b56494-0731-487a-8e57-cec397452002.

[8] van Overeem, S., Wang, X., and Van Kampen, E., "Handling Quality Improvements for the Flying-V Aircraft using Incremental Nonlinear Dynamic Inversion," *AIAA SCITECH 2023 Forum*, American Institute of Aeronautics and Astronautics, Reston, Virginia, 2023. https://doi.org/10.2514/6.2023-0105.

[9] Yang, J., and Zhu, J., "A hybrid NDI control method for the high-alpha super-maneuver flight control," *Proceedings of the American Control Conference*, Vol. 2016-July, 2016, pp. 6747–6753. https://doi.org/10.1109/ACC.2016.7526734.

[10] Kim, C., "A hybrid INDI control for ensuring flying qualities in failures of Xcg measurement subsystem," *Proceedings of the Institution of Mechanical Engineers, Part G: Journal of Aerospace Engineering*, Vol. 237, No. 4, 2023, pp. 972 – 991. https://doi.org/10.1177/09544100221113429.

[11] Sun, D., Hovakimyan, N., and Jafarnejadsani, H., "Design of Command Limiting Control Law Using Exponential Potential Functions," *Journal of Guidance, Control, and Dynamics*, Vol. 44, No. 2, 2021, pp. 441–448. https://doi.org/10.2514/1.G004972.

[12] Vugts, G., Stroosma, O., Vos, R., and Mulder, M., "Simulator Evaluation of Flightpath-oriented Control Allocation for the Flying-V," *AIAA SCITECH 2023 Forum*, American Institute of Aeronautics and Astronautics, Reston, Virginia, 2023. https://doi.org/10.2514/6.2023-2508.

[13] Torelli, R., Stroosma, O., Vos, R., and Mulder, M., "Piloted Simulator Evaluation of Low-Speed Handling Qualities of the Flying-V," *AIAA SCITECH 2023 Forum*, American Institute of Aeronautics and Astronautics, Reston, Virginia, 2023. https://doi.org/10.2514/6.2023-0907.

[14] de Zoeten, G. J., Varriale, C., and Vos, R., "Flight Performance Evaluation of the Flying-V," *AIAA AVIATION 2023 Forum*, American Institute of Aeronautics and Astronautics, Reston, Virginia, 2023. https://doi.org/10.2514/6.2023-3484.

[15] Matamoros, I., and de Visser, C. C., "Incremental Nonlinear Control Allocation for a Tailless Aircraft with Innovative Control Effectors," *2018 AIAA Guidance, Navigation, and Control Conference*, AIAA, 2018. https://doi.org/10.2514/6.2018-1116, URL https://arc.aiaa.org/doi/abs/10.2514/6.2018-1116.

[16] Pollack, T. S., "Advances in Dynamic Inversion-Based Flight Control Law Design," Ph.D. thesis, Delft University of Technology, Delft, 2024.

[17] Anonymous, "Type-Certificate Data Sheet," Tech. Rep. EASA.E.111 Issue 16, European Union Aviation Safety Agency (EASA), 10 2022.

[18] Åström, K. J., and Wittenmark, B., *Adaptive control*, Addison-Wesley series in electrical and computer engineering. Control engineering, Addison-Wesley, Reading, Mass., 1989. URL http://www.zentralblatt-math.org/zmath/en/search/?an=0697.93033.

[19] Slotine, J.-J. E., and Li, W., *Applied nonlinear control*, Prentice Hall, Englewood Cliffs, N.J., 1991. URL http://www.gbv.de/dms/ilmenau/toc/019505159.PDF.

[20] Sieberling, S., Chu, Q. P., and Mulder, J. A., "Robust Flight Control Using Incremental Nonlinear Dynamic Inversion and Angular Acceleration Prediction," *Journal of Guidance, Control, and Dynamics*, Vol. 33, No. 6, 2010, pp. 1732–1742. https://doi.org/10.2514/1.49978, URL https://doi.org/10.2514/1.49978.

[21] van 't Veld, R., van Kampen, E., and Chu, Q. P., "Stability and Robustness Analysis and Improvements for Incremental Nonlinear Dynamic Inversion Control," *2018 AIAA Guidance, Navigation, and Control Conference*, 2018. https://doi.org/10.2514/6.2018-1127, URL https://arc.aiaa.org/doi/abs/10.2514/6.2018-1127.

[22] Simplício, P., Pavel, M. D., van Kampen, E., and Chu, Q. P., "An acceleration measurements-based approach for helicopter nonlinear flight control using Incremental Nonlinear Dynamic Inversion," *Control Engineering Practice*, Vol. 21, No. 8, 2013, pp. 1065–1077. https://doi.org/https://doi.org/10.1016/j.conengprac.2013.03.009, URL https://www.sciencedirect.com/science/article/pii/S0967066113000634.

[23] Falkena, W., "Investigation of practical flight control systems for small aircraft," Ph.D. thesis, Delft University of Technology, Delft, 2012.

[24] Kim, C., Ji, C. H., Koh, G. O., and Kim, B. S., "Stability Margin and Structural Coupling Analysis of a Hybrid INDI Control for the Fighter Aircraft," *International Journal of Aeronautical and Space Sciences*, Vol. 22, No. 5, 2021, pp. 1154 – 1169. https://doi.org/10.1007/s42405-021-00394-8.

[25] Kumtepe, Y., Pollack, T. S., and van Kampen, E., "Flight Control Law Design Using Hybrid Incremental Nonlinear Dynamic Inversion," *AIAA Science and Technology Forum and Exposition, AIAA SciTech Forum 2022*, 2022. https://doi.org/10.2514/6.2022-1597.

[26] Lyu, H., Ye, Z., Chen, Y., Zhao, T., Gong, Z., Liu, X., Qin, B., and Chen, K., "Extended-State-Observer-Based Angular Acceleration Estimation for Supersonic Aircraft Lateral–Directional Control," *Applied Sciences*, Vol. 13, No. 11, 2023, p. 6598. https://doi.org/10.3390/app13116598.

[27] Li, M., Li, J., Tang, Y., and Sun, S., "An Extended INDI Approach and Application to Pitch Rate Control Laws Design of an Aircraft," *AIAA AVIATION 2021 FORUM*, AIAA, 2021. https://doi.org/10.2514/6.2021-3005.

[28] Grondman, F., Looye, G., Kuchar, R. O., Chu, Q. P., and van Kampen, E., "Design and Flight Testing of Incremental Nonlinear Dynamic Inversion-based Control Laws for a Passenger Aircraft," *2018 AIAA Guidance, Navigation, and Control Conference*, AIAA, 2018. https://doi.org/10.2514/6.2018-0385, URL https://arc.aiaa.org/doi/abs/10.2514/6.2018-0385.

[29] Pollack, T. S., and van Kampen, E., "Robust Stability and Performance Analysis of Incremental Dynamic-Inversion-Based Flight Control Laws," *Journal of Guidance, Control, and Dynamics*, Vol. 46, No. 9, 2023, pp. 1785–1798. https://doi.org/10.2514/1.G006576.

[30] Smeur, E. J. J., Chu, Q., and de Croon, G. C. H. E., "Adaptive Incremental Nonlinear Dynamic Inversion for Attitude Control of Micro Air Vehicles," *Journal of Guidance, Control, and Dynamics*, Vol. 39, No. 3, 2016, pp. 450–461. https://doi.org/10.2514/1.G001490.

[31] Niedermeier, D., and Lambregts, A. A., "Fly-By-Wire Augmented Manual Control-Basic Design Considerations," *28th Congress of the International Council of the Aeronautical Sciences*, Deutsches Zentrum für Luft- und Raumfahrt & Federal Aviation Administration, International Council of the Aeronautical Sciences, Brisbane, 2012.

[32] Favre, C., "Fly-by-wire for commercial aircraft: the Airbus experience," *International Journal of Control*, Vol. 59, No. 1, 1994, pp. 139–157. https://doi.org/10.1080/00207179408923072.

[33] Lombaerts, T., Looye, G., Ellerbroek, J., and Martin, M. R. y., "Design and Piloted Simulator Evaluation of Adaptive Safe Flight Envelope Protection Algorithm," *Journal of Guidance, Control, and Dynamics*, Vol. 40, No. 8, 2017, pp. 1902–1924. https://doi.org/10.2514/1.G002525.

[34] Lombaerts, T., and Looye, G., "Design and flight testing of manual nonlinear flight control laws," *AIAA Guidance, Navigation, and Control Conference*, American Institute of Aeronautics and Astronautics, Reston, Virigina, 2011. https://doi.org/10.2514/6.2011-6469.

[35] Sun, D., Jafarnejadsani, H., and Hovakimyan, N., "Command Limiting for Aerial Vehicles With Rate Control Augmentation Systems," *IEEE Transactions on Aerospace and Electronic Systems*, Vol. 57, No. 3, 2021, pp. 1702–1712. https://doi.org/10.1109/TAES.2021.3050674.

[36] Goupil, P., "AIRBUS state of the art and practices on FDI and FTC in flight control system," *Control Engineering Practice*, Vol. 19, No. 6, 2011, pp. 524–539. https://doi.org/10.1016/j.conengprac.2010.12.009.

[37] Mitchell, D. G., Klyde, H., David, Hoh, R. H., and Aponso, B. L., "Proposed Incorporation of Mission-Oriented Flying Qualities into MIL-STD-1797A." Tech. Rep. WL-TR-94-3162, Wright-Patterson AFB, OH,USA, 11 1994.

[38] Joosten, S., Stroosma, O., Vos, R., and Mulder, M., "Simulator Assessment of the Lateral-Directional Handling Qualities of the Flying-V," *AIAA SCITECH 2023 Forum*, American Institute of Aeronautics and Astronautics, Reston, Virginia, 2023. https://doi.org/10.2514/6.2023-0906.

[39] Hoh, R. H., Mitchell, D. G., Ashkqnas, I. L., Klein, R. H., Heffle, R. K., and Hodgkinson, J., "Proposed MIL Standard and Handbook - Flying Qualities of Air Vehicles," Tech. Rep. AFWAL-TR-82-3081.1, Systems Technology, Hawthorne,CA, 11 1982.

[40] Gibson, J. C., "Development of a design methodology for handling qualities excellence in fly by wire aircraft," Ph.D. thesis, TU Delft, 1999. URL http://resolver.tudelft.nl/uuid:6b564b35-cb74-436c-8c47-845bfbbb8b4d.

[41] Anonymous, "Easy Access Rules for Large Aeroplanes," Tech. Rep. CS25 Amendment 27, European Union Aviation Safety Agency (EASA), 1 2023. URL https://www.easa.europa.eu/en/document-library/easy-access-rules/easy-access-rules-large-aeroplanes-cs-25#group-publications.

II

Literature Study

2

Flying-V

This Chapter will cover the most recent developments regarding the TU Delft Flying-V aircraft to find the current challenges of the FCS. Section 2.1 will give a background in the design philosophy of the Blended-Wing-Body aircraft, together with an overview of the research that has been done on the Flying-V, shown in Section 2.2. The layout of the Flying-V, together with mass properties and used sensors and actuators, will be discussed in Sections 2.3, 2.4 and 2.8 respectively. The used reference frame definitions are explained, after which the Equations of Motion (EoM) and aerodynamic model are highlighted in Sections 2.5, 2.6 and 2.7 respectively. This Chapter provides an extensive background of the Flying-V project.

2.1. Blended Wing Body Aircraft

The Flying-V has been transformed from a mere concept aircraft, introduced by J. Benad [2], to a properly developed design with a multi-disciplinary work field tackling problems that arise from this idea. The Flying-V belongs to the BWB aircraft family, of which multiple different concepts have been developed over the years, which have been reviewed in several studies [19], [20]. Conventional aircraft, also known as CTW, have two wings that generate the majority of lift and a fuselage that carries the load. BWB aircraft incorporate the aircraft fuselage as a structural and lift-generating aspect, making for more aerodynamic efficiency and a more distributed structural load along the structure. Onkonkwo [19] describes the history of the BWB aircraft originating from military aircraft, after which research has been dedicated to developing a commercial BWB aircraft, as the inherent fuselage design reduces aerodynamic resistance and the noise signature of the aircraft. Both are currently challenges in the commercial aerospace sector. Bravo-Mosquera [20] poses the development of newer aircraft for civil aviation as he shows the development of design evolution in time, as shown in Figure 2.1. Progress was initially measured in range and fuel efficiency, but nowadays, it is mainly defined by noise and emissions, where fuel efficiency remains the same.

The BWB wing configuration is posed as the most promising, with Liebeck first evaluating the concept and finding a 15% reduction in takeoff weight and a 27% reduction in fuel burn per seat for his preliminary analysis [1]. Well-established companies and institutes such as Boeing, Airbus, NASA, and TU Delft have since been researching and testing BWB concepts, maturing the idea with the first full-scale test-flight being planned by JetZero, in collaboration with Northrop Grumman and Scaled Composites in early 2027 [21].

The Flying-V, however, is a slight alteration to the conventional BWB design, as a conventional BWB does not let itself be stretched or shrunk [3]. The Flying-V, however, does lend itself to be stretched or shrunk as the section where the passengers are housed is constant and can easily be expanded, giving a higher potential in developing a fleet of flying wing aircraft, as researched by Oosterom [3]. Figure 2.2 shows a side-by-side comparison of a CTW A350-900, the Flying-V 1000 series.

2.1.1. Concept Limitations

Unfortunately, despite the concept's great potential, some challenges must be solved before a BWB can be appropriately used in commercial aviation. These challenges primarily involve issues with stability & control, the integration of propulsion systems, airframe, and aero-acoustic aspects. A particular challenge in BWB design is maintaining an AoA of no more than 3 degrees during the cruise, a difficulty attributed to the low lift curve slope. This aspect also influences the lift coefficient needed during landing and takeoff, potentially necessitating a larger landing gear for higher attack angles.

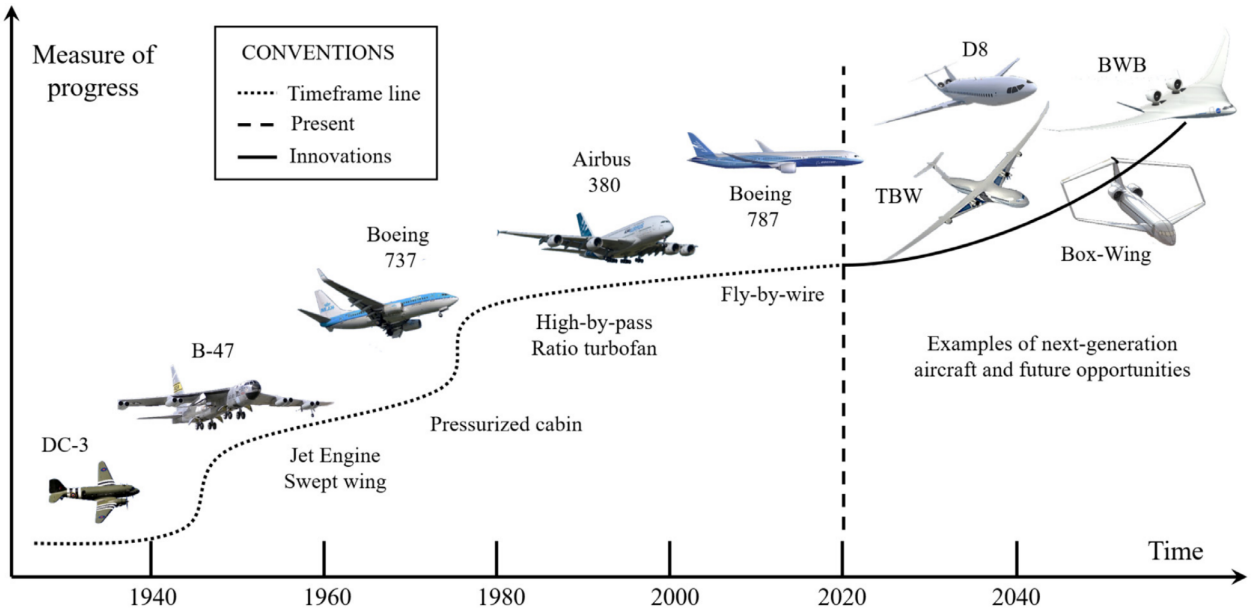

Figure 2.1: Progress in commercial aircraft design, from conventional designs to next-generation aircraft [20]

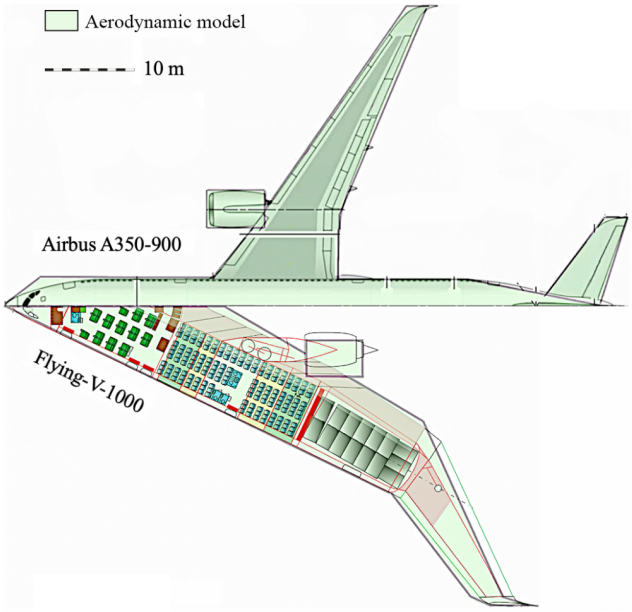

Figure 2.2: Planform comparison of CTW A350-900 and Flying-V 1000 [22]

Qin and colleagues have discovered that in terms of aerodynamics, an elliptic lift distribution is less efficient than a blend of elliptic and triangular distributions. Conversely, a purely triangular distribution contributes to minimal structural weight, underscoring the necessity of comprehensive aerodynamic studies within a multidisciplinary context for aircraft design. The BWB's low wing loading, a consequence of its entire structure contributing to lift, results in lower takeoff and landing speeds and reduces the required field length. However, this low wing loading also renders the aircraft more susceptible to gusts.

The BWB's cabin design presents structural challenges. The need for cabin pressurization typically favors a circular design, as seen in conventional aircraft. However, a BWB's integrated configuration makes this difficult, prompting a design shift towards a laterally stretched cabin. Additionally, the requirement for an airfoil-shaped cross-section and adequate cabin height necessitates a larger aircraft size. Mike Sinnett, former Boeing Vice-President of Product Development and Future Airplane Development, highlighted this issue and noted the challenges of BWB's larger wingspan and airport compatibility. He remarked on the trade-off between wingspan and range, indicating that BWB aircraft are more suited for long-range flights due to their large wingspan and cabin height requirements. Sinnett also pointed out potential operational drawbacks for BWB aircraft, such as slower loading and unloading times, which are particularly critical for

short flights.

There are further concerns with the BWB design, including the positioning of passengers further from the aircraft's center of gravity, which could increase motion sickness, and challenges in providing window seats in a wide-cabin layout. Emergency evacuation could also be more complex due to the placement of exits relative to passengers.

Designing a family of BWB aircraft introduces another layer of complexity. The process may require stretching the fuselage's non-uniform parts, as Liebeck demonstrated using a T-shaped plug to generate different BWB sizes. This poses structural challenges, especially with pressurized cabins. Liebeck does not delve into these structural challenges but does mention the advantage of automatically increased wing area and span with higher payloads in BWB family designs. He also notes that design commonality in such a family could reduce non-recurring and recurring costs by 23% and 12%, respectively. Liebeck suggests placing fuel in the outer wing, which does not scale the fuel capacity with different aircraft sizes.

2.2. Previous research about the Flying-V

Since Benad first wrote about the concept of the Flying-V in collaboration with Airbus in his paper, the Delft University of Technology has put in significant effort to develop this concept into a working model. Figure 2.3 shows a photograph from July 2020, where a scale model is flown for the first time. In 2022, Benad [23] made an extensive summary of all the work that has been done up until that moment, and Van Overeem also reviewed this separately, more focussed on the flight dynamics and control [13]. To avoid repeating the extensive research of both papers, the author will summarize the relevant aspects of this research and add new relevant research as an extension to Van Overeem's statement. As was stated, the

Figure 2.3: Flying-V scale model first test flight [1]

research on the Flying-V began in 2015 when the potential of the Flying-V was found to be an improvement to the Airbus A350-900 of 10% for the lift-to-drag ratio, a reduced noise profile and a 2% lower empty weight [2]. This research was followed up by an aerodynamic optimization for a cruise speed of 0.85M at 13000 m, leading to a more optimized design and a 25% aerodynamic efficiency increase compared to a NASA Common Research Model [6]. This research model was created by Vassberg et al.[24] to have a reference case for drag prediction studies. The model represents a modern long-range commercial aircraft operating at transonic flight conditions, such as the Airbus A350-900 (M=0.85). The design has since been further aerodynamically optimized to increase the lift-to-drag ratio[25][26]. Next, research was dedicated to finding the location of the Center of Gravity (CoG) and aerodynamic coefficients of a scale model of the Flying-V using wind-tunnel test and a scale model test flight, as shown in Figure 2.3, from which it was concluded that the Flying-V experiences pitch break-up above an AoA of 20 ° [5], [8], [9]. Marques [7] concluded, using CFD, that the wind tunnel results where influenced by the walls of the wind tunnel, concluding that there are signs of flow separation at and AoA of $\alpha = 32°$, compared to $\alpha = 20°$. The full-scale Flying-V simulations even suggest flow separation is extended beyond this point. Cappuyns dedicated research to assessing the handling qualities, where it was concluded that the Dutch roll is unstable and the lateral directional controllability is low for One Engine Inoperative conditions [4]. Even after a parametric optimization of the winglet structure, the yawing moment was still found to be unsatisfactory [27]. Using system identification methods, Siemonsma derived an aerodynamic model that shows potential; however, due to a lack of satisfactory flight test data, this model still has unacceptable deviations from wind-tunnel

[1] `https://www.tudelft.nl/en/ae/flying-v` visited at 15-02-2024

tests [28]. Nolet researched the potential use of split-flaps as an extension to the control surfaces, which showed an increase of yaw control authority of 85.5% at an $\alpha = 27.5°$ at the drawback of tripling the drag [29]. These split-flaps were also researched to reduce the pitch attitude at landing, providing the pilots with more vision [30]. The current simulation models have been evaluated in the SIMONA Full-Flight Simulator of the TU Delft to receive feedback from pilots regarding the handling qualities, with focus on the longitudinal handling qualities by Vugts [12] and Torelli [11] and the lateral handling qualities by Joosten [10]. These evaluations found that at low speeds (M $\approx$ 0.2) the handling qualities degrade due to low control authority and proper control allocation is recommended in all studies. Research to the first FCSs was applied for the longitudinal motion by Torelli [11] and the lateral motion by Joosten [10]. These FCSs were simple linear PID controllers, primarily used to reduce the adverse effects from the short period and Dutch roll eigenmodes. These were the first version of a FCS in the Flying-V.

Most relevant for this work has been the research done by Van Overeem [13] and Stougie [14], towards the implementation of a proper FCS, using INDI control. Völker also researched the possibility of implementing a FCS using bio-inspired Reinforcement Learning, which shows potential as an alternative control method compared to NDI[31]. Van Overeem first implemented an inner-loop INDI controller to make the Flying-V adhere to the required handling qualities. These *requirements* are derived from the recommended specifications from the military document for "Flying Qualities of Piloted Aircraft" document in either MIL-STD-1797 or MIL-HDBK-1797 [32]. Stougie added FEP to take into account the pitch break-up and found that rudder oscillations are present at low flying speeds (M $\approx$ 0.20), which is suggested to be a consequence of low control authority. Furthermore, it was found that the INDI control law can achieve the required Level 1 handling qualities. This FCS will be elaborated upon in Section 3.3.

As can be concluded, the research and development of the Flying-V aircraft are still progressing, and the project is maturing at every step. To help automate this process, Świderski developed a Python library that automates handling quality prediction evaluations [33]. This tool can be helpful if combined with the aircraft design process. Figure 2.4, summarizes this Section with a timeline, identifying three aspects of the progress of the project; general progress, progress in aerodynamic design & analysis and progress for the flight stability & control.

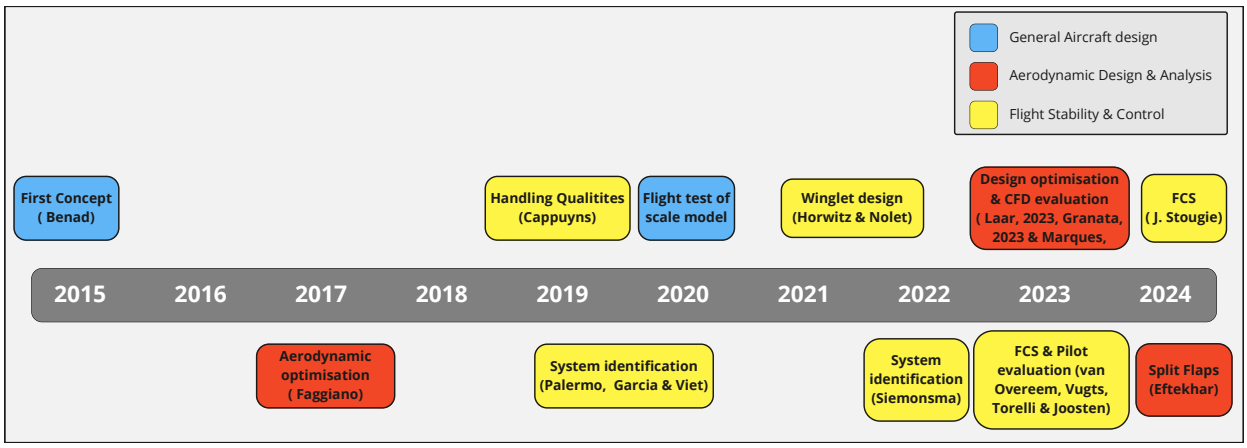

Figure 2.4: Timeline of research related to the Flying-V

2.3. Flying-V control surface layout

As the design of the Flying-V has evolved significantly since the start of the project, it shall be considered to design the FCS as versatile as possible, as to take into account potential changes in design. The aircraft's layout is essential when creating a FCS as this defines which control surfaces can stabilize and control the plane. Since the first development of the Flying-V, there have been changes in the layout of the elevons. An elevon is essentially a control surface with the handling capabilities of an elevator and an aileron, stabilizing the aircraft in the pitch and roll direction. The split lines of the two elevons were chosen arbitrarily. The rudder configuration has been constant across the different layouts, however the other configurations are described below and the layouts are shown in Figure 2.5. Table 2.1 shows the respective dimensions of the aircraft, which are used for the EoM in Section 2.6.

Figure 2.5a shows the initial control surface layout introduced by Cappuyns, where two elevons per side are used for pitch and roll control. For this configuration, VLM simulation results are present. This layout posed difficulties with the control authority, especially in the lateral direction, due to the short longitudinal distance from the rudder to the Center of Pressure (CoP), compared to a CTW aircraft.

Figure 2.5b shows the configuration with three elevons, introduced by Palermo et al. [8], which has been adopted as the control surface layout for the sub-scale model [34]. For this layout, WTE and flight test data are present, but only for the sub-scale model.

Figure 2.5c shows the configuration introduced by Nolet[29] and Eftekhar [30], where the most outboard elevon from the three elevon configuration is split, to implement a split flap, which can give the pilots more lateral control authority. For this configuration, no model identification has been done.

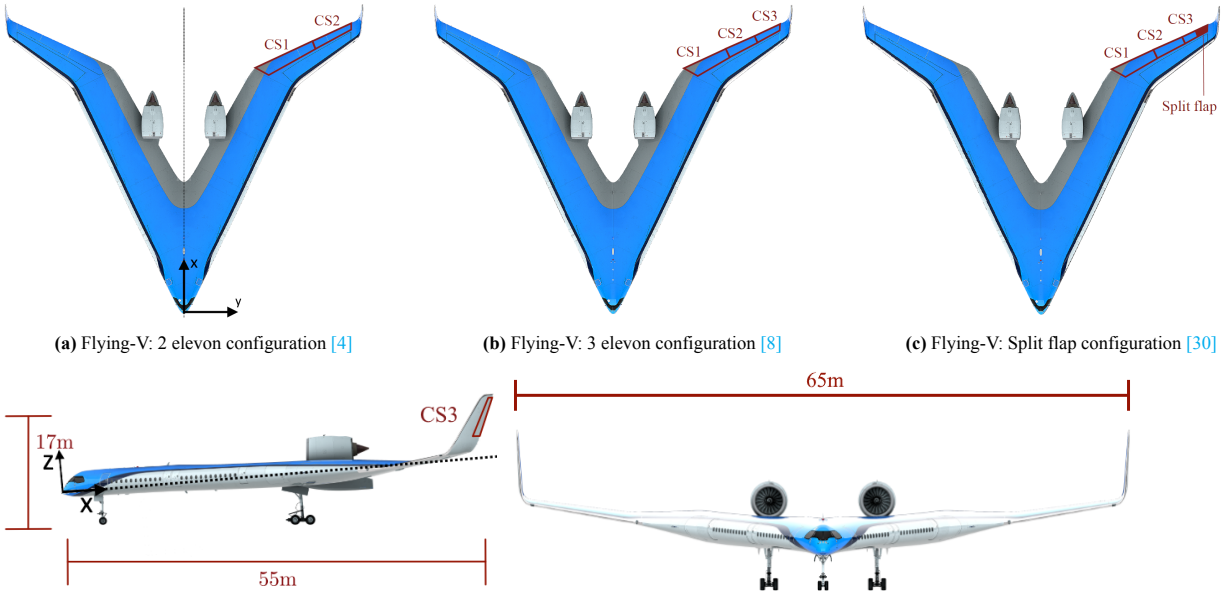

(a) Flying-V: 2 elevon configuration [4]

(b) Flying-V: 3 elevon configuration [8]

(c) Flying-V: Split flap configuration [30]

(d) Side view Flying-V

(e) Front view Flying-V

Figure 2.5: Control surface layout of Flying-V

Table 2.1: Flying-V V1000 dimensions [4]

Property	Description	Value	Unit
T_{dy}	Engine (thrust vector) y location w.r.t. centre line	$\pm$5.60	m
T_{dz}	Engine (thrust vector) z location w.r.t. centre line	0.800	m
S	Wing area	883	m^2
c_{MAC}	Wing Mean Aerodynamic Chord	18.74	m
x_{pilot}	Distance of pilot station, measured from nose	5.00	m
b	Wing span	65.0	m
L	Aircraft length	55.0	m

In previous research from Van Overeem [13] and Stougie[14], the layout with two elevons and a rudder, shown in Figure 2.5a was implemented. This layout has the most reliable data, especially for the control surfaces, and it is the only one identified for the full-scale Flying-V model. Other research has been focussing on the sub-scale model; however, this research will focus on improving the FCS of the full-scale Flying-V model. Therefore, the layout from Figure 2.5a is adopted to make a proper comparison with older research. The flight conditions for which the simulations will be done in this research are approach and cruise, for which specific parameters are given in Table 2.2

Table 2.2: Flight conditions considered in this research [13]

	Approach Condition	Cruise Condition
M	0.2	0.85
ρ_{air}	1.225 kg/m^3	0.2655 kg/m^3
a_{mach}	336.4 m/s	295.1 m/s
Maximum Take-off Mass (MTOM)	210,000 kg	240,000 kg
h	1000 m	13,000 m

2.4. Mass Properties

The mass properties of the Flying-V full-scale model have been estimated using the Odilila VLM, which is also used for calculating the aerodynamic properties [4]. The lumped mass model was used to estimate the moments of inertia, where different aircraft components are combined, and each element has a specific point mass at a CoG. The aircraft is assumed to be symmetrical, given that I_{xy} and I_{yz} can be set to zero [4]. Furthermore, it was found that I_{xz} is also equal to zero, leaving only the principle axes. Van Overeem and Stougie have also used this mass model[13], [14]. Equation 2.1 shows the moment of inertia matrix. Table 2.3 shows the mass and inertia properties for MTOM and empty weight. There are also two locations for the CoG, denoted by $p_{c.g.}$ and the location for the CoP. It is assumed the coordinates only differ in the X-axis, meaning from front to aft of the aircraft. The points for the CoG correspond with a Mean Aerodynamic Chord (MAC) of 45% for $p_{c.g.}$ = 29.372 m and a MAC of 57.5% for $p_{c.g.}$ = 31.714 m, both aft of the nose of the aircraft [13].

$$\boldsymbol{I_C} = \begin{bmatrix} I_{xx} & -I_{xy} & -I_{xz} \\ -I_{xy} & I_{yy} & -I_{yz} \\ -I_{xz} & -I_{yz} & I_{zz} \end{bmatrix} = \begin{bmatrix} I_{xx} & 0 & 0 \\ 0 & I_{yy} & 0 \\ 0 & 0 & I_{zz} \end{bmatrix} \tag{2.1}$$

Table 2.3: Mass properties and property centers for TU Delft Flying-V [13]

Mass Property	Value	Unit
m	[2.10 ·10^5 - 2.40·10^5]	[kg]
I_{xx}	3.9641·10^7	[kg · m^2]
I_{yy}	2.7619·10^7	[kg · m^2]
I_{zz}	6.5822·10^7	[kg · m^2]
I_{xz}, I_{xy}, I_{yz}	0	[kgm^2]
Point name	Location, aft of nose	Unit
$p_{c.g.}$	[29.372 ; 31.714]	[m]
p_{CoP}	32.18268	[m]

2.5. Reference frame of simulations

For continuity and clarity, it is critical to define in which reference frame the equations of motion hold. If these are used inconsistently or are not appropriately determined, the results will have no meaning. Several reference frames are relevant for the simulation of the Flying-V and have been documented clearly by Van Overeem [13]. To summarize, the applicable reference frames for the Flying-V and the Vehicle-Carried Normal Earth reference frame, $\mathcal{E}$, Body-fixed reference frame, $\mathcal{B}$ and the aerodynamic reference frame, $\mathcal{A}$. These notations will be used as subscripts if a specific notation is given. The following sections briefly summarize the use of each frame and its notation.

2.5.1. Vehicle-Carried Normal Earth Reference Frame,$\mathcal{E}$

The vehicle-carried normal Earth reference frame, or geodetic reference frame, is an inertial reference frame that holds the 2nd Law of Newton. This reference frame has its origin in the center of mass of the aircraft, with the $X_{\mathcal{E}}$-axis pointing north, $Y_{\mathcal{E}}$-axis pointing east and the $Z_{\mathcal{E}}$-axis pointing down to the center of the Earth. The coordinates of this reference frame are measured in λ for longitude, Φ for longitude, and h for altitude. The Earth is assumed to be a perfect sphere with the three different latitudes lining up together in the Earth's center [35]. A visual representation of this reference frame, for the earth's inertial reference frame, is given in Figure 2.6

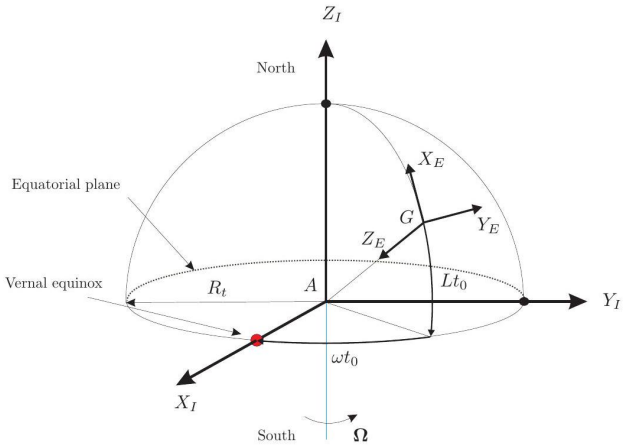

Figure 2.6: Vehicle-Carried Normal Earth Reference Frame [35]

2.5.2. Body-Fixed Reference Frame, $\mathcal{B}$

The body-fixed reference frame is a right-handed coordinate system attached to the aircraft's orientation, with its origin located at the aircraft's CoG. Cappuyns visualized the Flying-V in this reference frame, as shown in Figure 2.7. The $X_{\mathcal{B}}$-axis is in the symmetry plane of the aircraft, pointing forward. The $Z_{\mathcal{B}}$-axis is also located in the symmetry plane and is pointing downward, perpendicular to the $X_{\mathcal{B}-}$ axis. Lastly, the $Y_{\mathcal{B}}$-axis points right, across the wing, perpendicular to both the $X_{\mathcal{B}-}$ axis and the $Z_{\mathcal{B}}$-axis [35]. As can be seen in Figure 2.7, the body velocity vectors are given parallel to the axes and are given as $u_{\mathcal{B}}, v_{\mathcal{B}}, w_{\mathcal{B}}$ for the forward, sideward and downward velocity respectively. Furthermore, the body moments and rates are also given. Along the $X_{\mathcal{B}-}$ axis, l describes the roll moment where p gives the roll rate respectively. The same holds for m and q along the $Y_{\mathcal{B}}$-axis giving the pitch moment and rate, and for n and r along the $Z_{\mathcal{B}}$-axis giving the pitch moment and rate. On the $X_{\mathcal{B}-}$ axis, l represents the roll moment, while p indicates the roll rate. Similarly, along the $Y_{\mathcal{B}-}$ axis, m corresponds to the pitch moment and q to the pitch rate, and along the $Z_{\mathcal{B}-}$ axis, n and r denote the yaw moment and yaw rate, respectively.

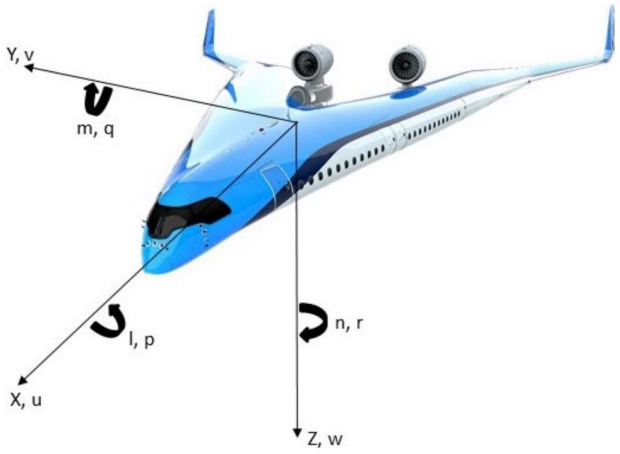

Figure 2.7: Body reference frame sign convention [4]

2.5.3. Aerodynamic Reference Frame, $\mathcal{A}$

The aerodynamic reference frame is coupled to the aerodynamic velocity vector of the aircraft, V_∞, also known as the free-stream velocity. This reference frame has its origin at the CoG of the aircraft, just as the body-fixed reference frame and rotates its axes to align the $X_{\mathcal{A}-}$ axis with the free-steam velocity. Figure 2.8 visually represents this transformation. The definition of the $Y_{\mathcal{A}-}$ and $Z_{\mathcal{A}-}$ axes are the same as for the body reference frame, only rotated with the AoA, α, and side slip angle, β [35].

2.5.4. Reference Frame Transformation

With multiple reference frames, it is important to transform between them. These transformations are mostly deducted from Mulder et al. [35, CH2]. These transformations will be described using $\mathbb{R}$, with subscripts

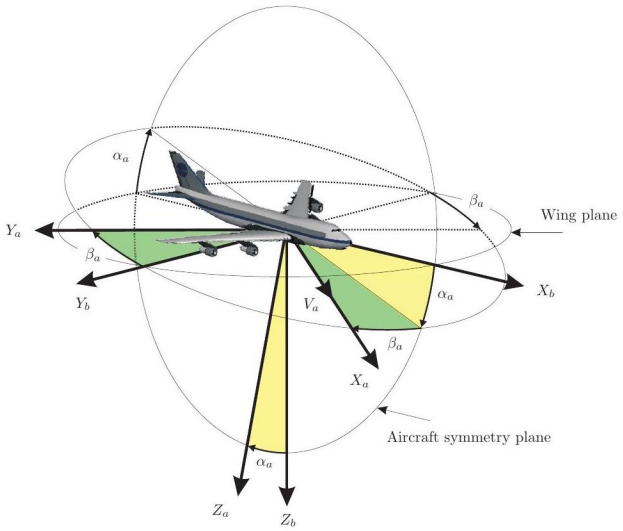

Figure 2.8: Visualisation of body-fixed reference frame transformed to the aerodynamic reference frame [35]

specifying the transition from one reference frame to another in coordinate transformation.

The first transformation considers changing from the vehicle-carried normal earth reference frame,$\mathcal{E}$ to the body-fixed reference frame, $\mathcal{B}$, and vice-versa. The rotation is done using a commonly known $\psi - \theta - \phi$ rotation sequence. These transformation matrices are shown in Equations 2.2 and 2.3.

$$\mathbb{R}_\phi = \begin{bmatrix} 1 & 0 & 0 \\ 0 & \cos(\phi) & \sin\phi \\ 0 & -\sin\phi & \cos\theta \end{bmatrix}, \mathbb{R}_\theta = \begin{bmatrix} \cos\theta & 0 & -\sin\theta \\ 0 & 1 & 0 \\ \sin\theta & 0 & \cos\theta \end{bmatrix}, \mathbb{R}_\psi = \begin{bmatrix} \cos\psi & \sin\psi & 0 \\ -\sin\psi & \cos\psi & 0 \\ 0 & 0 & 1 \end{bmatrix}$$

$$\mathbb{R}_\phi \mathbb{R}_\theta \mathbb{R}_\psi = \mathbb{R}_{\mathcal{E}\to\mathcal{B}}$$

$$\mathbb{R}_{\mathcal{E}\to\mathcal{B}} = \begin{bmatrix} \cos(\psi)\cos(\theta) & \sin(\psi)\cos(\theta) & -\sin(\theta) \\ \cos(\psi)\sin(\theta)\sin\phi - \sin(\psi)\cos(\phi) & \sin(\psi)\sin(\theta)\sin(\phi) + \cos(\psi)\cos(\phi) & \cos(\theta)\sin(\phi) \\ \cos(\psi)\sin(\theta)\cos(\phi) + \sin(\psi)\sin(\phi) & \sin(\psi)\sin(\theta)\cos(\phi) - \cos(\psi)\sin(\phi) & \cos(\theta)\cos(\phi) \end{bmatrix} \tag{2.2}$$

$$\mathbb{R}_{\mathcal{B}\to\mathcal{E}} = \begin{bmatrix} \cos(\psi)\cos(\theta) & \cos(\psi)\sin(\phi)\sin(\theta) - \cos(\phi)\sin(\psi) & \sin(\phi)\sin(\psi) + \cos(\phi)\cos(\psi)\sin(\theta) \\ \cos(\theta)\sin(\psi) & \cos(\phi)\cos(\psi) + \sin(\phi)\sin(\psi)\sin(\theta) & \cos(\phi)\sin(\psi)\sin(\theta) - \cos(\psi)\sin(\phi) \\ -\sin(\theta) & \cos(\theta)\sin(\phi) & \cos(\phi)\cos(\theta) \end{bmatrix} \tag{2.3}$$

The second transformation is done for changing from the body-fixed reference frame,$\mathcal{B}$, to the aerodynamic reference frame,$\mathcal{A}$. The transformation matrices are given in Equations 2.4 and 2.5.

$$\mathbb{R}_{\mathcal{B}\to\mathcal{A}} = \begin{bmatrix} \cos(\alpha)\cos(\beta) & \sin(\beta) & \cos(\beta)\sin(\alpha) \\ -\cos(\alpha)\sin(\beta) & \cos(\beta) & -\sin(\alpha)\sin(\beta) \\ -\sin(\alpha) & 0 & \cos(\alpha) \end{bmatrix} \tag{2.4}$$

$$\mathbb{R}_{\mathcal{A}\to\mathcal{B}} = \begin{bmatrix} \cos(\alpha)\cos(\beta) & -\cos(\alpha)\sin(\beta) & -\sin(\alpha) \\ \sin(\beta) & \cos(\beta) & 0 \\ \sin(\alpha)\cos(\beta) & -\sin(\alpha)\sin(\beta) & \cos(\alpha) \end{bmatrix} \tag{2.5}$$

2.6. Equations of Motion

Kinematics and dynamics are needed to properly model the behavior and movement of the Flying-V in the simulation model. These dynamics are highly non-linear and non-control affine, however control affinity is required for the implementation of an INDI control law, as will be discussed in Section 2.7. The EoM are shown below in the simulation model.

2.6.1. Assumptions

Before deriving the EoM that will be used in this research, some assumptions are made, which make it possible to neglect specific terms. These assumptions are elaborated by Mulder et al. [35] and implemented

by Cappuyns, Van Overeem, and Stougie [4], [13], [14].

- The aircraft is a rigid body and has a constant mass.
- The Earth is flat and non-rotating.
- There is zero wind and a perfect atmosphere.
- The resultant thrust lies in the symmetry plane (not for OEI).
- The gravitational acceleration,g_0, is constant.

It is assumed that gravity, thrust, and aerodynamics are the only forces acting on the aircraft. These are applied as point forces, all acting on the CoG [4]. Due to the flat-earth assumption, the vehicle-carried normal earth reference frame is similar to the inertial reference frame, and Newton's 2nd Law can be applied [35].

2.6.2. Derivations

The equations consist of 15 states, for which the state derivatives can be calculated through their respective equation of motion. These states are the earth-fixed position coordinates ($X_\mathcal{E}$,$Y_\mathcal{E}$,$Z_\mathcal{E}$), body velocities ($u_\mathcal{B}$,$v_\mathcal{B}$,$w_\mathcal{B}$), body angular velocities (p, q, r), Euler attitude angles (ϕ, θ, ψ) and aerodynamic attitude and velocity (α, β, V_∞). These equations are derived from Mulder et al. [35, CH3].

$$\begin{bmatrix} \dot{X}_\mathcal{E} \\ \dot{Y}_\mathcal{E} \\ \dot{Z}_\mathcal{E} \end{bmatrix} = \mathbb{R}_{\mathcal{B}\to\mathcal{E}} \begin{bmatrix} u_\mathcal{B} \\ v_\mathcal{B} \\ w_\mathcal{B} \end{bmatrix} = \begin{bmatrix} \mathrm{c}\psi\mathrm{c}\theta & \mathrm{c}\psi\mathrm{s}\theta\mathrm{s}\phi - \mathrm{s}\psi\mathrm{c}\phi & \mathrm{s}\psi\mathrm{s}\phi + \mathrm{c}\psi\mathrm{s}\theta\mathrm{c}\phi \\ \mathrm{s}\psi\mathrm{c}\theta & \mathrm{c}\psi\mathrm{c}\phi + \mathrm{s}\psi\mathrm{s}\theta\mathrm{s}\phi & \mathrm{s}\psi\mathrm{s}\theta\mathrm{c}\phi - \mathrm{c}\psi\mathrm{s}\phi \\ -\mathrm{s}\theta & \mathrm{c}\theta\mathrm{s}\phi & \mathrm{c}\theta\mathrm{s}\phi \end{bmatrix} \begin{bmatrix} u_\mathcal{B} \\ v_\mathcal{B} \\ w_\mathcal{B} \end{bmatrix} \tag{2.6}$$

$$\begin{bmatrix} \dot{u}_\mathcal{B} \\ \dot{v}_\mathcal{B} \\ \dot{w}_\mathcal{B} \end{bmatrix} = \frac{1}{m} \begin{bmatrix} F_x \\ F_y \\ F_z \end{bmatrix}_\mathcal{B} - \begin{bmatrix} p \\ q \\ r \end{bmatrix} \times \begin{bmatrix} u_\mathcal{B} \\ v_\mathcal{B} \\ w_\mathcal{B} \end{bmatrix} + g_0 \begin{bmatrix} -\sin\theta \\ \sin\phi\cos\theta \\ \cos\phi\cos\theta \end{bmatrix} \tag{2.7}$$

$$\begin{bmatrix} \dot{p} \\ \dot{q} \\ \dot{r} \end{bmatrix} = \begin{bmatrix} \frac{I_{zz}}{I_*} & 0 & \frac{I_{xz}}{I_*} \\ 0 & \frac{1}{I_{yy}} & 0 \\ \frac{I_{xz}}{I_*} & 0 & \frac{I_{xx}}{I_*} \end{bmatrix} \begin{bmatrix} M_x \\ M_y \\ M_z \end{bmatrix}_\mathcal{B} - \begin{bmatrix} \frac{I_{zz}}{I_*} & 0 & \frac{I_{xz}}{I_*} \\ 0 & \frac{1}{I_{yy}} & 0 \\ \frac{I_{xz}}{I_*} & 0 & \frac{I_{xx}}{I_*} \end{bmatrix} \left(\begin{bmatrix} p \\ q \\ r \end{bmatrix} \times \begin{bmatrix} I_{xx} & 0 & -I_{xz} \\ 0 & I_{yy} & 0 \\ -I_{xz} & 0 & I_{zz} \end{bmatrix} \begin{bmatrix} p \\ q \\ r \end{bmatrix} \right) \tag{2.8}$$

$$\begin{bmatrix} p \\ q \\ r \end{bmatrix} = \begin{bmatrix} \dot{\phi} \\ 0 \\ 0 \end{bmatrix} + \mathbb{R}_\phi \begin{bmatrix} 0 \\ \dot{\theta} \\ 0 \end{bmatrix} + \mathbb{R}_\phi \mathbb{R}_\theta \begin{bmatrix} 0 \\ 0 \\ \dot{\psi} \end{bmatrix} = \begin{bmatrix} 1 & 0 & -\sin\theta \\ 0 & \cos\phi & \sin\phi\cos\theta \\ -\sin\phi & \cos\phi\cos\theta & \cos\phi\cos\theta \end{bmatrix} \begin{bmatrix} \dot{\phi} \\ \dot{\theta} \\ \dot{\psi} \end{bmatrix} \tag{2.9}$$

$$\begin{bmatrix} \dot{\phi} \\ \dot{\theta} \\ \dot{\psi} \end{bmatrix} = \begin{bmatrix} 1 & \sin\phi\tan\theta & \cos\phi\tan\theta \\ 0 & \cos\phi & -\sin\phi \\ 0 & \frac{\sin\phi}{\cos\theta} & \frac{\cos\phi}{\cos\theta} \end{bmatrix} \begin{bmatrix} p \\ q \\ r \end{bmatrix} \tag{2.10}$$

where in Equation 2.8:

$$I^* = I_{xx}I_{yy} - I_{xz}^2$$

It can be seen that Equations 2.6 and 2.10 represent the kinematics of the system, as they do not require external forces or moments. Equations 2.7 and 2.8 represent the system's dynamics, with the forces and moments acting in the body reference frame. These forces and moments are defined in Equations 2.11 and 2.12, respectively. In the aerodynamic frame, the forward force, $F_{x,\mathcal{A}}$, equals the negative drag force, $-D$. Furthermore, the downward force, $F_{z,\mathcal{A}}$, is equal to the negative lift force, $-L$. Aerodynamic moments are generally measured from the body reference frame and thus need no transformation. Some extra moments are generated, related to the engine offset, d_{Ty}, which affects the aircraft being pushed down with thrust applied. The same applies to a yawing moment that is introduced if the engines do not provide equal thrust. Lastly, the aerodynamic moments act on the CoP, whereas the body moments act in the CoG. Assuming the CoP is in the symmetric plane of the aircraft, the shift of the moments has to be compensated. [36] The location of the CoP is denoted by p_{CoP} and the location of the CoG is denoted by $p_{c.g.}$.

$$\begin{aligned}\begin{bmatrix} F_x \\ F_y \\ F_z \end{bmatrix}_{\mathcal{B}} &= \mathbb{R}_{\mathcal{A}\to\mathcal{B}} \begin{bmatrix} F_x \\ F_y \\ F_z \end{bmatrix}_{\mathcal{A}} + \begin{bmatrix} T_1+T_2 \\ 0 \\ 0 \end{bmatrix}_{\mathcal{B}} \\ &= \begin{bmatrix} \cos(\alpha)\cos(\beta) & -\cos(\alpha)\sin(\beta) & -\sin(\alpha) \\ \sin(\beta) & \cos(\beta) & 0 \\ \sin(\alpha)\cos(\beta) & -\sin(\alpha)\sin(\beta) & \cos(\alpha) \end{bmatrix} \begin{bmatrix} F_x \\ F_y \\ F_z \end{bmatrix}_{\mathcal{A}} + \begin{bmatrix} T_1+T_2 \\ 0 \\ 0 \end{bmatrix}_{\mathcal{B}}\end{aligned} \tag{2.11}$$

$$\begin{bmatrix} M_x \\ M_y \\ M_z \end{bmatrix}_{\mathcal{B}} = \begin{bmatrix} M_x \\ M_y \\ M_z \end{bmatrix}_{\mathcal{A}} + \begin{bmatrix} 0 \\ F_{z,\mathcal{B}}(p_{CoP}-p_{c.g.}) \\ -F_{y,\mathcal{B}}(p_{CoP}-p_{c.g.}) \end{bmatrix} + \begin{bmatrix} 0 \\ -d_{Ty}(T_1+T_2) \\ d_{Tz}(T_1-T_2) \end{bmatrix}_{\mathcal{B}} \tag{2.12}$$

The aerodynamic forces are mostly approximated by system identification, which will be highlighted in Section 2.7. These aerodynamic forces often depend on the aerodynamic attitude and velocity $(\alpha, \beta, V_\infty)$. Therefore, the state derivatives will be derived here for these states, as those are not derived by Mulder et al. [35]. The relations in Equations 2.13, 2.14 and 2.15 will be used to change the body accelerations from Equation 2.7 into the aerodynamic rates and acceleration. The resulting wind frame EoM are shown in Equations 2.17,2.18 and 2.19. The definition of how γ is calculated throughout this research is given in Equation 2.20.

$$\alpha = \tan^{-1}\left(\frac{w_{\mathcal{B}}}{u_{\mathcal{B}}}\right) \tag{2.13}$$

$$\beta = \sin^{-1}\left(\frac{v_{\mathcal{B}}}{V_\infty}\right) \tag{2.14}$$

$$V_\infty = \sqrt{u_{\mathcal{B}}^2 + v_{\mathcal{B}}^2 + w_{\mathcal{B}}^2} \tag{2.15}$$

$$\begin{bmatrix} u_{\mathcal{B}} \\ v_{\mathcal{B}} \\ w_{\mathcal{B}} \end{bmatrix} = \begin{bmatrix} V_\infty \cos(\alpha)\cos(\beta) \\ V_\infty \sin(\beta) \\ V_\infty \sin(\alpha)\cos(\beta) \end{bmatrix} \tag{2.16}$$

$$\dot{\alpha} = \frac{F_{z,\mathcal{A}} - (T_1+T_2)\mathrm{s}(\alpha)}{V_\infty m \mathrm{c}(\beta)} + q - \tan(\beta)\left[p\mathrm{c}(\alpha) + r\mathrm{s}(\alpha)\right] + \frac{g_0}{V_\infty \mathrm{c}(\beta)}\left[\mathrm{c}(\alpha)\mathrm{c}(\phi)\mathrm{c}(\theta) + \mathrm{s}(\alpha)\mathrm{s}(\theta)\right] \tag{2.17}$$

$$\dot{\beta} = \frac{F_{y,\mathcal{A}} - (T_1+T_2)\mathrm{c}(\alpha)\mathrm{s}(\beta)}{mV_\infty} + p\mathrm{s}(\alpha) - r\mathrm{c}(\alpha) + \frac{g_0}{V_\infty}\left[\mathrm{c}(\beta)\mathrm{s}(\phi)\mathrm{c}(\theta) + \mathrm{c}(\alpha)\mathrm{s}(\beta)\mathrm{s}(\theta) - \mathrm{s}(\alpha)\mathrm{s}(\beta)\mathrm{c}(\phi)\mathrm{s}(\theta)\right] \tag{2.18}$$

$$\dot{V_\infty} = \frac{F_{x,\mathcal{A}} + (T_1+T_2)\mathrm{c}(\alpha)\mathrm{c}(\beta)}{m} + g_0\left[\mathrm{s}(\beta)\mathrm{s}(\phi)\mathrm{c}(\theta) + \mathrm{s}(\alpha)\mathrm{c}(\beta)\mathrm{c}(\phi)\mathrm{c}(\theta) - \mathrm{c}(\alpha)\mathrm{c}(\beta)\mathrm{c}(\theta)\right] \tag{2.19}$$

$$\gamma = \arcsin\left[\cos(\alpha)\cos(\beta)\sin(\theta) - \cos(\theta) * (\sin(\beta)\sin(\phi) + \sin(\alpha)\cos(\beta)\cos(\phi))\right] \tag{2.20}$$

2.7. Aerodynamic model

To properly simulate the dynamic behavior of the Flying-V, the aerodynamic characteristics have to be determined, and the forces acting on the system due to aerodynamics must be considered. The aerodynamic force coefficients are defined in Equation 2.21, whereas the aerodynamic moment coefficients are defined in Equation 2.22. These coefficients act in the aerodynamic reference frame and non-dimensionalize the forces and moments acting on the system.

$$C_x = \frac{F_{x,\mathcal{A}}}{\bar{q}S}, \quad C_y = \frac{F_{y,\mathcal{A}}}{\bar{q}S}, \quad C_z = \frac{F_{z,\mathcal{A}}}{\bar{q}S} \tag{2.21}$$

$$C_l = \frac{M_{x,\mathcal{A}}}{\bar{q}S\bar{c}}, \quad C_m = \frac{M_{y,\mathcal{A}}}{\bar{q}S\bar{c}}, \quad C_n = \frac{M_{z,\mathcal{A}}}{\bar{q}S\bar{c}} \tag{2.22}$$

with the dynamic pressure indicated defined as:

$$\bar{q} = \frac{1}{2}\rho_{air}V_\infty^2$$

With current research, it is possible to determine the aerodynamic behavior of the Flying-V using three different methods, which are:

1. Vortex Lattice Method results
2. Wind Tunnel Experiments
3. Flight Test Experiments

Each method has advantages and disadvantages, which will be briefly discussed below. After this, a conclusion is made about which method or combination of methods will be used to model the aerodynamic forces of the Flying-V.

2.7.1. Vortex Lattice Method

The following Section mainly refers to the work of Cappuyns since he established the framework for the VLM, which is used up until the current research [4]. A computational method to acquire aerodynamic data of the Flying-V is with the VLM. The full-scale Flying-V CAD model is imported into the parametric modelling tool, "BlackSwan", from which the geometry model is converted into a panel model, which can be used for VLM simulations and a strip model for inertia estimations. Airbus has provided the Delft University of Technology with Odilila, a VLM simulation tool. From these simulations, the aerodynamic coefficients from Equations 2.21 and 2.22 are interpolated at different intervals, at 3 Mach numbers; M = 0.2 (Approach), M=0.3 (Take-off) and M=0.85 (Cruise). For the interested reader, Cappuyns has described the VLM using Odilila, provided by Airbus, in great detail. [4, pp. 18-19].

Some assumptions, limitations, and model specifics done with the VLM from Cappuyns are listed below [4].

1. Simulations results for full-scale Flying-V
2. Incompressible flow is assumed, which is valid below $M \approx 0.7$
3. Reynolds number of $Re = 6.5 \times 10^6$ [4]
4. Layout with two elevons and one rudder per side
5. VLM does not capture pitch break-up tendencies above an AoA of 20 °
6. Simulations include engine geometry
7. Inviscid flow so zero lift drag, $C_{d,0}$ is not known

The data point range is given in Table 2.4

Table 2.4: VLM simulation data range for Flying-V simulations in Odilila [4]

Variable	Description	Range	Unit
CoG	Centre of Gravity	[45, 51.5, 57.5]	%MAC
M	A/C velocity in Mach	[0.2, 0.225, 0.25, 0.275, 0.3, 0.85]	-
α	Angle of Attack	[-5, 0, 5, 10, 12.5, 15, 16.5, 18, 20]	°
β	Sideslip Angle	[-1, 0, 1]	°
p^*	Normalised roll rate	[-1, 0, 1]	-
q^*	Normalised pitch rate	[-1, 0, 1]	-
r^*	Normalised yaw rate	[-1, 0, 1]	-
δ_{CS3_L}	Deflection of left rudder	[-30, 0, 30]	°
δ_{CS1_L}	Deflection of left outboard elevon	[-30, 0, 30]	°
δ_{CS2_L}	Deflection of left inboard elevon	[-30, 0, 30]	°
δ_{CS1_R}	Deflection of right inboard elevon	[-30, 0, 30]	°
δ_{CS2_R}	Deflection of right outboard elevon	[-30, 0, 30]	°
δ_{CS3_R}	Deflection of right rudder	[-30, 0, 30]	°

2.7.2. Wind Tunnel Experiments

As was described in Section 2.2, there have been several wind tunnel tests using different configurations of the Flying-V. After the initial designs of Benad [2] and optimisations by Faggiano [6] a 4.6% scale model was manufactured by Viet[5], Palermo [8] and Garcia [9]. However, This scale model did not include the engine and winglet geometry. From these WTEs, Garcia performed aerodynamic identification using the wind tunnel data [9]. Garcia concluded that the identification of the lateral force coefficient, C_y, could not be used. After this identification, van Empelen [37] added the engine geometry and did new wind tunnel tests, from which significant lift interference and pitching moment interference were observed. Unfortunately, no further identification has been made after the WTEs from van Empelen. Marques [7] later concluded that the influence of walls and struts present in the wind tunnel have to be compensated and underpredict

the stall region of the aircraft. However, this has to be validated so no further conclusions can be drawn.

From the identification of the WTE assumptions, limitations, and notes are listed below:

1. Experiments were done with a 4.6% scale model
2. Aerodynamic identification was made without the engine, and winglet effects included
3. Reynolds number of $Re = 1.0 \times 10^6$ [8]
4. Pitch break-up is captured above an AoA of 20 °
5. Experimental set-up contains three elevons and one rudder per side
6. Wall and strut interference with results that are not accounted for
7. No sideslip data is acquired
8. Lateral force coefficient, C_y, gives inaccurate results and should not be included

The data range of the wind tunnel test data, without the engine implementation, is shown in Figure 2.9

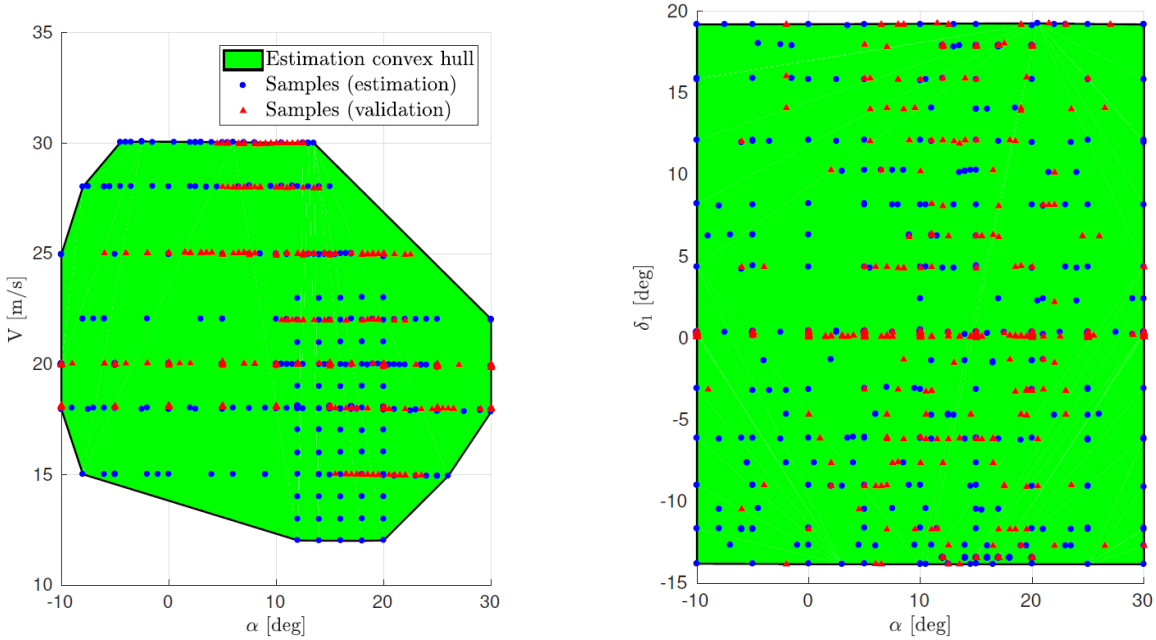

(a) Convex hull for free stream velocity and AoA

(b) Convex hull for most inboard eleven,δ_1, and AoA

Figure 2.9: Convex hulls of WTEs[9]

2.7.3. Flight Test Data

In 2020, a working 4.6% scale model was manufactured and tested using a physical flight test. However, compared to typical flight tests, this test focused on the concept's controllability, and catastrophic failure was out of the question [28]. Therefore, limited identification maneuvers, such as typical 3-2-1-1 or doublets, can be used for aerodynamic aircraft identification. Garcia, who was part as a flight test engineer, published results about this test flight, together with aerodynamic identification, using an Incremental Extended Kalman Filter[34]. Siemonsma also identified this flight test data using Incremental Extended Kalman Filtering [28]. Garcia found that the identification showed good prediction and reasonably uncorrelated residuals [34]. For C_x, C_y, C_z and C_n, the Relative Root Mean Squared Error (RRMSE) for the validation dataset was predicted below 7% and for C_l and C_m this was 10%. Lower means a better fit to the data. The model structure, which waGarcia identifies, mainly consists of low-order terms. Only the longitudinal force coefficient, C_x, contains a higher order term for the AoA. Siemonsma concluded that the flight test provided accurate longitudinal identification; however, the lateral identification was less reliable, as it was related to small control inputs during the test flight. The RRMSE found by Siemonsma ranges between 13% and 14% [28]. Furthermore, the regression model predicts the lateral modes with higher model terms. For a full overview of the result, the reader is advised to read the work of Garcia [34] and Siemonsma [28].

The flight test data also has some limitations and differences compared to the other models.

1. The flight test was done with the landing gear extended

2. The lateral identification is insufficient for implementation
3. Layout with three elevons and one rudder per side
4. External factors such as weather can influence results
5. Sensor inaccuracies can give estimation errors
6. Pitch break-up is not tested
7. Dutch roll is visible
8. Includes winglet and engine; however, does not match predicted engine model[28]
9. Holes in the aircraft for cooling and landing gear degrade the aerodynamic performance

Since the test flight does not contain specified increments in data ranges, it is difficult to specify the envelope in which data was acquired. However, Van Overeem [13] analyzed the data from the test flight and came up with clear ranges for the measured variables. No range for the V_{TAS} was provided; however, looking at the provided convex hulls from Garcia and Siemonsma and the raw flight test data, excluding take-off and landing, the range for the V_{TAS} is approximated. What should be noted is that Garcia and Siemonsma both refer to the use of the control surfaces as having either an elevator, δ_e, aileron, δ_a, or rudder, δ_r, even though there are three elevons and one rudder on either side. Unfortunately, neither Garcia nor Siemonsma has a direct definition of how the physical control surfaces are mapped. Garcia defined that using a control mixer, the elevons give pitch and roll inputs, and the rudder gives direct yaw input [34]. Also, the roll input is implemented with differential aileron deflection to deflect the ailerons more up than down to minimize adverse yaw motion[34]. Van Overeem explained the definition of the control mixer, referring to personal contact with Garcia [13]. He states that for a full pitch input from the pilot, this was translated to an 80% deflection of the elevons, all acting as a single surface. For a roll input, this was given to be 50%. Table 2.5 provides information about the physical control surface limits of the scale model aircraft. The control inputs are non-dimensionalized, and the identification data range from the flight test data is given in Table 2.6.

Table 2.5: Control surface deflection limits from flight test [13]

Control Surface	Deflection limits [deg]	
Elevon 1, left & right	[18, -25] (down,up)	with data mixer
Elevon 2, left & right	[25, -25] (down,up)	
Elevon 3, left & right	[25, -25] (down,up)	
Rudder, left & right	[27, -29] (left, right)	

Table 2.6: Flight test data identification range [13]

Parameter	Maximum Value	Minimum Value	Unit
V_{TAS}	≈ 36	≈ 22	[m/s]
δ_e	$3.2399 \cdot 10^{-1}$	$-3.1511 \cdot 10^{-1}$	[-]
δ_a	$3.6608 \cdot 10^{-1}$	$-4.5057 \cdot 10^{-1}$	[-]
δ_r	$2.6202 \cdot 10^{-1}$	$-2.4529 \cdot 10^{-1}$	[-]
$\dot{p}$	$3.0364 \cdot 10^{-3}$	$-2.6807 \cdot 10^{-3}$	[-]
$\dot{q}$	$6.1234 \cdot 10^{-5}$	$-6.1123 \cdot 10^{-5}$	[-]
$\dot{r}$	$1.4888 \cdot 10^{-3}$	$-7.1897 \cdot 10^{-4}$	[-]
α	$2.2014 \cdot 10^{-1}$	$8.0387 \cdot 10^{-3}$	[rad]
β	$1.3819 \cdot 10^{-1}$	$-1.0600 \cdot 10^{-1}$	[rad]

2.7.4. Comparison of results

From the different methods, different aerodynamic models have been identified. A conclusive model should be derived that will be used in this research. Since this research will continue from Van Overeem[13] and Stougie[14], their choices will also be considered. Stougie essentially took the model structure from Van Overeem [14]. Van Overeem set 3 requirements for the aerodynamic model:

- The aircraft's instabilities should be captured
- The most important aerodynamic coefficients shall be captured by the model structure
- The accuracy should be as good as possible

When Van Overeem was writing his research, the Flight Test Data (FTD) was already available; however, the work of Garcia [34] and Siemonsma[28] was not published yet, such that preliminary results and no

accuracy of the data was known. Van Overeem concluded that the VLM would be used as the baseline model, as he concluded that this model could capture the most essential aerodynamic coefficients, together with the Dutch roll instability. The accuracy was, however, low, the pitch break-up could not be modeled, and the range for the AoA was limited. Therefore, it was chosen to scale the WTE results using Froude scaling since the aircraft scale, and airspeeds of both results were different [38]. After scaling, the results were combined to extend the range of the AoA to 30 ° and to include the pitch break-up in the model. Figure 2.10a shows the data of the VLM and WTE, in approach, M=0.200, and cruise, M=0.850. The VLM results do not show the pitch break-up in the figure with C_m as a function of AoA. Figure 2.10b shows the combined model, which is implemented in the system from Van Overeem[13] and Stougie [14]. The FTD was not implemented as the uncertainty of the predicted parameters was unknown. A drawback of implementing the VLM as a baseline is the lack of a zero-lift drag coefficient, $C_{D,0}$. Van Overeem and Stougie took the reference aircraft's zero-lift drag coefficient for the Flying-V V1000 and the Airbus A350-900. This zero-lift drag is assumed to be 0.027 during cruise and 0.057 during approach [13].

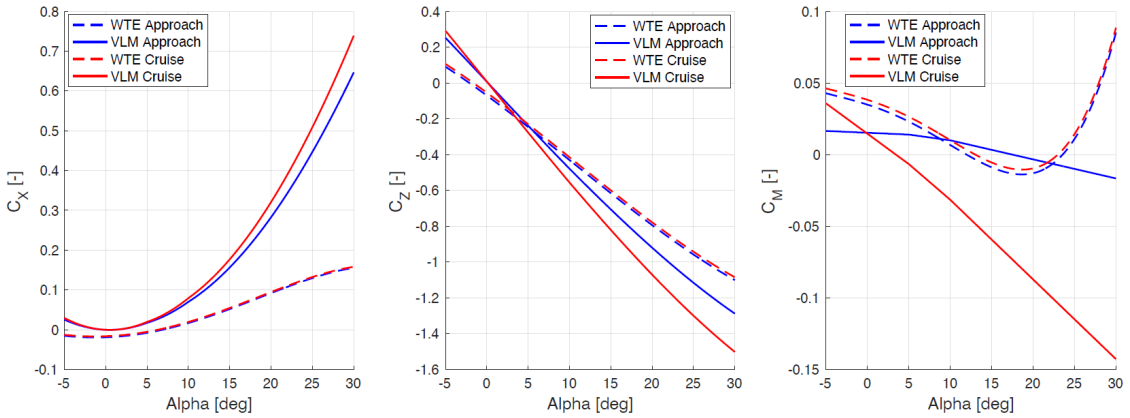

(a) Aerodynamic model results for VLM and WTE, non-scaled

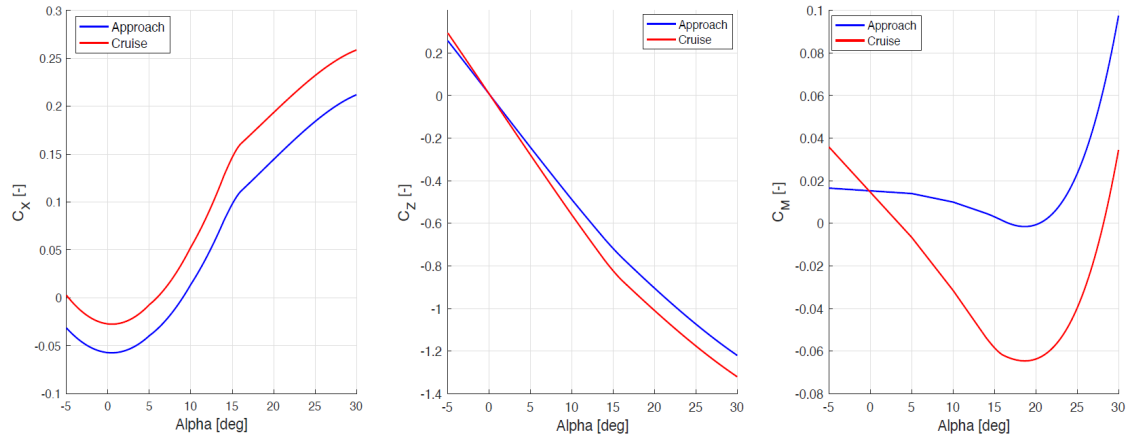

(b) Aerodynamic model results for VLM and WTE, scaled using Froude scaling and combined

Figure 2.10: VLM and WTE results and combined by Van Overeem [13]

In other previous studies, the preference for only using the VLM model is given. These were related to handling quality assessment in a flight simulator [10]–[12]. Furthermore, the flight performance assessment for take-off, landing, and cruise was assessed in normal conditions [22], and a preliminary neural-network flight controller was developed [31].

Even though there has been increasing work on identifying the Flying-V, this work primarily focuses on developing a FCS for the full-scale Flying-V. The only identification set for the full-scale is the VLM identification by Cappuyns [4]. It is chosen to stick with the model implemented by Van Overeem and Stougie, to compare the performance of the updated FCS.

The concluding aerodynamic model has the following inputs: CoG in %MAC, aircraft velocity in Mach (M), AoA in ° (α), sideslip angle in ° (β), normalized body rates in radians per second, (p^*, q^*, r^*) and

the control effectiveness matrix for the control surfaces. A simple linear interpolation is computed between data points, for which the data ranges are given in Table 2.4. For example, Equation 2.23 shows how the forward force coefficient, C_x, is computed. Furthermore, Equation 2.24 shows the respective control effectiveness matrix, which is needed for the control affinity of Hybri,d INDI, which will be explained in Section 3.2.3.

$$\begin{aligned} C_x = {} & C_{x_0}(\alpha) + C_{x\beta}(\alpha,\beta) + C_{x_{p^*}}(\alpha,p^*) + C_{x_{q^*}}(\alpha,q^*) \\ & + C_{x_{r^*}}(\alpha,r^*) + C_{x,CS3_L}(\alpha,\delta_{CS3_L}) + C_{x,CS1_L}(\alpha,\delta_{CS1_L}) \\ & + C_{x,CS2_L}(\alpha,\delta_{CS2_L}) + C_{x,CS2_R}(\alpha,\delta_{CS2_R}) + C_{x,CS1_R}(\alpha,\delta_{CS1_R}) + C_{x,CS3_R}(\alpha,\delta_{CS3_R}) \end{aligned} \tag{2.23}$$

$$\boldsymbol{G(x)u} = \frac{\rho_{air} V_\infty^2 Sc}{2} \boldsymbol{I}^{-1} \begin{bmatrix} C_{l,CS1_L} & C_{l,CS1_R} & C_{l,CS1_R} & C_{l,CS1_R} & C_{l,CS3_L} & C_{l,CS3_R} \\ C_{m,CS1_R} C_{m,CS1_R} C_{m,CS1_R} C_{m,CS1_R} C_{m,CS3_L} C_{m,CS3_R} \\ C_{n,CS1_R} & C_{n,CS1_R} & C_{n,CS1_R} & C_{n,CS1_R} & C_{n,CS3_L} & C_{n,CS3_R} \end{bmatrix} \begin{bmatrix} \delta_{CS1_L} \\ \delta_{CS1_R} \\ \delta_{CS2_L} \\ \delta_{CS2_R} \\ \delta_{CS3_L} \\ \delta_{CS3_R} \end{bmatrix} \tag{2.24}$$

2.8. Sensors and Actuators

Within control systems, the response of the control inputs and sensors does not happen instantly. This dynamics also has to be modeled as this can significantly influence the stability and robustness of the system [39]. Therefore, these dynamics will be modeled by a first-order lag system for the engine dynamics [40] and a second-order transfer function for the actuators [41] and both implemented by Stougie [14]. These transfer functions are shown in Equation 2.25. The actuator limits, shown in Table 2.7, have been derived from The engines used on the Flying-V are similar to those of the Airbus A350-900, the Rolls Royce Trent XWB-84, with maximum thrust specifications set by EASA [22], [42].

$$H_{act} = \frac{\omega_{act}^2}{s^2 + 2\zeta_{act}\omega_{act}s + \omega_{act}^2} = \frac{4000}{s^2 + 140s + 4000}, \quad H_{eng} = \frac{1}{0.2s + 1} \tag{2.25}$$

Table 2.7: Control Effector Parameters[13], [42]

Control effector	Notation	Actuator limits	Rate limit [deg/sec]	Dynamics
Outboard Elevator	$\delta_{CS1_L}, \delta_{CS1_R}$	[-25, 25] [°]	80	$H_{act}(s)$
Inboard Elevator	$\delta_{CS2_L}, \delta_{CS2_R}$	[-25, 25] [°]	80	$H_{act}(s)$
Rudder	$\delta_{CS3_L}, \delta_{CS3_R}$	[-30, 30] [°]	120	$H_{act}(s)$
Engine thrust	δ_{T1}, δ_{T2}	$[0, 3.176 \cdot 10^5]$ [N]	-	$H_{eng}(s)$

The engine dynamics in the current simulation model are simplified and idealistic. The maximum thrust used in this research is the Equivalent Bare Engine Take-Off Thrust; however, it is used as the maximum continuous thrust, which should be $T = 3.176 \cdot 10^5$N [32]. This thrust is used across the flight envelope as the maximum thrust, however is influenced by the flight regime [22].

Next to the control dynamics, the sensors will also be modeled. Sensor delays can become the system's limiting factor, especially for INDI. There is no physical full-scale model of the Flying-V yet, so there is no information about which sensors will be used. Therefore, as a baseline, the Cessna Citation II PH-LAB sensors are implemented in the model. The characteristics of these sensors are based on Grondmann [43] and Van 't Veld [44] and are changed by Stougie [14]. The final values for the sensor characteristics are given in Table 2.8. For specific values, it is indicated that the value has changed by using a right arrow to visualize that Stougie had to change these characteristics to achieve satisfactory results in his research [14]. Therefore, looking at Table 2.8, the body rate sensors and the sideslip sensor have been changed and do not correspond with the reference sensors from the Cessna Citation II. The changed values will initially be used in this research to validate the original model from which the base sensors will be used.

The accelerometers are used to measure the accelerations in the earth reference frame, $\mathcal{E}$. These accelerations are almost the same as the body accelerations. Therefore, when looking at Equation 2.7 and rewriting, the terms on the left represent the accelerations in the earth reference frame. The sensor dynamics can be simulated using the relation on the right, as those terms are all known in the simulation.

Table 2.8: Baseline Sensor Characteristics [14]

Sensor	Sampling rate [Hz]	Time delay [s]	Noise	Bias	Filter time constant
p, q, r [rad/s]	50	$0.1 \rightarrow 0.04$	$1 \cdot 10^{-9}$	$3 \cdot 10^{-5}$	$0.05 \rightarrow 0.03$
ϕ, θ [rad]	50	0.1	$1 \cdot 10^{-9}$	$4 \cdot 10^{-3}$	0.05
V [m/s]	$\frac{1}{0.065}$	0.325	$1 \cdot 10^{-4}$	2.5	0.05
α [rad]	50	0.1	$7.5 \cdot 10^{-8}$	$3 \cdot 10^{-5}$	0.05
β [rad]	50	0.1	$7.5 \cdot 10^{-8}$	$3 \cdot 10^{-5}$	$0.05 \rightarrow 0.1$
A_x, A_y, A_z [g]	50	0.1	$1 \cdot 10^{-5}$	$2.5 \cdot 10^{-3}$	0.05

$$\begin{bmatrix} \dot{u}_{\mathcal{B}} \\ \dot{v}_{\mathcal{B}} \\ \dot{w}_{\mathcal{B}} \end{bmatrix} + \begin{bmatrix} p \\ q \\ r \end{bmatrix} \times \begin{bmatrix} u_{\mathcal{B}} \\ v_{\mathcal{B}} \\ w_{\mathcal{B}} \end{bmatrix} = \begin{bmatrix} A_x \\ A_y \\ A_z \end{bmatrix}_{\mathcal{E}} = \frac{1}{m} \begin{bmatrix} F_x \\ F_y \\ F_z \end{bmatrix}_{\mathcal{B}} + g_0 \begin{bmatrix} -\sin\theta \\ \sin\phi\cos\theta \\ \cos\phi\cos\theta \end{bmatrix}$$

2.9. Simulation Model Limitations

Some simplifications and limitations are made to the simulation model, implemented from Stougie [14]. These add to the assumptions in Section 2.6.1.

- The aerodynamic force and moment coefficients are only impacted by the angle of attack in a non-linear fashion. No other effects are accounted for, such as control surface deflections, which also introduce non-linearity to the coefficients [13].
- To include the pitch break-up in the aerodynamic model, Froude scaling was used; however, for this, the relative density and moment of inertia matrix must be the same, which was not the case, such that inaccuracies could be explained by this [9].
- As was mentioned before, the VLM is used as a baseline for the aerodynamic model; however, this does not include zero lift drag, which is a limitation of the identification method by VLM [4]. Through the WTE it is not possible to acquire this constant for the full-scale model, which is why the zero lift constant from the reference aircraft, Airbus A350-900 is chosen [13].
- In this research, the gravitational constant, g_0, is chosen as a constant, whereas this variable depends on the altitude and changes on different parts of the earth [14].
- Zero wind is assumed in the simulations, with an assumed International Standard Atmosphere, with a temperature of 288.15K at an altitude of 0 m. [13].
- The engine dynamics use first-order dynamics with saturation at net maximum continuous thrust without changing across the flight envelope.
- The aerodynamic data for the control surface effectiveness parameters for the inboard eleven $CS1$ and outboard eleven, $CS2$ are decoupled for longitudinal and lateral maneuvers. $CS1$, does not influence roll or yaw axes, and $CS2$ and $CS3$ do not affect the pitch axis.
- There is only one inertia matrix available.

3

Flight Control System

This chapter will focus on the literature study of FCSs. An overview of different methodologies in FCSs are given, after which the role of Hybrid INDI will be shown within the bigger scope of FCS. This chapter will provide the reader with sufficient background information on the current limitations with the FCS of the Flying-V and how Hybrid INDI can resolve these limitations.

Section 3.1 will start with an introduction to different FCS structures used in aviation, after which NDI and INDI are highlighted as applied control structures for the Flying-V in Section 3.3. Section 3.2.3 highlights the proposed implementation of Hybrid INDI, with all the necessary added FCS systems. Next, Section 3.4 highlights the working principle of FEP, with its necessity within aviation. Within this chapter, research questions 1 and 2 will be answered by giving background information about the FCS of the Flying-V and the state-of-the-art of Hybrid INDI and FEP.

3.1. Flight Control System Overview

Ever since the introduction of the first aircraft, there has been a need for FCSs to control the aircraft. With the increasing complexity of the aircraft, more complex FCS is necessary. With the introduction of computer systems, this was kickstarted with digital flight computers, which primarily used linear controller techniques up until 1990 [45]. To ensure performance and safety, the flight envelope had to be extended using gain scheduling techniques [46]. In between these gain scheduling parameters, performance can still not be guaranteed due to nonlinearities and uncertainties [47]. Therefore, Slotine & Li [47] proposed nonlinear control techniques, from which multiple modern control techniques were born.

Figure 3.1 shows a flow chart view of the different nonlinear control methods established since the publication of Slotine & Li [47]. As the concept of FCS is too broad to go into full detail, only the relevant methods are highlighted. This chart will mainly be used to understand why it is a logical step to look into implementing Hybrid INDI as an addition to the current FCS of the Flying-V. The blocks that are colored green are currently used as a part of the FCS.

The Flying-V, as has been described in Section 2.6, is a nonlinear dynamic, non-control affine system with uncertain parameters, which needs to be controlled to achieve safety requirements from the aviation sector while also reaching specific performance parameters. Linear controllers can be implemented using scheduling techniques, which is inefficient. They can, however, be combined with a nonlinear controller structure, which will be elaborated in Section 3.2.1. The nonlinear control systems have five primary methodologies: optimal control, Reinforcement Learning (RL), Lyapunov-based control, and Feedback Linearization. These methods are elaborated, showing their implementation as a FCS within aviation.

3.1.1. Reinforcement Learning

This relatively new control methodology is based on the principle of trial and error. A RL algorithm is based on agents that want to achieve a goal. The goal is not provided to the agents; however, they are rewarded according to their actions. There are many approaches to RL, but the most prominent and applied method used is Actor Critic Deep RL [31]. Within Actor Critic Deep RL, there are Soft Actor-Critic (SAC) and Twin-Delayed Deep Deterministic Policy Gradient (TD3), among others. TD3 delayes updates to the agent

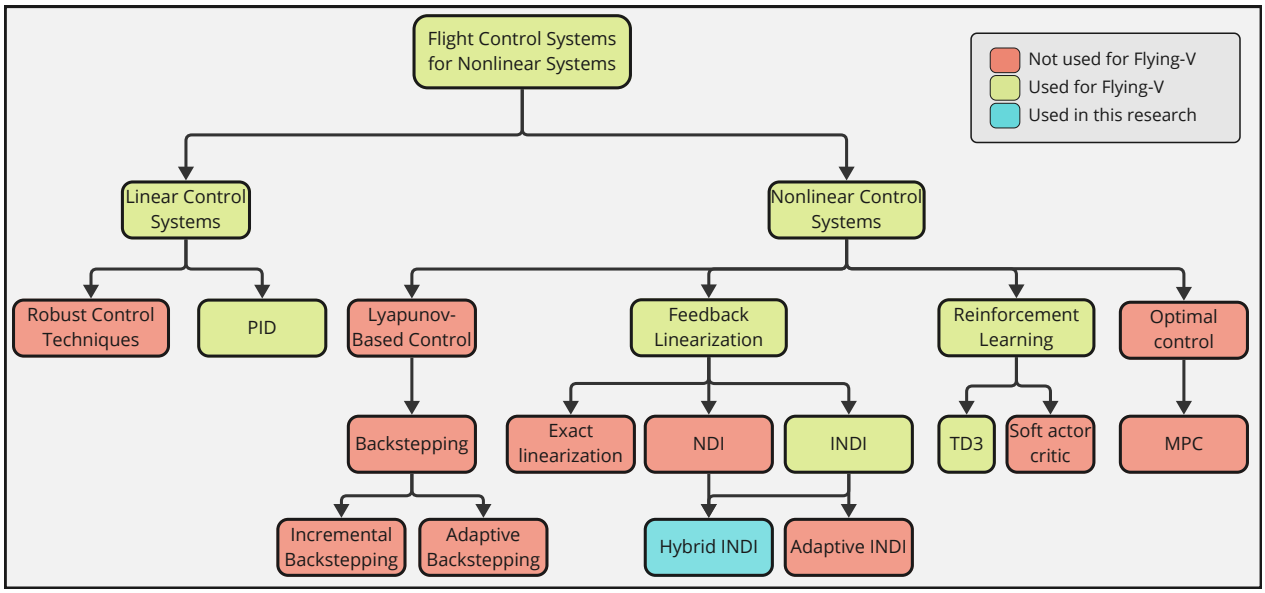

Figure 3.1: Flow chart of Flight Control Systems

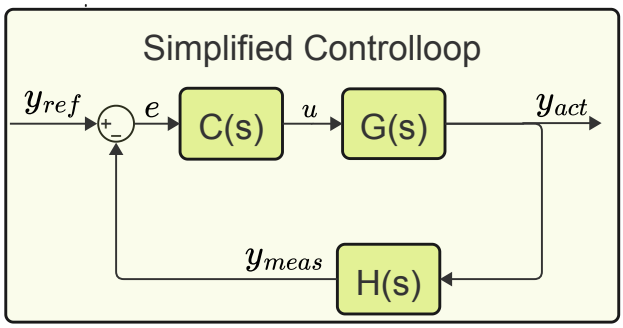

Figure 3.2: Simple closed loop system structure

which promotes stabilization of the system and adds noise to the system to increase robustness. SAC tries to maximize the rewards from the agents while maximizing the randomness of the inputs.

Völker et al. have implemented TD3 rather than SAC to the Flying-V as he poses that the latter creates more oscillatory behavior to control inputs [31]. Since it is rewarded for randomness, it can create unsafe maneuvers when trained on the aircraft. The research found that TD3 is robust to aerodynamic uncertainties, sensor noise, unfavorable initial conditions, and different reference signals. However, the controller's performance has not been tested to meet HQ requirements, and it is implemented solely for the longitudinal direction.

3.1.2. Optimal Control

Optimal control is based on finding an optimum command signal that can steer the system to a reference signal with the lowest cost to a specified cost function with constraints to the system [48]. Therefore, the system's limits, such as actuator limits, can be directly implemented to predict the input signal. Within optimal control are multiple methods, among which are Linear Quadratic Regulator (LQR) and Model Predictive Control (MPC). LQR is only applied in linear systems, so it does not apply to the Flying-V as the main controller structure. MPC can be used for nonlinear systems, where the MPC controller predicts future states within a finite horizon, from which an optimization is done [49]. In previous research, MPC has been primarily combined with FEP due to its ability to handle constraints [50]. As a main inner loop controller structure, the optimization is not guaranteed to be solved within the given time step and is therefore not chosen in this research.

3.1.3. Lyapunov Based Control

Lyapunov-based Control is a method to guarantee the stability of the closed-loop system by creating a virtual control law similar to feedback linearization, which will be controlled. Essentially, the goal of the closed-

loop system is to make the steady-state value of the system asymptotically stable [50]. An example of such a Lyapunov function is the function, $V(x) = \frac{1}{2}x^2$. The derivative of this function is $\dot{V}(x) = \boldsymbol{x}\dot{\boldsymbol{x}}$, for which the state derivative $\dot{\boldsymbol{x}}$ can be filled in from the EoM, from which a control law can be chosen which makes the derivative of the Lyapunov function, $\dot{V}(x)$, always converge to zero, making it asymptotically stable. Backstepping is the most common implementation of Lyapunov-based control, similar to NDI, as described below. Both methods cancel the system's nonlinear behavior and eliminate the gain scheduling needed with linear controllers [51]. An advantage of backstepping over NDI is the guaranteed closed-loop stability of the system, as the Lyapunov function guarantees this. However, deriving a control law for every cascading loop might get complex and is only helpful for several cascading loops. As a typical FCS consists of an outer loop that controls the aircraft attitude angles and an inner loop, which controls the attitude rates, the need for several cascading loops is not needed, and the choice for feedback linearization was chosen for the Flying-V, which is explained below.

3.1.4. Feedback Linearization

Feedback Linearization is a control methodology that depends on linearizing the nonlinear dynamics of the system. In feedback linearization, the goal is to cancel out the nonlinearities of a system such that the input-output behavior of the resulting closed-loop system is linear. Using the example of Figure 3.2, this means the controller would have the structure of $C(s) = G^{-1}(s)$, which gives a closed-loop structure, with ideal sensors of $y_{CL} = \frac{1}{2}$, which shows there is no way to control this system. Furthermore, as the system's dynamics are proper, where the order of the numerator has to be equal to or smaller than the denominator, the inverse will be an improper non-causal system. Physically this means that the system depends on the next time step, as it needs to compute the derivative of that time step. Therefore, feedback linearization has to be combined with an outer-loop controller, which can steer the system to the desired state. A linear controller such as PID can be used to linearize the system. Within the feedback linearization, there are two methods: exact linearization and input-output linearization, also known as NDI. The inner-loop dynamics must be fully linearized for exact linearizations, which means every state must be controllable. For NDI, linearizing the state, which the sensors will eventually measure, is only necessary. Exact linearization is not feasible for the Flying-V as all states have to be measurable and controllable, making the system unnecessarily complex, and some states are challenging to measure, such as thrust. Therefore, NDI will be elaborated further.

Nonlinear Dynamic Inversion

The key benefits of using NDI include its ability to work without gain-scheduling and directly include nonlinearity in control laws [39]. Additionally, NDI separates the aircraft's HQ aspects from those related to the airframe and engine. This separation means that desired handling characteristics can be more directly achieved during the design of the control system. Using NDI can lead to lower costs and shorter development times. It also makes it easier to apply the same control approach to different types of aircraft, helps deal with changes in aircraft models, and provides better control when the aircraft is at a high angle of attack compared to traditional control methods. A drawback of the conventional NDI lies in the dependence on the accuracy of the aerodynamic model and equations of motion. If a mismatch gets too high, this can reduce performance and cause instability.

3.2. Dynamic Inversion Control Laws

This Section will derive the control laws that are used within a NDI/INDI controller system and the definition, together with literature research about Hybrid INDI is presented.

3.2.1. Nonlinear Dynamic Inversion Control Law

As described above, the NDI control law is based on feedback linearization. This principle involves finding a direct relationship between a desired input and output state, hence the name input-output linearization [52]. Assuming full knowledge of the system's dynamics, the output states are differentiated until a direct relation occurs between input and output, from which the dynamics are inverted such that a control law is defined. To elaborate upon this definition, let us consider a general control affine Multiple Input-Multiple Output (MIMO) system, shown in Equation 3.1.

$$\begin{aligned} \dot{\boldsymbol{x}} &= \boldsymbol{f}(\boldsymbol{x}) + \boldsymbol{G}(\boldsymbol{x})\boldsymbol{u} \\ \boldsymbol{y} &= \boldsymbol{h}(\boldsymbol{x}) \end{aligned} \tag{3.1}$$

Here, the state vector $\boldsymbol{x} \in \mathbb{R}^n$, input vector $\boldsymbol{u} \in \mathbb{R}^m$ and output vector $\boldsymbol{y} \in \mathbb{R}^m$ are described by the smooth mapping functions, $\boldsymbol{f}, \boldsymbol{G}$, and $\boldsymbol{h}$. Following the approach described above, differentiating the output mapping function, with respect to the input states, gives Equation 3.2 [36], named the first Lie derivative.

$$\frac{\mathrm{d}\boldsymbol{h}(\boldsymbol{x})}{\mathrm{d}t} = \frac{\partial \boldsymbol{h}(\boldsymbol{x})}{\partial \boldsymbol{x}} \frac{\mathrm{d}\boldsymbol{x}}{\mathrm{d}t} = \nabla \boldsymbol{h}(\boldsymbol{x})\dot{\boldsymbol{x}} = \nabla \boldsymbol{h}(\boldsymbol{x})[\boldsymbol{f}(\boldsymbol{x}) + \bar{G}(\boldsymbol{x})\boldsymbol{u}] = \mathcal{L}_f \boldsymbol{h}(\boldsymbol{x}) + \mathcal{L}_g \boldsymbol{h}(\boldsymbol{x})\boldsymbol{u} \tag{3.2}$$

With the first Lie derivative, with order ρ_1, gives the first-order Lie derivative, $\mathcal{L}_f$, along mapping function $\boldsymbol{f}$ and $\mathcal{L}_g$, along mapping function $\boldsymbol{G}$. The output dynamics, $\boldsymbol{h}(\boldsymbol{x})$, with respect to each order,ρ_1, can be given by Equation 3.3 [52].

$$\boldsymbol{y}^{(\boldsymbol{\rho}_i)} = \begin{bmatrix} \mathcal{L}_f^{\rho_1} h_1(\boldsymbol{x}) \\ \vdots \\ \mathcal{L}_f^{\rho_m} h_m(\boldsymbol{x}) \end{bmatrix} + \begin{bmatrix} \mathcal{L}_{g_1}\mathcal{L}_f^{\rho_1 - 1} h_1(\boldsymbol{x}) h_1(\boldsymbol{x}) & \dots & \mathcal{L}_{g_m}\mathcal{L}_f^{\rho_1 - 1} h_1(\boldsymbol{x}) \\ \vdots & \ddots & \vdots \\ \mathcal{L}_{g_1}\mathcal{L}_f^{\rho_m - 1} h_m(\boldsymbol{x}) & \dots & \mathcal{L}_{g_m}\mathcal{L}_f^{\rho_m - 1} h_m(\boldsymbol{x}) \end{bmatrix} \boldsymbol{u} \tag{3.3}$$

The control law is formed until, for a certain order ρ_i, the $\mathcal{L}_{g_j}\mathcal{L}_f^{\rho_i - 1} h_i(\boldsymbol{x}) \neq 0$. giving the input-output relation given in Equation 3.4

$$\boldsymbol{y}^{(\boldsymbol{\rho}_i)} = \frac{\mathrm{d}^i \boldsymbol{h}(\boldsymbol{x})}{\mathrm{d}t^i} = \mathcal{L}_f^{\rho_i} h_i(\boldsymbol{x}) + \mathcal{L}_{g_j}\mathcal{L}_f^{\rho_i - 1} h_i(\boldsymbol{x})\boldsymbol{u} \tag{3.4}$$

To find the given control law, assuming it can be formed, the input vector, $\boldsymbol{u}$, will become a function of the output relation, given by Equation 3.5. The virtual command vector, $\boldsymbol{\nu}$ replaces the output measurement.

$$\boldsymbol{u} = \mathcal{L}_g \mathcal{L}_f^{\rho_i - 1} h(\boldsymbol{x})^{-1} \left[\boldsymbol{\nu} - \mathcal{L}_f^{\rho_i} h(\boldsymbol{x}) \right] \tag{3.5}$$

A visual representation of a general controller system, using a NDI control law, is given in Figure 3.3.

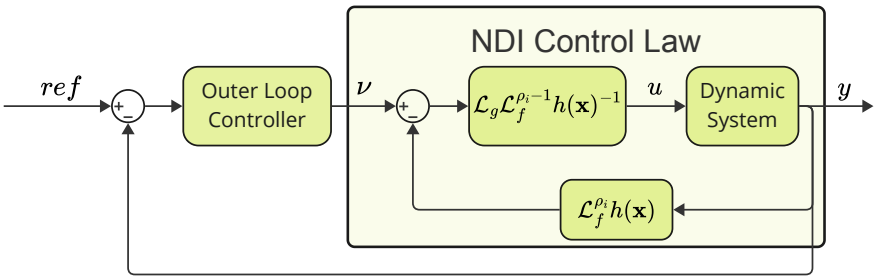

Figure 3.3: Nonlinear Dynamic Inversion controller system

3.2.2. Incremental Nonlinear Dynamic Inversion

The basic principle of INDI is strongly related to its model-based counterpart, NDI. Although NDI has a definite advantage over conventional gain scheduling, NDI falls short when it comes to model mismatch [36]. INDI solves some of these limitations, reducing the need for a detailed On-Board-Model (OBM), only the control effectiveness terms, which in itself can give a complex model [41]. With INDI, it is assumed the sampling time of the controller system is sufficiently high to make the Time-Scale-Seperation assumption hold, which yields that the state vector $\boldsymbol{x}$ changes significantly slower compared to the input vector $\boldsymbol{u}$, further elaborated upon by Falkena [53]. Stougie also studied the effect of the sampling time and concluded that with the set sampling frequency of f_s=100 Hz, the tracking error does not impose problems concerning this assumption [14]. This gives that $\boldsymbol{x} \approx \boldsymbol{x}_0$ [54]. Due to the control affine assumption, a first-order Taylor expansion is taken around the point $\boldsymbol{x}_0, \boldsymbol{u}_0$

$$\begin{aligned} \dot{\boldsymbol{x}} &= \boldsymbol{f}(\boldsymbol{x_0}) + \boldsymbol{G}(\boldsymbol{x_0}) + \frac{\partial}{\partial \boldsymbol{x}} \left[\boldsymbol{f}(\boldsymbol{x}) + \boldsymbol{G}(\boldsymbol{x})\boldsymbol{u}\right]_{\boldsymbol{x}_0, \boldsymbol{u}_0} (\boldsymbol{x} - \boldsymbol{x}_0) + \frac{\partial}{\partial \boldsymbol{u}} \left[\boldsymbol{f}(\boldsymbol{x}) + \boldsymbol{G}(\boldsymbol{x})\boldsymbol{u}\right]_{\boldsymbol{x}_0, \boldsymbol{u}_0} (\boldsymbol{u} - \boldsymbol{u}_0) \\ &= \dot{\boldsymbol{x}}_0 + \frac{\partial}{\partial \boldsymbol{x}} \left[\boldsymbol{f}(\boldsymbol{x}) + \boldsymbol{G}(\boldsymbol{x})\boldsymbol{u}\right]_{\boldsymbol{x}_0, \boldsymbol{u}_0} (\boldsymbol{x} - \boldsymbol{x}_0) + \frac{\partial}{\partial \boldsymbol{u}} \left[\boldsymbol{f}(\boldsymbol{x}) + \boldsymbol{G}(\boldsymbol{x})\boldsymbol{u}\right]_{\boldsymbol{x}_0, \boldsymbol{u}_0} (\boldsymbol{u} - \boldsymbol{u}_0) \end{aligned} \tag{3.6}$$

As it assumed the mapping function $\boldsymbol{f}$, representing the dynamics of the system, does not depend on the input vector and recognizing that $\boldsymbol{x} - \boldsymbol{x}_0 \approx 0$, the resulting simplified MIMO system from Equation 3.1 is given in Equation 3.7.

$$\begin{aligned}\dot{\boldsymbol{x}} &= \dot{\boldsymbol{x}}_0 + \frac{\partial}{\partial \boldsymbol{x}} \cancel{\left[\boldsymbol{f}(\boldsymbol{x}) + \boldsymbol{G}(\boldsymbol{x})\boldsymbol{u}\right]_{\boldsymbol{x}_0,\boldsymbol{u}_0}} (\boldsymbol{x} - \boldsymbol{x}_0) + \frac{\partial}{\partial \boldsymbol{u}} \left[\cancel{\boldsymbol{f}(\boldsymbol{x})} + \boldsymbol{G}(\boldsymbol{x})\boldsymbol{u}\right]_{\boldsymbol{x}_0,\boldsymbol{u}_0} (\boldsymbol{u} - \boldsymbol{u}_0) \\ &= \dot{\boldsymbol{x}}_0 + \frac{\partial}{\partial \boldsymbol{u}} \left[\boldsymbol{G}(\boldsymbol{x})\boldsymbol{u}\right]_{\boldsymbol{x}_0,\boldsymbol{u}_0} (\boldsymbol{u} - \boldsymbol{u}_0) \\ &= \dot{\boldsymbol{x}}_0 + \boldsymbol{G}(\boldsymbol{x})\Delta\boldsymbol{u}\end{aligned} \tag{3.7}$$

By assuming $\dot{\boldsymbol{y}} = \dot{\boldsymbol{x}}$, even though there is sensor dynamics, the virtual control law for the INDI loop can be made. The control surfaces can be controlled by manipulating Equation 3.7 into Equation 3.8. The virtual command signal is defined as the desired $\dot{\boldsymbol{x}}$ and was chosen by Stougie to be the rotational body accelerations, $\boldsymbol{\nu} = \dot{\boldsymbol{\omega}}$ [14]. Since $\boldsymbol{G}(\boldsymbol{x})$ is a non-square matrix, as shown in Equation 2.24, it will be replaced by $\boldsymbol{\mathcal{B}}^{-1}(\boldsymbol{x})$, which is the Moore-Penrose inversion of $\boldsymbol{G}(\boldsymbol{x})$ [41].

$$\boldsymbol{u} = \boldsymbol{u}_0 + \boldsymbol{\mathcal{B}}^{-1}(\boldsymbol{x})(\boldsymbol{\nu} - \dot{\boldsymbol{x}}_0) \tag{3.8}$$

A block diagram of a general INDI controller system is given in Figure 3.4.

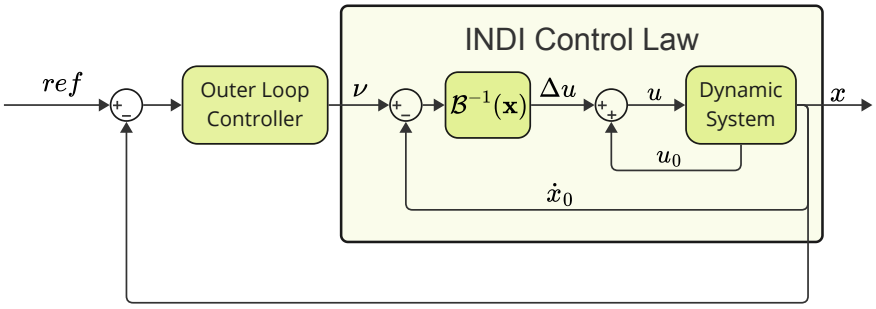

Figure 3.4: Incremental Nonlinear Dynamic Inversion controller system

Due to the absence of an angular acceleration sensor in the current controller system, the rotational body accelerations have to be approximated, which is currently done by a second-order filter [14]. As stated above, the sensor dynamics are neglected in the derivation above, but cannot be neglected and decrease performance and robustness of the current INDI controller structure [14].

3.2.3. Hybrid INDI

Hybrid INDI uses both the model information from NDI, which needs more information and is less robust to uncertainties, and INDI, which is more robust to uncertainties but is dependent on sensor performance [55]. As has been identified by Stougie, the body rate sensors are currently the limiting factor in the system. Therefore, this thesis hypothesizes that Hybrid INDI can solve this limitation since combining sensor data and model predictions will acquire angular accelerations.

As the term Hybrid INDI is relatively new and was first used by Yang&Zu [56] however, the method for which Hybrid INDI was invented has been used previously as there is no conclusive definition of Hybrid INDI. Most literature defines it as a method to fuse sensor-based and model-based NDI methods using a complementary filter [17], [18], [56], [57]. However, this research wants to extend that definition to define Hybrid INDI as the method to extend INDI by reducing the time delay effect using model-based predictions. In this form, it does not matter which method is, as long as its purpose is to counteract the time-delay effect of sensor-based INDI, generally applied to filtering the angular acceleration as this is a state derivative needed in Equation 2.8 for the body rates. Angular acceleration is a problematic state to measure, with limited sensors available.

Using this definition of Hybrid INDI, the research on Hybrid INDI can be separated into different methodologies: the Augmentation Matrix (AM), the Complementary Filter (CF), and other methods. It is important to note that the control system should be control affine for Hybrid INDI, as the model-based prediction is based on the principle of NDI. Therefore, the derivation for the control-affine EoM shall be used, as shown in 2.7. These methods will be explained below.

Complementary Filtering

A CF is a method of filtering multiple inputs and combining the best methods to complement each other's strengths and weaknesses. As an example for the angular acceleration estimation, this can be done by combining the inputs of an Inertial Measurement Unit (IMU), which has high-frequency measurement noise, and a model prediction, which has low-frequency estimation errors. The CF essentially combines these signals by filtering the IMU signal with a low-pass filter and filtering the model prediction with a high-pass filter. Yang & Zhu [16] was the first to apply such a complementary filtering method to the approximation for angular acceleration without an angular accelerometer. Figure 3.5b shows this representation with the model-prediction as $\dot{\boldsymbol{x}}_{obm}$ and the sensor measurements as $\dot{\boldsymbol{x}}_{meas}$, for example the IMU signal.

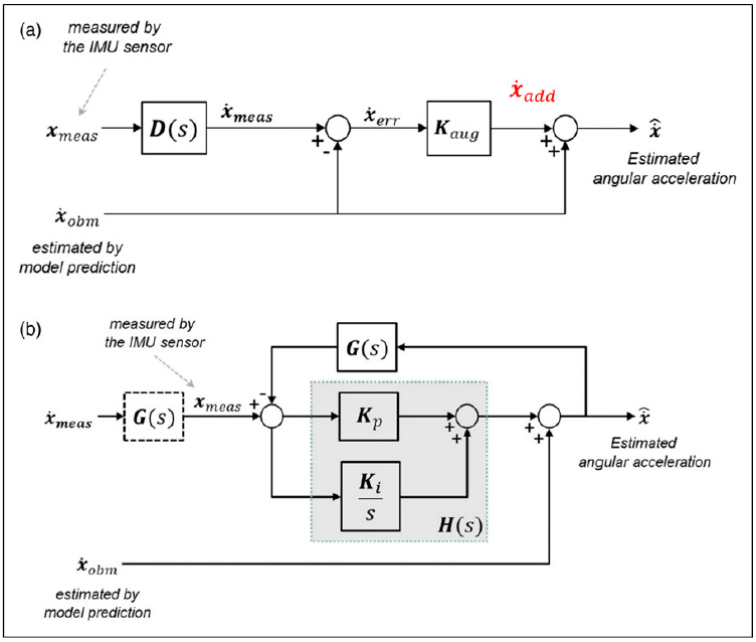

Figure 3.5: Angular acceleration estimation: (a) augmentation and (b) complementary filter. [18]

Since the introduction of the CF by Yang [16], the structure of the filters is similar across different literature, where $G(s)$ represents a diagonal matrix with pure integrators and $H(s)$ represents a diagonal matrix consisting of PI controllers [16]–[18], [58]. The estimated state derivatives, as shown in Figure 3.5b can be represented as shown in Equation 3.9

$$\hat{\dot{\boldsymbol{x}}}(s) = \frac{\boldsymbol{I}(s)}{\boldsymbol{I}(s) + \boldsymbol{G}(s)\boldsymbol{H}(s)}\dot{\boldsymbol{x}}_{obm}(s) + \frac{\boldsymbol{G}(s)\boldsymbol{H}(s)}{\boldsymbol{I}(s) + \boldsymbol{G}(s)\boldsymbol{H}(s)}\dot{\boldsymbol{x}}_{meas}(s) \tag{3.9}$$

This equation can be rewritten in terms to show the high-pass filter, $T(s)$, and the low-pass filter, $S(s)$, which is shown in Equation 3.10

$$\hat{\dot{\boldsymbol{x}}} = T(s)\dot{\boldsymbol{x}}_{obm}(s) + S(s)\boldsymbol{x}_{meas}(s) = \frac{s^2}{s^2 + \boldsymbol{K}_p s + \boldsymbol{K}_i}\dot{\boldsymbol{x}}_{obm}(s) + \frac{(\boldsymbol{K}_p s + \boldsymbol{K}_i)s}{s^2 + \boldsymbol{K}_p s + \boldsymbol{K}_i}\boldsymbol{x}_{meas}(s) \tag{3.10}$$

Looking at Equation 3.10, it can be concluded that the characteristic of these filters is that $T(s) + S(s)$ = 1, where both can be represented as a conventional 2nd order filter. By using a CF, it can be precisely controlled, depending on the desired damping of the reference signal, ζ and the natural frequency of the sensor that is used, the cross-over from the sensor to the model can be set, which are $\boldsymbol{K}_p = 2\zeta\omega_n$ and $\boldsymbol{K}_i = \omega_n^2$. It is noteworthy that the sensor measurement is directly utilized in the CF. For the IMU, this direct utilization of measurements eliminates the need for a derivative, which would otherwise amplify measurement noise. In research from Kim [18], it was concluded that this method of Hybrid INDI is more resistant to time delays compared to the conventional INDI controller.

Extended State Observer

Lyu [58] researched the implementation of an adjusted CF-based estimation, namely Extended-State-Observer (ESO)-based estimation. As a smaller ω_n of the CF filters out more sensor data, the robustness against uncertainties becomes reduced; however, it filters sensor noise more adequate [17]. Therefore, the ω_n should

be chosen carefully depending on the sensor noise properties [58]. Furthermore, the roll-off of the $S(s)$ filter is -20 dB/decade, looking at the high-frequency approximation. ESO provides an adjusted CF structure with a faster roll-off, where the residuals of the model-based approximation are estimated, giving the adjusted CF shown in Equation 3.11.

$$\hat{\dot{\boldsymbol{x}}} = T^{'}(s)\dot{\boldsymbol{x}}_{obm}(s) + S^{'}(s)\boldsymbol{x}_{meas}(s) = \frac{s^2 + \boldsymbol{K}_p s}{s^2 + \boldsymbol{K}_p s + \boldsymbol{K}_i}\dot{\boldsymbol{x}}_{obm}(s) + \frac{\boldsymbol{K}_i}{s^2 + \boldsymbol{K}_p s + \boldsymbol{K}_i}\boldsymbol{x}_{meas}(s) \quad (3.11)$$

The bode plots that compare both structures are shown in Figure 3.6. The roll-off of the low-pass filter is -40dB/decade, yielding better noise filtering.

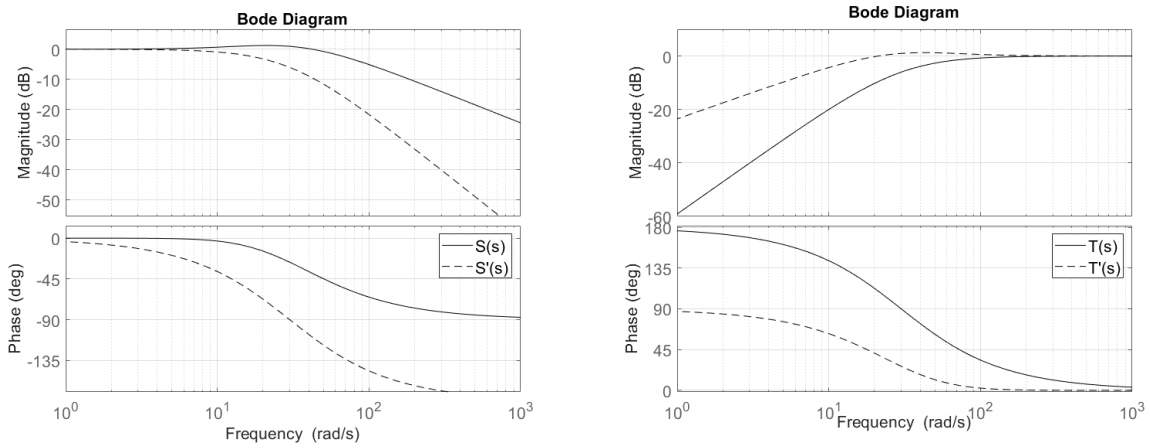

Figure 3.6: Bode plots of Complementary Filter: (a) Low-pass filter $S(s)$ and (b) High-pass filter $T(s)$. [58]

This structure shows superior noise reduction of the sensor measurements for the control input, compared to conventional CF. The CF method has also been combined with a robust μ-synthesis implementation, using a conventional CF as shown in Equation 3.9, with a damping coefficient of $\zeta = \frac{\sqrt{2}}{2}$ [59]. Here it was concluded that the robustness of the system, given as μ would remain lower, which is a sign of more robustness when the break-frequency, denoted as ω_n was lowered, essentially relying more on the model-based approximation. However, the CF method was not implemented in that specific research, as it yielded marginal improvements only in the nominal flight regime.

Augmentation Matrix

The AM is a methodology of linearly combining the sensor-based and the model-based derivative states. This principle is visualized in Figure 3.5a. Especially Kim, Ji & Kim have done extensive research on this methodology, showing its simplicity and even showing better robustness, comparing it to a CF [18], [57], [60]–[63]. Just as conventional INDI, this method uses a simple derivative of the body rate sensors, giving a derivative with differentiated sensor noise, time delay, and high-frequency structural couplings of the airframe. By using a synchronization filter, which will be explained in Section 3.3.2, these delays are compensated by boosting the gain- and phase margins of the system [63].

The AM principle works by evaluating the general INDI formulation for the inputs signal from 3.8 and adding an augmented input containing the model-based derivative states, shown in Equation 3.12.

$$\boldsymbol{u} = \boldsymbol{u}_0 + \boldsymbol{G}_{obm}^{-1}(\boldsymbol{x})\left[\boldsymbol{\nu} - \{\boldsymbol{K}_{\text{aug}}\,\dot{\boldsymbol{x}}_{\text{meas}} + (\boldsymbol{I} - \boldsymbol{K}_{\text{aug}})\,\dot{\boldsymbol{x}}_{\text{obm}}\}\right] \quad (3.12)$$

Here $\dot{\boldsymbol{x}}_{des}$ is the reference signal as given from the outer loop and provided as the virtual control law, $\boldsymbol{\nu}$. Next, $\boldsymbol{K}_{aug}$ is an n-dimensional diagonal matrix containing the gains to specify the ratio of sensor and model-based derivation for the derivative states. Each diagonal element of $k_{aug,i}$ is set from 0 to 1 since the combination of the measurements cannot exceed 1.

Filling in Equation 3.12, into the general control-affine structure shown in Equation 3.1 the dynamic EoM, gives:

$$\dot{\boldsymbol{x}} = \boldsymbol{f}(\boldsymbol{x}) + \boldsymbol{G}(\boldsymbol{x})\boldsymbol{u}_0 + [\boldsymbol{\nu} - \{\boldsymbol{K}_{aug}\dot{\boldsymbol{x}}_{meas} + (\boldsymbol{I} - \boldsymbol{K}_{aug})\,\dot{\boldsymbol{x}}_{obm}\}] \quad (3.13)$$

Next to this augmentation, the system is also bounded by setting a minimum and maximum bound, depending on the error computed from the model- and sensor-based method. These error states are calculated as shown in Equation 3.14.

$$\begin{aligned} e_{i,meas} &= f_i(x) + \sum_{j=1}^{m} g_{ij}(x)u_0 - \dot{x}_{i,meas} \\ e_{i,obm} &= f_i(x) + \sum_{j=1}^{m} g_{ij}(x)u_0 - \dot{x}_{i,obm} \end{aligned} \tag{3.14}$$

This bounds the maximum state derivatives that are fed to the inner-loop controller as:

$$\min\{e_{i,\text{ meas}}, e_{i,\text{ obm}}\} \leq f_i(x) + \sum_{j=1}^{m} g_{ij}(x)u_0 - [\{k_{\text{aug},i}\dot{x}_{i,\text{ meas}} + (1 - k_{\text{aug},i})\dot{x}_{i,\text{ obm}}\}] \leq \max\{e_{i,\text{ meas}}, e_{i,\text{ obm}}\} \tag{3.15}$$

For every state, the error depends on the certainty of the prediction of each method, given that the model-based method is used more accordingly at predictable parts in the flight envelope, as the predicted error will be less, making the bounds smaller, independent of changing the AM $\boldsymbol{K}_{aug}$. This also works at parts in the flight envelope where the model predictions are less reliable. From different research papers, Kim found the $\boldsymbol{K}_{aug}$ performs best if all scalar values on the diagonal are set to 0.8 [18]. This gives a good indication; however, it does not prove this will be the best configuration if applied, as the simulations were done for a fighter aircraft with a different sensor configuration.
In a direct comparison, Kim concluded that the AM method shows more robustness to CoG uncertainties on a fighter aircraft, especially when increasing the introduced time-delay of the sensors and actuators [18].

Other Methods

This subsection will explain other methods to reduce the influence of time delay on conventional INDI.

Predictive INDI

Sieberling et al. [36] proposed a different method of reducing the effect of time delay on INDI, namely Predictive INDI. This predictive filter uses previous data points from the IMU to predict the next body acceleration. The structure of this filter is shown in Equation 3.16. Here, the scalar values of θ_{ω_j} are computed using a least squares estimation of previous data measurements.

$$\dot{\omega}_{(t)} = \sum_{i=1}^{5} [\theta_{\omega_j}\omega_{(t-i\,\mathrm{dt})} + \theta_{r_j}r_{(t-i\,\mathrm{dt})}] + \epsilon \tag{3.16}$$

This method is shown to be more accurate compared to conventional Euler differentiation or five-point schemes [36]. The influence of time delay is reduced as the predictive filter underestimates the angular accelerations, providing damping to fast changes and remaining stable. Predictive INDI was shown to be robust against uncertainties, albeit less robust than conventional INDI, but the influence of time delay is less for Predictive INDI [36].

Feedforward-Proportional-Integral Control

Another method of implementing Hybrid INDI was suggested by Yang [56], [64], where the signals of the model-based INDI and sensor-based INDI are combined using a feedforward-proportional-integral method. A visual representation is shown in Figure 3.7. This structure depends on the timescale separation principle, where the inner loop uses angular accelerations as the command signal.

The feedforward signal contains the dynamics of the inner loop, which are used to calculate the required command inputs before they are allocated to each control surface. The angular acceleration measurements are subtracted from their reference values and used in a PI structure, where the proportional aspect is implemented to improve the system dynamic performance, and the integral is used to eliminate steady-state errors and reduce the effect of system uncertainties [56]. It is unclear from the research which method is used to measure the angular acceleration, but the possibility to use angular acceleration sensors, using a complementary filter or Kalman Filtering, is proposed [56]. A similar structure as the complementary filter can be seen, comparing this structure to Figure 3.5b, however here the measurements and model prediction

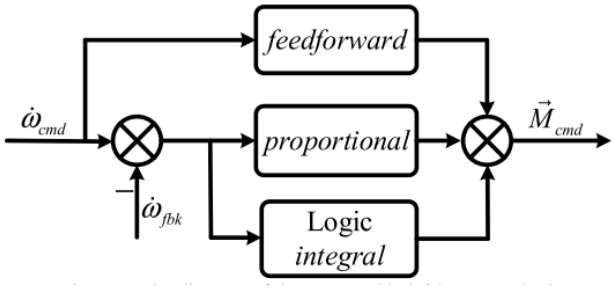

Figure 3.7: Hybrid INDI structure using a feedforward-proportional-integral structure [56]

are not synchronized. The system response is shown to have superior robustness and dynamic response performance; however, nothing is noted about time delay in this research, which makes it unsatisfactory as a method for this research, together with the lack of synchronization.

Choice of model implementation

For this research, the Hybrid INDI implementation is the CF. This structure is proven in previous research to be an effective and straightforward implementation, similar to the application for which this research will use it [17], [18]. The AM shows potential but has only been highlighted by Kim et al., suggesting tuning for different control channels. Furthermore, Lyu shows ESO has better noise reduction capacity than the CF, which is especially clear when looking at the control surface response. However, ESO shows worse tracking performance compared to CF. As there have been several projects at the TU Delft using a CF, this will be the method of choice in this research [17], [59].

3.3. Flight Control System of the Flying-V

From the literature, it has become clear that there have been two methods yet to implement a FCS to the Flying-V, namely Twin-Delayed Deep Deterministic Policy Gradient by Völker et al. [31] and INDI by Van Overeem and Stougie [13], [14]. Völker et al. concluded that with such a Twin-Delayed Deep Deterministic agent, it is feasible to control an aircraft without having any prior used model. Although there is potential in this method, the FCS is not mature yet, so for this research, it was chosen to continue with the methods applied by Van Overeem and Stougie.

This Section will elaborate upon the current FCS using an INDI control law. Figure 3.8 shows a schematic representation of the current state-of-the-art FCS as designed by Stougie [14]. The outer loop controllers, synchronization filter, Control Allocation (CA), PCH, and current limitations are highlighted. The controller systems within this original controller system are run at f_s=100 Hz, where the actuator and aircraft dynamics are run continuously. The sensor dynamics are run at given sampling rates in Table 2.8.

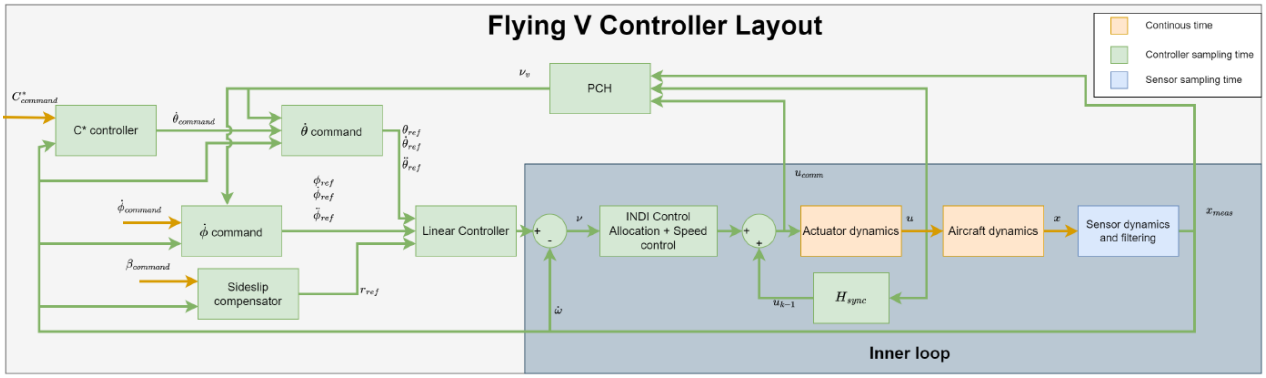

Figure 3.8: Schematic overview of FCS of Flying-V [14]

3.3.1. Outerloop Controllers

The INDI control is controlled by linear outer-loop controllers, which control each respective virtual command signal, $\boldsymbol{\nu}$. The different outer-loop controllers are highlighted below.

C^* controller

The C^* control law has been implemented, as pilots cannot control pitch rate and load factor independently [65], shown in Equation 3.17. Therefore, a control law was designed so that pilots could control the aircraft consistently across the entire flight range. Pilots try to maneuver the aircraft with the same low load factor, providing that the pitch rate will be dominant at low velocity, whereas, at higher velocity, the load factor will be dominant [65]. This balance point is set by a cross-over speed, V_{CO}, at which both states are equally dominant.

$$C^* = \frac{V_{CO}}{g} q + n_{z,pilot} \tag{3.17}$$

The C^* control law has been implemented by Stougie et al. as it is commonly used in Airbus aircraft, enhancing pilots' familiarity when flying with the Flying-V [14], [66]. Looking at Figure 3.9, the C^*_{cmd} from the pilot is first compensated by a term, $\frac{\cos(\theta)}{\cos(\phi)}$, as this limits the C^*_{cmd} from the pilot in turns and high pitch attitude [14], [67].

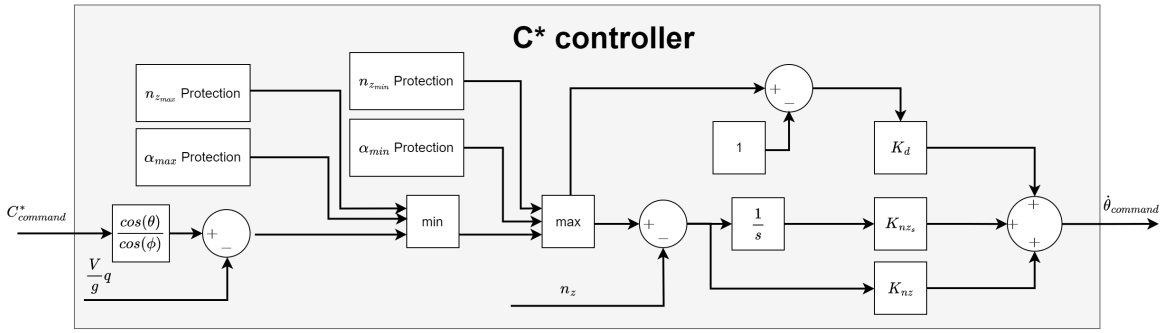

Figure 3.9: Schematic overview of C^* controller of Flying-V [14]

Stougie implemented longitudinal FEP for the minimum and maximum pilot load factor and minimum and maximum AoA. Therefore, these signals are put in a min/max block. After the FEP, the load factor at the pilot station, $n_{z,pilot}$, is calculated. Using the control law shown in Equation 3.18, the $\dot{\theta}_{cmd}$ is acquired.

$$\dot{\theta}_{ref} = K_d(n_{z,pilot,cmd} - 1) + \left(\frac{K_{nzs}}{s} + K_{nz}\right)(n_{z,pilot,cmd} - n_{z,pilot,meas}) \tag{3.18}$$

Euler rate controllers

From the C^* controller and the pilot stick, the $\dot{\theta}_{cmd}$ and $\dot{\phi}_{cmd}$ are given, for which the block diagram is shown in Figures 3.10a and 3.10b respectively. For the $\dot{\phi}_{cmd}$, a FEP law for the protection of the roll angle is in place, similar to the C^* controller. Both Euler rate controllers are the same in structure, where a feedforward term is used to increase tracking performance [68]. The PCH signal is subtracted from the Euler acceleration reference signal, as this will compensate for saturation, which will be explained in Section 3.3.4. The reference signals used for the virtual roll and pitch command control are acquired from these controllers.

Sideslip controller

The virtual yaw command is not computed using a pure yaw command, however a sideslip command is used, based on Lombaerts [69]. This controller calculates the body velocity $w_{\mathcal{B}}$, by taking the general assumption $w_{\mathcal{B}} \approx V_\infty \alpha$ [14]. Figure 3.11 shows the block diagram of this controller.

Linear Controller

The last outer-loop controller converts the inputs to each virtual command input, $\boldsymbol{\nu}$. This linear controller structure has been based on previous research and implemented by Stougie [14], [43], [67]. Each virtual command input is shown in Equation 3.19.

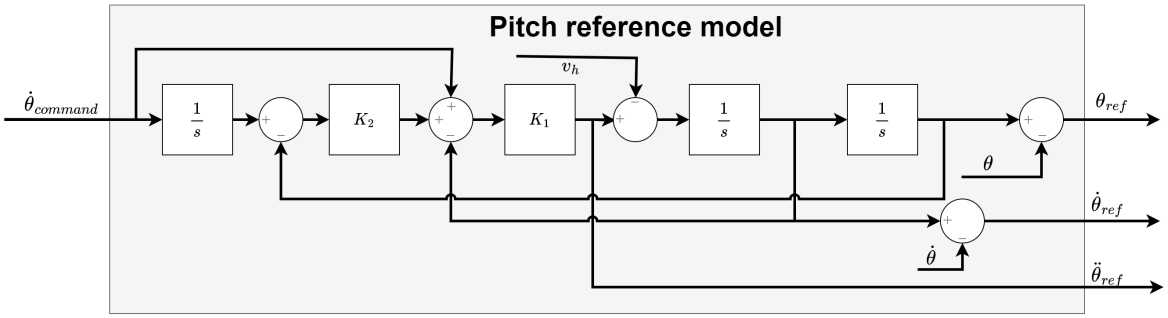

(a) Schematic overview of $\dot{\theta}$c controller of Flying-V [14]

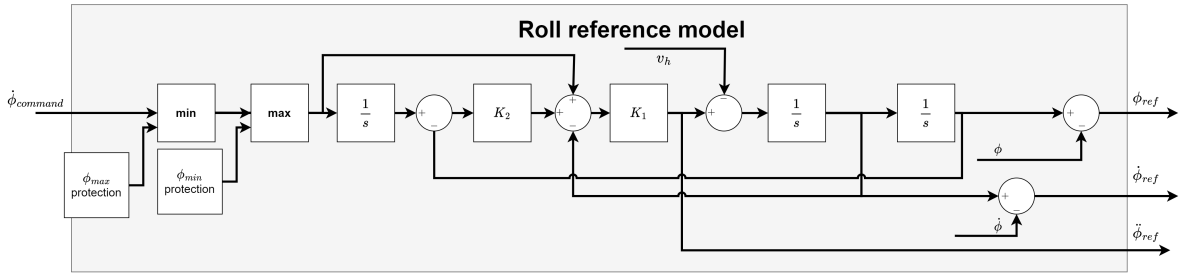

(b) Schematic overview of $\dot{\phi}$c controller of Flying-V [14]

Figure 3.10: Euler rate controllers

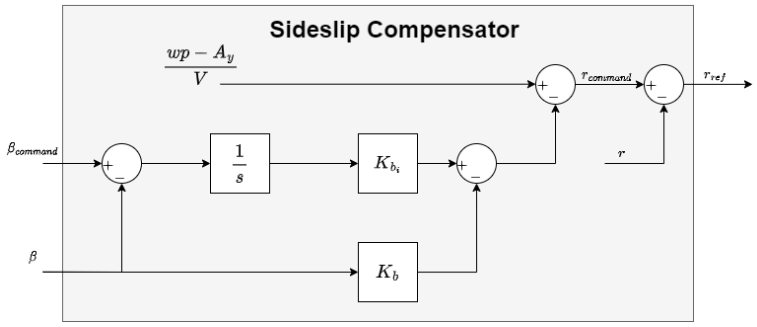

Figure 3.11: Schematic overview of Sideslip controller of Flying-V [14]

$$\begin{aligned} \nu_p &= \left(K_\phi + \frac{K_{\phi I}}{s}\right) \cdot \phi_{ref} + K_{\dot{\phi}} \cdot \dot{\phi}_{ref} + K_{\ddot{\phi}} \cdot \ddot{\phi}_{ref} \\ \nu_q &= K_\theta \cdot \theta_{ref} + K_{\dot{\theta}} \cdot \dot{\theta}_{ref} + K_{\ddot{\theta}} \cdot \ddot{\theta}_{ref} \\ \nu_r &= K_r \cdot r_{ref} \end{aligned} \tag{3.19}$$

3.3.2. Synchronization Filter

As described previously, a synchronization filter is essential when implementing an INDI scheme, which considers actuator and sensor dynamics. In physical systems, the sensors and actuators do not respond instantly but experience delays and dynamics [59], [70]. Therefore, if not accounted for, the system will respond oscillatory as the delays between the actuators and sensors, also known as latency, are not synchronized [44]. To compensate for this behavior, the delays that occur in the feedback loop have to be compensated. One method for compensating the latency is using an Average Square Difference Function to identify the latency and adding a pure time delay. For this, the characteristics of the actuators and sensors do not have to be known. However, this does not directly compensate for any change in latency depending on the dynamics of the system. Typically, for sensor-based INDI, a second-order filter is used to compensate for the filtering of the body rate sensor [43], [59], [70]. Van 't Veld concluded that the effect of delay on the actuator can mostly be neglected, compared to the sensor delay, and that, additionally to the second-order filter, a pure time delay should also be added to compensate for the difference in time delay of both sensors [44]. Moreover, as was noted in Section 3.3, the simulation runs a discrete controller and continuous system for which the inclusion of actuator delay in the controller would decrease the system stability and is therefore not included [14], [44].

The synchronization filter becomes more complex for systems that use Hybrid INDI. As the filtering and hybridization have to be fed back, this has to be synchronized. Therefore, the synchronization filter is chosen depending on the method chosen for hybridization. The transfer function for a Hybrid INDI system, going from desired input, $\boldsymbol{\nu}$, to ideal actuator input, $\boldsymbol{u_{cmd}}$, is given in Equation 3.20 [57].

$$\frac{\boldsymbol{u_{cmd}}}{\boldsymbol{\nu}} = \frac{\boldsymbol{H}_{act}\left[\boldsymbol{f}_{ac}(x) + \boldsymbol{G}_{ac}(x)\right]}{\left(\dot{\boldsymbol{x}}_{est} - \boldsymbol{G}_{obm}(x)\boldsymbol{H}_{sync}\boldsymbol{u_{cmd}}\right)e^{-\tau s} + \boldsymbol{G}_{obm}(x)} \tag{3.20}$$

Here H_{act} represents the ideal actuator dynamics, $[f_{ac}(x) + g_{ac}(x)]$ is the ideal aircraft dynamic, g_{obm} is the control effectiveness matrix that the controller uses and $\dot{\boldsymbol{x}}_{fb}$ is the feedback signal. For the CF, the synchronization filter is similar to the CF itself, also including the sensor and actuator dynamics. This is shown in Equation 3.21 [17], [58].

$$\boldsymbol{H_{sync}} = \hat{\boldsymbol{H}}_{act}(s)\Big[T(s) + S(s)L(s)\Big] \tag{3.21}$$

Here the $T(s)$ and $S(s)$ functions are the same as for the CF, depending if the notation from Equation 3.9 or 3.11 is chosen. The function $L(s)$ represents the sensor dynamics, and $\hat{H}_{act}$ is the approximation of the actuator dynamics. It should also be noted that the onboard model prediction shall also be multiplied by the actuator dynamics otherwise the measured state and model-based state would also be out of sync.

For the AM, since the feedback state derivative is a linear combination of the measured state and estimated state, the synchronization filter is given in Equation 3.22 [61].

$$\boldsymbol{H}_{sync} = \frac{\boldsymbol{K}_{aug}\boldsymbol{G}_{ac}(\boldsymbol{x})L(s)\boldsymbol{H}_{act}}{\boldsymbol{K}_{aug}\boldsymbol{G}_{obm}(\boldsymbol{x})} \tag{3.22}$$

It can be concluded that this representation cancels the effect of the control effectiveness matrix if the onboard model perfectly matches the aircraft model; however, this is impossible. Since the ideal control effectiveness is unknown, Kim et al. have proposed using either a 2nd-order or 4th-order system that represents the actuator, sensor, and high-order aircraft dynamics and synchronizing this. Since the current model of the Flying-V does not simulate high-order dynamics, a 2nd-order filter is satisfactory, where the sensors and actuators' responses must be known to match the filter [57].

3.3.3. Control Allocation

The Flying-V has an overactuated control surface layout as there are four elevons and two rudders to control the body rates of the aircraft. Therefore, the control surface effectiveness matrix is not square as given in Equation 2.24. Hence, a given control command can be solved by different control surface deflection positions [41]. For these control problems, Control Allocation (CA) was introduced, effectively solving the optimal configuration for the control surfaces to achieve the given control command. The known model for the control surfaces is currently a control affine structure, where the control surface inputs are linearly related to their respective moment coefficients, as shown in Section 2.7. Even though this assumption probably does not hold for the actual model, there is no known model for this, such that the CA can be a simple linear method for this research. For this research, a simple cascading algorithm, implemented by Stougie et al., is used [14], [41]. This method is based on using a pseudo-inverse of the control effectiveness matrix, $\boldsymbol{G(x)}$, which is shown in Equation 3.23. Recalling Equation 3.8, the desired moments generated by the control surfaces, indicated by $\boldsymbol{\nu} - \dot{\boldsymbol{x}}$ multiplied with the matrix $\boldsymbol{\mathcal{B}}^{-1}(\boldsymbol{x})$ gives the incremental control surface deflection, $\Delta\boldsymbol{u}$. The maximum incremental control deflections are defined using Equation 3.24 [14].

$$\boldsymbol{\mathcal{B}^{-1}(x)} = \boldsymbol{G}^T(\boldsymbol{G}\boldsymbol{G}^T)^{-1} \approx \boldsymbol{G(x)}^{-1} \tag{3.23}$$

$$\begin{aligned}\Delta\boldsymbol{u}_{max} &= \min\left(\dot{\boldsymbol{u}}_{max}\frac{\omega_{act}}{2\zeta_{act}}, \boldsymbol{u}_{max} - \boldsymbol{u}_0\right)\\ \Delta\boldsymbol{u}_{min} &= \max\left(\dot{\boldsymbol{u}}_{min}\frac{\omega_{act}}{2\zeta_{act}}, \boldsymbol{u}_{min} - \boldsymbol{u}_0\right)\end{aligned} \tag{3.24}$$

If none of the demanded control deflections is over the limits, the calculated incremental control deflections are calculated with Equation 3.24. If this is not the case, the following three scenarios will be checked, as per Stougie [14]:

1. If the rudder, left or right, has reached its limit:
   - The rudder will be positioned at either its limit or at the required yaw moment divided by $C_{l_{\delta_{rud}}}$.
   - The corresponding column in the control effectiveness matrix $\boldsymbol{G(x)}$ and the row related to the yaw moment will be removed. Additionally, the desired yaw moment will be removed from $\boldsymbol{\nu - \dot{x}}$.
   - The new $\boldsymbol{\nu - \dot{x}}$ will be recalculated by subtracting the generated moment by the rudder from $\boldsymbol{\nu - \dot{x}}$.
2. Else, if either elevon 2 left or right (or both) have reached their limits, the following steps should be taken:
   - Determine which of these two control surfaces is the most over its limit and calculate $a = u/u_{lim}$. Scale the other control surface with a to preserve the direction between these two control surfaces.
   - Calculate the new $\boldsymbol{\nu - \dot{x}}$ by subtracting the generated moments from $\boldsymbol{\nu - \dot{x}}$.
   - Remove the rows related to δ_{CS2_L} and δ_{CS2_R} from $\boldsymbol{G(x)}$
3. Else, if either elevon 1 left or right (or both) have reached their limits, the following steps should be taken:
   - Determine which of these two control surfaces is the most over its limit and calculate $a = u/u_{lim}$. Scale the other control surface with a to preserve the direction between these two control surfaces.
   - Calculate the new $\boldsymbol{\nu - \dot{x}}$ by subtracting the generated moments from $\boldsymbol{\nu - \dot{x}}$.
   - Remove the rows related to δ_{CS1_L} and δ_{CS1_R} from $\boldsymbol{G(x)}$

If one of the inboard or outboard control surfaces is at its deflection limit, the other control surfaces are no longer scaled to prevent them from staying locked at their deflection limit, which means degradation. The ratio between moments is temporarily not guaranteed until the control surface is no longer at its deflection limit.

After this, there are four cases:

1. $\boldsymbol{G(x)}$ has more columns than rows: in this case, the Moore-Penrose pseudo-inverse is used to invert the $\boldsymbol{G(x)}$.
2. $\boldsymbol{G(x)}$ has the same amount of rows as columns: it can be inverted normally.
3. $\boldsymbol{G(x)}$ has fewer columns than rows: The problem is now over-determined. To minimize the error, the pseudo-inverse, $\mathcal{B}^{-1}(\boldsymbol{x})$ is used from Equation 3.23
4. $\boldsymbol{G(x)}$ is empty, meaning there are no control surfaces left to allocate, which yields the desired moments that cannot be met.

The new inverted matrix $\mathcal{B}^{-1}(\boldsymbol{x})$ and $\boldsymbol{\nu - \dot{x}}$ can be used to allocate control surfaces. If some control surfaces reach their limit, the algorithm will restart until no surfaces exceed the limit or no more surfaces are left.

3.3.4. Pseudo Control Hedging

The general representation of INDI was first derived without considering the limitations of the actuators used [54]. Even though the dynamics of the actuators can be taken into account using transfer functions, the real-life limits cannot be set. Therefore, Pseudo Control Hedging (PCH) was introduced as a method to compensate the input signal for actuator position and rate limits. When PCH was first introduced Johnson and Calise [71, p. 6] described it as: "The reference model is moved backward (hedged) by estimating the amount the plant did not move due to system characteristics the control designer does not want the adaptive control element to 'know' about". This is done by looking at the limits of the actuator and subtracting the commanded virtual control input from the actual virtual control input. The advantage of PCH is the adaptability in the command signal, compared to doing this in a control law, making it easier for certification [43]. Furthermore, PCH can be used as an effective anti-windup technique for the linear outer-loop controller [44].

Mathematically, the PCH is implemented using an addition to the provided pilot-command signal, $\boldsymbol{\omega_{cmd}}$, which in the current model represents the angular rate commands. These rate commands are now fed into a first-order reference model named in the literature, where the command signal will be changed depending on actuator saturation [41]. This reference model is given in Equation 3.25

$$\boldsymbol{\nu}_{rm} = \boldsymbol{K_{rm}} \left(\boldsymbol{\omega_{cmd}} - \boldsymbol{\omega_{rm}} \right) \tag{3.25}$$

where $\boldsymbol{K_{rm}}$ is a diagonal matrix containing gains to scale to the desired virtual control input, $\boldsymbol{\nu_{cmd}}$. This $\boldsymbol{\nu_{rm}}$ is the derivative of the command signal, which is used as a feedforward term to increase tracking performance [68]. The reference model angular rate is calculated using Equation 3.26

$$\boldsymbol{\omega_{rm}} = \frac{1}{s} \left(\boldsymbol{\nu_{rm}} - \boldsymbol{\nu_h} \right) \tag{3.26}$$

where $\boldsymbol{\nu_h}$ is the hedged feedback from the actuators. The control hedge uses the commanded control input per control surface and the measured control surface deflection after saturation filtering. Since, due to the synchronization filtering, only the previous input state, $\boldsymbol{u_{k-1}}$ is known, the virtual hedge, $\boldsymbol{\nu_h}$ is also taken from the previous step [44]. As the hedge subtracts the oversaturated control input, the hedge signal has to be converted back to the virtual command signal, which is the angular acceleration. Therefore, the required hedge is multiplied by the control effectiveness matrix, $\boldsymbol{G(x)}$. The notation for the hedge signal is given in Equation 3.27.

$$\boldsymbol{\nu_h = G(x)\,(u_{cmd} - u_m)} \tag{3.27}$$

Stougie implemented this structure; however, the yaw moment was not included in this implementation as a sideslip compensator was implemented rather than a yaw compensator [14]. Figure 3.12 visualizes this structure in more detail than the one given in Figure 3.8.

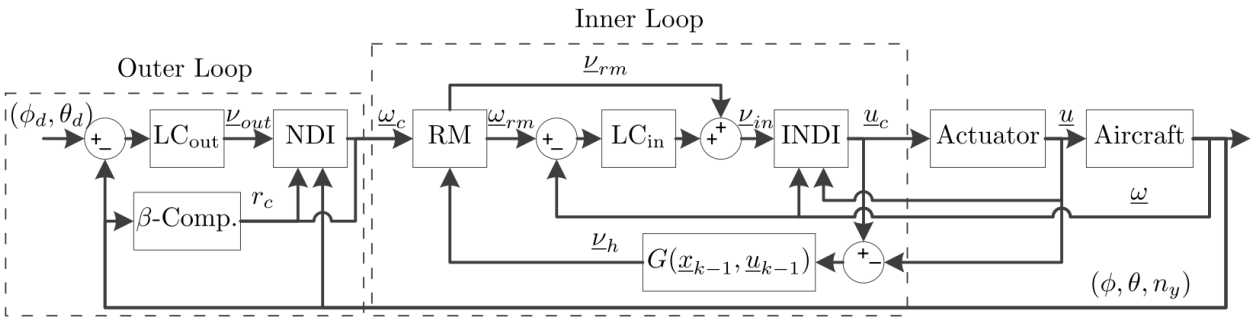

Figure 3.12: Detailled structure of INDI controller with PCH [44]

3.3.5. Limitations of current system

The current problems exist when implementing the system in real life. Even though the most recent INDI FCS made by Stougie, the system can operate within level 1 handling qualities, as long as the time delay of the body rate sensor is not larger than $t = 0.04$s. This margin is unsatisfactory as the base sensor delay that is used in these simulations is taken from sensors used in the PH-LAB Cessna Citation from Delft University of Technology and is equal to $\tau = 0.1$s at a sampling rate of $f_s = 50Hz$ [14]. Even though there might exist sensors that satisfy the requirements, it is also possible to make the system less dependent on sensor delay, which is where Hybrid INDI is suggested as a possible solution for this [14]. To understand the problem with time delay in sensors while implementing INDI, recall Equation 3.8.

$$\boldsymbol{u = u_0 + \mathcal{B}^{-1}(x)(\nu - \dot{x}_0)}$$

Here $\dot{\boldsymbol{x}}_0)$ represents the measured state derivatives; however, with time delay, this shall be replaced by $\dot{\boldsymbol{x}}_m = \dot{\boldsymbol{x}}_0 + \dot{\boldsymbol{x}}_\tau$. The dynamics are not fully canceled if this is plugged into Equation 3.8, which can result in a performance decrease or even instability. Stougie showed stability margin HQ requirements were not met, for which the delay of the sensors had to be decreased [14]. The results from Stougie are shown in Table 3.1. In time-domain response, Stougie noticed chatter of the rudder control surface, which was reduced by changing the β sensor filter characteristic, however this did not solve the problem.

Table 3.1: Tuning results. Green being within level 1, and Yellow being within level 2 Handling Qualities [14]

(a) Longitudinal tuning results for cruise conditions.

Description	No sensors	Adjusted sensors	Baseline sensors
Linear Analysis			
GM ν_q $[dB]$	20.37	6.08	5.35
PM ν_q $[deg]$	65.34	48.06	34.5
ω_{sp} $[rad/s]$	1.81	1.82	2.18
ζ_{sp} $[-]$	1.29	1.12	0.79
CAP $[g^{-1}s^{-2}]$	0.433	0.388	0.368
ω_{BW} $[rad/s]$	3.27	3.17	3.12
τ_p $[s]$	0.029	0.021	0.038
$score_{LOES}$ $[-]$	4.67	4.05	10.79
ω_{CO} $[rad/s]$	34.7	7.72	6.19
Simulation with C^*_{comm} step input of 1.8 at t = 1s. T_{sim} = 20s			
max(δ_{CS}) $[deg]$	10.97	11.21	11.20
$\delta_{CS_{activity}}$ $[deg/s]$	0.17	0.69	0.77
ST C^* $[s]$	3.89	2.72	4.48
OSC^* $[-]$	0.08	0.08	0.13

(b) Lateral tuning results for cruise conditions

Description	No sensors	Adjusted sensors	Baseline sensors
Linear Analysis			
GM ν_p $[dB]$	24.28	7.91	6.97
PM ν_p $[deg]$	63.16	52.95	48.98
GM ν_r $[dB]$	26.29	7.19	5.85
PM ν_r $[deg]$	75.95	49.28	22.82
$1/T_s$ $[s^{-1}]$	0.074	0.065	0.07
T_r $[s]$	0.513	0.604	0.52
ω_{dr} $[rad/s]$	1.036	2.66	3.81
ζ_{dr} $[-]$	0.26	0.52	0.74
$\omega_{dr}\zeta_{dr}$ $[rad/s]$	0.27	1.37	2.83
$score_{LOES}$ $[-]$	3.54	3.74	3.77
ω_{CO_p} $[rad/s]$	36.29	6.69	5.10
ω_{CO_r} $[rad/s]$	29.75	5.96	5.56
Simulation with $\dot{\phi}_{comm}$ block input of 3 deg between t = 1s and t = 14s. T_{sim} = 18s			
max(δ_{CS}) $[deg]$	6.04	7.74	4.1
$\delta_{CS_{activity}}$ $[deg/s]$	0.75	1.78	1.29
ST $\dot{\phi}$ $[s]$	5.27	4.42	5.53
Simulation with Wind step v_{wind} = 16 m/s at t = 1s. T_{sim} = 15s			
$\delta CS_{activity}$ $[deg/s]$	1.89	3.07	6.91

3.4. Flight Envelope Protection

FEP will be another key focus point in this research to guarantee a more safe control system. Because of the airframe instabilities of the Flying-V, the FEP system should prevent the aircraft from entering potentially unstable flight conditions. This is important for both the automatic pilot and when the pilot is manually flying the aircraft. In the original controller system, implemented by Stougie [14], there is FEP based on the works of Lombaerts [67] and Oudin [72]. The following sections will describe the current FEP system that has been implemented, followed by improvement possibilities. Other methods of advancing the FEP will be discussed to fulfill and implement these improvements.

3.4.1. Current Flight Envelope Protection in the Flying-V

In the original FEP structure, laws are in place to limit the commanded pitch and roll rate. The pitch rate protection is implemented using a combination of AoA and load factor limits. These limits are combined in a respective C^* controller that combines the commanded load factor from the pilot's stick and the pitch rate [67]. Figure 3.9 shows the layout of this controller structure. The AoA protection is controlled with a proportional controller with different gains, depending on whether a minimum or maximum load protection is relevant. This protection starts at an AoA higher than 15 degrees and lower than 0 degrees. When this protection is inactive, the limits are at +2.5g and -1g. The load factor protection is calculated using Equation 3.28 from Lombaerts [67]. Here, the $C_{L,max}$ is set to the lift coefficient at AoA of 25 degrees, and $\Delta C_{L,max}$ is set to 0.01, which is meant for uncertainty about the maximum lift coefficient.

$$n_{z,max} = \max\left(1, \min\left(2.5, 1 + \frac{(C_{L,max} - \Delta C_{L,max})\,\overline{qS}}{w}\cos(\phi) - n_y \sin(\phi) - \cos(\gamma) + \frac{T}{w}\sin(\alpha)\cos(\phi)\right)\right) \tag{3.28}$$

For the roll rate protection, the maximum roll angle is first calculated using Equation 3.29 [67].

$$\begin{aligned} \phi_{max} &= \min\left(66, \arccos\left(\frac{mg\cos(\gamma)}{T\sin\alpha + (C_{L,max} - \Delta C_{L,max})\,\overline{q}S}\right)\right) \\ \dot{\phi}_{max} &= K_{\phi_{FEP}}(\phi_{max} - \phi) \text{ and } \dot{\phi}_{min} = K_{\phi_{FEP}}(-\phi_{max} - \phi) \end{aligned} \tag{3.29}$$

Using this equation, the maximum and minimum roll rates are set using a proportional controller, which changes sign if this maximum value is reached and the protection starts within two degrees of the limit [14], with the upper limit of the roll angle always being $\pm$ 66 degrees.

It was found that gain scheduling was necessary, dependent on the air density. Final results show that the FEP shows overshoot in the AoA protection of approximately 3 degrees, keeping the AoA below the 30 degrees at which the aircraft becomes unstable. Stougie concluded with some recommendations. Firstly, a single, known CoG is simulated, so robustness is not tested. Furthermore, the minimum protection laws have not been tested, and no airspeed protection is in place. Stougie suggests looking at extending the FEP to a PD controller, taking into account the derivative of the AoA [14].

3.4.2. Industry Flight Envelope Protection

Following the conclusions from Stougie, the industry standards and research of implementations of FEP are researched. Airbus and Boeing have different visions of how the FEP should be handled within the industry. Rogers [73], a former aircraft pilot for United Airlines, evaluated these implementations and a subjective conclusion from test pilots. Boeing uses 'Soft Envelope Protection', for which the pilots can override the protections set by the FCS. In contrast, Airbus uses 'Hard Envelope Protection', which will prevent the pilots from exceeding the set limits of the aircraft. Rogers concluded that a perfect system would combine both with Airbus's priority for the system. The advantage of the hard limits is that inexperienced pilots cannot exceed the limits of the aircraft, thus avoiding unsafe operations. Contrary to this, Boeing believes the pilots should be able to take full advantage of the aircraft, and these limits do not give full potential, which could be necessary in unexpected situations [73]. The soft limits are more complicated to implement due to the force feedback, which also adds failure modes [74]. Therefore, for this research, the hard limits will be used as implemented by Airbus.

For certification of a FEP system, there are specific requirements set by EASA. These requirements are stated in the Code of Federal Regulations, part 25 [75] and summarized for the FEP system by Lambregts [74]. The most critical requirements, including recommendations by Lambregts for the FEP, are listed below.

- **Stall Protection**
  - Stalls must be prevented during any pilot maneuver and wind shear or gusts at low speeds.
  - Stall has to be prevented by a AoA and minimum speed protection.
- **High Speed Protection**
  - The overspeed warning should not be triggered in any maneuver with the protection enabled.
- **Normal load factor protection**
  - According to CS 25.143(l) [75, pp.151]
    1) The positive limiting load factor must not be less than:
       a) 2.5g for the EFCS normal state.
       b) 2.0g for the extended EFCS normal state with the high lift devices.
    2) The negative limiting load factor must be equal to or more negative than:
       a) -1.0g for the EFCS normal state.
       b) 0.0g for the extended EFCS normal state with high lift devices.
- **Roll Angle Limiting**
  - With all engines operating, as per CS 25.147(f) [75, pp. 165], the aircraft should be able to roll up to a bank angle of 60 degrees, or 30 degrees below an altitude of 1000 ft.

The requirements make it unclear what the set limits should be for pitch attitude. From the literature regarding the Fault Tolerant Control of Airbus, these limits were stated and do correspond with the other limits that EASA set [76]. Figure 3.13 shows a diagram indicating the outermost envelope in different scenarios. Manual flight can reach these limits, whereas the auto-pilot would stay within stricter boundaries.

It should be noted that Goupil [76] indicates a limit of 66 degrees for the roll angle, as used in more literature, together with the current system that was implemented [14], [67], [77]. Therefore, the limit is assumed to be set to $\pm$ 66 degrees. This condition is doubtful, as is pointed out by Lambregts [74] , and the auto-pilot will return to a maximum bank angle of 33 degrees [67]. For this research, it will be assumed, following Figure 3.13, that the limits for the pitch attitude are set to be -15 degrees and +30 degrees. It also follows that next to the currently implemented load factor limits with AoA protection, an additional pitch attitude protection will be implemented. Over- and under-speed protection are not implemented as under-speed is closely related to AoA as the consequence of exceeding the set limit results in a stall. Therefore, the AoA protection is assumed to cover this state. Overspeed is typically protected using an audible warning, which is not related to the FCS.

Regarding the control structures for these systems, the literature does not specify which control structure is used to implement the FEP. However, all literature that refers to it suggests the use of linear PID controllers [66], [76].

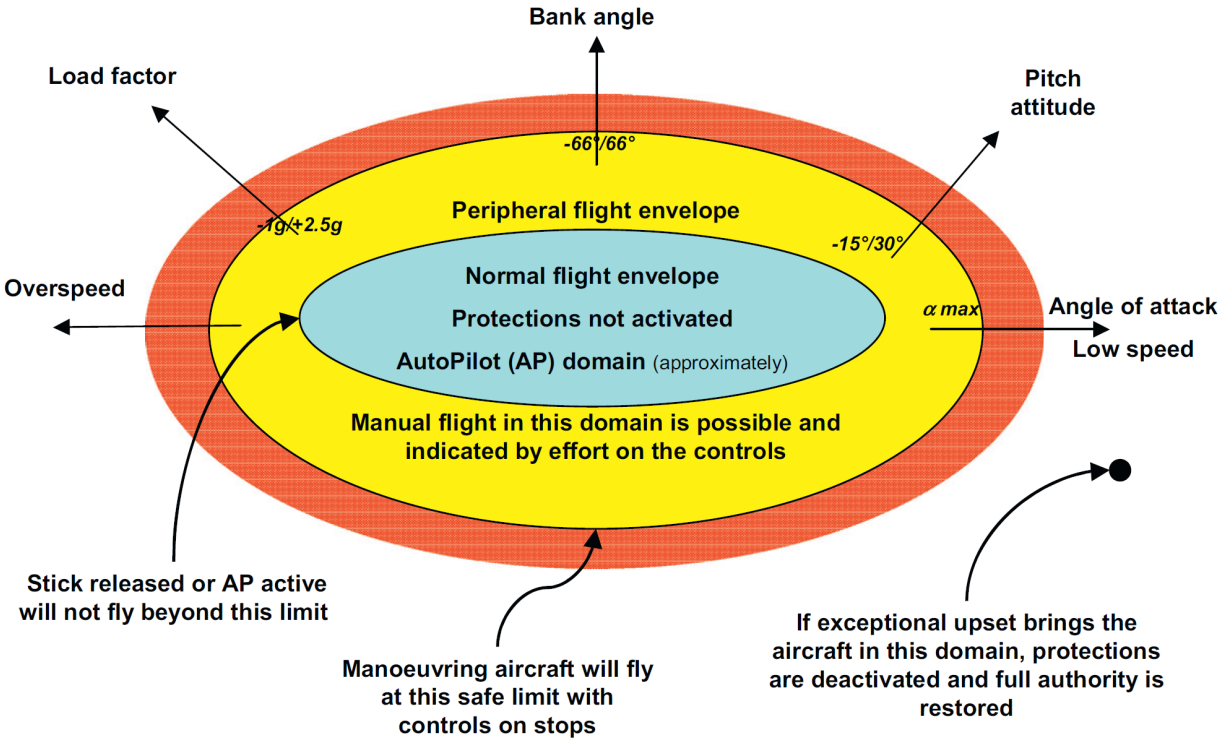

Figure 3.13: Flight Envelope Limits for Airbus [76]

3.4.3. State-of-the-art Flight Envelope Protection

Using the requirements set by regulatory instances, such as EASA, and the implementation limits set by Airbus, the different state-of-the-art methods will be researched to properly implement these findings. There have been different approaches to implementing these limits. Most methods require the online identification of parameters that can be used to estimate the limits of the system [48], [50], [51], [78], [79]. Even though this method might have potential, it is not within the scope of this research as adaptive control is not being implemented. Xie et al. [80] research the implementation of a neural network with fuzzy rules, which is a different approach but not part of this research's scope.

A feasible approach for this research with a Hybrid INDI controller would be the research from Falkena [81]. He compares a control limiting structure, a command limiting structure, and a virtual control limiting structure, and a command limiting structure, MPC based control law. Here it was concluded that the control limiting structure did not perform properly and preference went to the command limiting structure, as it is a versatile simple method.

Command limiting maps the angle limits to the rate commands using a parameter projection as to prevent singularities and make the limit commands continuous [82]. Each state needs a different mapping function, however each mapping function is relatively simple compared to control limiting [81]. An example of how the pitch rate command can be mapped from the limits of the pitch angle is shown in Equation 3.30 from Falkena [81].

$$
\begin{aligned}
g &= (\theta - (\theta_{max} + \theta_{min})/2)^2 - (\theta_{max} - (\theta_{max} + \theta_{min})/2)^2 \\
\nabla g &= 2(\theta - (\theta_{max} + \theta_{min})/2) \\
q_{\text{cmd}} &= \begin{cases} q_{\text{cmd}} & \text{if } g \leq 0 \\ & \text{or if } g = 0 \text{ and } \nabla g q_{\text{cmd}} \leq 0 \\ 0 & \text{otherwise} \end{cases}
\end{aligned} \tag{3.30}
$$

The protection system we developed uses a method that sets limits on commands. This method considers the negative effects of aircraft aerodynamics, the unusual attitude of the aircraft, and the aircraft's structure [67]. It is built into a standard flight control system that adjusts based on the plane's situation. Lombaerts extended the functionality of this FEP to include protection to the aircraft's energy using an automatic control for the throttle based on a total energy control system. In this research, Lombaerts et al. concluded that the command limiting algorithm was especially effective for adding protections to excessive pilot input, which is desirable to implement the hard limits from the Airbus philosophy.

3.4.4. Exponential Potential Function Command Limiting Flight Envelope Protection

This research employs an exponential potential function to implement a command limitation for FEP, as per the methodology outlined by Sun et al. [83], [84]. This protection scheme is based on exponential potential functions, only bringing relevant protection near the set protection limit. The following definition follows for this control law: consider a state, x_1, which will be protected, where its state derivative, x_2, is known, together with the reference signal of $x_{2,ref}$, assuming a rate controller, the implemented FEP is shown in Equation 3.31. It should be noted that for minimum protection, the minimum value should be smaller or equal to zero.

$$
\begin{aligned}
x_{2,FEP,max} &= x_{2,ref}(1-u_p^+), \quad \text{where } u_p^+ = \begin{cases} e^{\eta(x_1(t)-x_{1,max}+\zeta x_2(t))}, \text{ if } e^{\eta(x_1(t)-x_{1,max}+\zeta x_2(t))} \leq 2 \\ 2, \text{ if } e^{\eta(x_1(t)-x_{1,max}+\zeta x_2(t))} > 2 \end{cases} \\
x_{2,FEP,min} &= x_{2,ref}(1-u_p^-), \quad \text{where } u_p^- = \begin{cases} e^{-\eta(x_1(t)-x_{1,min}+\zeta x_2(t))}, \text{ if } e^{-\eta(x_1(t)-x_{1,min}+\zeta x_2(t))} \leq 2 \\ 2, \text{ if } e^{-\eta(x_1(t)-x_{1,min}+\zeta x_2(t))} > 2 \end{cases}
\end{aligned}
\tag{3.31}
$$

For this representation, two tuning parameters per protected state, namely η and ζ, are similar to a proportional and derivative gain, respectively. Increasing η will increase the margin before the FEP will become active, where the damping coefficient, ζ, will set how strict the FEP will dampen the rate at which the state derivative x_2 is approaching the protected state. Figure 3.14 shows a representation where the influence of η is shown.

Each colored line, except the blue line, shows the rate, x_2, at which the state approaches the protected state, x_1. Next, for each rate, x_2, there are three values for η, showing at which rate the potential function approaches $g_2(x)$=0. For increasing x_2, the function $g_2(x)$ passes zero before it is at its protected state. When x_2 is negative, i.e., the state moves away from its protected state, the function crosses zero above the protected state. The parameter η defines how abruptly the potential function limits the signal, with a higher η giving a more abrupt gradient to the protected state.

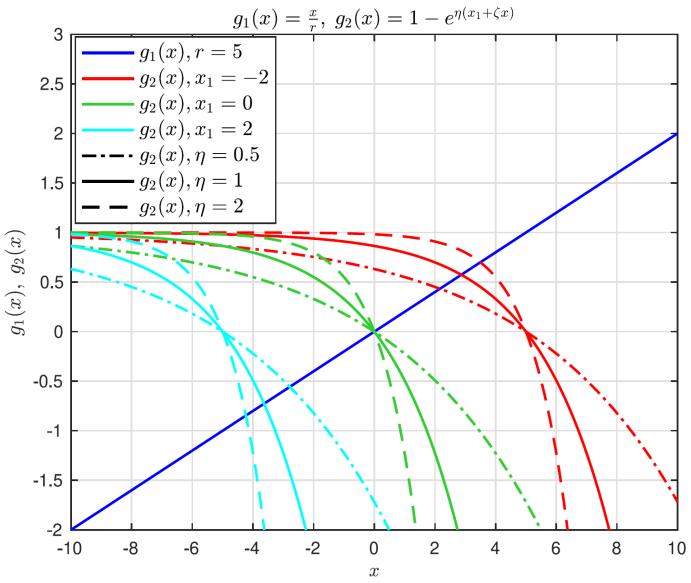

Figure 3.14: Exponential potential function with tune parameter influence [84]

4

Handling Quality Requirements

The evaluation of FCS should be based on its stability and handling qualities to ensure its verification. There are several methods for assessing these aspects, which will be highlighted below. These assessments are conducted using evaluation methods employed by civil aviation authorities, such as the Federal Aviation Administration (FAA) and European Union Aviation Safety Agency (EASA). Moreover, as has been shown by Van Overeem et al., among others, the civil specifications are not quantifiable [13]. Therefore, the use of an older military standard is used, denoted by MIL-STD-1797A revision 3, which specifies certain lower and upper bounds about assessing FCS characteristics[32]. In this Chapter, Section 4.1 refers to which classifications and flight phases will be used to evaluate the aircraft. Next, Section 4.2 will denote the stability assessment for both the longitudinal and lateral directions. Section 4.3 shows the dynamic stability & handling quality requirements. Section 4.4 will describe which assessments will be used in this research to evaluate the implemented FCS. This chapter will conclude research question 1.

4.1. Aircraft Classification

For evaluating handling requirements, it is important to know in which class, category, and flight phase an aircraft is being tested. It is obvious that for certain requirements, there is a difference between fighter jets and jumbo jets. Therefore, there are different classes and flight phases to which requirements can be checked. These are shown in Tables 4.1, 4.2 and 4.3. Most specified requirements have a minimum and maximum value or levels of compliance with the requirements. For this research, it is important to state that the Flying-V V1000 will be evaluated in the bold flight phases given in Table 4.3 [14], categories B and C respectively. Furthermore, the Flying-V V1000 is a Class III aircraft, looking at the MTOM shown in Table 2.2.

Table 4.1: Aircraft class identification.[85]

Class I	Small light aircraft (MTOM <6000 kg)
Class II	Medium weight, low to medium manoeuvrability aircraft 6000 kg <MTOM <30000 kg)
Class III	Large, heavy, low to medium maneuverability aircraft (MTOM >30000 kg)
Class IV	High maneuverability aircraft (e.g. aerobatic or fighter)

Table 4.2: Aircraft flight phase identification [85]

Category A	Non-terminal flight phases require rapid maneuvering, precision tracking, or precise flight path control.
Category B	Non-terminal flight phases require gradual maneuvering, less precise tracking, and accurate flight path control.
Category C	Terminal flight phases require gradual maneuvering and precision flight path control.

Table 4.3: Flight phase categories [85]

Flight phase category	Flight phase
A	Air-to-air combat
	Ground attack
	Weapon delivery/launch
	Reconnaissance
	In-flight refuel (Reciever)
	Terrain following
	Maritime search
	Aerobatics
	Close formation flying
B	Climb
	Cruise
	Loiter
	In-flight refuel (tanker
	Descent
	Aerial delivery
C	**Take off**
	Approach
	Overshoot
	Landing

4.2. Stability Assessment

The first assessment that will be done on the FCS is evaluating the tracking performance, which will be done by looking at conventional step-input responses to reference signals of the FCS and assess their performance based on specified parameters. Furthermore, the gain and phase margins will be evaluated for the specified flight conditions. Afterward, the LOES will be presented as needed to assess the handling requirements, given in Section 4.3.

4.2.1. Tracking performance

The tracking performance of the system will be evaluated using the metrics given below:

- Overshoot (OS)
- Settling Time (ST)
- Control Surface Activity ($\text{CS}_{activity}$)
- Maximum Control Surface Deflection (CS_{max})

These metrics will be used as guidelines to compare results of the FCS, but will not be used as hard requirements. The goal is all metrics is for them to be minimized.

As shown in Figure A.3, Overshoot can be defined as shown in Equation 4.1.

$$\text{OS} = \frac{y_{max} - y_{ss}}{y_{ss}} \times 100\% \tag{4.1}$$

Here, it is visible that overshoot will be given as a percentage of the steady-state value. Next, the settling time can be evaluated by the time it takes the system response to get within 2% of the commanded step response. Note that these metrics shall be evaluated carefully, as it is not the time for the signal to cross the commanded step response and have a large overshoot.

Control input activity and maximum control input serve as key metrics for assessing the sensitivity of control surfaces in time domain, shown by the chatter response of the control surfaces, typically attributed to high control gains. The control input activity is evaluated similarly as by Stougie, shown in Equation 4.2[14].

$$\text{CS}_{activity} = \frac{\int_0^T |\delta_{CS}| dt}{T} \tag{4.2}$$

4.2.2. Gain and Phase margin

Gain and phase margins are metrics to evaluate the stability of a system [86]. An implementation similar to that of Stougie will be taken, where the system transfer function will be calculated for the approach and cruise flight conditions, from which bode plots can be made. The gain and phase margins are taken from these bode plots, where the phase margin is defined as the phase difference, $\varphi[deg]$, compared to a phase of -180 °, at the cross-over frequency. Furthermore, the gain margin is the difference between the 0 dB cross-over line and the magnitude of the signal at which the phase crosses -180 °. For level 1 specifications, a general rule is that the gain margin should be higher than 6 dB, and the phase margin should be at least 45 ° [32]. These margins are taken in the controller system, shown in Figure 3.8, at the virtual command error signal after the summation of the inner-loop, before the INDI CA.

4.2.3. Low Order Equivalent System

To obtain the CAP and short-period parameters, the LOES has to be acquired. Stougie has described this in great detail [14]. From the linearisation of the nonlinear controller system, a linear High Order Equivalent System (HOS) is acquired, using the Control System Toolbox from MATLAB ®[1]. To assess the required HQ, the HOS has to be reduced to a LOES, from which the metrics that will be evaluated are acquired. It has to be fit for both the longitudinal and lateral dynamics within a frequency range from 0.1 - 10 rad/s [32]. For the longitudinal fit, the pitch rate and load factor are combined into a single fit [32]. The load factor, $n_z^{'}$, is taken at the CoG [32]. For the lateral LOES, the bank angle and sideslip angle systems from a pilot aileron input are given in Equation 4.4. Stougie used these reductions and described a method to validate the fitting of the LOES to the full, HOS using MUAD [14]. MUAD describes the region for the pilot in which the handling qualities are unchanged, even though the dynamics change, which is shown in Table 4.4 [87]. All the parameters in Equations 4.3 and 4.4 are unknown and will be approximated using a fitting function, as shown in Equation 4.5. The fitting function compares magnitudes, $G[db]$, and the phase, $\varphi[deg]$ for the HOS and LOES and minimizes the difference, thus finding the parameters. As Stougie found, the frequencies for the pilot are most relevant around 1-4 rad/s, for which specific weights were set to highlight the frequency fit around those frequencies [14].

$$\frac{q(s)}{\delta_{es}(s)} = \frac{K_\theta s\left(s+\frac{1}{T_{\theta 1}}\right)\left(s+\frac{1}{T_{\theta 2}}\right)e^{-\tau_e s}}{\left(s^2+2\zeta_{ph}\omega_{ph}s+\omega_{ph}^2\right)\left(s^2+2\zeta_{ph}\omega_{ph}s+\omega_{sp}^2\right)} \quad \text{and}$$
$$\frac{n_z'(s)}{\delta_{es}(s)} = \frac{K_n\left(s+\frac{1}{T_{h1}}\right)e^{-\tau_n s}}{\left(s^2+2\zeta_{ph}\omega_{ph}s+\omega_{ph}^2\right)\left(s^2+2\zeta_{ph}\omega_{ph}s+\omega_{sp}^2\right)} \tag{4.3}$$

$$\frac{\phi}{\delta_{as}} = \frac{K_\phi\left(s^2+2\zeta_\phi\omega_\phi s+\omega_\phi^2\right)e^{-\tau_{e_p}s}}{\left(s+\frac{1}{T_s}\right)\left(s+\frac{1}{T_r}\right)\left(s^2+2\zeta_d\omega_d s+\omega_d^2\right)} \quad \text{and} \quad \frac{\beta}{\delta_{as}} = \frac{\left(A_3s^3+A_2s^2+A_1s+A_0\right)e^{-\tau_{e_\beta}s}}{\left(s+\frac{1}{T_s}\right)\left(s+\frac{1}{T_r}\right)\left(s^2+2\zeta_d\omega_d s+\omega_d^2\right)} \tag{4.4}$$

Table 4.4: MUAD envelope [14]

	Upper bound	Lower bound
Gain	$\frac{3.16s^2+31.61s+22.79}{s^2+27.14s+1.84}$	$\frac{9.55\cdot10^{-2}s^2+9.92s+2.15}{s^2+11.60s+4.95}$
Phase	$\frac{68.89s^2+1100.12s-275.22}{s^2+39.94s+9.99}$	$\frac{475.32s^2+184100s+29456.1}{s^2+11.66s+3.89\cdot10^{-2}}e^{-0.0072s}$

$$M = \Sigma\left(\left(GM_{HOS}-GM_{LOES}\right)\cdot w_G M\right)+\Sigma\left(\left(\varphi_{HOS}-\varphi_{LOES}\right)\cdot w_\varphi\right) \tag{4.5}$$

4.3. Stability and Handling Quality Assessment

This Section will cover the stability and HQ assessment criteria commonly used and required by EASA. In previous research, using similar dynamics properties as in this research, the Flying-V HQ requirements were tested and shown below in Table 4.5. The different flight stages are evaluated using Figure 4.1, showing which HQ are relevant for this research, which assesses approach and cruise HQs.

[1] https://nl.mathworks.com/help/control/index.html?s_tid=CRUX_lftnav

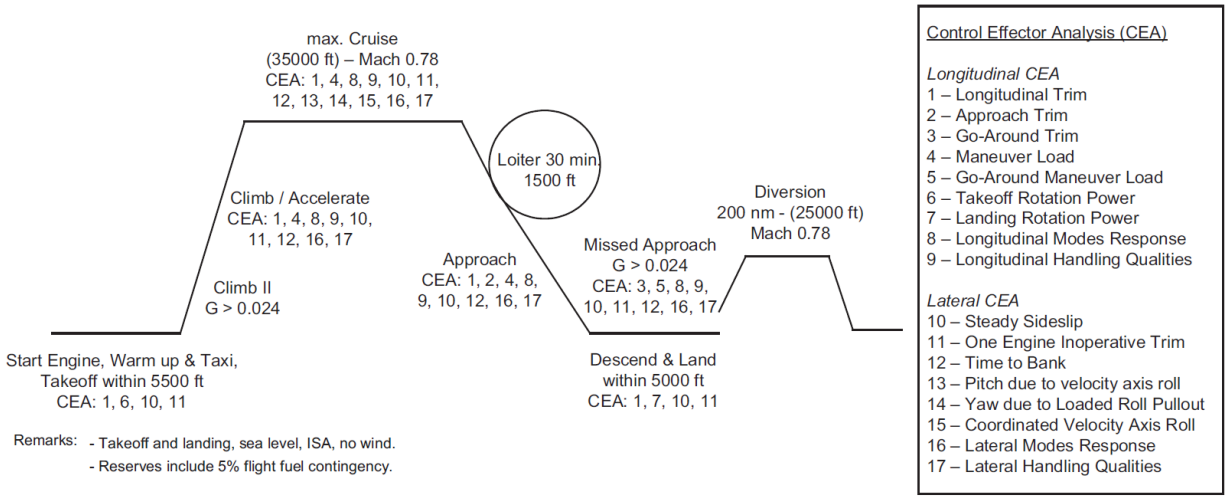

Figure 4.1: Flight stages with a Control Effector Analysis. [88]

Table 4.5: Required Flight Handling Qualities assessed in previous research [4], [10], [11], [13], [14]

Flight Stage	1	2	3	4	5	6	7	8	9	10	11	12	13	14	15	16	17
Cruise Phase	✓			✓				✓	✓	×	✓	✓	✓	✓	✓	✓	✓
Approach Phase	✓	✓		✓				✓	✓	✓		✓				✓	✓

4.3.1. Longitudinal Trim[75, CS25.161(c)]

This criterion is related to the capacity of the aircraft to be trimmed to maintain a steady cruise with a load factor of 1g. This criterion has to be met for both the forward and aft position of the CoG [75], which has been highlighted by Van Overeem [13]. As this handling requirement is not related to controller performance, as it is a steady-state handling quality, it will not be evaluated in this research.

4.3.2. Approach Trim [75, CS25.161(c)]

This criterion is also mentioned in the CS25.161(c) requirements, specifying that trim should be possible for either a glide, with engines off or at approach conditions, with landing gear extended, at a glide path of 3 °, just as with the longitudinal trim handling quality from Section 4.3.1, this handling requirement is not relevant to controller performance and therefore not evaluated in this research.

4.3.3. Go-Around Trim

This handling quality is irrelevant for the cruise of approach phase and thus will not be highlighted in this research.

4.3.4. Manoeuvre Load [75, CS25.143(l)]

As was given previously in Section 3.4.2, this requirement specifies limits for the load factor of the aircraft, which are shown below:

1) The positive limiting load factor must not be less than:
    a) 2.5g for the EFCS normal state.
    b) 2.0g for the EFCS normal state with the high lift devices extended.
2) The negative limiting load factor must be equal to or more negative than:
    a) -1.0g for the EFCS normal state.
    b) 0.0g for the EFCS normal state with high lift devices extended.

4.3.5. Go-Around Manoeuvre Load

This handling quality is irrelevant for the cruise of approach phase and thus will not be highlighted in this research.

4.3.6. Take-off Rotation Power

This handling quality is irrelevant for the cruise of approach phase and thus will not be highlighted in this research.

4.3.7. Landing Rotation Power

This handling quality is irrelevant for the cruise of approach phase and thus will not be highlighted in this research.

4.3.8. Longitudinal Modes Response

Short Period

The short period is an oscillating pitch rate transient response of the aircraft generated by an elevator input. This motion is governed by a natural frequency, ω_{sp}, and a damping coefficient, ζ_{sp}. The short period is quantified using the longitudinal handling quality shown in Section 4.3.9, about the CAP. Furthermore, these eigenmodes have damping requirements, shown in Table 4.6.

Table 4.6: Short Period Damping Criteria [85]

	Level 1		Level 2		Level 3
Flight phase	$\zeta_{s\,\min}$	$\zeta_{s\,\max}$	$\zeta_{s\,\min}$	$\zeta_{s\,\max}$	$\zeta_{s\,\min}$
Cat A	0.35	1.30	0.25	2.00	0.10
Cat B	0.30	2.00	0.20	2.00	0.10
Cat C	0.50	1.30	0.35	2.00	0.25

Phugoid

The phugoid eigenmode is a slow oscillating motion where the aircraft oscillates in pitch attitude. Generally, this mode is satisfactory, but it should be noted that it is desirable to decouple the phugoid and short period by a natural frequency factor of 10, where the natural frequency of the phugoid is small [85]. Table 4.7 gives the damping coefficient requirements. These coefficients are acquired from the LOES.

Table 4.7: Phugoid Damping Coefficient Requirements [85]

Level of flying qualities	Minimum ζ_p
1	0.04
2	0
3	Unstable, period $T_p > 55$ s

4.3.9. Longitudinal Handling Qualities

Multiple resources have provided metrics to evaluate the longitudinal HQ, about which a discussion exists. In 1982, Mitchell et al. [89] proposed a military specification handbook to evaluate HQ for aircraft, especially fighter aircraft. In 1990, the first revision of MIL-STD-1797A was published based on these specifications [85]. Mitchell et al. [90] came up with a revision of the specifications in 1992 and proposed a different interpretation. The Department of Defense followed with several revisions, with revision 3 being the most up-to-date [32] but did not follow up on the recommendations. Therefore, discussion exists about the usefulness of which HQ shall be used and what metrics are considered adequate. In this research, the requirements evaluated by Stougie will be used to validate the control laws. They are described below.

Control Anticipation Parameter (CAP)

As was mentioned in Section 4.3.8, the CAP is a quantifiable measure to see how well the short period is anticipated in the control design. CAP is the instantaneous angular pitching acceleration per unit of steady-state normal acceleration [85]. The CAP is calculated with Equation 4.6. The natural frequency, ω_{sp}^2, and time constant,T_{θ_2}, can be found using the LOES Equation 4.3. T_{θ_2} indicates the lag between the pitch attitude response and the flight path angle response, also known as incidence lag [85]. The requirements and level specifications of the CAP are given in Appendix A, in Figure A.1.

$$CAP = \frac{\dot{q}}{n_{z_{ss}}} = \frac{\omega_{sp}^2}{n_\alpha}, n_\alpha = \frac{V_\infty}{g_0 T_{\theta_2}} \tag{4.6}$$

A CAP, which is considered too low, indicates a sluggish response of the aircraft due to an elevator input, whereas a high CAP gives an unexpectedly fast response [14]. In previous research, Cappuyns [4], Van Overeem [13], Stougie [14] and Torelli [11] all computed the CAP of the Flying-V for approach and cruise. Table 4.8 shows these results, specifying if the Level 1 requirements were met. It should be noted that the flight conditions are used, as shown in Table 2.2. As Cappuyns used V_{TAS} for the CAP evaluation, the Mach numbers are slightly different compared to the others. All research used the same definition given for an aft CoG and forward CoG, which is also used in this research, specified in Table 2.3. Stougie did not include handling quality evaluation on aft CoG flight conditions. Different aerodynamic models were used for the evaluations as well. Cappuyns and Torelli used the VLM, which does not include the pitch break-up.

Table 4.8: Previous CAP evaluations of the Flying-V, checking if level 1 requirements were met

	Forward CoG [45% MAC]	**Aft CoG [57.5% MAC]**
Cappuyns [4] (VLM)		
M ≈ 0.2275	✓	✓
M ≈ 0.847	✓	✓
Van Overeem et al.[13] (VLM+WTE)		
M = 0.2	✓	×
M = 0.85	×	✓
Stougie et al. [14] (VLM+WTE)		
M = 0.2	✓	-
M = 0.85	✓	-
Torelli et al. [11] (VLM)		
M = 0.2	-	×
M = 0.3	✓	-

Gibson's Criteria

Gibson devised a set of criteria to evaluate the aircraft's performance during short-period oscillations. These metrics include the dropback ratio, flight path delay, and pitch rate overshoot ratio [91]. Originating from a pilot's perspective, these parameters can be directly acquired through system responses without needing a LOES [44] , which makes this method especially helpful for non-linear systems.

Figure A.2 visualizes a typical pitch response from which the Gibson criteria can be derived. Firstly, the dropback ratio defined as $\frac{DB}{q_{ss}}$ can be calculated by looking at the pitch attitude response. Dropback is the ratio between the pitch angle when the pilot's stick is released and the steady-state pitch angle. The dropback ratio is the dropback divided by the steady-state pitch rate command before the stick was released. This is shown in Figure A.2 in the bottom figure as DB/q+ and DB/q-, since the dropback can be positive or negative.

Secondly, the flight path delay is a metric to calculate how much the flight path angle lags behind the pitch command. The flight path angle response and the point at which the pitch rate command is started and ended are needed to compute this value. From the flight path angle plot, the slope should be taken at the endpoint of the pitch rate command as a function of time, barely touching the flight path response. If this slope is taken to the intersection with the x-axis, the point at which the pitch rate command is given is compared to where the slope intersects with the y-axis, which is the flight path delay. Gibson relates the flight path angle delay to the short period and the time constant, T_{θ_2}, by the relation in Equation 4.7. Stougie has evaluated the flight path delay in the form of the bandwidth of the flight path, ω_{BW_γ}. This bandwidth is defined as $1/T_{\theta_2}$ [90].

$$t_\gamma = \frac{2\zeta_{sp}}{\omega_{sp}}, \quad T_{\theta_2} = \frac{DB}{q_{ss}} + t_\gamma \tag{4.7}$$

Lastly, the step response properties are governed by the same metrics as shown in Section 4.2. These are shown in Figure A.2. The interesting properties are the maximum pitch rate q_m, at time, t_q, and the steady

state value of the pitch angle with a steady state time.

The Gibson criteria are verified by Stougie et al. [14], using the metrics shown above, and validated using the proposed incorporation of the MIL-STD-1797A by Hoh et al. [90]. These requirements are shown in Figure A.3. Stougie concluded that all requirements achieved level 1 HQs [14].

Pitch attitude Bandwidth

Bandwidth can be defined as the maximum frequency at which a closed-loop tracking task can be completed in a stable manner. Within aviation, a proper method to specify bandwidth is when the phase, φ_{BW} is $\geq$ -135° and the gain margin, ω_{BW} is $\geq$ 6dB [32].

To assess whether the bandwidth is sufficient, it is compared to the bandwidth time constant, calculated using Equation 4.3.9[32]. Here the ω_{180} is frequency at which the phase, φ_{BW}, = -180 °. Furthermore, $\varphi_{2\omega_{180}}$ is the phase at twice the frequency of ω_{180}.

$$\tau_p = -\frac{(\varphi_{2_{\omega_{180}}} + 180°)}{57.3 \cdot 2 \cdot \omega_{180}}$$

NOTE: if phase is nonlinear between ω_{180} and $2\omega_{180}$,
τ_p shall be determined from a linear least squares
fit to phase curve between ω_{180} and $2\omega_{180}$ [90]

Previous research makes it unclear how this requirement shall be evaluated regarding opening the control loops. MIL-STD-1797A specifies it as an open-loop, pilot-in-the-loop requirement, suggesting opening the controller system's inner and outer feedback loop [32]. However, from different literature, the following statement was given by Hodgkinson et al. [92], partly representing the group that documented the bandwidth criterion in Mitchell et al.[89]:

> "The responses on the left side of Figure 1 are 'open-loop'. That is, they depict the aircraft's response to the pitch response error perceived by the pilot. When the pilot operates on the errors, the 'closed-loop' responses on the right depict the aircraft's response to a target elevation change."

Figure A.4 shows what Hodgkinson et al. are referring to as the left and right sides of the figure, which leaves us to believe that the open-loop requirement, as indicated by MIL-STD-1797A, uses, in fact, a closed-loop FCS from which the pilot follows an open-loop tracking task.

Next, Gibson [93] highlights the inconsistency with the MIL-STD-1797A[32] and Mitchel et al., the founders of the bandwidth criterion [90] and concludes that the Gibson dropback ratio and pitch rate overshoot ratio are more consequential for acceptable bandwidth, compared to the pitch bandwidth. Figures A.6 and A.5 show the inconsistency between the two requirements. This research will evaluate the bandwidth criterion to compare with Stougie. Stougie specified a minimum bandwidth for level 1 HQ of $\omega_{BW} = 3$rad/s and maximum equivalent time delay of $\tau_{p,max} = 0.12$s; however, these metrics are not found in either the specified boundaries in MIL-STD-1797A and the revision of Mitchell et al. As MIL-STD-1797A does not specify boundaries for Category B flight phase, but only for Category A and C flight phases, which is needed for cruise evaluation, the revision data from Mitchell et al. is used [90]. Figure 4.2 shows the relevant boundaries of the bandwidth and equivalent time delay requirement.

As discussion exists about the interpretation and usefulness of this HQ, other longitudinal HQ are also evaluated. Stougie found that with his implementation, the bandwidth is satisfactory for level 1 handling requirements [14], which also holds for the newly defined boundaries of the HQ.

4.3.10. Steady Sideslip [75, CS25.177(c)]

During the steady heading sideslip maneuver, the aircraft must maintain a fixed sideslip angle while proceeding along a straight trajectory. This performance must be demonstrated under all operational states of the aircraft, including scenarios where all engines are functioning and in One Engine Inoperative (OEI) scenarios. For a majority of aircraft, a sideslip angle of $\beta = 15°$ is typically considered adequate [75].

Joosten et al. concluded that with the implementation of a linear FCS, there was a lack of cross-control required during the maneuver, which was found unconventional by the test pilots [10]. This requirement will be tested to track the sideslip angle using a step input, however the OEI test scenario will not be tested.

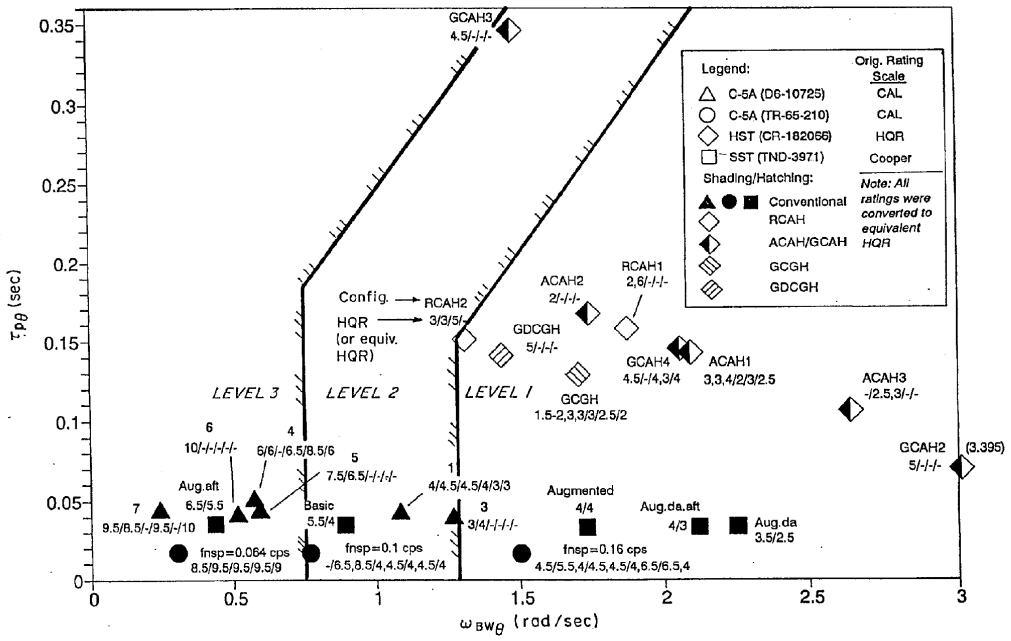

Figure 4.2: Bandwidth Criteria as per Mitchell et al.[90]: Categories B and C, Classes I, II, and III

4.3.11. One Engine Inoperative [75, CS25.161(d)]

In a OEI condition, an engine malfunction is simulated, where the aircraft should maintain its trim in longitudinal and lateral direction. The lateral trim for the bank angle shall not exceed 5 ° and the $V_{TAS} = 1.3V_{SR1}$, which indicates the stall speed of the aircraft with maximum landing weight with flaps in the approach position [75].

Previous research by Joosten et al. concluded that with the implementation of a linear FCS, this maneuver is passed [10]. The current simulation model inadequately represents the engine model and controller system, and as improving its accuracy falls outside the scope of this research, this requirement will not be evaluated.

4.3.12. Time to Bank [75, CS25.147(f)]

This requirement specifies a bank-to-bank maneuver where the aircraft is tested in agility. It specifies that the aircraft should be in a 30 ° banked turn and rolled to the other side in a 60 ° roll maneuver, which should be done under 7 seconds. The rudder may be used to get rid of any sideslip. This requirement is specified for both the cruise and approach conditions, where in approach condition, the aircraft should be in landing configuration. Before the maneuver, the aircraft shall be trimmed, and this trim condition cannot be changed during the maneuver.

Previous research by Joosten et al. concluded that with the implementation of a linear FCS, this maneuver is passed [10].

4.3.13. Pitch/Coordinated Velocity Axis Roll and Yaw due to Loaded Roll Pullout [75, CS25.143(h)]

These requirements can be coupled, as Perez et al. [88] specified, with the control authority of the control surfaces to a bank angle due to inertial couplings. The handling requirements resulting from this are defined such that the aircraft can make large bank maneuvers in different flight conditions and phases. These requirements are denoted in CS25.143(h) [75] and given in Table 4.9. The ‘asymmetric WAT-Limited‘ thrust setting provides a Weight, Altitude, and Temperature (WAT) combination, where a OEI thrust setting should be able to provide for the minimum climb gradient as specified in CS 25.121 [75].

Table 4.9: Aircraft Coordinated Turn Capability [75]

Configuration	Speeds	Bank Angle	Thrust/Power Setting	Minimum Climb Gradient
Cruise	V_{FTO}	40°	Asymmetric WAT-Limited	1.0%
Approach	V_{REF}	40°	Symmetric for −3° Flight Path Angle	-

In previous research, Joosten et al. [10] have evaluated this parameter for the Flying-V, concluding that with and without a FCS the handling qualities were not sufficient, as unrealistic control surface deflections were needed to sustain this handling quality.

As the OEI requirements are not evaluated in this research, this requirement will not further be assessed.

4.3.14. Lateral Modes Response

This Section will cover the relevant lateral mode response requirements for aperiodic roll, spiral mode, and dutch roll.

Aperiodic Roll

The first lateral eigenmode that will be considered is the aperiodic roll, also known as the roll subsidence mode, which is a fast eigenmode excited by an aileron input from the pilot[85]. This eigenmode feels like a lag in the response for the pilot and is indicated as T_r from the LOES of the lateral motion from Equation 4.8 [85]. The time constants for handling quality levels are given in Table 4.10 [85]. There are no minimum requirements following from MIL-STD-1797A [32].

Table 4.10: Roll mode time constant [s] maximum values [85]

Flight phase	Level 1, $T_r[s]$	Level 2, $T_r[s]$	Level 3, $T_r[s]$
Cat A, C	1.0	1.4	10
Cat B	1.4	3.0	10

Spiral [32, Sec 4.5.1.2]

The spiral mode is an eigenmode characterized by a gradual increase in bank angle after a disturbance. In a stable spiral mode, it naturally returns to level flight following an initial roll disturbance. In contrast, if the spiral mode is unstable, the roll angle will progressively increase in response to such a disturbance. The spiral mode is allowed to be unstable, as long as the time to double in amplitude of the movement is longer than 20 seconds, for Level 1 qualities [32]. The given requirements are shown in Table 4.11 and the relation between the doubling amplitude and the time constant T_s from the LOES of the lateral motion from Equation 4.8 [53].

$$T_2 = -T_s \ln(2) \tag{4.8}$$

Table 4.11: Spiral Mode Handling Requirements [32]

Flight Phase Category	Level 1 T_2 [s]	Level 2 T_2 [s]	Level 3 T_2 [s]
A and C	12	8	4
B	20	8	4

Dutch Roll [32, Sec 4.6.1.1]

The Dutch roll is a coupled yaw and roll movement, introduced by a disturbance in the sideslip, introducing a yawing motion, which is then translated into a rolling motion [85]. As can be seen in the LOES approximation from Equation 4.4, the Dutch roll damping, ζ_d and eigenfrequency, ω_d, are both relevant, and the combination of both also is given in the requirements in Table 4.12

Table 4.12: Dutch roll Level 1 flying quality requirements [85]

Flight phase	ζ_d	$\zeta_d\omega_d$	ω_d
Cat A	0.19	0.35	0.5
Cat B	0.08	0.15	0.5
Cat C	0.08	0.10	0.5

4.3.15. Lateral Handling Qualities

The lateral handling qualities will be evaluated similarly to the longitudinal handling qualities in number 9.

Lateral Control Departure Parameter [32, Sec 4.8.4.3.1]

The Lateral Control Departure Parameter (LDCP) has been introduced to prevent aircraft resistance to uncontrollable spinning of the aircraft [32]. Therefore, the LDCP depends on the rolling and yawing moment responses to a sideslip disturbance introduced by an aileron input. Equation 4.9 shows the handling quality requirement, which essentially has to be larger or equal to zero [32]. Therefore, this requirement cannot be influenced by the FCS and will not be evaluated in this research.

$$\text{LCDP} : C_{n_\beta} - C_{l_\beta} \frac{C_{n_{\delta a}}}{C_{l_{\delta a}}} > -0.001 \tag{4.9}$$

Directional Control [75, CS25.147(a)]

With the wings level, it should be possible with an OEI situation, yaw in the direction of the inoperative engine, with a change of heading angle up to 15 °, which must be done for $1.3V_{SR1}$. As this requirement includes an OEI situation, this research does not further evaluate it.

4.4. Conclusion

This chapter discusses the different methods used to evaluate the performance of a flight control system, which is used to answer research question 1. Two conceptual methods will be implemented to assess the FCS: stability and handling quality assessment. The overshoot, settling time, control input activity, and maximum control input are evaluated to assess the controller's stability. Minimization is desirable for these metrics, but no strict requirements are present. The handling qualities have more design guidelines and requirements. Several requirements were explained, however there shall be a clear distinction to handling qualities that can be improved by a controller or are dependent on the airframe of the aircraft. Only transient responses can be improved by the controller. Thus, some handling requirements necessary for approach and cruise will not be evaluated, partly because they have been validated in previous research. Table 4.13 shows the handling requirements which will be focussed on in this research.

Table 4.13: Required Flight Handling Qualities assessed in this research

Flight Phase	1	2	3	4	5	6	7	8	9	10	11	12	13	14	15	16	17
Cruise Phase	×			✓				✓	✓	✓	×	✓	×	×	×	✓	×
Approach Phase	×	×		✓				✓	✓	✓		✓				✓	×

III

Additional Results

5

Simulation Model Modifications

As described in Section 1, there have been changes between the original and updated models, which seem correct to the author. This chapter will describe what has been changed per sub-part of the original model and why the author believes the updated implementation is the proper method. At the end of the chapter, a side-by-side comparison the evaluated HQs is shown in Table 5.1, showing the difference in response. The changes to the C^* controller are part of the model modifications but have been highlighted in Part I.

5.1. Initial problems with original controller system

It was concluded that the aircraft had unexpected behavior during a testing run within the SIMONA Full-Flight Simulator using the original controller system [94]. Firstly, when the flight path angle, γ would be kept constant the aircraft's altitude was decreasing. Secondly, when giving a sideslip command, the angle would not exceed $\beta \approx 3\ ^\circ$. Lastly, the test pilots noticed an aggressive response to throttle changes. These problems indicate problems with the simulation model, for which changes had to be made to make the simulation model more mature.

5.2. Sensor subsystem

This Section will discuss the changes made to the sensor subsystem. The modifications included adjustments to the general sensor dynamics, changes to body acceleration filtering, changes to body acceleration measurements, and changes to altitude estimation.

5.2.1. Sensor dynamics subsystem

A noticeable aspect when linearizing the controller system was the low gain drop-off at high frequencies. When investigating this problem, it was concluded that the sensor dynamics block gave an incorrect frequency response when linearizing it to continuous time. The baseline model is a continuous-time first-order sensor dynamics model with a continuous-time delay block and a first-order pade approximation. Figure 5.1a and 5.1b show the time and frequency response of the continuous time sensor dynamics with delay, updated sensor dynamics with delay and original sensor dynamics with delay. The gain drop-off of the original sensor dynamics is incorrect, which gives overestimated gain margins at higher frequencies. Furthermore, Figure 5.1a shows the original sensor dynamics leads compared to the continuous system dynamics.

5.2.2. Body rate acceleration state estimation

Within the original controller system, the body rate acceleration is needed as a feedback signal for the INDI inner loop. Stougie et al. calculated this estimation by filtering the body rate sensor measurement using a second-order filter, for which the visual representation is shown in Figure 5.2. This implementation indicates that the filter, a part of the FCS, can distinguish between the measured signal's delay and the measured signal's dynamics, which is not the case. The updated implementation places the input signal of the second-order filter for $\dot{\boldsymbol{x}}_{meas}$, which represents the body acceleration state vector after the sensor dynamics.

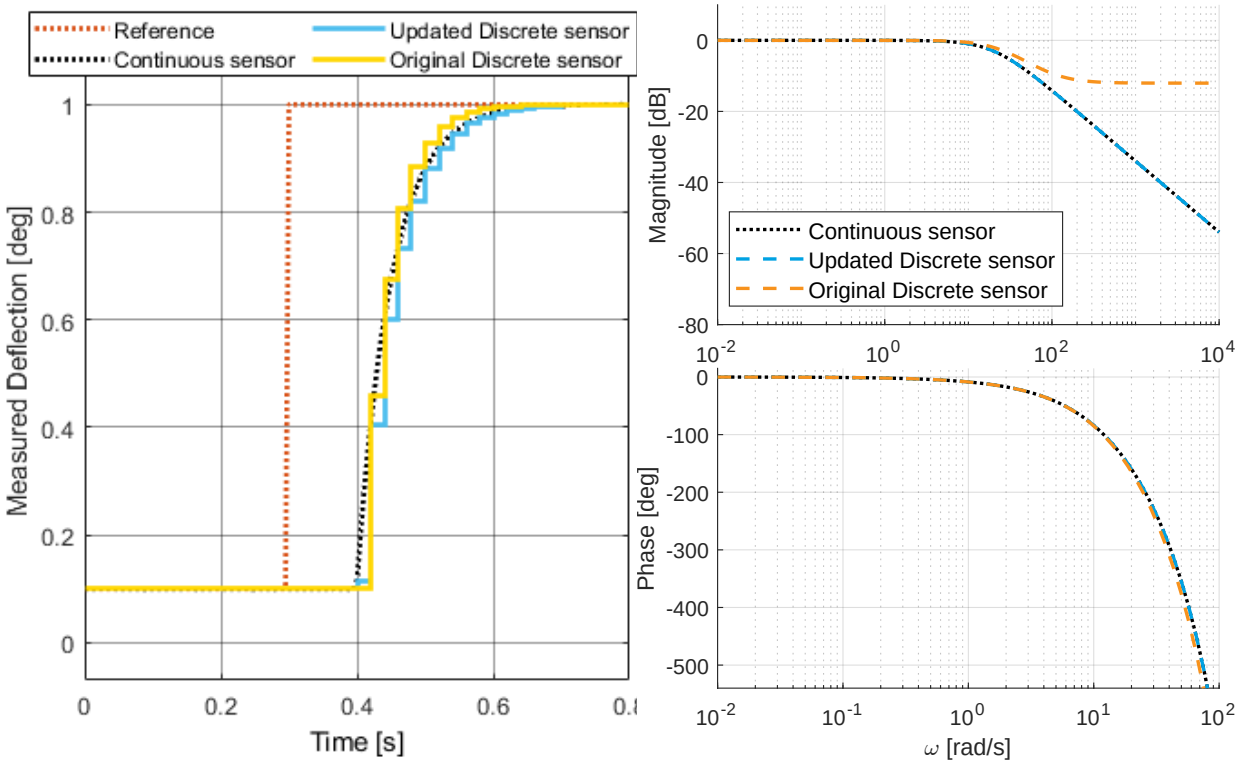

(a) Time-domain step response of different sensor dynamics

(b) Frequency-domain step response of different sensor dynamics

Figure 5.1: Sensor dynamics response for continuous model, original and updated discrete dynamics

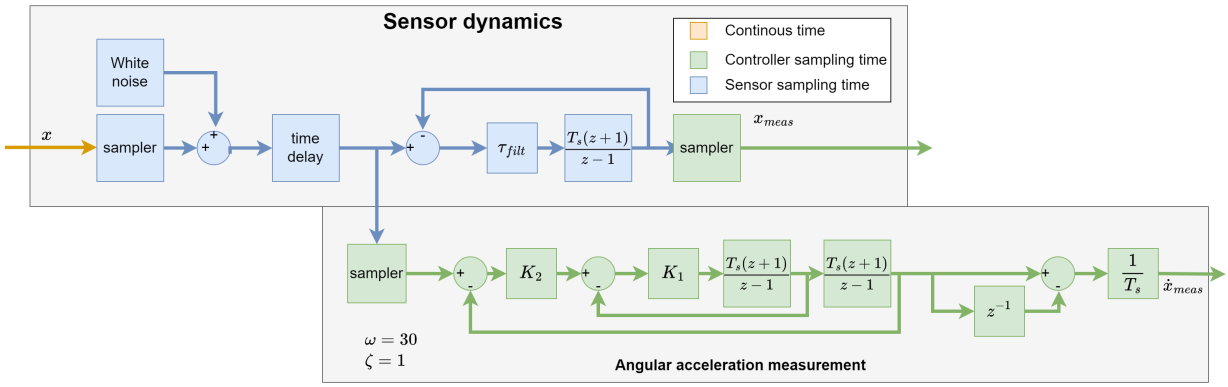

Figure 5.2: Sensor dynamics and body acceleration estimation [14]

5.2.3. Body acceleration measurement

Within the original controller system, it was assumed the body accelerations would be measured directly, excluding their respective gravity components. However, in physical linear accelerometers, the gravity component of the measurement cannot be distinguished from the body accelerations. As the body acceleration measurements are an essential part of the FCS, as they are used for load factor feedback and pitch eigenmode estimation, the computation of the body accelerations must be done as realistically as possible. Therefore, the accelerations that are measured by the accelerometer at point p(x,y,z) from the CoG are shown in Equation 5.1 [85]. However, these will be composed of the gravity component, so when the incremental body acceleration, which will be zero in steady flight, the gravity vector shown in Equation 2.7 is added to Equation 5.1. The addition of the gravity vector will add noise and bias, as the measured Euler states are used for this estimation.

$$
\begin{aligned}
a'_x &= \frac{F_{x,\mathcal{B}}}{m} - x\left(q^2 + r^2\right) + y(pq - \dot{r}) + z(pr + \dot{q}) \\
a'_y &= \frac{F_{y,\mathcal{B}}}{m} - y\left(p^2 + r^2\right) + z(qr - \dot{p}) \\
a'_z &= \frac{F_{z,\mathcal{B}}}{m} + y(qr + \dot{p}) - z\left(p^2 + q^2\right)
\end{aligned}
\tag{5.1}
$$

5.2.4. Altitude estimation

In the original controller system, the altitude of the aircraft was calculated by Equation 5.2, while the coordinate $Z_{\mathcal{E}}$, was set to zero.

$$h = \frac{1}{s}(V_\infty * sin(\gamma)) = \frac{1}{s}(V_\infty * sin(\theta - \alpha)) \tag{5.2}$$

which assumes that $\gamma = \theta - \alpha$. The statement is generally considered valid, but it assumes small angles for θ and α. When we remove this assumption and take $Z_{\mathcal{E}}$ for the altitude, which holds for a flat earth, we resolve the problem of an altitude change when γ is zero.

5.3. Flying-V Dynamics subsystem

This Section will highlight the changes to the Flying-V dynamics subsystem. Firstly, the aerodynamic coefficients are interpolated using the aerodynamic data sets described in Section 2.7. However, upon further investigation, the interpolation for CS1 was not interpolated across the AoA data points, giving too high estimations of the control surface effectiveness. This was done consistently across the aircraft dynamics, CA subsystem, and PCH. Next, actuator library blocks from the Aerospace Blockset from MATLAB SIMULINK® [1] are used in the updated model, where there was a minor difference compared to the original model, regarding the rate saturation.

Lastly, the Dynamics subsystem consisted of multiple Zero-Order-Hold (ZoH) signals, as otherwise, there would be an algebraic loop. However, these were unnecessary when the wind coordinates, α and β, would be calculated continuously. These were initially calculated using the body velocities in discrete time, which led to feeding back discrete states into a continuous time state estimation of the aerodynamic coefficients.

5.4. General changes

This Section highlights changes to the original model, which were found during the development of the updated INDI model. Firstly, as was stated in Part I, the distance from the CoG to the pilot station was previously miscalculated. The distance from the nose to the CoG has been given to be 29.372 m for 47.5% MAC [13]. The distance from the nose to the cockpit is provided to be x_{pilot} [13], but this distance was taken as the distance from the pilot station to CoG, whereas this should be x_a = 22.9474 m.

Next, the gain for the speed control has been reduced from K_T = 100000 to K_T = 20000. The scope of this research was not to improve the thrust control; however, with the original gain, an error of 1 m/s for V_∞ resulted in an additional $\approx$ 30 % of max thrust. Therefore, reducing it seems reasonable, but no further research has been done on speed control.

5.5. Original INDI and Updated INDI control system comparison

The updated INDI control system is created using the abovementioned changes. The resulting HQ results have been listed in Table 5.1, where the gains have been kept the same, but the model structure has changed. The test cases have been made the same as those from research from Stougie to make a direct comparison.

Table 5.1 shows the changes in HQ requirements and step response tests for cruise condition. It can be concluded that the sideslip problem has been solved, where the model at least comes to a steady state sideslip of $\beta = 15°$, albeit after t=165s. It is interesting to note, that the changes improve the stability of the aircraft looking at the stability margins.

[1] https://www.mathworks.com/products/aerospace-blockset.html

Table 5.1: Tuned Cruise Condition for INDI with adjusted sensor configuration

(a) Longitudinal MIL-STD-1797A handling quality requirements

Description	Original	Updated
Response to C^* step command of 1.8 at t = 1 s, T_{sim} = 20 s		
OS [%]	10.86	5.893
ST [s]	3.800	3.950
$CS_{activity}$ [deg/s]	5.533	17.69
CS_{max} [deg]	13.01	15.50
Linear Analysis		
GM q [dB]	6.12	7.864
PM q [deg]	37.40	45.97
ω_{sp} [rad/s]	2.348	4.583
ζ_{sp} [-]	1.14	1.173
CAP [$g^{-1}s^{-2}$]	0.09488	2.092
ω_{BW} [rad/s]	2.713	2.09
τ_p [s]	0.0251	0.184
$score_{LOES}$ [-]	15.85	11.73

(b) Lateral MIL-STD-1797A handling quality requirements

Description	Original	Updated
Response to $\dot{\phi}$ block command of $\pm 3^\circ$ at t = 1 s until t = 14s, T_{sim} = 18 s		
OS [%]	81.34	71.07
ST [s]	2.865	3.165
$CS_{activity}$ [deg/s]	14.364	23.34
CS_{max} [deg]	9.294	19.93
Response to β step command of -15° at t = 1 s, T_{sim} = 120 s		
OS [%]	56.00	0.1656
ST [s]	∞	165.0
$CS_{activity}$ [deg/s]	16.170	12.28
CS_{max} [deg]	30	25
Linear Analysis		
GM p [dB]	7.872	7.686
PM p [deg]	46.00	45.14
GM r [dB]	6.591	7.479
PM r [deg]	39.82	44.17
$\frac{1}{T_s}$ [s^{-1}]	0.06358	7.698 $\times 10^{-4}$
T_r [s]	0.9427	0.1993
ω_{dr} [rad/s]	2.620	1.533
ζ_{dr} [-]	0.3891	0.6784
$\omega_{dr}\zeta_{dr}$ [rad/s]	1.01942	1.040
$score_{LOES}$ [-]	5.878	3.205

6

Trim Routine

This Chapter will elaborate on the steps to acquire a proper trim condition. The controller system is developed using a non-linear dynamic model, from which a linear approximation is computed at a pre-defined flight condition, approach, and cruise in this research. This linear approximation is computed using the Control System Toolbox from MATLAB ®[1]. The trim condition is crucial, as the linear model uses a state derivative response to compute frequency domain characteristics. If this state derivative is not zero, the results are unreliable.

The original model used a trimming routine, implemented by van Overeem [13], in which reduced EoM were used in combination with the fmincon()[2] function from MATLAB was used to set the state derivatives to zero. However, it was found in this research that this trim routine was not reliable, especially for the approach. The trim states for the original implementation are shown in Table 6.1, with Figures 6.1a and 6.1b showing the aircraft is not in steady-flight.

Table 6.1: Original trim routine at Approach and Cruise

	$m\ [kg]$	**h** $[m]$	M [-]	$\boldsymbol{V_\infty}\ [m/s]$	$\alpha\ [\ deg]$	$CS1_{L/R}[^\circ]$	$CS2_{L/R}\ [^\circ]$	$CS3_{L/R}\ [^\circ]$	$T_{1/2}\ [kN]$
Approach	2.10×10^5	1000	0.204	68.7	23.1	21.4	21.4	0	146
Cruise	2.40×10^5	13000	0.850	250.7	7.06	7.71	7.71	0	68.4

Due to this result, the trimming routine has been changed. Instead of using fmincon(), the findop()[3] routine from MATLAB® has been implemented. This routine uses the Simulink® model, containing the dynamics and specifying the input and output states, limits, and if a state needs to be in steady state. This routine was already in place for the linearisation. Still, it was not implemented correctly, so the initial trim states were improper, and the model's condition was trimmed and not checked. The resulting trimmed states are given in Table 6.2, with the corresponding Figures 6.2a and 6.2b for approach and cruise, respectively.

Table 6.2: Updated trim routine at Approach and Cruise

	$m\ [kg]$	**h** $[m]$	M [-]	$\boldsymbol{V_\infty}\ [m/s]$	$\alpha\ [\ deg]$	$CS1_{L/R}[^\circ]$	$CS2_{L/R}\ [^\circ]$	$CS3_{L/R}\ [^\circ]$	$T_{1/2}\ [kN]$
Approach	2.10×10^5	1000	0.200	67.3	23.3	20.1	21.4	0	268
Cruise	2.40×10^5	13000	0.850	250.8	7.01	6.41	9.40	0	124

[1] https://nl.mathworks.com/help/control/index.html?s_tid=CRUX_lftnav
[2] https://nl.mathworks.com/help/optim/ug/fmincon.html
[3] https://nl.mathworks.com/help/control/ref/dynamicsystem.findop.html

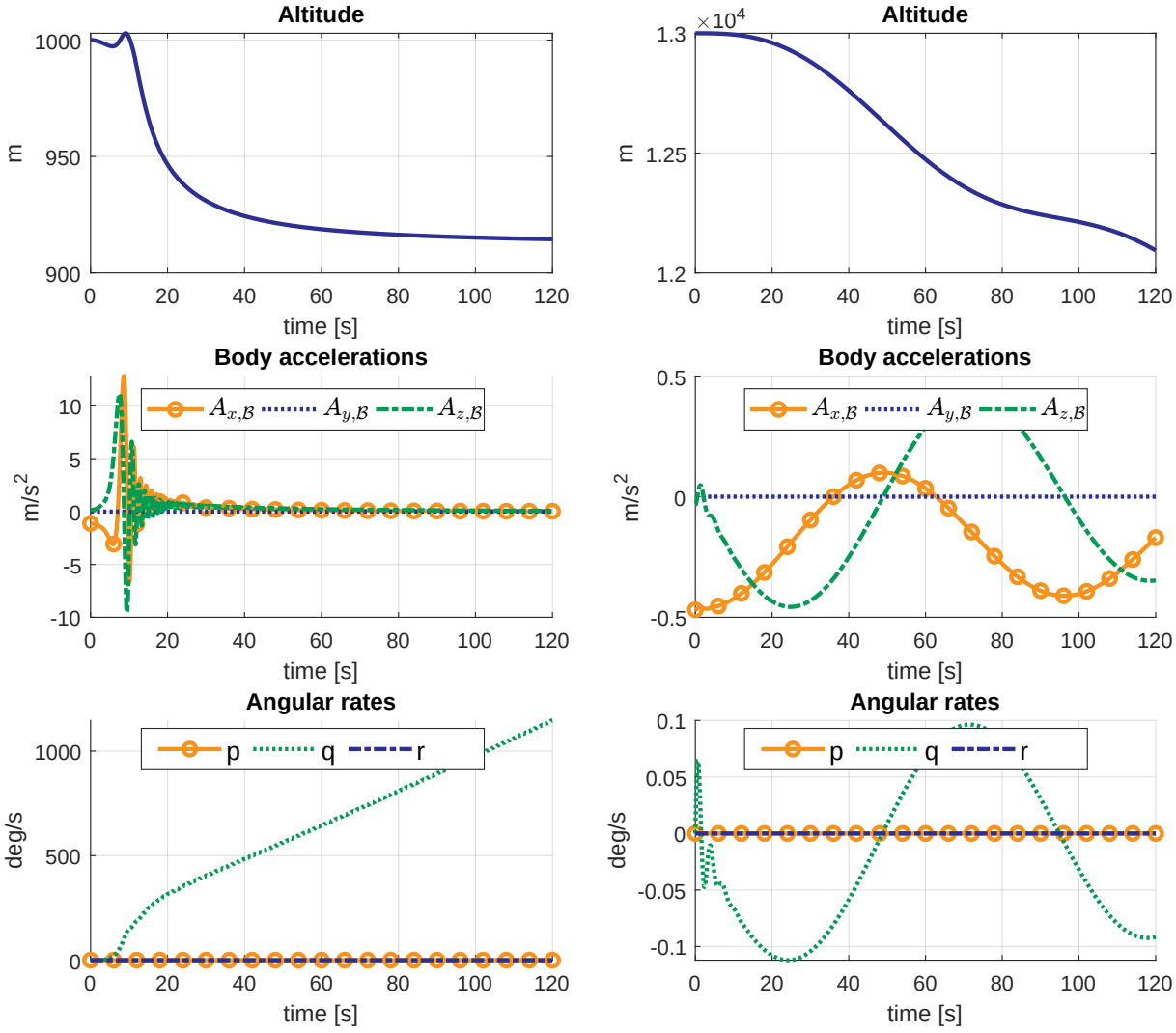

(a) Approach condition of bare-airframe

(b) Cruise condition of bare-airframe

Figure 6.1: Bare-airframe trim test of original trim routine

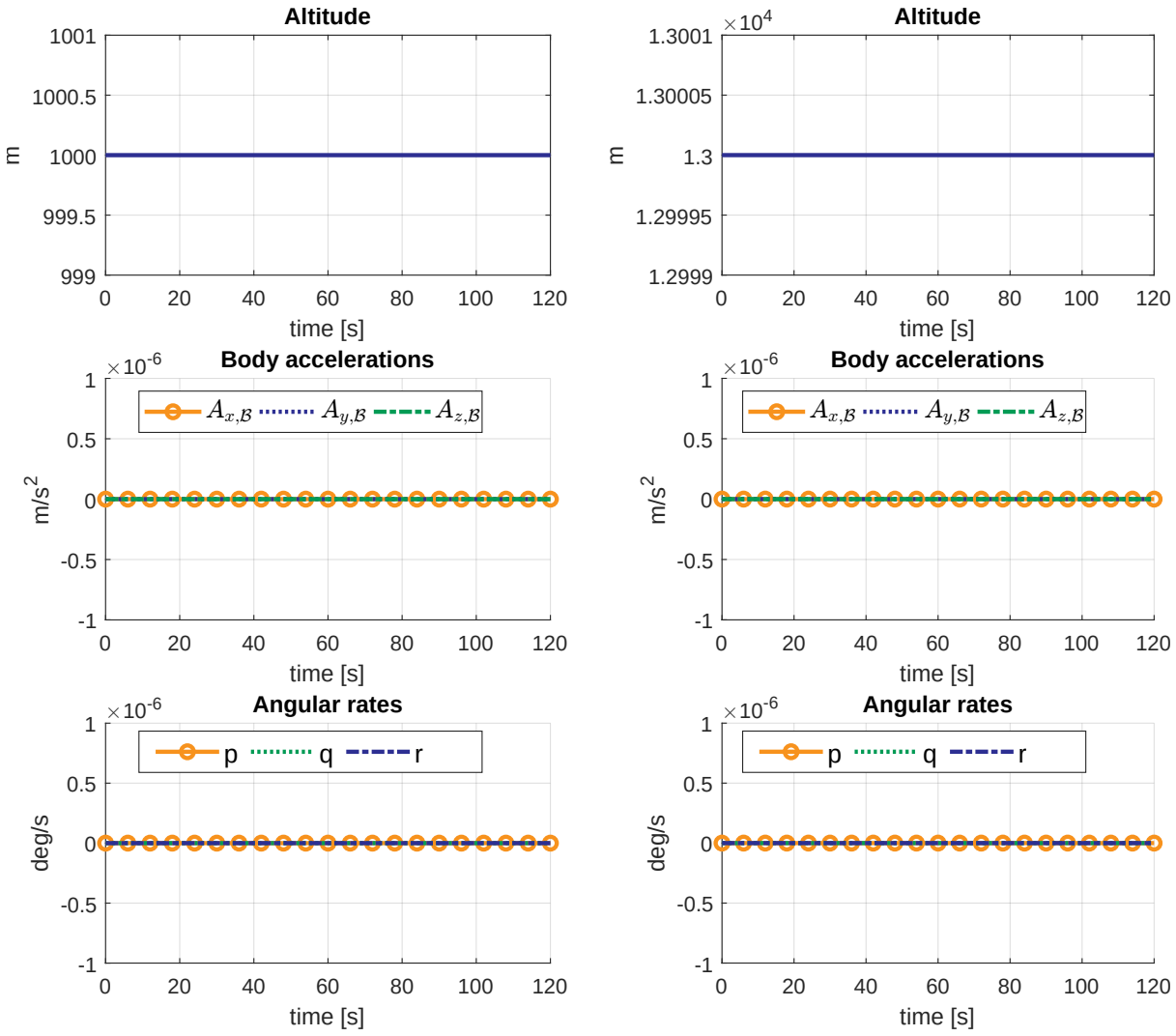

(a) Approach condition of bare-airframe

(b) Cruise condition of bare-airframe

Figure 6.2: Bare-airframe trim test of updated trim routine

7

Linearisation Verification

As described in Chapter 6, the previous trim routine has been changed, as linearising an improper trim result can result in an unreliable linear approximation. Therefore, this Chapter will highlight the verification of the linearisation routine by comparing the step response of the non-linear INDI controller system to the linearised transfer functions for each respective state, shown in Figure 7.1.

As is described in the scientific paper in Part I, the linearised transfer functions, defined as the HOS, are reduced using the LOES approximation from Stougie et al. [14], from which specific HQ requirements are deducted. Therefore, it is crucial to verify the linearization as it forms the basis of the results presented in this research. A proper method for verifying the linear approximation is by comparing the step response of the non-linear and linear systems. The initial response must be accurate, especially since linearization does not capture transient coupled dynamics. As a result, there will be a growing deviation as time increases.

Figure 7.1 shows the response of the Euler angles, wind angles and body rates, following from the pilot command inputs described in the scientific paper and shown below:

- $\dot{\phi}$ block command of $\pm 3^\circ$ at t = 1 - 7s, T_{sim} = 18 s
- C^* step command of 1.8 (ΔC^*= 0.8) at t = 1 s, T_{sim} = 20 s
- β step command of -15° at t = 1 s, T_{sim} = 120 s

Figure 7.1 shows the response to each respective command, where the bold lines represent the non-linear response, dotter line shows the linearised response with the updated trim routine and the dashed line shows the linearised response with the routine from Stougie et al. [14]. Firstly, it can be concluded that the initial transient response of both linear models accurately represent the non-linear response. This is shown, as the dotted and dashed lines, initially coincide with the non-linear response. Furthermore, it can be concluded that the updated trim routine gives a different, but similar response compared to the original trimmed system, from Stougie et al.[14]. Therefore, the initial trim is not as important as was thought initially, however the updated trim routine is prefered.

It can be concluded that the linear models accurately represent the non-linear response, for the tested scenarios and states. Therefore, the linear models can be used for the analyses done in Part I

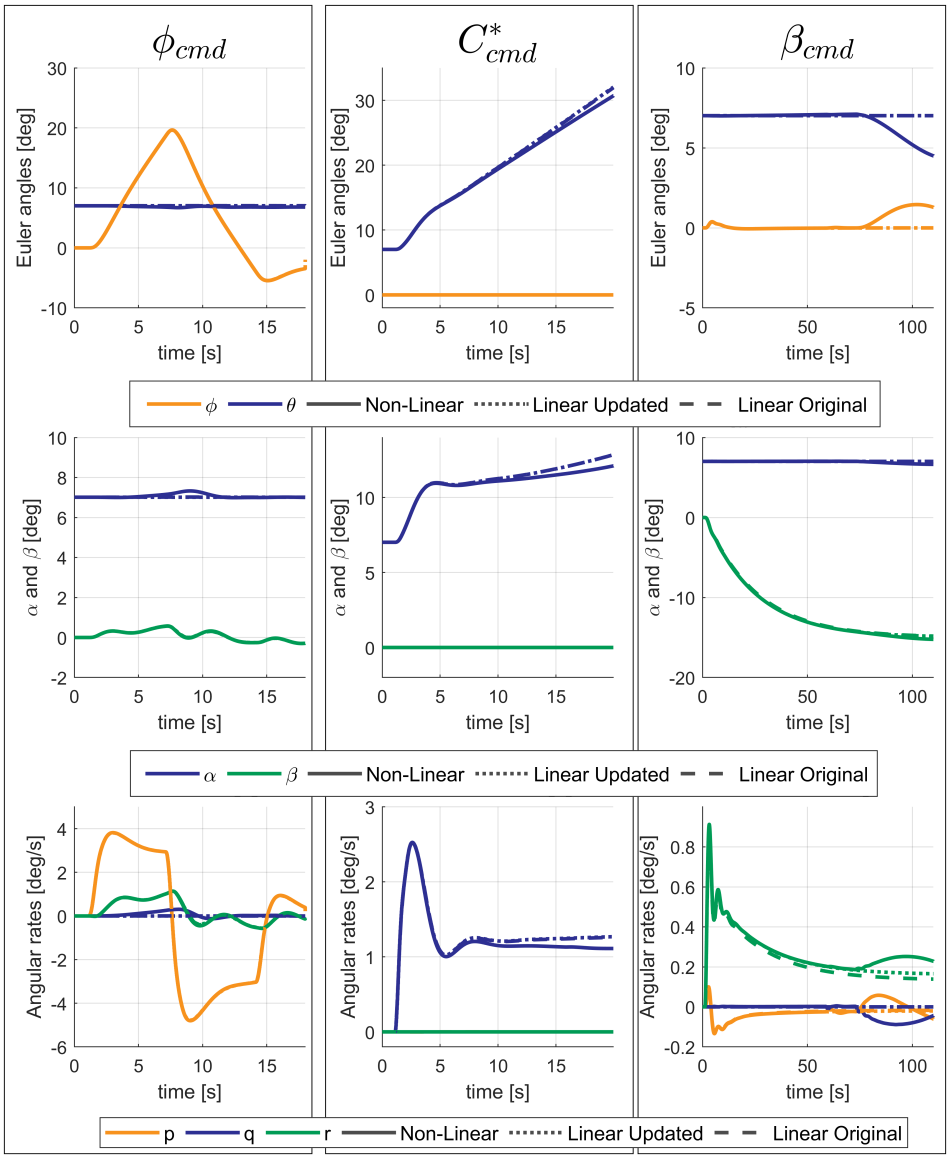

Figure 7.1: Verification of linearisation method using updated INDI model in cruise

8

Additional Handling Quality results

As described in Section 4.3, particular HQ are validated within this research. Most of the stated HQ from this Section have been validated in the scientific paper in Part I, however the results of the Gibson criteria and Time-to-bank have not been evaluated. Therefore, this Chapter shows the results of those HQ requirements.

Looking at Figure 8.1, the relevant time domain response plots are presented to acquire the Gibson criteria requirements, namely:

- Dropback ratio, $\frac{DB}{q_{ss}}$
- Flight path time delay, τ_γ
- Pitch rate overshoot ratio, $\frac{q_{max}}{q_{ss}}$

The dropback ratio is computed by looking at the slope of the pitch angle, making a linear fit to that line, and calculating where this line crosses the y-axis. Next, the flight path angle time delay is calculated using a similar method. The difference between these metrics gives T_{θ_2}. Lastly, the overshoot ratio is calculated by dividing the absolute maximum value after the pilot command by the steady-state pitch rate. Dropback ratio and overshoot ratio are used in Figure A.2a to validate level 1 HQ. Both approach and cruise satisfy this requirement. Table 8.1 shows the results from the Gibson requirement.

Parameter	Approach	Cruise
DB/q_{ss}	0.825	2.02
τ_γ [rad/s]	0.675	0.989
$\frac{q_{peak}}{q_{ss}}$ [-]	1.53	1.91

Table 8.1: Gibson criteria for approach and cruise

Next, Figure 8.2 shows the time to bank requirement, stated by EASA [75, CS25.147(f)]. This requirement set that the aircraft should be able to make a bank-to-bank maneuver from an initial roll angle of ϕ = 30 deg to ϕ = -30 deg. This requirement is met for approach and cruise as is shown in Figures 8.2a and 8.2b, respectively.

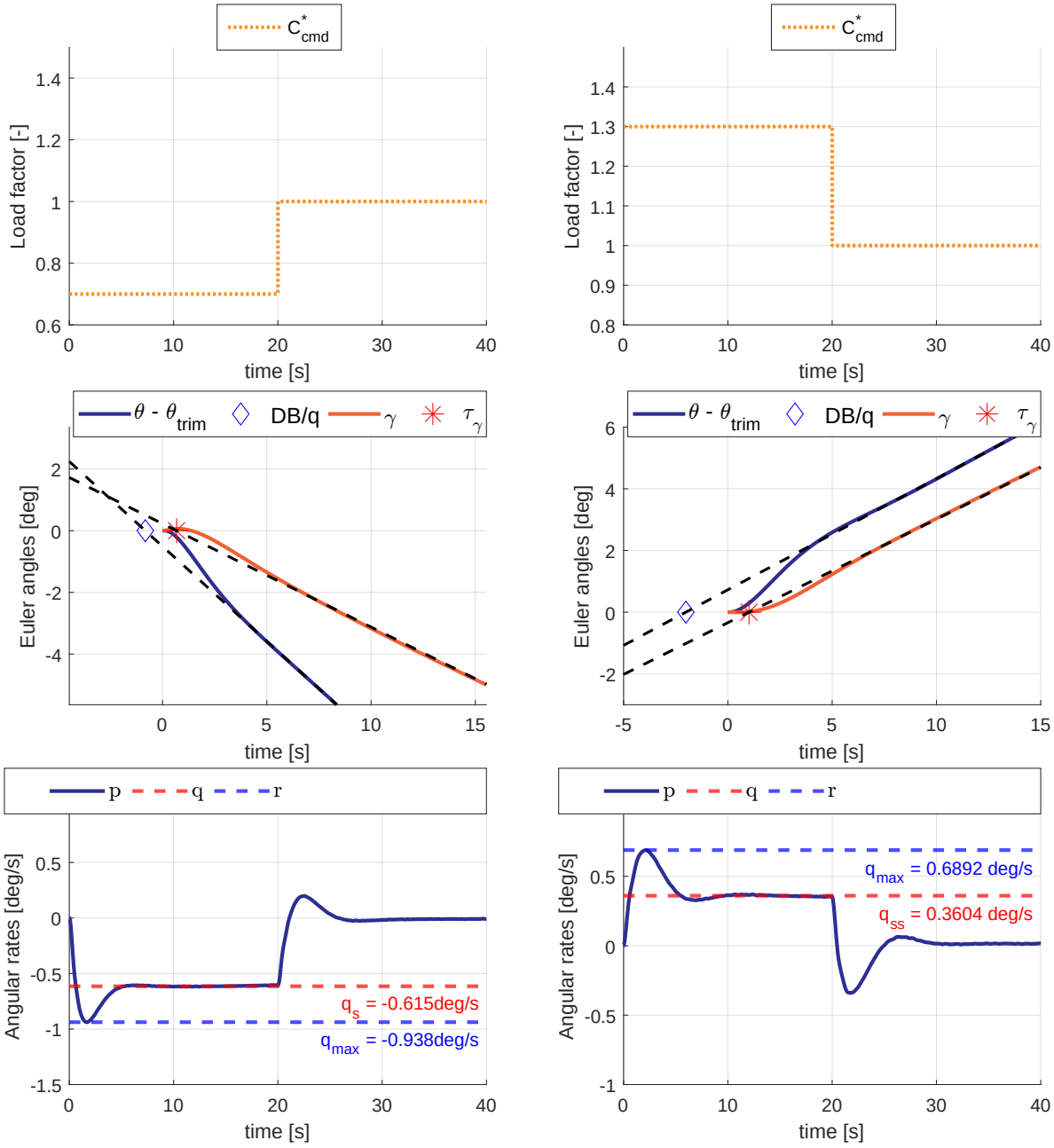

(a) Gibson approach condition, result to C^*_{cmd} = 0.7 from t=0s until t=20s

(b) Gibson cruise condition, result to C^*_{cmd} = 1.3 from t=0s until t=20s

Figure 8.1: Gibson criteria results in approach and cruise condition

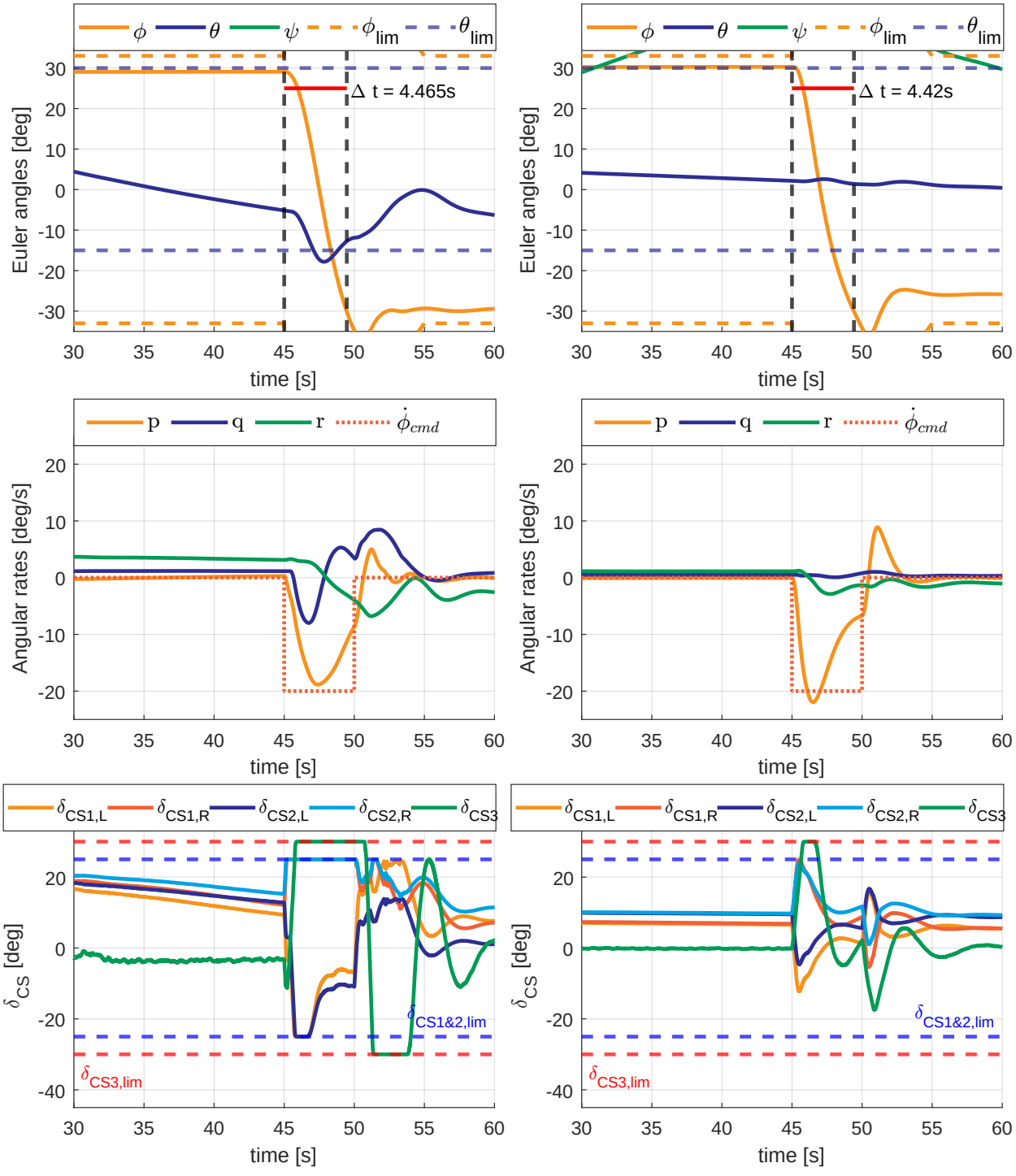

(a) Bank to bank in cruise, t = 4.465s

(b) Bank to bank in cruise, t = 4.420s

Figure 8.2: Bank to bank HQ requirement for approach and cruise

9

Additional Hybrid INDI uncertainty results

This Chapter shows additional results, based on conclusions in the scientific paper in Part I, regarding the influence of uncertainties. The Hybrid INDI model was shown to be fault tolerant to at least 80% of uncertainty combination for the given 750 samples. Figure 9.1 shows the approach condition's respective uncertainty step response figures. Starting with Figure 9.1a, the load factor is less dominant at approach condition, as is described in Section 3.3.1, whereas the pitch rate is higher, compared to the cruise condition shown in the paper. There are, however, more oscillations in the control surfaces, and the magnitude of the control surface deflections is higher compared to cruise, as the control surface effectiveness is lower for approach condition.

Looking at Figure 9.1b, the tracking of roll rate, p, is more oscillatory compared to the cruise condition. It seems as if the tracking is not correct, however this is related to the difference between $\dot{\phi}$ and p being larger with larger θ. For approach θ is almost three times as large in trim as cruise. The rudder deflections, $CS3$, exceed the limits, but as these results are derived from linearised transfer functions, these limits are not included in the transfer function.

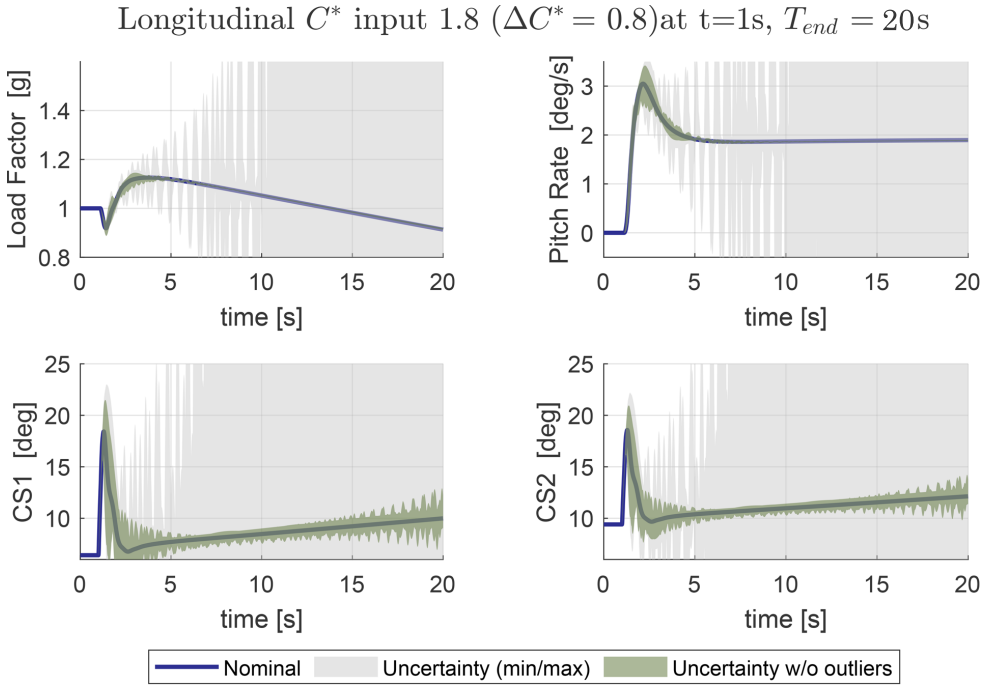

(a) Step response C^*_{cmd}

Next, comparing the sideslip response, looking at Figure 9.1c, and the paper, the comparison is similar to the $\dot{\phi}$ step response. In approach, the control surface deflections are higher due to lower control surface

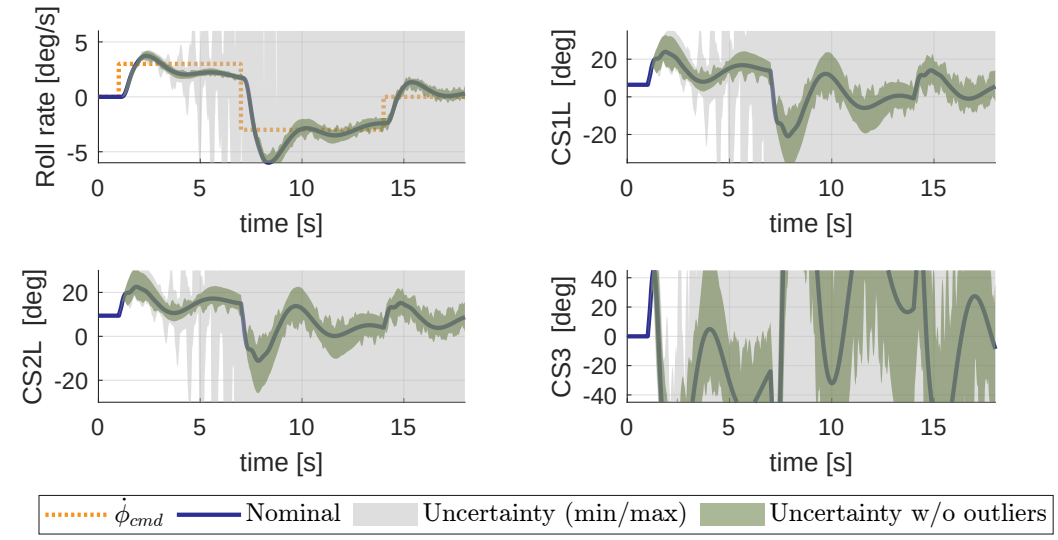

(b) Step response $\dot{\phi}_{cmd}$

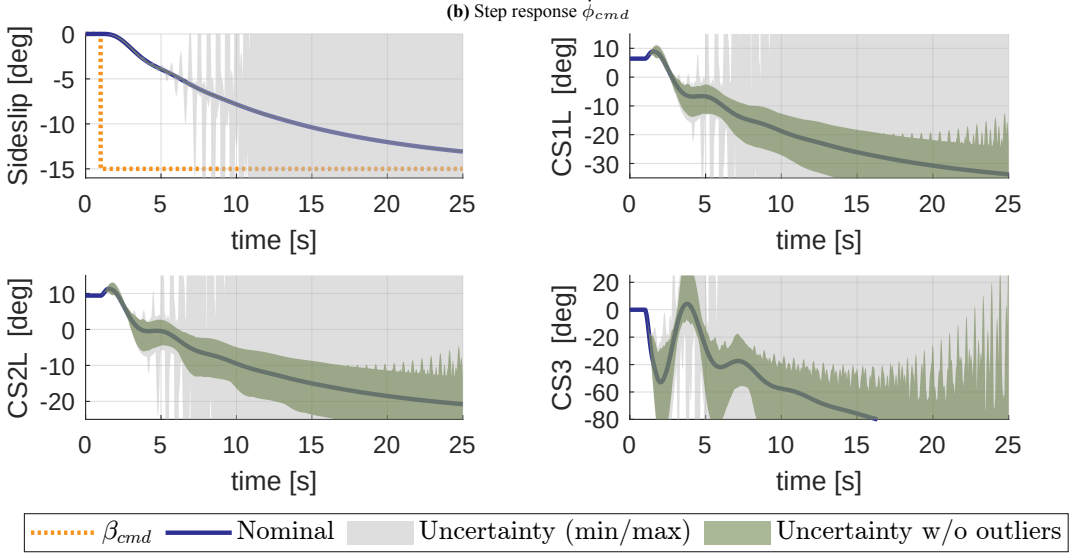

(c) Step response $\dot{\phi}$ including all defined uncertainties, 750 Samples

Figure 9.1: Step response at Approach condition, 750 Samples of uncertainty parameters

effectiveness, and the rudder deflections exceed the nominal limit. The uncertainties hardly influence the β response, and the controller settles slower than the cruise condition.

Figure 9.2 shows the uncertainty impact in the frequency domain for the approach condition, similar to the paper for the cruise condition. Especially the aerodynamic uncertainty has a significant effect on the stability margins. The other uncertainty boundaries are identical, compared to the cruise condition, however, at approach, it is important to be less reliant on model information as aerodynamic mismatch can rapidly decrease performance.

Lastly, Figure 9.3 shows the boxplot for the HQ uncertainties for approach. The general trend is similar to the boxplot in the paper for cruise condition. HQs which are not met for the nominal system, show that the median will not meet the requirements. For the longitudinal HQs, the LOES fit never falls within the set requirement, giving problems evaluating the short period and CAP. For the lateral HQ, the LOES meets the requirements, and thus, we can conclude that the lateral handling qualities are met for the approach using the given samples.

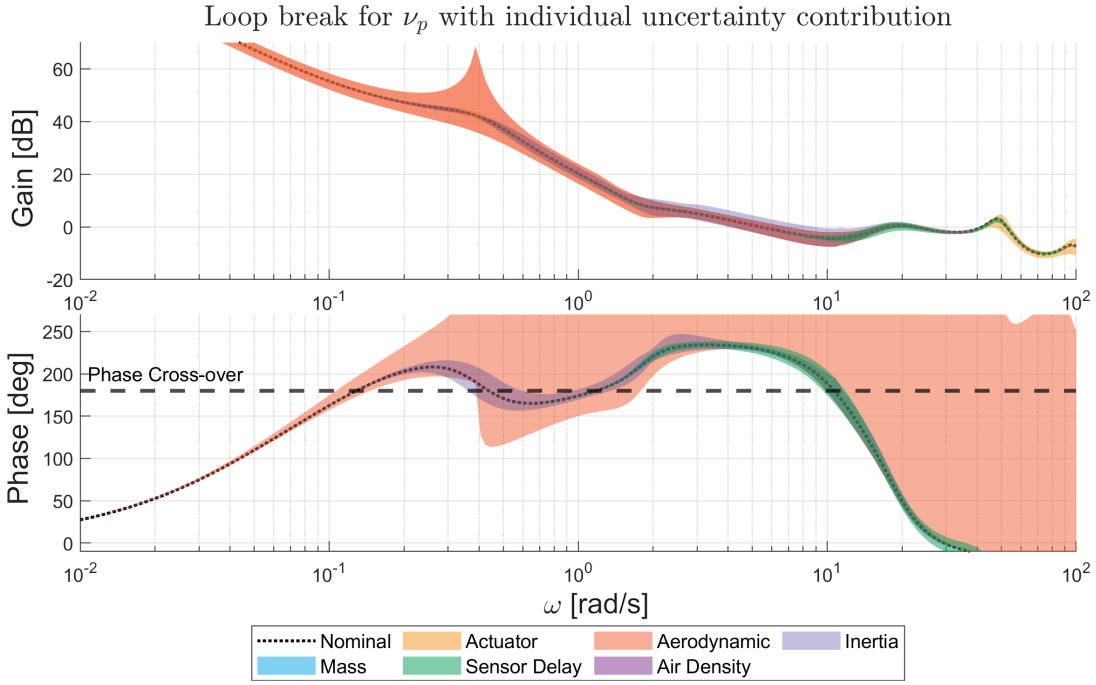

Figure 9.2: Broken loop uncertainty for approach at point A for ν_p, with individual uncertainty contribution

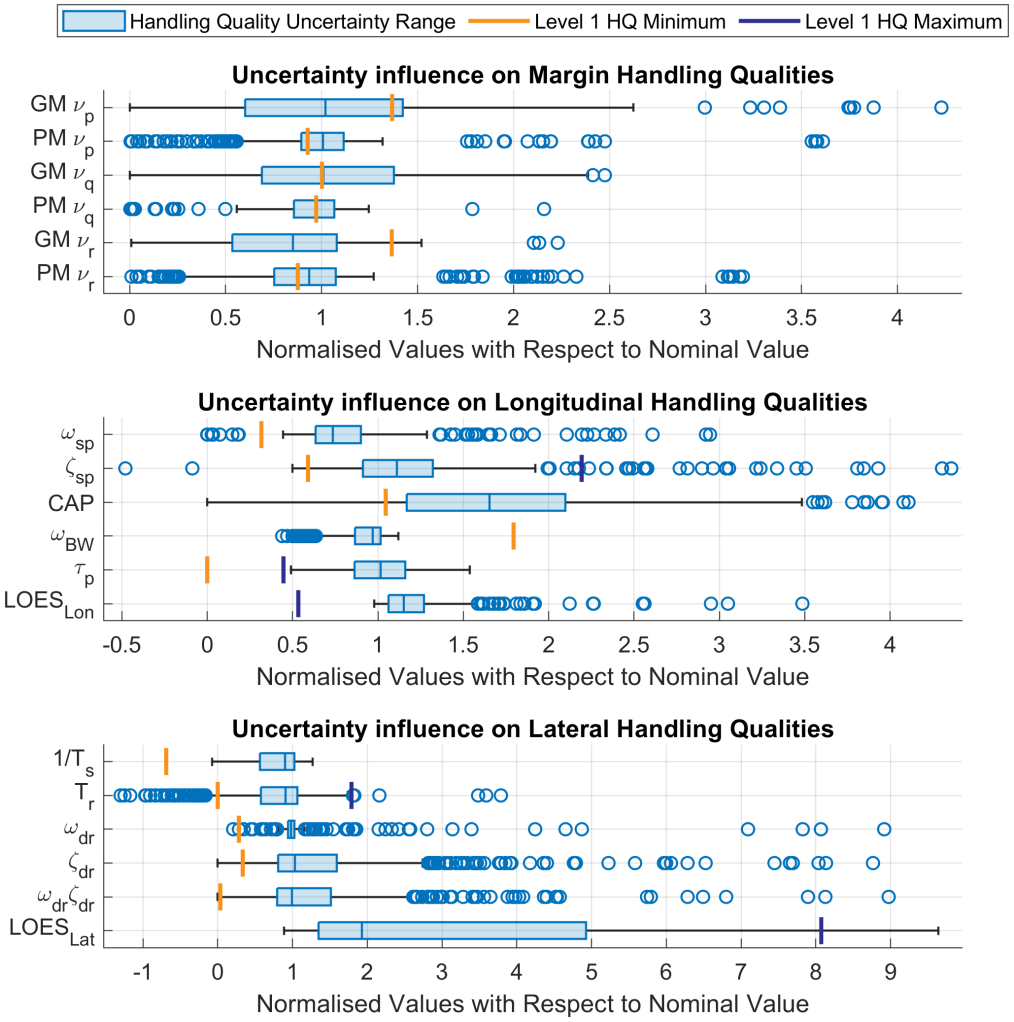

Figure 9.3: Boxplots with uncertainties for set HQ requirements in approach, 750 samples

10

Additional Flight Envelope Protection Results

This Chapter fills in as an addition to the results that are presented in the scientific paper in Part I, regarding the FEP. In the paper, three different test scenarios were set, from which conclusions were drawn, however only the most severe scenario was presented in the paper, namely the combined control input. The defined test cases are:

- Longitudinal command: C^*_{cmd} = +3 at t=1s until t=130s, C^*_{cmd} = -3 at t=130s until t=150s, T_{sim}=200s
- Lateral command: $\dot{\phi}_{cmd}$ +-20 deg/s using 321 step command at t =1s until t = 181s, T_{sim}=200s
- Combined command: C^*_{cmd} = +3 at t=20s until t=130s, C^*_{cmd} = -3 at t=130s until t=180s and $\dot{\phi}_{cmd} = \pm$ 20 deg/s, at t=3s until t=153s, T_{sim}=200s

The results of each test are presented as follows: Figures 10.1,10.2 and 10.3 present the results for longitudinal, lateral, and combined command, respectively. As the results for the combined command for the updated model and the original model in cruise are already presented in the paper, these are not shown in Figure 10.3. In Figures 10.1 and 10.2, the longitudinal and lateral FEP results are presented in the order of the original approach, updated approach, original cruise, and updated cruise. This gives four subfigures per respective figure.

Focussing on Figures 10.1a and 10.1b, showing the longitudinal command response in approach condition, it can be concluded that both FEP perform well, as none of the protected states cross their respective limits. It should be noted that the original response exceeds the θ_{lim} because the original model lacks θ protection. The aircraft is initially trimmed at α = 23.3 deg, which exceeds the protected limit of α_{lim} = 22 deg, set by Stougie et al. [14]. Both FEP systems bring the AoA back to its limit and stay at the limit until a C^*_{cmd} = -3 is given at t = 130s. For Figures 10.1c and 10.1d, showing the longitudinal command response in cruise condition, the original model becomes unstable as there is actuator saturation, such that the AoA cannot be protected. The updated model performs as expected and first settles on the θ limit, after which the AoA keeps increasing until it settles. At this point, the θ angle starts decreasing, as the AoA protection limits the $\dot{\theta}_{cmd}$. For the lateral command response, firstly looking at Figures 10.2a and 10.2b, showing the approach condition, it can be concluded that both responses do not satisfy the set protection limits. The original model became unstable as the roll rate oscillated onto instability. The ϕ protection works as expected for the updated model and settles at the set protection limits. However, due to actuator saturation and the roll and pitch channels coupling, there is an excessive overshoot of load factor and θ angle between t = 0s and t=60s. The aircraft is undergoing a significant loss of altitude without a C^* command, which implicates the coupling of the roll and pitch channels.

Looking at Figures 10.2c and 10.2d, showing the lateral command response in cruise condition, gives once again that the original FEP becomes unstable, at the point a reverse $\dot{\phi}_{cmd}$ is given. The updated FEP performs as expected, only exceeding the load factor protection. This is an inherent design problem related to the control structure of the outer-loop controllers. As the C^* controller outputs a $\dot{\theta}_{cmd}$ the protection limits for load factor and AoA are implemented in the C^* controller, where the θ protection is implemented at the $\dot{\theta}$ controller, giving highest priority to the θ protection. Therefore, the FEP structure limits the pitch-down maneuver as the θ_{min} protection is active, so the load factor cannot be limited.

Figure 10.3 shows the original response to a combined control input at approach, which becomes unstable. The other results for this condition are shown in the paper in Part I.

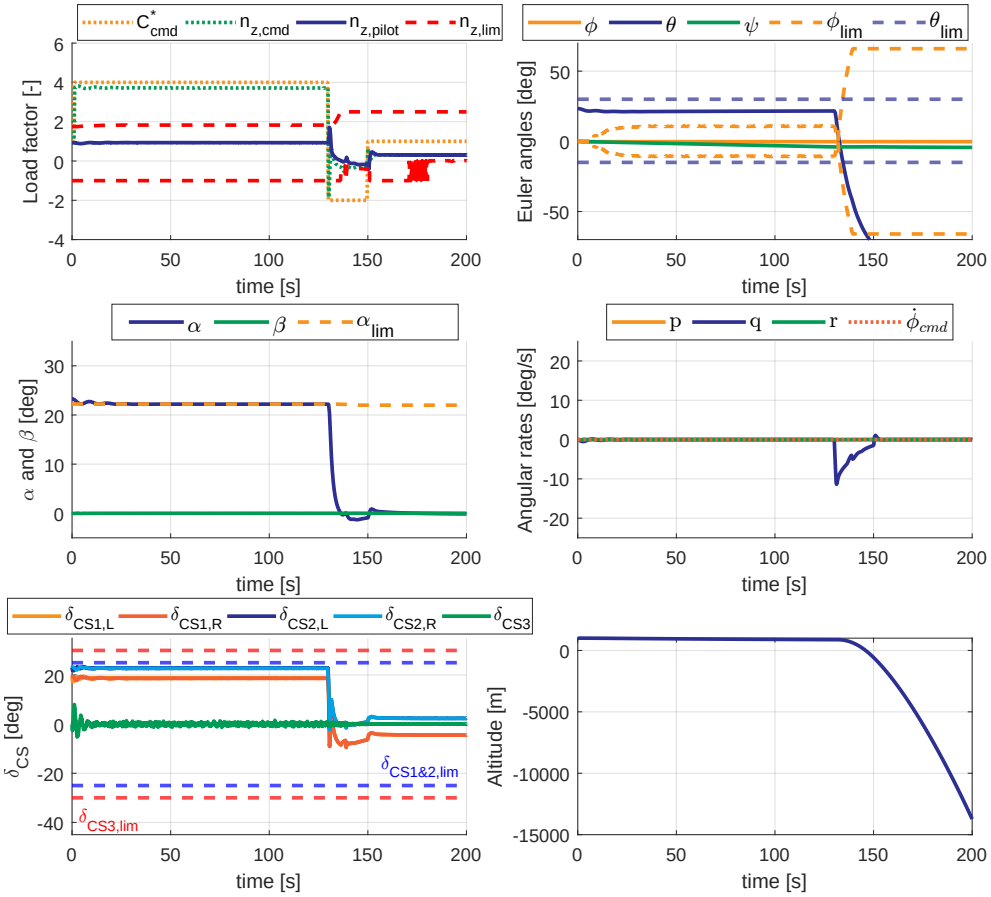

(a) Original FEP Approach: Longitudinal command

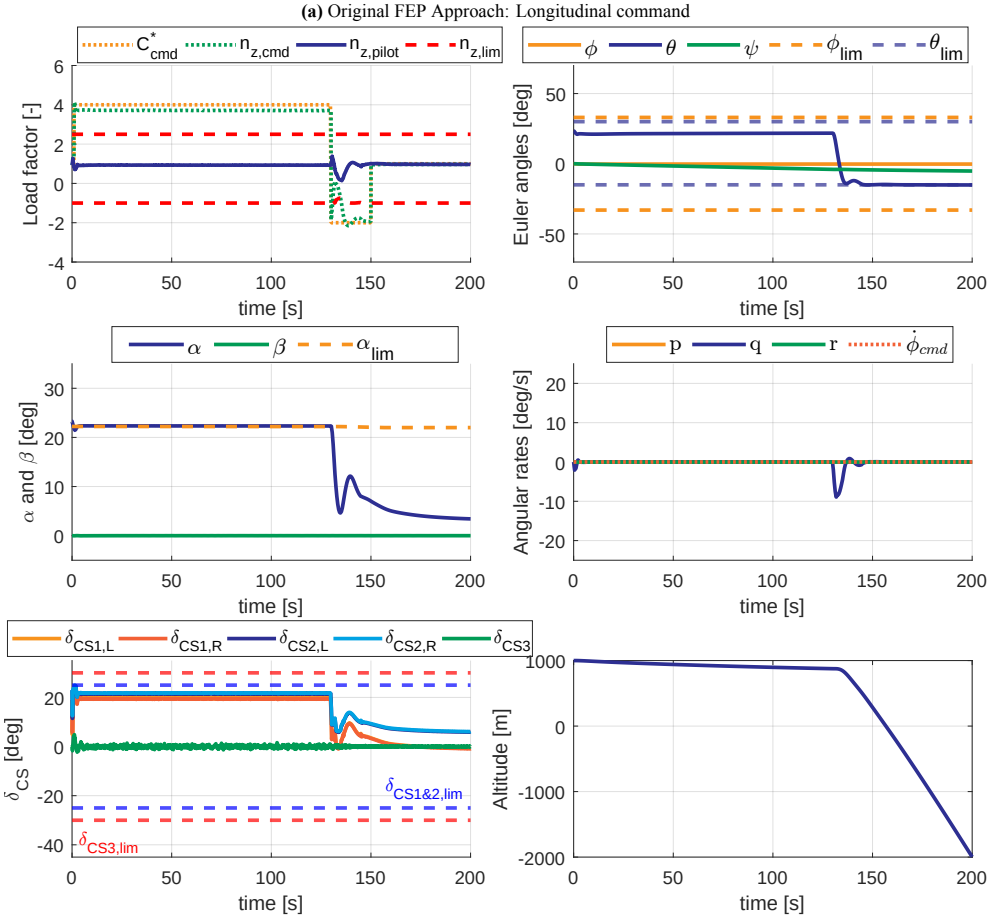

(b) Updated FEP Approach: Longitudinal command

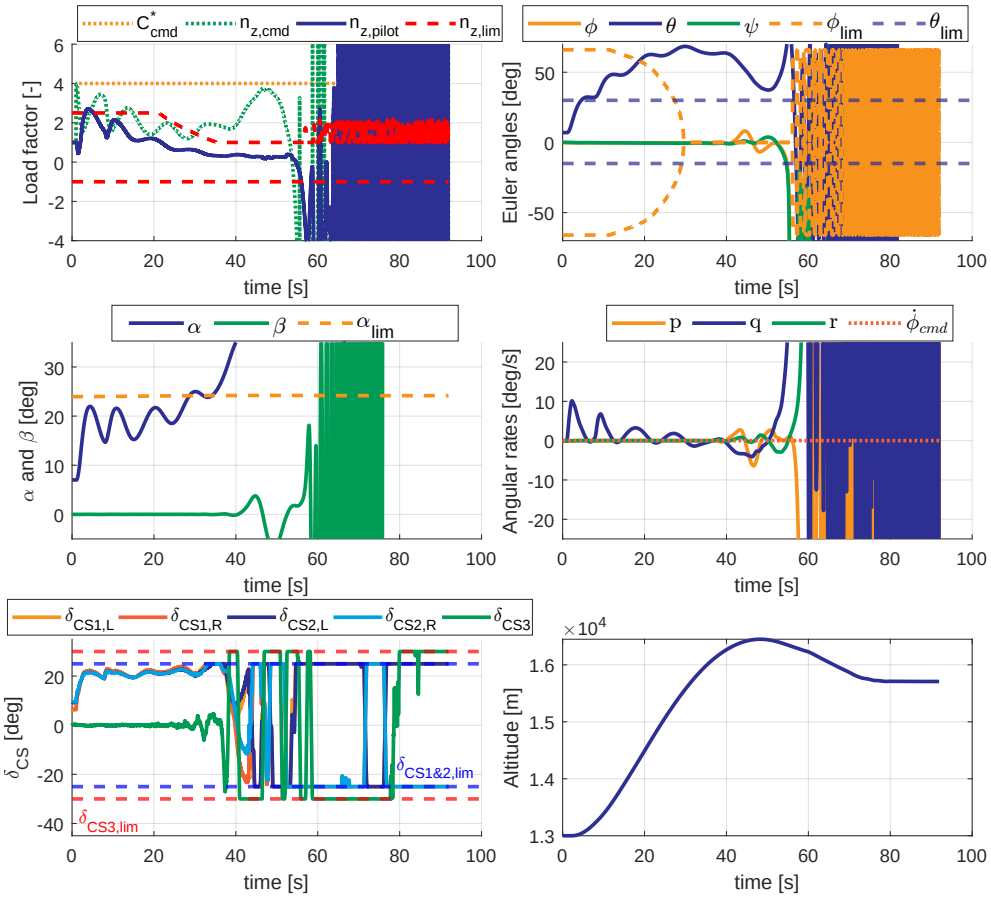

(c) Original FEP Cruise: Longitudinal command

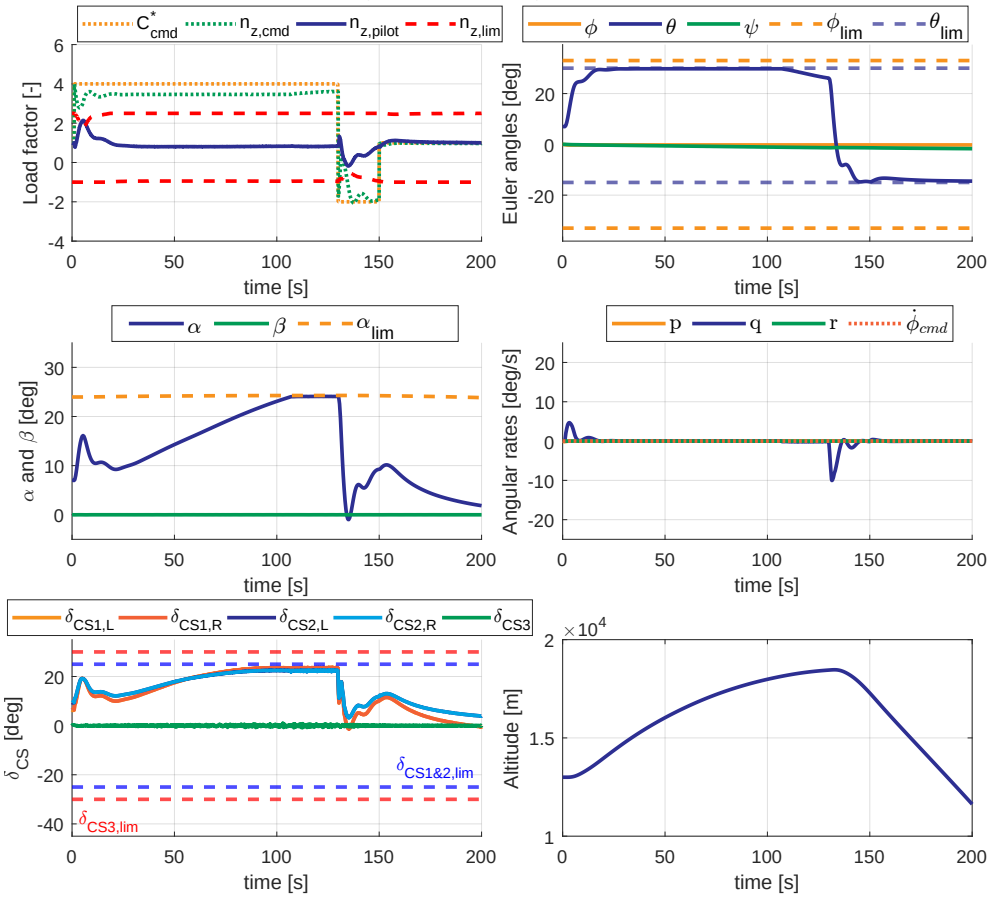

(d) Updated FEP Cruise: Longitudinal command

Figure 10.1: FEP test with longitudinal command, tested for approach and cruise for original and updated FEP

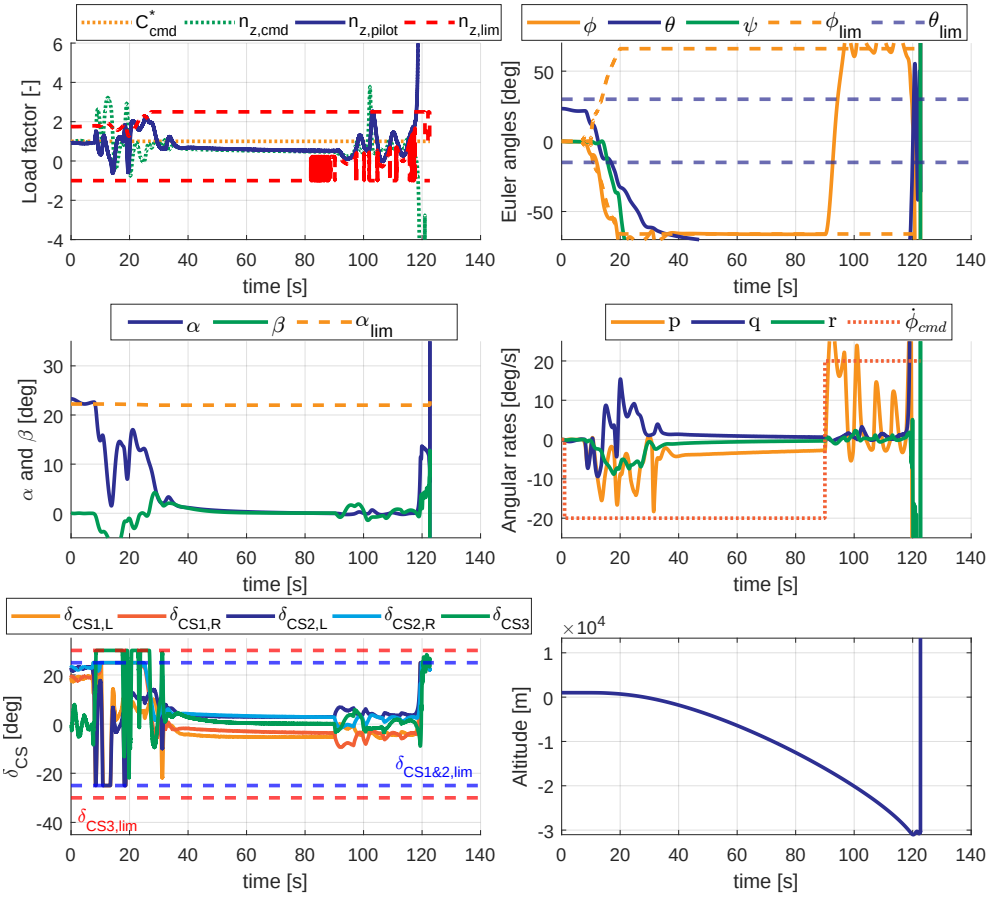

(a) Original FEP Approach: Lateral command

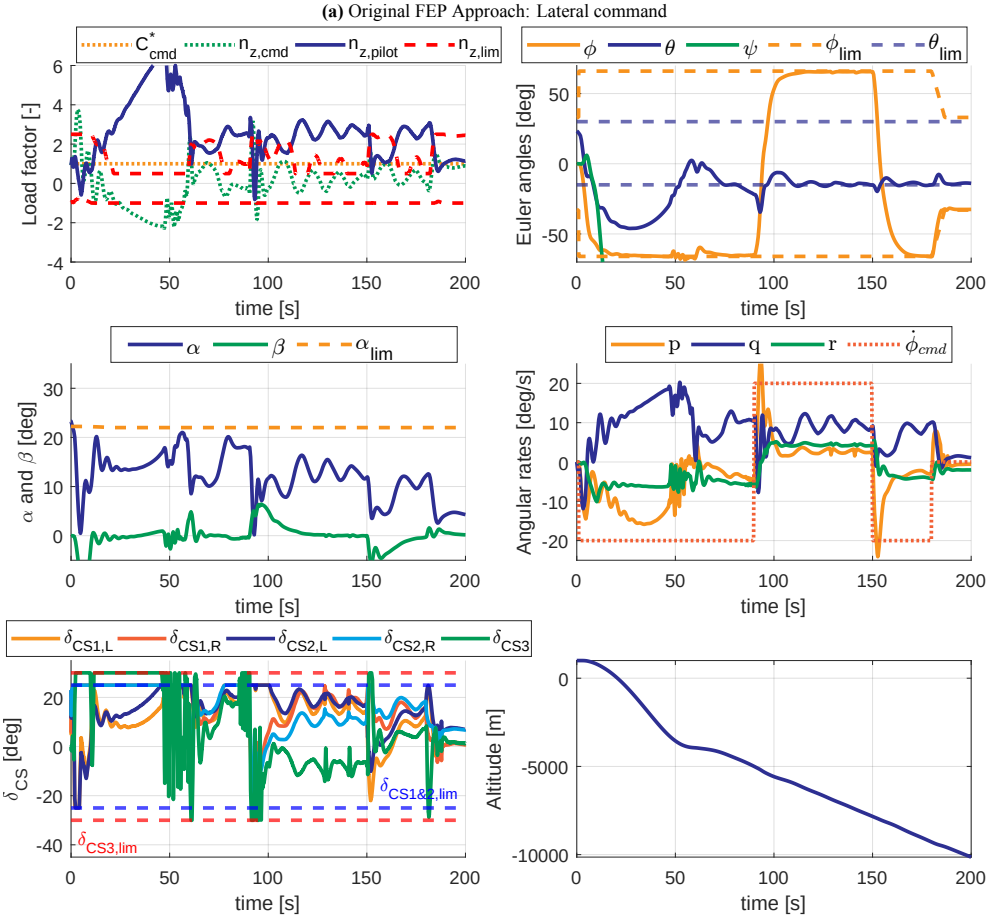

(b) Updated FEP Approach: Lateral command

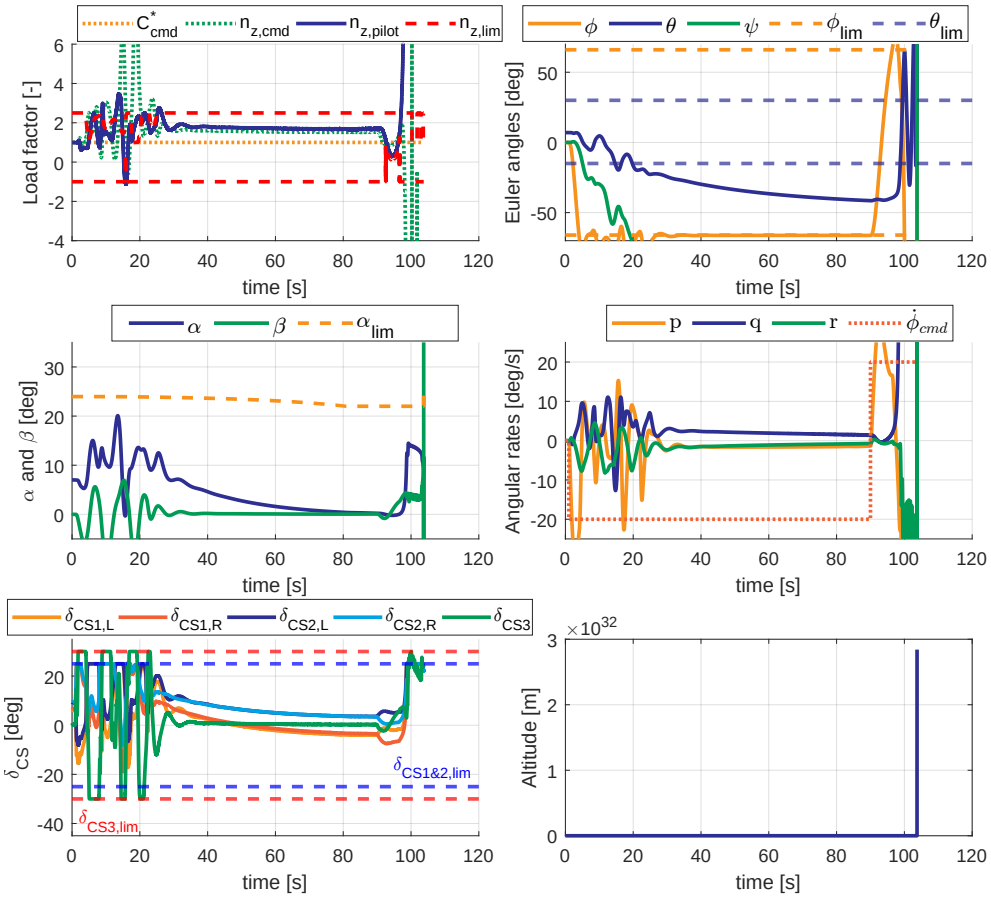

(c) Original FEP Cruise: Lateral command

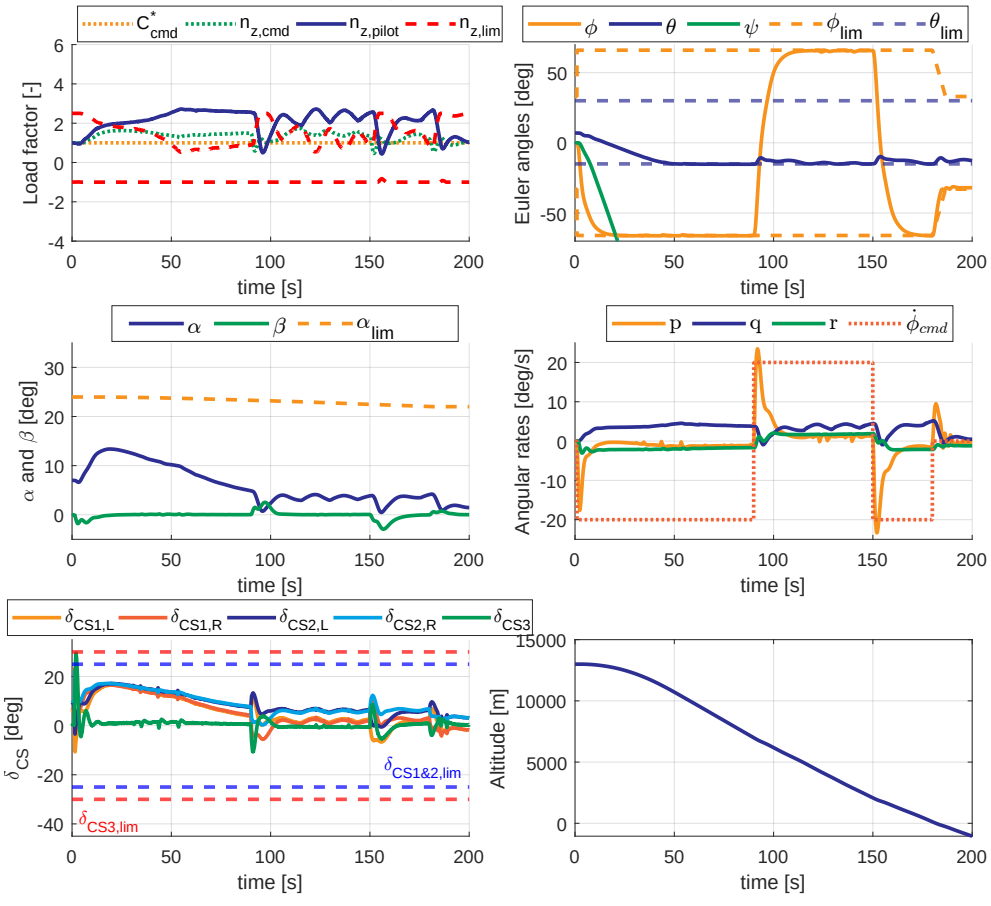

(d) Updated FEP Cruise: Lateral command

Figure 10.2: FEP test with lateral command, tested for approach and cruise for original and updated FEP

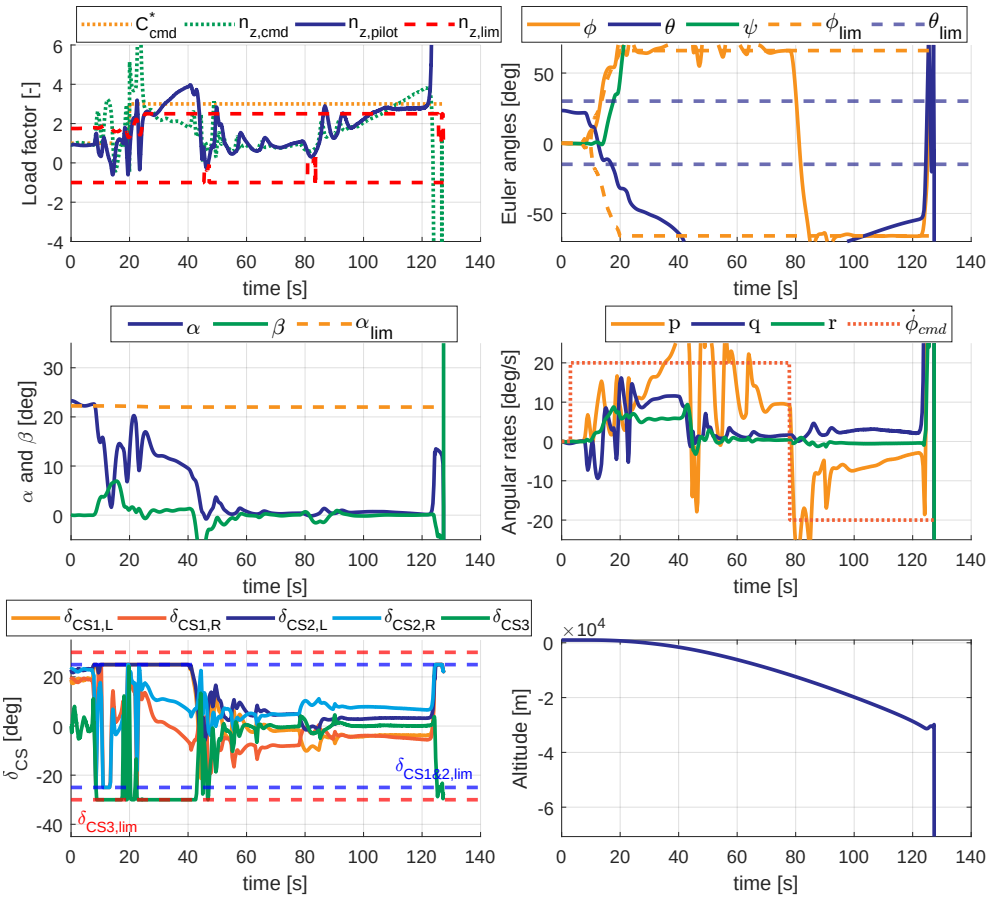

Figure 10.3: Original FEP Approach: Combined command

IV

Conclusion & Recommendations

11

Conclusion

This Chapter will conclude this research by answering the set research questions in Chapter 1 and evaluating the goal of this research. Firstly, each research question is repeated and answered.

1. What are the current limitations of the Flight Control System of the Flying-V?

Research question 1 has been answered using literature research, shown in Chapters 2 - 4, and findings shown in Chapter 5. It was concluded that the original Flight Control System (FCS), implemented by van Overeem and further matured by Stougie et al., using an Incremental Nonlinear Dynamic Inversion (INDI) control structure, experiences stability margin issues due to time-delay performance degradation. Performance degradation due to time delays is a known drawback of an INDI control system. Stougie et al. changed the sensor characteristics of the body rate sensors and β sensor to increase the stability margins and mitigate chatter of the rudder, respectively. Furthermore, during pilot testing in the Full-Flight Simulator of TU Delft (SIMONA), it was concluded that the sideslip reference tracking would not exceed $\beta \approx 3°$ [94].

To provide more elaborate insight in these limitations, sub-question 1 was answered:

1a. What requirements can be used to verify the FCS?

Chapter 4 gives an insight in the commonly used Handling Qualities (HQ) verfications used to verify performance of a FCS. The MIL-STD-1797A is used for verification and quantification of controller performance, eventhough there is discussion about the applicability of certain metrics, especially for large commercial aircraft, such as the Flying-V. It was concluded that several time-domain and frequency domain requirements would be used, to verify the performance of the FCS.

When working on the simulation model from Stougie et al., it was concluded that several mistakes were made with the model implementation, influencing the HQ results as these are acquired by linearising the simulation model. The aircraft was not in a proper trim, which is crucial for a reliable linear approximation. With the updates made to the original FCS, without changing the control law, it was concluded that the problem with the sideslip reference tracking was resolved. Furthermore, incorrect HQ requirement boundaries were set by Stougie et al. for the pitch attitude bandwidth, equivalent time delay, and eigenmode parameters.

Next, to the HQ limitations, the original Flight Envelope Protection (FEP) was evaluated. The original FEP protects the load factor experienced by the pilot, Angle of Attack (AoA), and Euler roll angle. With the test cases, Stougie et al. presented, the FEP exceeded and oscillated around the AoA protection limit. However, the load factor and roll angle protection showed proper performance for the presented test cases. For the AoA oscillations, a damping term was suggested to counteract the oscillatory behavior and it was recommended to extend the FEP by adding protected states.

2. What is the state of the art in Hybrid INDI control and FEP?

This question has been answered by Chapter 3, highlighting Hybrid INDI and FEP methods. Stougie et al. suggested the implementation of a Hybrid INDI control law to overcome the stability margin issues found in his research. The basic principle of Hybrid INDI is to combine the model-based INDI and sensor-based INDI information and merging these to create a control law, that compensates for the drawbacks of each

approach. From the literature research, it was found that three promising methods could be implemented to merge these different control laws, namely Complementary Filter (CF), Augmentation Matrix (AM), and Extended-State-Observer (ESO). These have been implemented in different research and show superior performance with increased time-delay compared to sensor-based INDI. Eventually, Hybrid INDI using a CF was chosen because it is a straightforward, tuneable method with good tracking performance.

Focussing on the FEP, there are multiple methods for which different model structures are necessary. Most methods that were found were based on an adaptive control law, which does not fall in the scope of this research. An interesting research paper from Falkena et al. [53] compares different methods: a control limiting structure, a command limiting structure, a Model Predictive Control (MPC) control law, and a virtual control limiting structure. Falkena found that command limiting protection is versatile, showing adequate protection performance. Therefore, this method was chosen, specifically an exponential potential function command limiting structure, based on Sun et al. [84]. Industry standards regarding envelope protection extend to overspeed protection and pitch attitude protection; however, as overspeed protection is an audible warning, this protection limit is not implemented in the control law.

3. How are performance and fault-tolerance affected by the implementation of Hybrid INDI as the Flight Control System of the Flying-V?

Research question 3 has been answered by the results presented in the scientific paper in part I and the additional results shown in Chapter 9. This research question is answered using two methods, first the nominal performance is evaluated for the sensor-based INDI and Hybrid INDI, using the base sensor configuration. Next, the fault tolerance of the Hybrid INDI controller system is evaluated using parametric uncertainty and assessing the fault tolerance in the time and frequency domain.

First, to compare the nominal performance of the sensor-based INDI and Hybrid INDI, both simulation models were tested using three different time domain test cases: longitudinal, lateral, and directional step responses. All tests were evaluated using several metrics, namely, Overshoot (OS), Settling Time (ST), Control Surface Activity ($CS_{activity}$) and Maximum Control Surface Deflection (CS_{max}), for which a trade-off between HQ and time-domain response was found. The most notable difference was found for settling time of the sideslip response, in cruise. For the HQ comparison Hybrid INDI proved to be satisfactory for the phase margin requirements in both approach and cruise, however the gain margin requirements were not met for all control channels. The sensor-based INDI model showed too low stability margins, as was concluded by Stougie et al. [14].

Next, two separate sub-questions were formulated to answer the question related to fault tolerance. Starting with sub-question 3a:

> 3a. How does the Hybrid INDI controller handle model uncertainties in the mass, inertia, control surface characteristics, and aerodynamic uncertainties?

By implementing parametric uncertainties with the following model-based parameters, it was found that the Hybrid INDI shows better stability margins when relying more on the sensor-based part of the model. Furthermore, using a sample size of 750 samples, it was found that mass uncertainty hardly influences the stability margins and control surface characteristics, only degrade the margins beyond the cross-over frequency. Aerodynamic uncertainty behaves differently for approach compared to cruise. For cruise, it primarily influences the gain margins, whereas, for approach, it impacts both gain and phase margins, drastically reducing the stability margins. Inertia uncertainty behaves similarly for approach and cruise, impacting gain and phase margins across the frequency domain and around cross-over.

Next sub-question 3b is answered:

> 3b. How does the Hybrid INDI controller handle sensor uncertainties looking at time delay and air density uncertainty?

Opposite to the model uncertainties, the Hybrid INDI gives better stability margins when relying more on the model-based INDI, providing sensor uncertainties. The effect of time delay only influenced the margins when the time delay would be increased in increments with a common integer multiple of the body rate sensor sampling time. When looking at the frequency response, it was shown that the uncertainty in air-density measurement did not influence the stability margins, whereas the time delay influence was most noticeable from the cross-over onward for both gain and phase margin.

To conclude this research question, the combined effect of model-based and sensor-based uncertainty was

tested, similar to the nominal model, with time-domain tests and uncertainty impact on HQ parameters. These analyses showed that the current implementation of Hybrid INDI is not fault-tolerant to the combined uncertainties. For the 750 sampled uncertainties, at least 82.8 % of the samples fall within the set threshold of three Median Absolute Deviation, which removes outliers from the samples for both approach and cruise. Furthermore, for the HQ assessment, the trend for approach and cruise was similar for the following conclusions. The median is above the minimum for all stability margin requirements that satisfy level 1 HQ requirement. Next, the Low Order Equivalent System (LOES) approximation gives unsatisfactory results, also making the results of the short period and CAP questionable as those are based on the LOES approximation. The lateral LOES approximation gave better results, for which it can be concluded that for the majority of the uncertainty samples, the HQ requirements are met.

4. How can FEP be improved to enhance the overall safety of the Flying-V aircraft?

Research question 4 continues upon the literature research from research question 2, where the state-of-the-art FEP was researched. The term safety reflects the ability of the updated FEP control law to keep the Flying-V within set boundaries, for more excessive pilot inputs. As was concluded in the scientific paper, in part I, the test cases for the original FEP were not challenging enough to show the deficiencies embedded in the implementation. Only the longitudinal approach condition remained stable for all test cases of the original system, as the pilot command was limited by the AoA protection since the aircraft is trimmed above the set limit.

The updated FEP keeps the aircraft stable in all test cases, however does exceed set protection limits, especially in approach condition. This is happening due to the controller structure and actuator saturation. For the controller structure, pitch protection will have the highest priority of staying within set limits. Furthermore, a set roll command influences the pitch behavior due to the coupling of command channels. Due to actuator saturation, the aircraft lacks control authority to keep the protected states from crossing their limit, which does not lead to instability. It can be inferred that the updated FEP is safer because it does not result in instability for excessive pilot inputs, unlike the original model.

5. How will the FCS perform with a Hybrid INDI including an enhanced FEP compared to the current FCS?

Lastly, research question 5 combines the findings of the conclusions mentioned above, which indicates that the Hybrid INDI implementation outperforms the original FCS both in performance, measured by HQ requirements, maturity, as the updated model solved underlying problems with the original simulation model and safety, as the updated FEP makes handling the Flying-V aircraft safer compared to the original FEP implementation.

To conclude, this research started with the goal to improve performance, mature the simulation model, and enhance safety looking at envelope protection concerning the FCS of the Flying-V aircraft by implementing a Hybrid INDI controller with an enhanced FEP system. It can be concluded that this goal has been achieved, explicitly comparing it to the original FCS. However, the updated FCS does not reach all set requirements, some requirements have not been tested, the current implementation is not fault-tolerant against the set uncertainties and the FEP exceeds its set protection limits. Therefore, Chapter 12 will continue with recommendations for further research.

12

Recommendations for future work

As was concluded in Chapter 11, the goal of this research has been achieved. However, several aspects still need research to further improve, mature, and enhance the safety of the FCS of the Flying-V.

To start with improving the FCS, from evaluating the HQ requirements, it was concluded that two aspects need further research: LOES approximation and adding control authority. As has become apparent from the HQ results, the Hybrid INDI does not meet the set requirements. As shown in the uncertainty assessment, the LOES approximation is inconsistent and essential for proper result evaluation. The current method fits two individual frequency response datasets to the same LOES. However, research can be dedicated to finding a robust process with better overall approximations. Next, research should be devoted to finding a suitable control surface layout to improve control authority, especially for approach condition. This research also posed questions to how the Flying-V aircraft is currently validated using the set HQ. Although these are useful, there is discussion about how the requirements shall be assessed and if they apply to the use-case of the Flying-V aircraft.

To further mature the simulation model, it is recommended that a more accurate aerodynamic dataset is added with data across the flight envelope, mainly focusing on accurate control surface effectiveness data. Furthermore, as has become apparent from the uncertainty simulations, the inertia uncertainty influences the stability margins around the cross-over. With the current simulation model, only one inertia matrix is available for Maximum Take-off Mass (MTOM). Therefore, the inertia property shall be researched for different p_{CoG} and mass.

Lastly, to improve safety, research should be dedicated to correctly identifying the flight envelope of the Flying-V and researching different methods to implement the CA and PCH, as control saturation should prevent outer-loop controllers from demanding extra control input, however as was concluded from the FEP results, the actuator saturation is the main reason the protected states exceed their limits and in case of the original model even make the system unstable.

Bibliography

[1] R. Liebeck, "Design of the Blended Wing Body Subsonic Transport," *Journal of Aircraft*, vol. 41, no. 1, pp. 10–25, 2004. DOI: 10.2514/1.9084.

[2] J. Benad, "The Flying V - A new Aircraft Configuration for Commercial Passenger Transport," in *Deutscher Luft- und Raumfahrtkongress 2015, Rostock*, Deutsche Gesellschaft für Luft- und Raumfahrt, Nov. 2015. DOI: 10.25967/370094.

[3] W. Oosterom and R. Vos, "Conceptual Design of a Flying-V Aircraft Family," in *AIAA AVIATION 2022 Forum*, Reston, Virginia: American Institute of Aeronautics and Astronautics, Jun. 2022, ISBN: 978-1-62410-635-4. DOI: 10.2514/6.2022-3200.

[4] T. Cappuyns, "Handling Qualities of a Flying V Configuration," Ph.D. dissertation, TU Delft, 2019. [Online]. Available: http://resolver.tudelft.nl/uuid:69b56494-0731-487a-8e57-cec397452002.

[5] R. Viet, "Analysis of the flight characteristics of a highly swept cranked flying wing by means of an experimental test," Ph.D. dissertation, TU Delft, 2019. [Online]. Available: http://resolver.tudelft.nl/uuid:90de4d9e-70ae-4efc-bd0a-7426a0a669c3.

[6] F. Faggiano, R. Vos, M. Baan, and R. Van Dijk, "Aerodynamic Design of a Flying V Aircraft," in *17th AIAA Aviation Technology, Integration, and Operations Conference*, Reston, Virginia: American Institute of Aeronautics and Astronautics, Jun. 2017, ISBN: 978-1-62410-508-1. DOI: 10.2514/6.2017-3589.

[7] A. Marques Cavaleiro Machado Jorge, "Quantifying Wind Tunnel Effects on the Flying V," Ph.D. dissertation, Delft University of Technology, Dec. 2023. [Online]. Available: https://repository.tudelft.nl/islandora/object/uuid%3Ab9076ade-2d6e-4faf-882c-1f6115a1317a?collection=education.

[8] M. Palermo and R. Vos, "Experimental Aerodynamic Analysis of a 4.6%-Scale Flying-V Subsonic Transport," in *AIAA Scitech 2020 Forum*, Reston, Virginia: American Institute of Aeronautics and Astronautics, Jan. 2020, ISBN: 978-1-62410-595-1. DOI: 10.2514/6.2020-2228.

[9] A. Ruiz Garcia, R. Vos, and C. de Visser, "Aerodynamic Model Identification of the Flying V from Wind Tunnel Data," in *AIAA AVIATION 2020 FORUM*, 2020. DOI: 10.2514/6.2020-2739.

[10] S. Joosten, O. Stroosma, R. Vos, and M. Mulder, "Simulator Assessment of the Lateral-Directional Handling Qualities of the Flying-V," in *AIAA SCITECH 2023 Forum*, Reston, Virginia: American Institute of Aeronautics and Astronautics, Jan. 2023, ISBN: 978-1-62410-699-6. DOI: 10.2514/6.2023-0906.

[11] R. Torelli, O. Stroosma, R. Vos, and M. Mulder, "Piloted Simulator Evaluation of Low-Speed Handling Qualities of the Flying-V," in *AIAA SCITECH 2023 Forum*, Reston, Virginia: American Institute of Aeronautics and Astronautics, Jan. 2023, ISBN: 978-1-62410-699-6. DOI: 10.2514/6.2023-0907.

[12] G. Vugts, O. Stroosma, R. Vos, and M. Mulder, "Simulator Evaluation of Flightpath-oriented Control Allocation for the Flying-V," in *AIAA SCITECH 2023 Forum*, Reston, Virginia: American Institute of Aeronautics and Astronautics, Jan. 2023, ISBN: 978-1-62410-699-6. DOI: 10.2514/6.2023-2508.

[13] S. van Overeem, X. Wang, and E. Van Kampen, "Handling Quality Improvements for the Flying-V Aircraft using Incremental Nonlinear Dynamic Inversion," in *AIAA SCITECH 2023 Forum*, Reston, Virginia: American Institute of Aeronautics and Astronautics, Jan. 2023, ISBN: 978-1-62410-699-6. DOI: 10.2514/6.2023-0105.

[14] J. Stougie, T. S. Pollack, and E. Van Kampen, "Incremental Nonlinear Dynamic Inversion control with Flight Envelope Protection for the Flying-V," in *AIAA SCITECH 2024 Forum*, Orlando, Florida: American Institute of Aeronautics and Astronautics, Jan. 2024, ISBN: 978-1-62410-711-5. DOI: 10.2514/6.2024-2565.

[15] C. Kim, I. Yang, G.-O. Koh, and B. S. Kim, "A study on longitudinal control law design and flying quality parameter optimization for highly maneuverable fighter," *Journal of Institute of Control, Robotics and Systems*, vol. 24, no. 8, pp. 767–776, 2018. DOI: 10.5302/J.ICROS.2018.18.0067.

[16] J. Yang and J. Zhu, "An angular acceleration estimation method based on the complementary filter theory," in *2016 IEEE International Instrumentation and Measurement Technology Conference Proceedings*, IEEE, May 2016, pp. 1–6, ISBN: 978-1-4673-9220-4. DOI: 10.1109/I2MTC.2016.7520548.

[17] Y. Kumtepe, T. S. Pollack, and E. van Kampen, "Flight Control Law Design Using Hybrid Incremental Nonlinear Dynamic Inversion," in *AIAA Science and Technology Forum and Exposition, AIAA SciTech Forum 2022*, 2022, ISBN: 9781624106316. DOI: 10.2514/6.2022-1597.

[18] C. Kim, "A hybrid INDI control for ensuring flying qualities in failures of Xcg measurement subsystem," *Proceedings of the Institution of Mechanical Engineers, Part G: Journal of Aerospace Engineering*, vol. 237, no. 4, pp. 972–991, Mar. 2023, ISSN: 20413025. DOI: 10.1177/09544100221113429.

[19] P. Okonkwo and H. Smith, "Review of evolving trends in blended wing body aircraft design," *Progress in Aerospace Sciences*, vol. 82, pp. 1–23, Apr. 2016, ISSN: 03760421. DOI: 10.1016/j.paerosci.2015.12.002.

[20] P. D. Bravo-Mosquera, F. M. Catalano, and D. W. Zingg, "Unconventional aircraft for civil aviation: A review of concepts and design methodologies," *Progress in Aerospace Sciences*, vol. 131, p. 100 813, May 2022, ISSN: 03760421. DOI: 10.1016/j.paerosci.2022.100813.

[21] M. Verdon, *JetZero Got a $235M Air Force Grant for a Full-Scale Blended-Wing Jet – Robb Report UK*, Aug. 2023. [Online]. Available: https://robbreport.co.uk/motors/aviation/this-new-blended-wing-jet-concept-which-burns-50-percent-less-fuel-could-hit-the-skies-by-1234703549/.

[22] G. J. de Zoeten, C. Varriale, and R. Vos, "Flight Performance Evaluation of the Flying-V," in *AIAA AVIATION 2023 Forum*, Reston, Virginia: American Institute of Aeronautics and Astronautics, Jun. 2023, ISBN: 978-1-62410-704-7. DOI: 10.2514/6.2023-3484.

[23] J. Benad and R. Vos, "Design of a Flying-V Subsonic Transport," in *33rd Congress of the International Council of the Aeronautical Sciences, ICAS 2022*, vol. 2, 2022, pp. 961–973, ISBN: 9781713871163.

[24] J. Vassberg, M. Dehaan, M. Rivers, and R. Wahls, "Development of a Common Research Model for Applied CFD Validation Studies," in *26th AIAA Applied Aerodynamics Conference*, Reston, Virigina: American Institute of Aeronautics and Astronautics, Aug. 2008, ISBN: 978-1-60086-987-7. DOI: 10.2514/6.2008-6919.

[25] Y. A. Laar, *Aerodynamic Design of a Flying V Aircraft in Transonic Conditions*, 2023. [Online]. Available: https://repository.tudelft.nl/islandora/object/uuid%3A591093b2-5cdc-41c5-b564-3786f43d51db.

[26] F. Granata, "Aerodynamic Optimization of a Flying V Aircraft using a Vortex Lattice Method," Ph.D. dissertation, Sep. 2023. [Online]. Available: https://repository.tudelft.nl/islandora/object/uuid%3A35d70826-c242-4eb1-a10a-2a61955b7182.

[27] J. Horwitz, "Parametric Design of the Flying-V Winglets for Improved Lateral-Directional Stability and Control," Ph.D. dissertation, TU Delft, 2021. [Online]. Available: http://resolver.tudelft.nl/uuid:d7513b36-b9fd-4f8a-8726-f5c7ee7f3a6b.

[28] K. Siemonsma, *Aerodynamic model identification of the Flying-V using flight data*, Oct. 2022. [Online]. Available: https://repository.tudelft.nl/islandora/object/uuid%3A3cf35fb2-4fe7-49d7-9076-068c44fb2016.

[29] S. Nolet, "Improving the Flying V Directional Control Power by the Implementation of Split Flaps," Ph.D. dissertation, Apr. 2022. [Online]. Available: https://repository.tudelft.nl/islandora/object/uuid%3A18847b0d-597d-4539-968f-ebc8a14c905e.

[30] S. Eftekhar, "High Lift Split Flaps for the Flying-V," Ph.D. dissertation, Delft University of Technology, Jan. 2024.

[31] W. Völker, Y. Li, and E. Van Kampen, "Twin-Delayed Deep Deterministic Policy Gradient for altitude control of a flying-wing aircraft with an uncertain aerodynamic model," in *AIAA SCITECH 2023 Forum*, Reston, Virginia: American Institute of Aeronautics and Astronautics, Jan. 2023, ISBN: 978-1-62410-699-6. DOI: 10.2514/6.2023-2678.

[32] Anonymous, "Flying Qualities of Piloted Aircraft," Department of Defense, Tech. Rep. MIL-STD-1797A Notice 3, Aug. 2004.

[33] A. Świderski, "Automating the Handling Qualities Predictions of the Flying-V," Ph.D. dissertation, Mar. 2023. [Online]. Available: https://repository.tudelft.nl/islandora/object/uuid%3Ae9b906e8-2a7b-4464-9c78-dd0d9ecde137.

[34] A. Ruiz Garcia, M. Brown, D. Atherstone, N. v. Arnhem, and R. Vos, "Aerodynamic Model Identification of the Flying V from Sub-Scale Flight Test Data," in *AIAA SCITECH 2022 Forum*, Reston, Virginia: American Institute of Aeronautics and Astronautics, Jan. 2022, ISBN: 978-1-62410-631-6. DOI: 10.2514/6.2022-0713.

[35] J. Mulder, W. van Staveren, J. van der Vaart, *et al.*, *Flight Dynamics*. Delft, Mar. 2013, vol. 1.

[36] S. Sieberling, Q. P. Chu, and J. A. Mulder, "Robust Flight Control Using Incremental Nonlinear Dynamic Inversion and Angular Acceleration Prediction," *Journal of Guidance, Control, and Dynamics*, vol. 33, no. 6, pp. 1732–1742, 2010. DOI: 10.2514/1.49978. [Online]. Available: https://doi.org/10.2514/1.49978.

[37] S. A. van Empelen and R. Vos, "Effect of Engine Integration on a 4.6%-Scale Flying-V Subsonic Transport," in *AIAA 2021-0939 Session: Aerodynamic Testing: Ground, Wind-Tunnel and Flight Testing I*, AIAA Scitech 2021 Forum, 2021. DOI: 978-1-62410-609-5.

[38] G. K. Ananda, M. Vahora, O. D. Dantsker, and M. S. Selig, "Design Methodology for a Dynamically-Scaled General Aviation Aircraft," in *35th AIAA Applied Aerodynamics Conference*, Jun. 2017. DOI: 10.2514/6.2017-4077. [Online]. Available: https://arc.aiaa.org/doi/abs/10.2514/6.2017-4077.

[39] R. van 't Veld, *Incremental Nonlinear Dynamic Inversion Flight Control: Stability and Robustness Analysis and Improvements*, Delft, Oct. 2016.

[40] V. Stepanyan, N. Nguyen, and K. Krishnakumar, "Adaptive Control of a Transport Aircraft Using Differential Thrust," in *AIAA Guidance, Navigation, and Control Conference*, Reston, Virigina: American Institute of Aeronautics and Astronautics, Aug. 2009, ISBN: 978-1-60086-978-5. DOI: 10.2514/6.2009-5741.

[41] I. Matamoros and C. C. de Visser, "Incremental Nonlinear Control Allocation for a Tailless Aircraft with Innovative Control Effectors," in *2018 AIAA Guidance, Navigation, and Control Conference*, AIAA, 2018. DOI: 10.2514/6.2018-1116. [Online]. Available: https://arc.aiaa.org/doi/abs/10.2514/6.2018-1116.

[42] Anonymous, "Type-Certificate Data Sheet," European Union Aviation Safety Agency (EASA), Tech. Rep. EASA.E.111 Issue 16, Oct. 2022, p. 8.

[43] F. Grondman, G. Looye, R. O. Kuchar, Q. P. Chu, and E. van Kampen, "Design and Flight Testing of Incremental Nonlinear Dynamic Inversion-based Control Laws for a Passenger Aircraft," in *2018 AIAA Guidance, Navigation, and Control Conference*, AIAA, 2018. DOI: 10.2514/6.2018-0385. [Online]. Available: https://arc.aiaa.org/doi/abs/10.2514/6.2018-0385.

[44] R. van 't Veld, E. van Kampen, and Q. P. Chu, "Stability and Robustness Analysis and Improvements for Incremental Nonlinear Dynamic Inversion Control," in *2018 AIAA Guidance, Navigation, and Control Conference*, 2018. DOI: 10.2514/6.2018-1127. [Online]. Available: https://arc.aiaa.org/doi/abs/10.2514/6.2018-1127.

[45] G. J. Balas, "Flight control law design: An industry perspective," *European Journal of Control*, vol. 9, no. 2-3, pp. 207–226, 2003. DOI: 10.3166/ejc.9.207-226.

[46] K. J. Åström and B. Wittenmark, *Adaptive control* (Addison-Wesley series in electrical and computer engineering. Control engineering), English. Reading, Mass.: Addison-Wesley, 1989. [Online]. Available: http://www.zentralblatt-math.org/zmath/en/search/?an=0697.93033.

[47] J.-J. E. Slotine and W. Li, *Applied nonlinear control*, English. Englewood Cliffs, N.J.: Prentice Hall, 1991. [Online]. Available: http://www.gbv.de/dms/ilmenau/toc/019505159.PDF.

[48] N. Govindarajan, C. C. De Visser, E. Van Kampen, K. Krishnakumar, J. Barlow, and V. Stepanyan, "Optimal control framework for estimating autopilot safety margins," *Journal of Guidance, Control, and Dynamics*, vol. 38, no. 7, pp. 1197–1207, Jan. 2015, ISSN: 15333884. DOI: 10.2514/1.G000271.

[49] J. M. Maciejowski and C. N. Jones, "MPC fault-tolerant flight control case study: flight 1862," *IFAC Proceedings Volumes*, vol. 36, no. 5, pp. 119–124, Jun. 2003, ISSN: 14746670. DOI: 10.1016/S1474-6670(17)36480-7.

[50] L. Sonneveldt, *Adaptive backstepping flight control for modern fighter aircraft.* [s.n.], 2010, ISBN: 9789085705734.

[51] P. van Gils, E. Van Kampen, C. C. de Visser, and Q. P. Chu, "Adaptive Incremental Backstepping Flight Control for a High-Performance Aircraft with Uncertainties," in *AIAA Guidance, Navigation, and Control Conference*, Reston, Virginia: American Institute of Aeronautics and Astronautics, Jan. 2016, ISBN: 978-1-62410-389-6. DOI: 10.2514/6.2016-1380.

[52] X. Wang, E. van Kampen, Q. Chu, and P. Lu, "Stability Analysis for Incremental Nonlinear Dynamic Inversion Control," *Journal of Guidance, Control, and Dynamics*, vol. 42, no. 5, pp. 1116–1129, May 2019, ISSN: 0731-5090. DOI: 10.2514/1.G003791.

[53] W. Falkena, "Investigation of practical flight control systems for small aircraft," Ph.D. dissertation, Delft University of Technology, Delft, 2012, ISBN: 978-94-6203-258-3.

[54] P. Simplício, M. D. Pavel, E. van Kampen, and Q. P. Chu, "An acceleration measurements-based approach for helicopter nonlinear flight control using Incremental Nonlinear Dynamic Inversion," *Control Engineering Practice*, vol. 21, no. 8, pp. 1065–1077, 2013, ISSN: 0967-0661. DOI: https://doi.org/10.1016/j.conengprac.2013.03.009. [Online]. Available: https://www.sciencedirect.com/science/article/pii/S0967066113000634.

[55] T. S. Pollack, "Advances in Dynamic Inversion-Based Flight Control Law Design," Ph.D. dissertation, Delft University of Technology, Delft, 2024.

[56] J. Yang and J. Zhu, "A hybrid NDI control method for the high-alpha super-maneuver flight control," in *Proceedings of the American Control Conference*, vol. 2016-July, 2016, pp. 6747–6753, ISBN: 9781467386821. DOI: 10.1109/ACC.2016.7526734.

[57] C. Kim, C. H. Ji, G. O. Koh, and B. S. Kim, "Stability Margin and Structural Coupling Analysis of a Hybrid INDI Control for the Fighter Aircraft," *International Journal of Aeronautical and Space Sciences*, vol. 22, no. 5, pp. 1154–1169, Oct. 2021, ISSN: 20932480. DOI: 10.1007/s42405-021-00394-8.

[58] H. Lyu, Z. Ye, Y. Chen, *et al.*, "Extended-State-Observer-Based Angular Acceleration Estimation for Supersonic Aircraft Lateral–Directional Control," *Applied Sciences*, vol. 13, no. 11, p. 6598, May 2023, ISSN: 2076-3417. DOI: 10.3390/app13116598.

[59] T. S. Pollack and E. van Kampen, "Robust Stability and Performance Analysis of Incremental Dynamic-Inversion-Based Flight Control Laws," *Journal of Guidance, Control, and Dynamics*, vol. 46, no. 9, pp. 1785–1798, 2023. DOI: 10.2514/1.G006576.

[60] C. Kim, C. H. Ji, and B. S. Kim, "Development of Flight Control Law for Improvement of Uncommanded Lateral Motion of the Fighter Aircraft," *International Journal of Aeronautical and Space Sciences*, vol. 21, no. 4, pp. 1059–1077, Dec. 2020, ISSN: 20932480. DOI: 10.1007/s42405-020-00308-0.

[61] C. H. Ji, C. Kim, and B. S. Kim, "A Hybrid Incremental Nonlinear Dynamic Inversion Control for Improving Flying Qualities of Asymmetric Store Configuration Aircraft," *Aerospace*, vol. 8, no. 5, p. 126, May 2021, ISSN: 2226-4310. DOI: 10.3390/aerospace8050126.

[62] C. H. Ji, C. Kim, and B. S. Kim, "Flight Control Law for Stabilizing Transient Response of the Aircraft during Gun Firing," *Aerospace*, vol. 10, no. 4, 2023. DOI: 10.3390/aerospace10040365.

[63] C. Kim, T. Jin, G.-O. Koh, and B. S. Kim, "Control law design to improve the unexpected pitch motion in slow down turn maneuver," *Proceedings of the Institution of Mechanical Engineers, Part G: Journal of Aerospace Engineering*, vol. 236, no. 1, pp. 123–139, 2022. DOI: 10.1177/09544100211008602.

[64] J. Yang and J. Zhu, "Prop-hanging control of a thrust vector vehicle with hybrid Nonlinear Dynamic Inversion method," in *2016 IEEE International Conference on Robotics and Automation (ICRA)*, IEEE, May 2016, pp. 2999–3005, ISBN: 978-1-4673-8026-3. DOI: 10.1109/ICRA.2016.7487465.

[65] D. Niedermeier and A. A. Lambregts, "Fly-By-Wire Augmented Manual Control-Basic Design Considerations," in *28th Congress of the International Council of the Aeronautical Sciences*, Deutsches Zentrum für Luft- und Raumfahrt & Federal Aviation Administration, Brisbane: International Council of the Aeronautical Sciences, Sep. 2012.

[66] C. Favre, "Fly-by-wire for commercial aircraft: the Airbus experience," *International Journal of Control*, vol. 59, no. 1, pp. 139–157, 1994. DOI: 10.1080/00207179408923072.

[67] T. Lombaerts, G. Looye, J. Ellerbroek, and M. R. y. Martin, "Design and Piloted Simulator Evaluation of Adaptive Safe Flight Envelope Protection Algorithm," *Journal of Guidance, Control, and Dynamics*, vol. 40, no. 8, pp. 1902–1924, 2017. DOI: 10.2514/1.G002525.

[68] M. Li, J. Li, Y. Tang, and S. Sun, "An Extended INDI Approach and Application to Pitch Rate Control Laws Design of an Aircraft," in *AIAA AVIATION 2021 FORUM*, AIAA, 2021. DOI: 10.2514/6.2021-3005.

[69] T. Lombaerts and G. Looye, "Design and flight testing of manual nonlinear flight control laws," in *AIAA Guidance, Navigation, and Control Conference*, Reston, Virigina: American Institute of Aeronautics and Astronautics, Aug. 2011, ISBN: 978-1-60086-952-5. DOI: 10.2514/6.2011-6469.

[70] E. J. J. Smeur, Q. Chu, and G. C. H. E. de Croon, "Adaptive Incremental Nonlinear Dynamic Inversion for Attitude Control of Micro Air Vehicles," *Journal of Guidance, Control, and Dynamics*, vol. 39, no. 3, pp. 450–461, 2016. DOI: 10.2514/1.G001490.

[71] E. Johnson and A. Calise, "Pseudo-Control Hedging: A New Method For Adaptive Control," *Advances in Navigation Guidance and Control Technology Workshop*, Feb. 2001.

[72] S. Oudin, "Low Speed Protections for a Commercial Airliner : a Practical Approach," in *AIAA Guidance, Navigation, and Control Conference*, American Institute of Aeronautics and Astronautics, 2017. DOI: 10.2514/6.2017-1023.

[73] R. Rogers, "Pilot Authority And Aircraft Protections," Air Line Pilots Association (ALPA), Tech. Rep., Mar. 1999.

[74] A. A. Lambregts, "Flight Envelope Protection for Automatic and Augmented Manual Control," in *Proceedings of the EuroGNC 2013, 2nd CEAS Specialist Conference on Guidance, Navigation & Control*, Council of European Aerospace Societies (CEAS), 2013, pp. 1364–1383.

[75] Anonymous, "Easy Access Rules for Large Aeroplanes," European Union Aviation Safety Agency (EASA), Tech. Rep. CS25 Amendment 27, Jan. 2023. [Online]. Available: https://www.easa.europa.eu/en/document-library/easy-access-rules/easy-access-rules-large-aeroplanes-cs-25#group-publications.

[76] P. Goupil, "AIRBUS state of the art and practices on FDI and FTC in flight control system," *Control Engineering Practice*, vol. 19, no. 6, pp. 524–539, Jun. 2011, ISSN: 09670661. DOI: 10.1016/j.conengprac.2010.12.009.

[77] J. Farineau, "Lateral electric flight control laws of a civil aircraft based upon eigenstructure assignment technique," in *Guidance, Navigation and Control Conference*, Reston, Virigina: American Institute of Aeronautics and Astronautics, Aug. 1989. DOI: 10.2514/6.1989-3594.

[78] L. Tang, M. Roemer, J. Ge, A. Crassidis, J. Prasad, and C. Belcastro, "Methodologies for adaptive flight envelope estimation and protection," in *AIAA Guidance, Navigation, and Control Conference and Exhibit*, 2009, ISBN: 9781563479786. DOI: 10.2514/6.2009-6260.

[79] E. R. van Oort, *Adaptive backstepping control and safety analysis for modern fighter aircraft*. [s.n.], 2011, ISBN: 9789085707356.

[80] R. Xie, H. He, X. Meng, and X. Fan, "Neural-Network-Based Dynamic Flight Envelop Protection Within Integrated Aircraft Control System," *Journal of Guidance, Control, and Dynamics*, vol. 46, no. 6, pp. 1083–1094, Jan. 2023, ISSN: 15333884. DOI: 10.2514/1.G006872/ASSET/IMAGES/LARGE/FIGURE12.JPEG. [Online]. Available: https://arc.aiaa.org/doi/10.2514/1.G006872.

[81] W. Falkena, C. Borst, Q. P. Chu, and J. A. Mulder, "Investigation of Practical Flight Envelope Protection Systems for Small Aircraft," *Journal of Guidance, Control, and Dynamics*, vol. 34, no. 4, pp. 976–988, Jul. 2011, ISSN: 0731-5090. DOI: 10.2514/1.53000.

[82] M. Krstić, I. Kanellakopoulos, and P. Kokotović, *Nonlinear and Adaptive Control Design*. New York: Wiley, 1995, pp. 511–514.

[83] D. Sun, H. Jafarnejadsani, and N. Hovakimyan, "Command Limiting for Aerial Vehicles With Rate Control Augmentation Systems," *IEEE Transactions on Aerospace and Electronic Systems*, vol. 57, no. 3, pp. 1702–1712, Jun. 2021, ISSN: 0018-9251. DOI: 10.1109/TAES.2021.3050674.

[84] D. Sun, N. Hovakimyan, and H. Jafarnejadsani, "Design of Command Limiting Control Law Using Exponential Potential Functions," *Journal of Guidance, Control, and Dynamics*, vol. 44, no. 2, pp. 441–448, Feb. 2021, ISSN: 1533-3884. DOI: 10.2514/1.G004972.

[85] M. V. Cook, *Flight Dynamics Principles: A Linear Systems Approach to Aircraft Stability and Control*. Butterworth-Heinemann, 2013, ISBN: 978-0-08-098242-7. DOI: 10.1016/C2010-0-65889-5.

[86] B. J. Bacon and A. J. Ostroff, "Reconfigurable flight control using nonlinear dynamic inversion with a special accelerometer implementation," in *AIAA Guidance, Navigation, and Control Conference and Exhibit*, Aug. 2000. DOI: 10.2514/6.2000-4565. [Online]. Available: https://arc.aiaa.org/doi/abs/10.2514/6.2000-4565.

[87] C. Miller, "Nonlinear dynamic inversion baseline control law: Flight-test results for the full-scale advanced systems testbed F/A-18 airplane," in *AIAA Guidance, Navigation, and Control Conference 2011*, 2011, ISBN: 9781600869525.

[88] R. E. Perez, H. H. T. Liu, and K. Behdinan, "Multidisciplinary Optimization Framework for Control-Configuration Integration in Aircraft Conceptual Design," *Journal of Aircraft*, vol. 43, no. 6, pp. 1937–1948, Nov. 2006, ISSN: 0021-8669. DOI: 10.2514/1.22263.

[89] R. H. Hoh, D. G. Mitchell, I. L. Ashkqnas, R. H. Klein, R. K. Heffle, and J. Hodgkinson, "Proposed MIL Standard and Handbook - Flying Qualities of Air Vehicles," Systems Technology, Hawthorne,CA, Tech. Rep. AFWAL-TR-82-3081.1, Nov. 1982.

[90] D. G. Mitchell, H. Klyde David, R. H. Hoh, and B. L. Aponso, "Proposed Incorporation of Mission-Oriented Flying Qualities into MIL-STD-1797A.," Wright-Patterson AFB, OH,USA, Tech. Rep. WL-TR-94-3162, Nov. 1994.

[91] S. Tang, "Fault-Tolerant Flight Control with Sensor-Based Nonlinear Dynamic Inversion," Nov. 2014.

[92] J. HODGKINSON, J. WOOD, and R. HOH, "An alternate method of specifying bandwidth for flying qualities," in *Guidance and Control Conference*, Reston, Virigina: American Institute of Aeronautics and Astronautics, Aug. 1982. DOI: 10.2514/6.1982-1609.

[93] J. C. Gibson, "Development of a design methodology for handling qualities excellence in fly by wire aircraft," Ph.D. dissertation, TU Delft, 1999, ISBN: 90-407-1841-5. [Online]. Available: http://resolver.tudelft.nl/uuid:6b564b35-cb74-436c-8c47-845bfbbb8b4d.

[94] D. Atmaca, O. Stroosma, and E. van Kampen, "Piloted Simulator Assessment of an Incremental Nonlinear Dynamic Inversion Controller for the Flying-V," Delft, 2024.

[95] J. Roskam, *Airplane Flight Dynamics and Automatic Flight Controls* (Airplane Flight Dynamics and Automatic Flight Controls dl. 1). Design Analysis and Research Corporation, 1995, ISBN: 9781884885174. [Online]. Available: https://books.google.nl/books?id=RDZUG%E2%80%93o9HMC.

V

Appendices

A

Handling Qualities

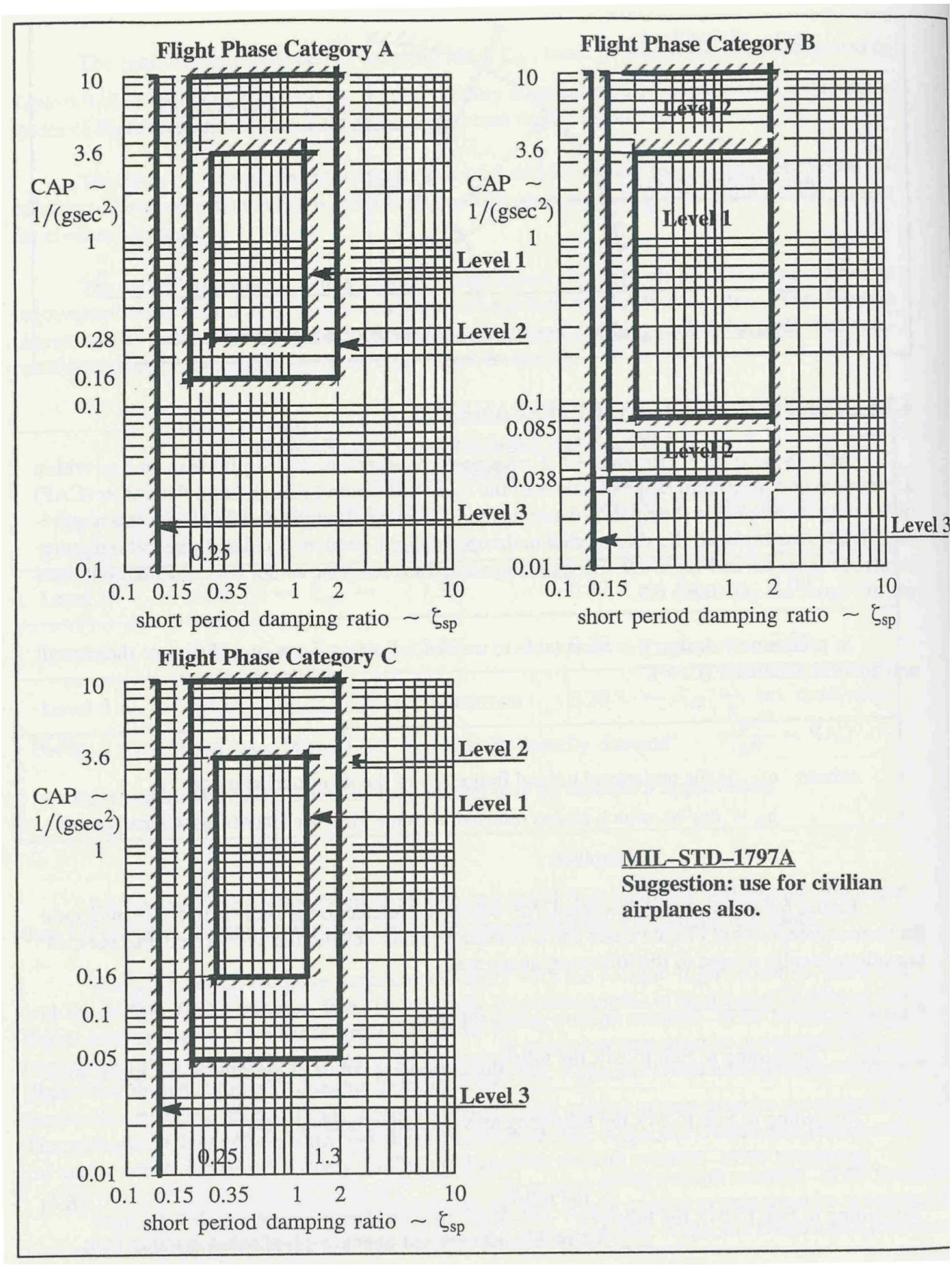

Figure A.1: Control Anticipation Parameter as a function of short period damping handling quality requirements [95]

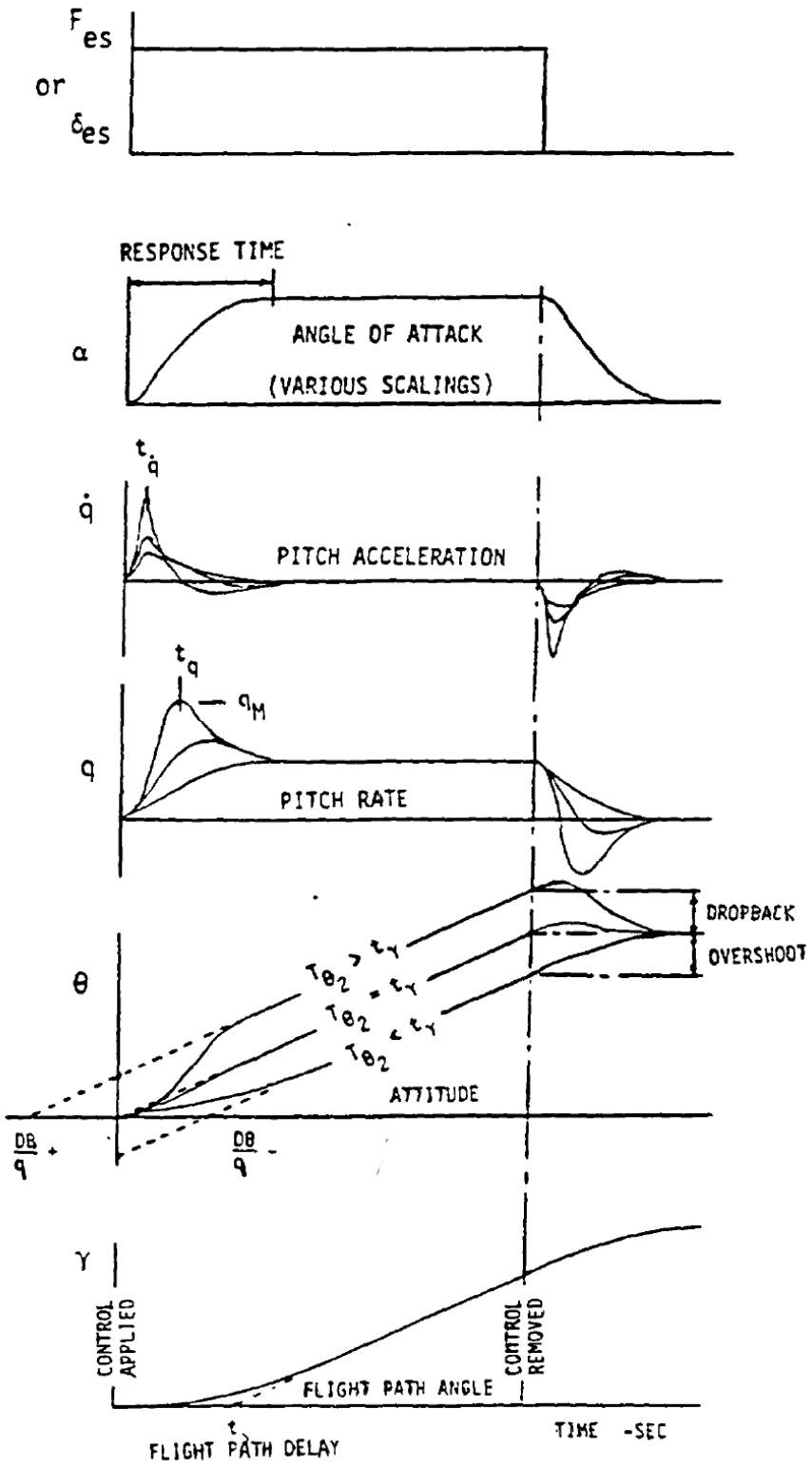

Figure A.2: Short period response, for Gibson criteria [32]

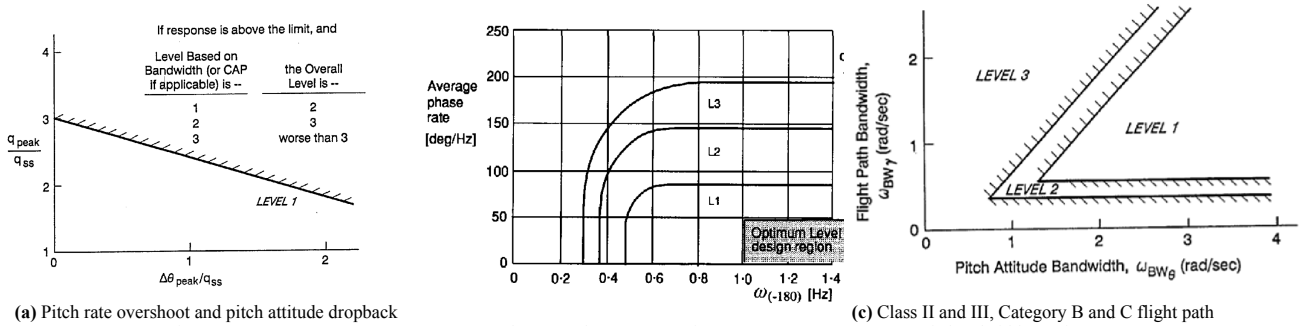

(a) Pitch rate overshoot and pitch attitude dropback requirement [90]

(b) Phase rate frequency requirement [93]

(c) Class II and III, Category B and C flight path angle bandwidth requirements [90]

Figure A.3: Gibson Criteria

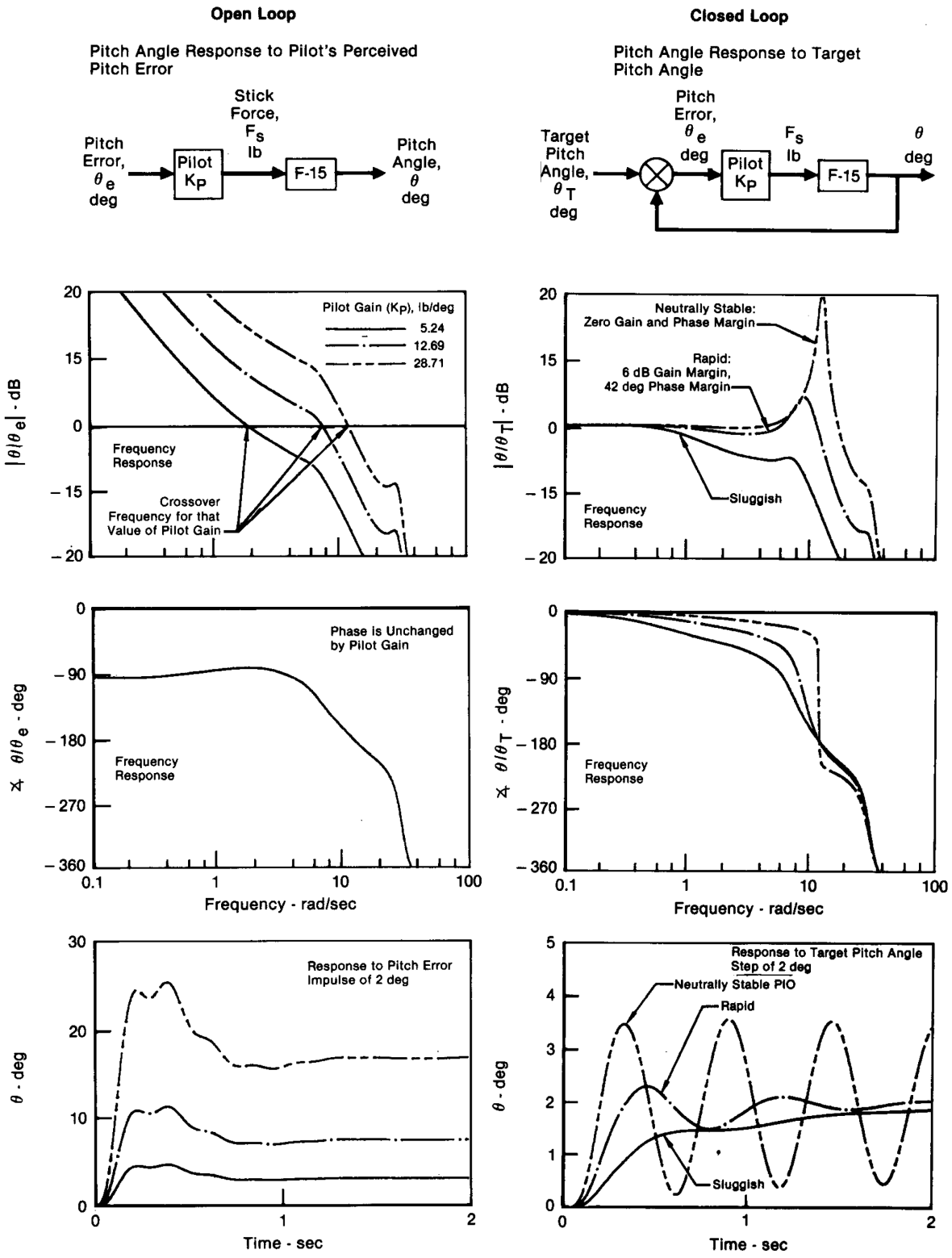

Figure A.4: Open-loop and closed-loop interpretation of pitch bandwidth criterion [92]

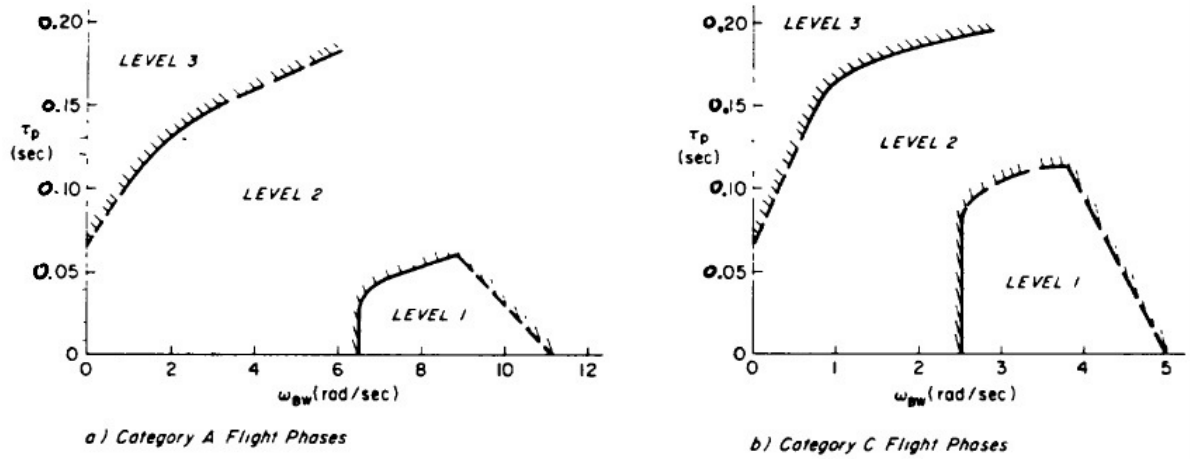

Figure A.5: Bandwidth criterion as per MIL-STD-1797A [90]

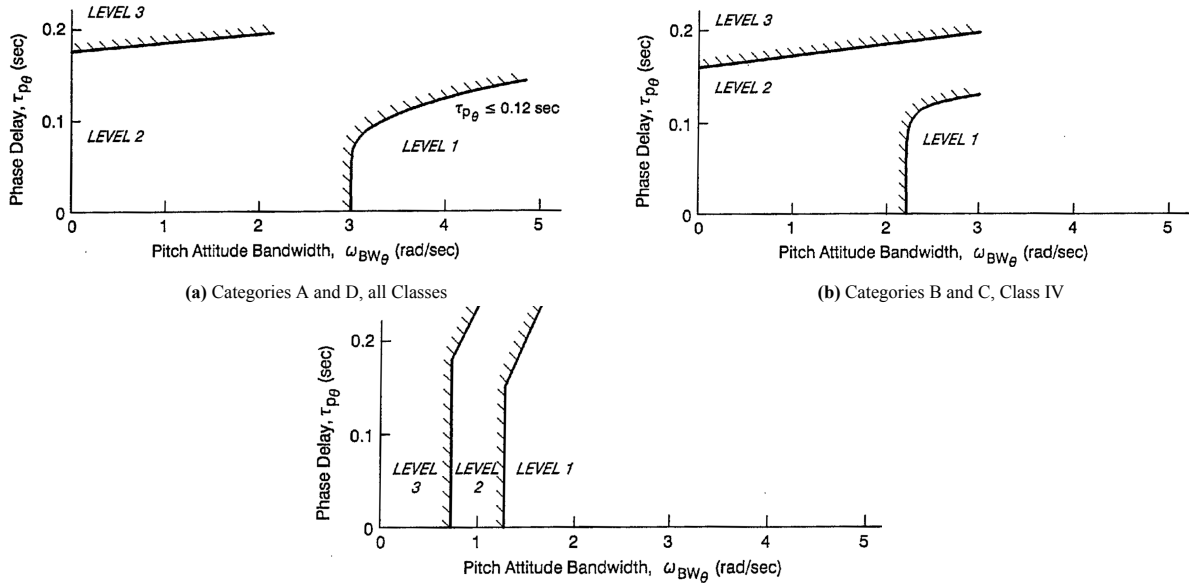

(a) Categories A and D, all Classes

(b) Categories B and C, Class IV

(c) Categories B and C, Classes I, II, and III

Figure A.6: Bandwidth Criteria as per Mitchel et al.[90]